Versatile femtosecond optical parametric oscillator frequency combs for metrology

Karolis Balskus

Submitted for the degree of Doctor of Philosophy
Heriot-Watt University
School of Engineering and Physical Sciences
November 2015

Abstract

This thesis addresses the development of broadly tunable, high repetition rate frequency combs in the mid-IR region. A novel PPKTP crystal design was used to provide phasematching for parametric oscillation and simultaneously give efficient pump+idler sum-frequency generation (SFG). This innovation enabled a fully stabilized idler comb from a 333-MHz femtosecond optical parametric oscillator to be generated in which the carrier envelope offset frequency f_{CEO} together with the repetition frequency f_{REP} were stabilised. This OPO platform was then extended to demonstrate, via harmonic pumping, a fully stabilized 1-GHz OPO frequency comb from a 333-MHz pump laser. Next, an alternative route to a 1-GHz OPO comb was investigated by synchronously pumping an OPO directly with a 1-GHz Ti:sapphire laser. Here the comb was fully stabilized for the signal, idler and pump pulses by using a narrow linewidth CW diode laser developed for the project and whose design is also presented. A further increase in the comb mode spacing was performed with a Fabry-Pérot cavity. A stabilised cavity was used to filter 1.5 μm signal pulses from a 333-MHz repetition rate OPO frequency comb to yield a 10-GHz comb. The length of the Fabry-Pérot cavity was dither locked to a single-frequency ECDL and later on directly to the OPO frequency comb. Finally the 333-MHz OPO comb was demonstrated in an optical frequency metrology experiment. The frequency comb mode number and the absolute frequency of a narrow-linewidth CW laser were measured and the performance of the OPO comb was found to be comparable to that of a commercial fibre laser comb used as a benchmark in the experiment.

Acknowledgements

The results presented in this thesis could not be achieved without a support of many people.

First of all, I would like to thank to my supervisor Professor Derryck Reid, who helped me so much during these 3 years at Heriot-Watt University. You are a bright, patient, talented person. Your way of guiding me through photonic-land was impressive. The effort which you showed towards me made me respond with great experimental results. I wish you the best.

I had the privilege to work with one of the kindest persons I have ever met. Richard McCracken was extremely supportive and helpful. Being near him made me improve much faster than I could ever imagine. The work in the laboratory would not be so fun without Richard by my side.

Beyond this support, I had the pleasure to get know with other members in Ultrafast Optics Group: Dr. Zhaowei Zhang, Dr. Thomas Schratwieser, Dr. Carl Farrell, Dr. Cristtel Ramirez, Dr. Christopher Leburn, Oguzhan Kara, Luke Maidment, Dr. Teresa Ferreiro and Dr. Tobias Lamour. I will always remember you. You all were very supportive and friendly when an equipment or knowledge was needed. Working with you has been extremely easy. Thank you all.

I would like to say thank you to all the staff of Heriot-Watt University. It was my pleasure to be around you, work with you. You are awesome people.

Finally, I would like to say thank you to all my family who supported me during the good and bad times. It was much easier with your support. Dad, I did it! I love you all.

List of publications by the candidate

Peer reviewed journal articles

[1] K. Balskus, Z. Zhang, R. A. McCracken, and Derryck T. Reid, "Mid-infrared 333-MHz frequency comb continuously tunable from 1.95 to 4 μm," Optics Letters 40, 4178-4181 (2015).

[2] K. Balskus, S. M. Leitch, Z. Zhang, R. A. McCracken, and D. T. Reid, "1-GHz harmonically pumped femtosecond optical parametric oscillator frequency comb," Optics Express 23, 1283-1288 (2015).

[3] T. C. Schratwieser, K. Balskus, R. A. McCracken, C. Farrell, C. G. Leburn, Z. Zhang, T. P. Lamour, T. I. Ferreiro, A. Marandi, A. S. Arnold, and D. T. Reid, "^{87}Rb-stabilized 375-MHz Yb:fibre femtosecond frequency comb," Opt. Express 22, 10494–10499 (2014).

[4] R. A. McCracken, K. Balskus, Z. Zhang, and D. T. Reid, "Atomically referenced 1-GHz optical parametric oscillator frequency comb," Optics Express 23, 16466-16472 (2015).

[5] Zhaowei Zhang, Karolis Balskus, Richard A. McCracken, and Derryck T. Reid, "Mode-resolved 10-GHz frequency comb from a femtosecond optical parametric oscillator," Optics Letters 40, 2692-2695 (2015).

[6] Karolis Balskus, Melissa Fleming, Richard A. McCracken, Zhaowei Zhang and Derryck T. Reid, "Carrier-envelope offset frequency stabilization in a femtosecond optical parametric oscillator without nonlinear interferometry," submitted to Optics Letters.

[7] K. Balskus, S. Schilt, V. J. Wittwer, P. Brochard, T. Ploetzing, N. Jornod, R. A. McCracken, Z. Zhang, A. Bartels, D. T. Reid, and T. Sudmeyer, "Optical parametric oscillator frequency comb for frequency metrology in the near-infrared," submitted to Optics Express.

Conference papers

[8] R. A McCracken, K. Balskus, Z. Zhang and D. T Reid, "Observations of complex frequency comb structure in a harmonically-pumped femtosecond optical parametric oscillator," 23rd International Laser Physics Workshop (LPHYS'14), Journal of Physics: Conference Series (2015).

[9] K. Balskus, S. Leitch, Z. Zhang, R. McCracken, and D. T. Reid, "1-GHz Harmonically Pumped Femtosecond Optical Parametric Oscillator Frequency Comb," in CLEO:2015, Paper STh1N.6 (Optical Society of America, 2015), p. STh1N.6.

[10] K. Balskus, S. M. Leitch, Z. Zhang, R. A. McCracken, D. T. Reid, "1-GHz harmonically

pumped femtosecond optical parametric oscillator frequency comb," paper presented at Ultrafast Optics 2015, Beijing, China (2015).

[11] Karolis Balskus, Zhaowei Zhang, Richard A. McCracken, and Derryck T. Reid, "Mid-Infrared 333-MHz Frequency Comb Continuously Tunable from 1.95 μm to 4.0 μm," in CLEO:2015 Paper STh1N.7, (Optical Society of America, 2015), p. STh1N.7.

[12] K. Balskus, Z. Zhang, R. A. McCracken, D. T. Reid, "Mid-infrared 333-MHz frequency comb continuously tunable from 1.95 μm to 4.0 μm," poster presented at CLEO/Europe, Munich, Germany (2015).

[13] K. Balskus, Z. Zhang, R. A. McCracken, D. T. Reid, "Mid-infrared 333-MHz frequency comb continuously tunable from 1.95 μm to 4.0 μm," paper presented at Ultrafast Optics 2015, Beijing, China (2015).

[14] S. Schilt, K. Balskus, V. J. Wittwer, P. Brochard, T. Ploetzing, N. Jornod, R. A. McCracken, Z. Zhang, A. Bartels, D. T. Reid, T. Sudmeyer, "Noise characterization and optical frequency measurement with an optical parametric oscillator frequency comb," 8th Symposium on Frequency Standards and Optical Metrology (2015).

[15] R. A. McCracken, K. Balskus, Z. Zhang, D. T. Reid, "Composite 1-GHz optical parametric oscillator frequency comb from 400 – 1900 nm," paper presented at Ultrafast Optics 2015, Beijing, China (2015).

[16] R. A. McCracken, K. Balskus, Z. Zhang, D. T. Reid, "Composite 1-GHz optical parametric oscillator frequency comb from 400 - 1900 nm," poster session presented at CLEO: Science and Innovations 2015, San Jose, United States (2015).

[17] Z. Zhang, K. Balskus, R. A. McCracken, D. T. Reid, "Comb-mode resolved laser frequency comb by Fabry-Pérot-cavity filtering of a femtosecond optical parametric oscillator," paper presented at Ultrafast Optics 2015, Beijing, China (2015).

[18] R. A. McCracken, K. Balskus, Z. Zhang, and D. T. Reid, "Atomically referenced 1-GHz optical parametric oscillator frequency comb," paper presented at Ultrafast Optics 2015, Beijing, China (2015).

Contents

Chapter 1. Introduction

1.1 Aim

In this thesis I describe the generation of stable, broadband, high precision optical frequency combs which could be used in a number of application areas. Specifically, I describe the development and characterization of a stabilised optical parametric oscillator frequency comb in the mid-infrared (IR) region. One area of emphasis is the increase to GHz rates of the repetition frequency; the associated increase in the comb mode separation is useful since individual comb modes can be identified using optical spectrographs of standard resolution. Routes to higher repetition rates which were investigated included harmonically pumping the OPO and filtering it with a Fabry-Pérot cavity to extend the spacing up to 10 GHz. Another area of emphasis is the extension of the wavelength coverage of OPO combs, which led to a comb suitable for use in high resolution spectroscopy and metrology experiments. The metrology experiment confirmed that the comb can be used for precise measurements of an unknown optical frequency. In this chapter I will introduce the principles and applications of stabilised frequency combs. Finally, a research outline is presented.

1.2 Stabilised optical frequency combs

In the time domain a modelocked laser emits pulses every round trip which in the frequency domain comprise a collection of modes, uniformly spaced by the repetition frequency. For a true frequency comb, the repetition rate and carrier-offset frequencies must be stabilised. The repetition rate drifts due to cavity length changes because of temperature effects, while the carrier-envelope-offset frequency f_{CEO} changes due to environmental factors changing the intracavity dispersion. After the stabilisation of f_{REP} and f_{CEO}, the comb line separation and position in the frequency domain are fixed, resulting in a locked frequency comb. Frequency combs can be used in spectroscopy, astronomy, metrology and attosecond pulse generation [1, 2, 3]. The first absolute frequency measurement of a Cs D line was done in 1999 [4]. The f_{CEO} of Ti:sapphire laser was stabilised with the f-2f self-referencing technique. A Ti:sapphire frequency comb was used as a reference to determine the frequency of a CW laser locked to a rubidium transition line and in 2001 the Ti:sapphire laser comb was used to measure the absolute optical frequency of a calcium transition [5]. Since then a number of different applications have been enabled by stabilised laser combs.

Stabilised frequency combs can be achieved directly from lasers, but also from an optical parametric oscillator (OPO) by pumping with a femtosecond laser. Such OPOs represent the highest average power and most efficient sources of mid-IR combs [6]. Their output wavelengths have (to date) been extended up to 4.8 μm [6, 7] and instrument-limited f_{CEO} beat linewidths of 15 Hz have been achieved [8]. Degenerate OPOs have been reported which emit spectra instantaneously covering 900 cm^{-1} at 3 μm [9]. Table 1 shows the most cited papers on the frequency combs in the mid-IR region and the papers presented in this thesis are specifically marked. Almost all of those systems used PPLN as the gain crystal and covered wavelengths from 1.9-4.8 µm in the idler. There are also several degenerate OPOs, which were pumped with Erbium doped fiber lasers at 1.56 µm. Those OPOs oscillated at a 3.1-µm central wavelength and spanned from 2.5-3.8 µm at most. For degenerate OPOs increasing the wavelength is challenging since a longer wavelength pump source must be used and moreover, the PPLN crystal is less transmissive at wavelengths above 5 µm. Thulium based fiber laser systems have been used to increase the OPO output wavelength up to 4 µm [10]. A further increase up to 5.6 µm was achieved by using a Kerr-lens modelocked Cr^{2+}:ZnSe laser system to pump a GaAs OPO [11, 12]. In this thesis I will present a comb, which could be tuned from 1.95-4.0 µm, thus representing an octave spanning frequency comb which was lockable at every idler wavelength. Another important parameter is the repetition rate. As we can see from Table 1, the pump laser repetition rates are below 1 GHz, but in emerging applications like the use of combs in astronomical spectrographs a GHz or even multi-GHz mode spacing is preferable and therefore the need to increase the repetition rate of the comb is obvious. Several articles have demonstrated GHz repetition rate combs [13, 14, 15]. These high repetition rate combs were implemented for a signal wavelength at around 1.5 µm and their extension into the mid-IR region is still in progress. In my thesis I will present a 333-MHz frequency comb, whose mode spacing could be increased up to 1-GHz via harmonic pumping. The 333-MHz comb was also filtered with a Fabry-Pérot cavity up to 10 GHz. All the experiments showed great potential and genuine competitiveness in comparison with other systems.

Table 1. Near- to mid-infrared coverage of OPO frequency combs, with work from this thesis indicated (*).

Year	Power (mW)	Coverage (µm)	f_{REP} (MHz)	Pump laser	Process	Reference
2007	-	1.9-2.4	200	Ti:sapp	OPO	[6]
2009	1500	2.8-4.8	136	Yb-fiber	OPO	[7]
2010	1000	2.8-4.8	137	Yb-fiber	OPO	[16]
2011	60	2.5-3.8	80	Er-fiber	deg. OPO	[9]
2011	10	4.4-5.4	182	Cr^{2+}:ZnSe	OPO	[11]
2011	60	2.6-3.6	100	Er-fiber	deg. OPO	[17]
2012	400	2.8-4.8	137	Yb-fiber	OPO	[18]
2012	37	3.1-5.9	75	Tm-fiber	deg. OPO	[10]
2012	-	1.6	1000	Ti:sapp	deg. OPO	[46]
2013	100	3.23-3.4	100	Yb:KGW	OPO	[19]
2014	220	2.7-4.2	90	Yb-fiber	OPO	[20]
2014	8.5	3.05-3.15	500	Er-fiber	deg. OPO	[21]
2015	26	3.5-5.6	175	Cr^{2+}:ZnS	OPO	[12]
2015	50	1.46	1000	Ti:sapp	OPO	[22]*
2015	0.3	1.46	10000	Ti:sapp	OPO	[23]*
2015	20	1.95-4.0	333	Ti:sapp	OPO	[24]*
2015	-	1.56	1000	Ti:sapp	OPO	[14]*

1.3 Thesis outline

This thesis is organised as follows:
Chapter 2 introduces the fundamentals of nonlinear optics together with a description of ultrashort pulse propagation. The linear and nonlinear effects described here form the basis of the OPO systems reported.

Chapter 3 present details of the Ti:sapphire laser and the OPO sources. The OPO was pumped by a repetition-frequency stabilised Laser Quantum 333 MHz Ti:sapphire laser, which is described in detail. The OPO design and characterization is presented.

Chapter 4 reports a fully stabilized idler comb from a 333-MHz femtosecond optical parametric oscillator in which the carrier envelope offset f_{CEO} was stabilised in the mid-infrared region. The design of a novel PPKTP crystal is presented which provided phasematching for parametric oscillation and efficient pump+idler sum-frequency generation (SFG). An introduction to the stabilisation of the repetition rate, carrier-envelope-offset and their characterization by measurements of the phase-noise and two-sample frequency deviation is presented.

Chapter 5 presents for the first time a locked femtosecond frequency comb achieved from a harmonically-pumped OPO. A noise analysis together with measurements of the timing jitter are presented.

Chapter 6 reports the demonstration of a fully stabilized 1-GHz OPO frequency comb. All the outputs from the OPO and the pump laser were locked. Fully stabilized frequency combs for the signal, idler and pump pulses were achieved by using a narrow linewidth CW diode laser developed for the project and whose design is also presented.

Chapter 7 details a stabilized Fabry-Pérot cavity which was used to filter a 333-MHz repetition rate OPO frequency comb to yield a 10-GHz comb. The length of the Fabry-Pérot cavity was dither locked to a single-frequency ECDL and later directly on to the OPO frequency comb.

Chapter 8 presents the results of measuring the frequency comb mode number and the absolute frequency of a narrow-linewidth CW laser. The acquired heterodyne beat in the radio frequency (RF) region could be easily compared with a well-known Rb reference. The linewidth of the comb line was determined by heterodyning a frequency comb line with the ultra-narrow linewidth CW laser. Frequency noise power spectral density (PSD) measurements were used to reveal all of the noise accumulated in the system.

Chapter 9 contains conclusions from the experiments presented in this thesis. Future improvements to the systems are proposed.

References

[1] F. Keilmann, C. Gohle, and R. Holzwarth, "Time domain mid infrared frequency comb spectrometer," Optics Letters 29, 1542-1544 (2004).

[2] T. Steinmetz, T. Wilken, C. Araujo-Hauck, R. Holzwarth, T. W. Hänsch, L. Pasquini, A. Manescau, S. D'Odorico, M. T. Murphy, T. Kentischer, W. Schmidt, and T. Udem, "Laser frequency combs for astronomical observations," Science 321, 1335–1337 (2008).

[3] R. K. Shelton, L. S. Ma, H. C. Kapteyn, M. M. Murnane, J. L. Hall, and J. Ye, "Phase-coherent optical pulse synthesis from separate femtosecond lasers," Science 293, 1286-1289 (2001).

[4] Th. Udem, J. Reichert, R. Holzwarth, and T. W. Hansch, "Absolute Optical Frequency Measurement of the Cesium D_1 Line with a Mode-Locked Laser," Phys. Rev. Lett. 82, 3568 (1999).

[5] T. Udem, S. A. Diddams, K. R. Vogel, C. W. Oates, E. A. Curtis, W. D. Lee, W. M. Itano, R. E. Drullinger, J. C. Bergquist, and L. Hollberg, "Absolute frequency measurement of the Hg^+ and Ca optical clock transition with a femtosecond laser," Phys. Rev. Lett. 86, 4996-4999 (2001).

[6] J. H. Sun, B. J. S. Gale, and D. T. Reid, "Composite frequency comb spanning 0.4–2.4 μm from a phase-controlled femtosecond Ti:sapphire laser and synchronously pumped optical parametric oscillator," Optics Letters 32, 1414 (2007).

[7] F. Adler, K. C. Cossel, M. J. Thorpe, I. Hartl, M. E. Fermann, and J. Ye, "Phase-stabilized, 1.5 W frequency comb at 2.8-4.8 μm," Optics Letters 34, 1330 (2009).

[8] T. I. Ferreiro, J. Sun, and D. T. Reid, "Frequency stability of a femtosecond optical parametric oscillator frequency comb," Optics Express 19, 24159 (2011).

[9] N. Leindecker, A. Marandi, R. L. Byer, and K. L. Vodopyanov, "Broadband degenerate OPO for mid-infrared frequency comb generation," Optics Express 19, 6296 (2011).

[10] Nick Leindecker, Alireza Marandi, Robert L. Byer, Konstantin L. Vodopyanov, Jie Jiang, Ingmar Hartl, Martin E. Fermann, and Peter G. Schunemann, "Nearly 3-6 μm Spectral Comb Derived from Tm Mode-locked Laser using GaAs-based Degenerate OPO," Conference on Lasers and Electro-Optics CF3B.3 (2012).

[11] K. L. Vodopyanov, E. Sorokin, I. T. Sorokina, and P. G. Schunemann,"Mid-IR frequency comb source spanning 4.4-5.4 μm based on subharmonic GaAs optical parametric oscillator," Optics Letters 36, 2275-2277 (2011).

[12] Viktor O. Smolski, Sergey Vasilyev, Peter G. Schunemann, Sergey B. Mirov, and Konstantin Vodopyanov, "Cr:ZnS Laser-pumped Subharmonic GaAs OPO with an Instantaneous

Bandwidth 3.6-5.6 μm," CLEO: 2015 OSA Technical Digest (online) (Optical Society of America, 2015), paper SW4O.2 (2015).

[13] Markku Vainio, Mikko Merimaa, Lauri Halonen, and Konstantin Vodopyanov, "Degenerate 1 GHz repetition rate femtosecond optical parametric oscillator," Optics Letters 37, 4561-4563 (2012).

[14] R. A. McCracken, K. Balskus, Z. Zhang, and D. T. Reid, "Atomically referenced 1-GHz optical parametric oscillator frequency comb," Optics Express 23, 16466-16472 (2015).

[15] R. Gebs, T. Dekorsy, S. A. Diddams, and A. Bartels, "1-GHz repetition rate femtosecond OPO with stabilized offset between signal and idler frequency combs," Optics Letters 16, 5397-5405 (2008).

[16] Florian Adler, Piotr Masłowski, Aleksandra Foltynowicz, Kevin C. Cossel, Travis C. Briles, Ingmar Hartl, and Jun Ye, "Mid-infrared Fourier transform spectroscopy with a broadband frequency comb," Optics Express 18, 21861-21872 (2010).

[17] Nicholas Leindecker, Alireza Marandi, Konstantin L. Vodopyanov, Robert L. Byer, "Mid-IR spectral comb with broad instantaneous bandwidth using subharmonic OPO," Proc. SPIE 7917-7918 (2011).

[18] A. Foltynowicz , P. Masłowski, A. J. Fleisher, B. J. Bjork, J. Ye, "Cavity-enhanced optical frequency comb spectroscopy in the mid-infrared application to trace detection of hydrogen peroxide," Applied Physics B 110, 163-175 (2012).

[19] Zhaowei Zhang, Tom Gardiner, and Derryck T. Reid, "Mid-infrared dual-comb spectroscopy with an optical parametric oscillator," Optics Letters 38, 3148-3150 (2013).

[20] Yuwei Jin, Simona M. Cristescu, Frans J. M. Harren, and Julien Mandon, "Two-crystal mid-infrared optical parametric oscillator for absorption and dispersion dual-comb spectroscopy," Optics Letters 39, 3270-3273 (2014).

[21] Kirk A. Ingold, Alireza Marandi, Charles W. Rudy, Konstantin L. Vodopyanov, and Robert L. Byer, "Fractional length sync pumped degenerate optical parametric oscillator for 500 MHz 3 μm midinfrared frequency comb generation," Optics Letters 39, 900-903 (2014).

[22] K. Balskus, S. M. Leitch, Z. Zhang, R. A. McCracken, and D. T. Reid, “1-GHz harmonically pumped femtosecond optical parametric oscillator frequency comb," Optics Express 23, 1283-1288 (2015).

[23] Zhaowei Zhang, Karolis Balskus, Richard A. McCracken, and Derryck T. Reid, ”Mode-resolved 10-GHz frequency comb from a femtosecond optical parametric oscillator,” Opt. Lett. 40, 2692-2695 (2015).

[24] K. Balskus, Z. Zhang, R. A. McCracken, and Derryck T. Reid, "Mid-infrared 333-MHz frequency comb continuously tunable from 1.95 to 4 μm," Optics Letters 40, 4178-4181 (2015).

Chapter 2. Fundamentals of optical parametric oscillators

2.1 Introduction

This chapter presents the fundamental concepts of nonlinear optics which are necessary to understand the operation of optical parametric oscillators (OPOs) and supercontinuum generation in photonic crystal fiber (PCF).

2.2 Fundamentals of nonlinear optics

A high intensity electromagnetic field disturbs the position of electrons in a material and leads to a nonlinear relationship between the irradiance and the amplitude of the resulting electronic oscillations. The electrons start to emit different frequencies to that of the incident light. This nonlinear response is responsible for second-harmonic generation (SHG), sum frequency generation (SFG), different frequency generation (DFG) and parametric amplification, which can be explained in terms of the second-order χ^2 susceptibility. Other nonlinear effects such as self-phase modulation (SPM), two-photon absorption and four-wave mixing are associated with the third-order χ^3 susceptibility.

2.2.1 Nonlinear susceptibility

An intense wave propagating in a dielectric material displaces the valence electrons from their original positions, causing an electric polarization of the material. At high intensities this electric polarization is not proportional to the electric field, so the induced dipoles emit electromagnetic waves at different frequencies. The electric polarisation is proportional to the electric field strength expressed as an electric susceptibility χ_e. For a weak electric field $E(\omega)$ the electric polarization $P(\omega)$ is expressed as

$$P(\omega) = \epsilon_0 \chi^1 E(\omega) \tag{1}$$

where ϵ_0 is the vacuum permittivity and χ^1 is the first-order - linear - susceptibility. This expression is valid only for weak electric fields such as an incoherent white light source or low peak power laser beams. In the case of intense fields, such as the femtosecond pulses emitted from a modelocked laser cavity, the polarization of the dielectric medium can be described by extending equation (1) [1] as

$$P(\omega) = \epsilon_0 \chi^1 E(\omega) + \epsilon_0 \chi^2 E(\omega)^2 + \epsilon_0 \chi^3 E(\omega)^3 + ... \tag{2}$$

where χ^2 and χ^3 are the second- and third-order electric susceptibilities respectively. Each susceptibility term χ^n is related different nonlinear processes. The linear or first-order term of the susceptibility χ^1 is associated with the linear refractive index and its dependence on the frequency, and gives rise to linear dispersion, birefringence, and linear absorption (Beer's law). The second-order electric susceptibility χ^2 is responsible for all interactions involving three-wave mixing, such as second-harmonic generation (SHG), sum and difference frequency generation (SFG and DFG), parametric oscillation and amplification.

The third-order nonlinear susceptibility χ^3 mediates four-wave mixing effects, including third-harmonic generation (THG), the Kerr effect (self-focusing, self-phase modulation(SPM), cross-phase modulation (CPM), Raman scattering and Brillouin-scattering processes.

2.2.2 Pulse propagating in a nonlinear medium

The nonlinear interactions related to the χ^2 susceptibility occur without energy dissipation into the medium since the photon energy is conserved. These nonlinear processes are highly efficient because all interactions between the different frequencies proceed through virtual energy levels and therefore no thermal effects occur and no cooling is required. The only limiting factors are the material damage threshold and photo-refractive effects. Second-order effects are observed only in non-centrosymmetric materials.

In centrosymmetric materials only first- and third-order χ^3 effects are obtained because of the lattice symmetry. The applied external electric field equally polarizes the dipole and therefore the nonlinear susceptibility χ^2 is equal to zero.

2.2.3 Media exhibiting χ^2 nonlinearity

As mentioned before a number of nonlinear interactions take place in second-order χ^2 materials. The most common two-wave mixing can be expressed as

$$E(\omega) = E_1 \mathrm{cos}(\omega_1 t) + E_2 \mathrm{cos}(\omega_2 t) \tag{3}$$

in which a third field E can be generated. As we take into account first- (χ^1) and second-order (χ^2) susceptibility terms of the equation we can express the polarization field as [2]

$$\begin{aligned} P(\omega_1, \omega_2) = {} & \epsilon_0 \chi^1 [E_1 \mathrm{cos}(\omega_1 t) + E_2 \mathrm{cos}(\omega_2 t)] \\ & + \epsilon_0 \chi^2 [2 E_1 E_2 \mathrm{cos}(\omega_1 t) \mathrm{cos}(\omega_2 t) \\ & + E_1^2 \mathrm{cos}^2(\omega_1 t) + E_2^2 \mathrm{cos}^2(\omega_2 t)] \end{aligned} \tag{4}$$

This equation can be simplified by using the trigonometric identities, $\mathrm{cos}^2(x) = (1 + \mathrm{cos}(2x))/2$ and $\mathrm{cos}(x)\mathrm{cos}(y) = (\mathrm{cos}(x - y) + \mathrm{cos}(x + y))/2$. The result implies that two waves show the possibility of generating different frequencies in a second order χ^2 material, each corresponding to a different physical effect:

$$\begin{aligned} &P = \epsilon_0\chi^1[E_1\cos(\omega_1 t) + E_2\cos(\omega_2 t)] && \text{Linear dispersion and refraction}\\ &\frac{\epsilon_0\chi^2 E_1E_2}{2}\cos([\omega_1 - \omega_2]t)] && \text{Difference frequency generation}\\ &\frac{\epsilon_0\chi^2 E_1E_2}{2}\cos([\omega_1 + \omega_2]t)] && \text{Sum frequency generation}\\ &\frac{\epsilon_0\chi^2 E_1^2}{2}\cos(2\omega_1 t) && \text{Second harmonic generation}\\ &\frac{\epsilon_0\chi^2 E_2^2}{2}\cos(2\omega_2 t) && \text{Second harmonic generation}\\ &\frac{\epsilon_0\chi^2}{2}[E_1^2 + E_2^2) && \text{Electro-optical rectification} \end{aligned} \tag{5}$$

The first term corresponds to the interference field, giving rise to linear refraction and dispersion, while the second and third terms represent difference frequency generation (DFG) and sum frequency generation (SFG). Each wave ω_1 and ω_2 interacting with a nonlinear medium can generate an independent second harmonic SHG wave. The last term describes electro optical rectification (EOR).

The evolution of three waves interacting with each other in a χ^2 material is described by using coupled-wave equations which will be presented later in this chapter. The coupled wave equations are solved by assuming that all the interacting waves are monochromatic and the pulses are narrowband. In the case of ultrashort or broadband pulses the coupled wave equations do not accurately describe the pulse evolution. A more accurate broadband pulse propagation through a χ^2 medium can be provided using the nonlinear envelope equation (NEE) [3]. Conforti demonstrated in 2010 that ultra-broadband second order parametric interactions can be described by a single-wave envelope equation. The evolution of a pulse in the transparency region of the nonlinear medium can be modeled using the Conforti equation. In plane geometries the resulting single-wave envelope equation is

$$\begin{aligned} &\frac{\delta A}{\delta z'} + iDA = -i\frac{\chi^2\omega_0^2}{4\beta_0 c^2}\left(1 + \frac{i}{\omega_0}\frac{\delta}{\delta\tau}\right)[A^2\exp^{i\omega_0 t - i(\beta_0 - k_1\omega_0)z}\\ &+ 2|A|^2\exp^{-i\omega_0 t + i(\beta_0 - k_1\omega_0)z}] \end{aligned} \tag{6}$$

where A$(z,\, \tau)$ is the broadband complex electric field envelope at a reference frequency of ω_0, $k(\omega) = \frac{\omega}{c}\sqrt{1 + \chi^{(1)}(\omega)}$ is the propagation constant and v_g is the group velocity at the reference frequency. $\tau = t - \frac{z}{v_g}$ represents a coordinate system moving with the reference group frequency, $D = \sum\limits_{m>=2}^{\infty} \frac{i^{m+1}}{m!}\beta_m \frac{d^m}{dt^m}$ and $\beta_m = \frac{\delta^m k}{\delta\omega^m}$.

This NEE includes all possible second order parametric processes that could occur in χ^2 media. The method describes how broadband pulses interact with each other, where SFG and DFG processes appear by taking into account group velocity mismatch and inter-wave phase relationships. The equation can be solved by implementing a split-step Fourier method [4]. The linear left-hand side of the equation was solved in the frequency domain and the nonlinear right-hand side was integrated by a second-order Runge-Kutta scheme for the nonlinear step.

2.2.4 Media exhibiting χ^3 nonlinearity

In our experiments photonic crystal fibre (PCF) was used for supercontinuum generation as part of the frequency comb locking scheme. The supercontinuum generation occurs because of the Kerr effect, which is an intensity dependent effect. A strong electric field propagating through a Kerr medium modulates the refractive index n of the medium, therefore femtosecond pulses can experience SPM, acquiring an instantaneous frequency shift which results in spectral pulse broadening. Together with SPM, other nonlinear optical effects may take place such as four-wave mixing, SHG and parametric amplification. The refractive index n for Kerr medium can be expressed as

$$n(t) = n_0 + n_2 I(t) \tag{7}$$

where n_0 is the refractive index of the material, n_2 is the nonlinear index and $I(t)$ is the optical intensity. The additional phase shift experienced by the pulse over a propagation distance L is

$$\phi_{SPM}(t) = \frac{\omega n_2 L}{c} I(t) \tag{8}$$

This time-dependent phase shift results in a instantaneous frequency shift, with a femtosecond pulse experiencing red-shifting and blue-shifting of its wavelengths because of the third-order χ^3 electric susceptibility. New frequencies are created as a high peak power pulse is propagating through the Kerr medium (Figure 1). As the pulse spectrally broadens, four-wave mixing processes appear. These nonlinear processes require phase-matching to be fulfilled but because fibers can be very long, femtosecond pulses of even low peak power can experience broadening. As an intense pulse continues to propagate through a χ^3 nonlinear medium, its spectrum will broaden because of SPM, four-wave mixing and Raman scattering processes.

The generalised nonlinear Schrodinger equation must be solved in order to characterise ultrafast pulse propagation in a fiber. The equation used by John Dudley and Roy Tayler [5] describes an optical pulse envelope evolution (the spectral broadening in fibers)

$$\frac{\delta A}{\delta z} + \frac{\alpha}{2} A - \sum_{k>=2} \frac{i^{k+1}}{k!} \beta_k \frac{\delta^k A}{\delta T^k} = i\gamma(1 + i\tau_{shock} \frac{\delta}{\delta T})(A(z,t) \int_{-\infty}^{\infty} R(T^{'}) |A(z, T - T^{'})|^2 dT^{'}) \tag{9}$$

The left side of the equation models linear propagation effects. α is a constant related to the linear power loss. The sum over β_k represents the effective wavevector expansion of all β terms (the dispersion coefficients related to the Taylor expansion of $\beta(\omega)$ about a central frequency ω_0) which depends on the photonic crystal fiber (PCF) properties. $A(z,t)$ is the field/pulse complex spectral envelope after propagating z distance. The right side of the equation contains nonlinear effects. γ is the Kerr medium nonlinearity coefficient based on the nonlinear refractive index n_2 and A_{eff} (the effective mode area). The nonlinear coefficient γ is frequency dependent according to the relation

$$\gamma = \frac{\omega_0 n_2(\omega_0)}{cA_{eff}(\omega_0)} \tag{10}$$

where ω_0 is the fundamental frequency, $n_2(\omega_0)$ is the nonlinear refractive index and $A_{eff}(\omega_0)$ is the effective mode area [6]. The integral represents a nonlinear Raman scattering process with the nonlinear response function of silica $R(T^{'})$

$$R(t) = (1-\mathcal{F}_{\mathcal{R}})\delta(t) + \mathcal{F}_{\mathcal{R}} h_R(t) = (1-\mathcal{F}_{\mathcal{R}})\delta(t) + \mathcal{F}_{\mathcal{R}} \frac{\tau_1^2+\tau_2^2}{\tau_1\tau_2^2} \exp^{\frac{-t}{\tau_2}} \sin(\frac{t}{\tau_1})\Theta(t) \tag{11}$$

where $\mathcal{F}_{\mathcal{R}} = 0.18$ is the fractional contribution of the delayed Raman response, $\tau_1 = 12.2$ fs and $\tau_2 = 32$ fs. The $\Theta(t)$ and $\delta(t)$ are the Heaviside step function and Dirac delta function accordingly.

The time-dependent term on the right-hand side of the equation describes the nonlinearity dispersion. The time derivative describes the nonlinearity dispersion characterized by the time scale $\tau_{shock} = \frac{1}{\omega_0}$ which is the optical shock formation time. As the pulse propagates through the PCF, it exhibits more and more nonlinearity and therefore the optical shock term τ_{shock} can be tailored to fulfill the function. With certain parameters of a fiber, the evolution of the pulse can be simulated. The input data requires three parameters to be included: $E(t)$, the nonlinear coefficient γ and the fiber dispersion in the form of its D-curve. From the D-curve the dispersion expansion coefficients can be calculated. The dispersion of a fiber is related to its the second-order dispersion

$$D = -\frac{2\pi c}{\lambda^2}\beta_2 = -\frac{2\pi c}{\lambda^2}\frac{\delta^2\beta}{\delta\omega^2} \tag{12}$$

where D represents dispersion (ps/nm/km), c is the the speed of light and λ is the wavelength.

The purpose of the modelling was to determine the pulse spectral broadening in photonic crystal fiber (PCF). As an ultrashort high peak power pulse enters the fiber, because of the Kerr effect, the pulse spectrally expands. Depending on the pulse peak power, the spectral broadening can be extremely efficient. As the pulse propagates through the PCF, its duration can also increase. As a result the peak power of the pulse falls and therefore most of pulse broadening happens in the first several cm of the highly nonlinear fiber. We used a 30-cm PCF, but a supercontinuum spreading down to 500 nm could be achieved in only the first half of the fiber length. The Dudley equation can be used to estimate the necessary fiber length so that the broadening can be achieved in the shortest possible length of the fiber and the temporal expansion can be minimized.

As described later in Chapter 4(a), a supercontinuum was produced by focusing 10% of the Ti:sapphire pump power into an NKT PCF (NL-2.0-740). A ThorLabs C110TMD-B aspheric lenses (f=6.24 mm) focal length lens was placed in front of the PCF to permit focusing of the

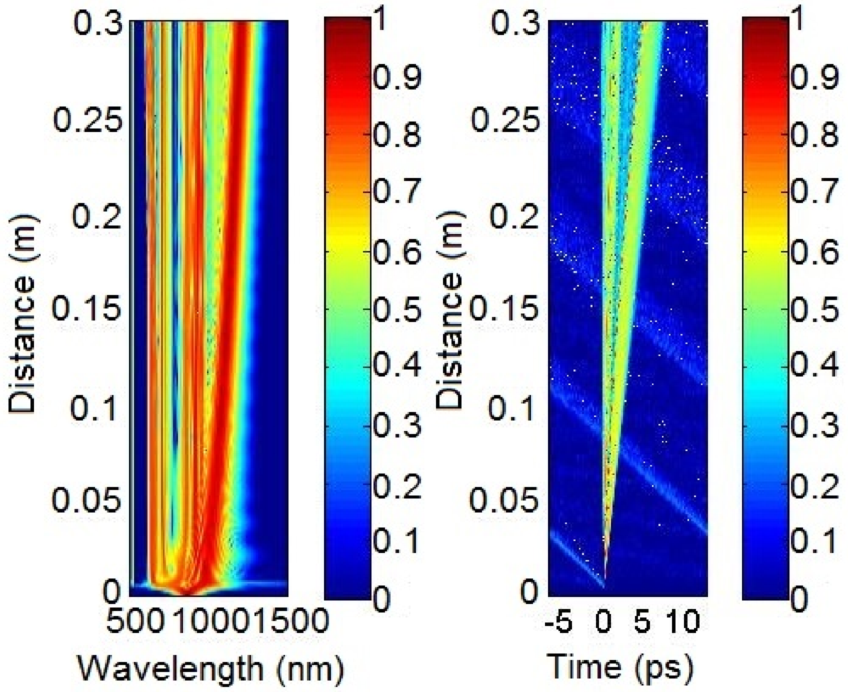

Figure 1. The simulated spectral (left) and temporal (right) broadening of the pump pulses from the 333 MHz Ti:sapphire laser in a 30 cm PCF. A supercontinuum output reaching as low as 510 nm can be generated.

pump beam into the PCF. The nonlinear fiber had a length of 30 cm with a core diameter of 2 μm and a zero dispersion at 740 nm wavelength. For the simulation we used 100 mW average input power, $\gamma = 0.018$, pulse duration τ_P=30 fs and a Gaussian-shaped pump pulse. After a coupling of 67% had been achieved, an output spectrum spanning from 510 nm to 1200 nm was measured. The experimental and theoretical spectra of the supercontinuum were found to overlap quite well. The numerical calculation of the Dudley nonlinear equation for our parameter fibre is presented in Figure 1.

2.3 Parametric nonlinear frequency conversion

Earlier I discussed frequency doubling, sum and difference frequency generation, parametric oscillation and amplification, and supercontinuum generation are the result of different optical nonlinear processes. In order to efficiently generate new frequency components a phasematching condition must be ensured. In the following sub-sections I will introduce the coupled-wave equations and the solutions for several nonlinear processes appearing in our experiments.

2.3.1 The coupled wave equations

An intense electric field induces a nonlinear response of the dielectric medium leading to the generation of new frequencies. These interacting fields are coupled to each other. The coupled wave equations describe the relationship between these fields, and how the energy is exchanged between three interacting waves in a second order χ^2 material when the waves are propagating through a non-centrosymmetric medium. The radiated field created by the medium can be addressed by solving the standard wave equation containing an additional second order nonlinear polarization term [1]

$$\bigtriangledown^2 E - \frac{1}{c^2}\frac{\delta^2 E}{\delta t^2} = \frac{1}{\epsilon_0 c^2}\frac{\delta^2 P}{\delta t^2} \tag{13}$$

The equation can be solved by assuming that all three waves are propagating in the same direction and that $\omega_1 < \omega_2 < \omega_3$. The electric fields of the three interacting waves in a second-order χ^2 medium can be written

$$\begin{aligned} \frac{dE_{1i}}{dz} &= -\frac{i\omega_1}{cn_1} d'_{ijk} E_{3j} E^*_{2k} \exp^{(-i\Delta kz)} \\ \frac{dE^*_{2k}}{dz} &= \frac{i\omega_2}{cn_2} d'_{kij} E_{1i} E^*_{3j} \exp^{(+i\Delta kz)} \\ \frac{dE_{3j}}{dz} &= -\frac{i\omega_3}{cn_3} d'_{jik} E_{1i} E_{2k} \exp^{(+i\Delta kz)} \end{aligned} \tag{14}$$

These equations are used to explained any frequency conversion appearing in a second order χ^2_{ijk} material due to a susceptibility component. d'_{ijk} is the effective nonlinear susceptibility component ($d_{ijk} = \frac{\chi^2_{ijk}}{2}$) describing the nonlinear coupling between these fields [7] and Δk is the wave vector mismatch

$$\Delta k = k_3 - k_2 - k_1 \tag{15}$$

where

$$k_m = \frac{2\pi n(\lambda_m)}{\lambda_m} \tag{16}$$

The waves interact efficiently only if the wave vector mismatch Δk is equal to or close to zero. This can be achieved in birefringent materials by the technique known as phasematching. Phasematching between different frequencies in the same nonlinear crystal can be achieved by manipulating the refractive index which in a birefringent medium can be done by changing the crystal angle when the propagating waves are different in polarizations. In this work we employ quasi-phasematching, where $\Delta k \neq 0$, since we are using periodically poled potassium titanyl phosphate (PPKTP).

2.3.2 Quasi-phasematching

Quasi phasematching can be achieved in dispersive χ^2 materials. If three waves are interacting, their relative phase after a certain propagation length will experience a phase slip of π. The propagation length during which the phase slip remains between 0 and π is called the coherence length. The conversion of the photon energy is efficient only up to the coherence length. In this case forward conversion is efficient but after the coherence length the converted energy reduces and back conversion takes place. The coherence length can be written in terms of the wave-vector mismatch as:

$$L_{coherence} = \frac{\pi}{\Delta k} \tag{17}$$

Back conversion can be stopped and the forward conversion obtained again by adding a phase step of π after the waves propagate through one coherence length $L_{coherence}$. The phasematching condition is optimised for the forward conversion of the energy from the fundamental frequency to other ones by periodically flipping the polarity of the phase, to ensure continuous forward conversion

$$\begin{aligned} \frac{dE_{1i}}{dz} &= -\frac{i\omega_1}{cn_1} d'_{ijk} E_3 E_2^* \exp^{(-i\Delta kz + i\pi)} \\ \frac{dE_{2k}^*}{dz} &= \frac{i\omega_2}{cn_2} d'_{kij} E_1 E_3^* \exp^{(+i\Delta kz + i\pi)} \\ \frac{dE_{3j}}{dz} &= -\frac{i\omega_3}{cn_3} d'_{jik} E_1 E_2 \exp^{(+i\Delta kz + i\pi)} \end{aligned} \tag{18}$$

The phase slip repeats every two periods of coherence length, a length known as the quasi phasematching period:

$$\Lambda_g = 2L_{coherence} = \frac{2\pi}{\Delta k} \tag{19}$$

As a result the quasi-phasematching condition is

$$\Delta k_{(QPM)} = k_3 - k_2 - k_1 - \frac{2\pi}{\Lambda_g} = 0 \tag{20}$$

The quasi-phasematching condition can be achieved by modifying the grating period so that Δk is equal to or close to zero. Implementation of Eq.(14) results in a final grating period calculation formula which is a required parameter when specifying a nonlinear crystal PPKTP, PPLN, etc.

$$\Lambda_g = [\frac{n(\lambda_3)}{\lambda_3} - \frac{n(\lambda_2)}{\lambda_2} - \frac{n(\lambda_1)}{\lambda_1}]^{-1} \tag{21}$$

Periodically flipping the grating period along the crystal length with sub µm precision lets us manufacture an efficient frequency conversion crystal with no need for birefringent phasematching (QPM). The main advantage of quasi-phasematching is that all of the interacting waves can have the same polarization which is a more efficient interaction than in comparison with a birefringent phasematching where the interacting waves have different polarizations. The QPM interaction ensures a much higher efficiency and is therefore preferentially used in optical parametric oscillators (OPO) for frequency conversion of high repetition rate femtosecond pulses.

2.3.3 Second harmonic generation

To analyse second harmonic generation (SHG) using the coupled wave equations an assumption of low conversion efficiency is made. This assumption of $\frac{dE_1}{dz} \approx \frac{dE_2}{dz} \approx 0$ results in only one equation

$$\frac{dE_3}{dz} = -\frac{i\omega_3}{cn_3} d'_{ijk} E_1 E_2 \text{exp}^{(+i\Delta kz)} \tag{22}$$

and by implementing

$$\begin{aligned} E_3 &= a\text{exp}(i\Delta kz) + b \\ \frac{dE_3}{dz} &= ai\Delta k\text{exp}(i\Delta kz) \end{aligned} \tag{23}$$

we obtain

$$a = -\frac{\omega_3 d'_{ijk} E_1 E_2}{cn_3 \Delta k} \tag{24}$$

After applying the boundary condition that there is no second harmonic generation at the crystal entrance i.e. at $z = 0$, $E_3 = 0$ we find that:

$$b = -a = \frac{\omega_3 d'_{ijk} E_1 E_2}{cn_3 \Delta k} \tag{25}$$

and therefore

$$E_3 = \frac{2\omega_3 d'_{ijk} E_1 E_2}{cn_3 \Delta k} [1 - \text{exp} i\Delta kz] \tag{26}$$

The generated second harmonic intensity is

$$I_{2w}(z) = \frac{8\omega^2 (d'_{ijk})^2 I_\omega^2 z^2}{c^3 n_1 n_2 n_3 \epsilon_0} \text{sinc}^2(\Delta kz/2) \tag{27}$$

If $\Delta k = 0$ the intensity of the second harmonic grows quadratically with the propagation through the crystal distance z. The intensity is quadratically dependent on the frequency of the input wave. The $(d'_{ijk})^2$ tensor, refractive indexes of n_1, n_2 and n_3 are determined by the linear and nonlinear crystal properties.

2.3.4 Sum and difference frequency generation

The coupled wave equations for sum and different frequency generation can be solved by assuming that there is no pump depletion and the wave vector mismatch is equal to zero i.e. perfect phasematching is ensured. In the case of sum frequency generation, the frequency ω_3 is generated as a result of ω_1 and ω_2 wave mixing

$$\omega_1 + \omega_2 = \omega_3 \tag{28}$$

As the waves travel through the nonlinear crystal, the energy is transferred from one frequency to another. Forward and backward energy conversion can occur. The simplest case is when we assume that the phase mismatch is equal to zero. As in an OPO, we can assign waves as the pump and signal which interact to create a third idler wave. In this case the pump is much stronger than the signal, so we assume that the ω_2 wave is strong with no depletion. The strong field amplitude E_2 of ω_2 is assumed to not change ($\frac{dE_2}{dz} = 0$) when the signal pulse ω_1 is weak. The solution of the coupled wave equations for sum frequency generation is:

$$\begin{aligned} E_1(z) &= E_1(0)\mathrm{cos}(\Gamma' z) \\ E_3(z) &= -E_1(0)\sqrt[2]{\frac{\omega_3 n_1}{\omega_1 n_3}}\mathrm{sin}(\Gamma' z) \end{aligned} \tag{29}$$

resulting in

$$E_3(z) = iE_1(0)\sqrt[2]{\frac{\omega_3 n_1}{\omega_1 n_3}}\mathrm{sin}(\Gamma' z)\mathrm{exp}^{i\phi_2} \tag{30}$$

where (Γ') is a coupling coefficient for SFG [1]

$$(\Gamma')^2 = \frac{4\omega_1^2\omega_3^2 d'_{ijk}|E_2|^2}{k_1 k_3 c^4} \tag{31}$$

and ϕ_2 is the phase of E_2. The equations represent forward and backward energy conversion from one frequency to another one when the waves are propagating through the nonlinear crystal.

The same simplifications can be made for difference frequency generation (DFG). In this case the pump frequency assigned as ω_3 ($\frac{dE_3}{dz} = 0$) is mixed with another frequency ω_1. The solution for ω_1 under the perfect phasematching condition ($\Delta k = 0$) is:

$$E_1(z) = E_1(0)\mathrm{cos}h(\Gamma' z) \tag{32}$$

and the generation of ω_2 can be expressed as

$$E_2^*(z) = -i\sqrt[2]{\frac{\kappa_2}{\kappa_1}}E_1(0)\mathrm{sin}h(\Gamma' z) \tag{33}$$

where $\kappa_i = \frac{2i\omega_i^2 d_{eff} A_p}{k_i c^2}$. d_{eff} is the nonlinear conversion efficiency which depends on the propagation angle and polarisations of the waves traveling through the nonlinear crystal
($d_{eff} = \vec{u} * (\vec{d_{ijk}}\vec{E_j}\vec{E_k})$).
As all three waves are travelling through the nonlinear crystal, the weak frequency ω_1 experiences amplification and the wave at frequency ω_2 grows from zero at the expense of a strong wave at the pump frequency ω_3

$$\omega_2 = \omega_3 - \omega_1 \tag{34}$$

In a nonlinear OPO crystal, as the pump, signal and idler waves are interacting, the pump is depleted and new frequencies are created and amplified. This is essential for acquiring the carrier envelope offset (CEO) frequencies of the signal, idler or pump pulses depending on what we want to achieve.

2.3.5 Parametric gain

In χ^2 materials it is possible not only to generate but also to amplify waves. This can be done in optical parametric oscillators (OPOs) which can increase the field of the chosen wave. In OPOs the three interacting waves are designated the idler, signal and pump according to the relation $\omega_{idler} \leq \omega_{signal} < \omega_{pump}$. An OPO typically contains high reflectivity cavity mirrors coated for signal or idler frequencies so that the cavity is singly resonant for either the signal or idler waves (see Figure 2). We can make a doubly resonant OPO too if both the signal and idler waves can oscillate in the cavity at once or even a degenerate OPO when signal and idler wavelengths overlap. The coupled wave solution for the OPO is

$$\begin{aligned} A_s(z) &= A_s(0)\cosh(gz) \\ A_i(z) &= \sqrt[2]{\frac{\omega_2 n_1}{\omega_1 n_2}}\frac{A_p}{|A_p|}A_i^*(0)\sinh(gz) \end{aligned} \tag{35}$$

We assume that the idler does not oscillate in the OPO cavity and is zero at the beginning. Perfect phasematching is also assumed. The coefficient $g = \sqrt[2]{\Gamma' - (\frac{\Delta k}{2})^2} = \sqrt[2]{\kappa_1\kappa_2^* - (\frac{\Delta k}{2})^2}$ and $\kappa_i = \frac{2i\omega_i^2 d_{eff} A_p}{k_i c^2}$. OPOs are widely tunable frequency converters operating in continuous wave (CW) or pulsed regime. Their pulse duration and wavelength tunability are determined by the mirrors used and the nonlinear crystal properties. This thesis concerns OPOs which are pumped synchronously and therefore the repetition rates of the OPOs are limited to the repetition rate of the pump laser. In order to resonate the signal or idler pulses in the OPO, the cavity length must be perfectly matched to the pump laser's cavity length. The pulse is further amplified only if after every round trip it meets another pump pulse coming from the pump laser inside the nonlinear crystal placed inside the OPO cavity [8]. Synchronously pumped OPOs are limited by the repetition rate of the pump laser, but it is possible to run the optical parametric oscillator at a harmonic of the pump repetition rate when the cavity length is an integer [9] or integer fraction [10] of the pump laser cavity length. This principle is the basis of the study presented in Chapter 5.

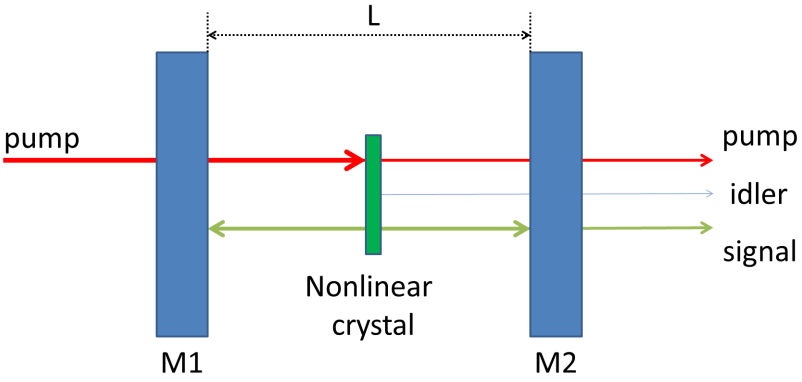

Figure 2. A general schematic of a signal wave oscillating in a two mirror based OPO. The signal wave is resonant and idler is not resonant. The idler leaves the cavity after the M2 mirror where the oscillating signal wave is contained inside two mirrors and only a small portion of its power leaves the cavity.

2.4 Ultrashort pulses

An ultrashort pulse propagating through a material is changed in its shape in both the temporal and frequency domains via linear and nonlinear processes. Mirror coatings can also change the shape of the pulse since they usually add additional dispersion which is important to know in order to understand ultrashort pulse dynamics.

2.4.1 Ultrashort pulse description

Ultrashort pulses leaving a mode-locked oscillator have a broadband optical spectrum resulting in durations of order of <100 femtoseconds (10^{-15}). The ultrashort pulse can be expressed in the time-domain by a complex envelope function where the real electric field is oscillating at an angular frequency ω_0 which corresponds to the central wavelength of the pulse

$$E(t) \propto Re[A(t)\exp^{i\omega_0 t}] \tag{36}$$

where A(t) is the normalized electric field amplitude. The spectral amplitude of the ultrashort pulse can be extracted by Fourier-transforming the temporal field

$$A(\omega) = \frac{1}{\sqrt{2\pi}} \int_{-\infty}^{\infty} A(t)\exp^{-i\omega_0 t} dt \tag{37}$$

The real power spectrum of the pulse can be obtained by $|A(\omega)|^2$.

An ultrashort pulse is characterized by a spectral width in frequency space $\Delta\nu_P$ and a pulse duration $\Delta\tau_P$ via fixed the duration-bandwidth product ($\Delta\tau_P\Delta\nu_P$). In laser physics pulses are specified by measuring the full width at half-maximum (FWHM) in the time and frequency domain. The shape of the pulse determines the duration-bandwidth product. For $sech^2$ pulses the product is 0.315, while for Gaussian pulses it is 0.44. The fixed duration-bandwidth relationship means that for a certain spectral bandwidth of the pulse, a lower limit of pulse duration exists. The value of the duration-bandwidth product therefore indicates whether the pulse is transform limited or not. If the duration-bandwidth product is higher than the minimum "transform-limited" value, it means the pulse is chirped.

2.4.2 Optical dispersion

The refractive index of any material depends on the frequency of the wave interacting with it. Each frequency of the ultrashort pulse will travel with different velocities. This results in a phase delay which changes the pulse shape as it travels through a material causing the pulse to broaden in time. In this scenario the pulses traveling in the material become chirped and the duration-bandwidth product becomes larger than the minimum value. The contribution of this frequency-dependent phase term is:

$$A(\omega)' = A(\omega)\exp^{(i\phi(\omega))} \tag{38}$$

and its effect can be observed in the time domain via the inverse Fourier transformation

$$A(t)' = \frac{1}{\sqrt{2\pi}} \int_{-\infty}^{\infty} A(\omega)' \exp^{-i\omega_0 t} d\omega \tag{39}$$

The spectral phase of a pulse can be expressed by a Taylor expansion of wave vector k, representing a spectral phase change as a function of of angular frequency ω, in respect to the central frequency ω_0:

$$\begin{aligned} &\phi(\omega) = \phi(\omega_0) && \\ &+ (\omega - \omega_0)[\frac{\delta\phi}{\delta\omega}] && \text{Linear } \phi(\omega) \\ &+ \frac{1}{2}(\omega - \omega_0)^2[\frac{\delta^2\phi}{\delta\omega^2}] && \text{GDD} \\ &+ \frac{1}{6}(\omega - \omega_0)^3[\frac{\delta^3\phi}{\delta\omega^3}]... && \text{TOD} \end{aligned} \tag{40}$$

The first element represents the phase accumulated at the central frequency ω_0 of the ultrashort pulse. Since this is the same frequency, it has no effect on the shape of the pulse. The second term is the first-order differential term. It describes the linear variation of the carrier wave phase with the frequency. It has no effect on the pulse shape and in the time domain it is known as the group-delay τ_G.

The relationship between the group delay and the group velocity is

$$v_G = \frac{L}{\tau_G} \tag{41}$$

The group velocity is the speed at which the pulse envelope is propagating through the medium.

Higher order terms change the pulse shape. The third term contains the information of how fast the second term changes with the frequency. It is known as the group-delay-dispersion (GDD, fs^2) [11].

$$GDD = \frac{\delta^2\phi}{\delta\omega^2} = \frac{\delta\tau_G}{\delta\omega} \tag{42}$$

The fourth term describes the evolution of the pulse shape when one edge of the pulse is stretching and other one is steepening resulting in the separation of the pulse (pulse break-up). The differential term is called third-order dispersion (TOD, fs^3)

$$TOD = \frac{\delta^3\phi}{\delta\omega^3} \tag{43}$$

As a result the intracavity dispersion must be taken into account, if we want to generate an ultrashort pulse. All these and higher order spectral phase terms must remain flat and negligible across the full-bandwidth of the pulse.

2.4.3 Material dispersion

When the ultrashort pulse leaves the laser cavity through the output coupler, the pulse straight away exhibits temporal broadening since each material has a wavelength (frequency) dependent refractive index $n(\lambda)$. Material dispersion and the refractive index are described by the Sellmeier equation, which provide n_λ for a given material. Practical expressions of the spectral phase terms are:

$$\begin{aligned}
v_P &= \frac{c}{n} && \text{Phase velocity} \\
v_G &= c[n - \lambda\frac{\delta n}{\delta\lambda}]^{-1} && \text{Group velocity} \\
\tau_G &= \frac{L}{c}[n - \lambda\frac{\delta n}{\delta\lambda}] && \text{Group delay} \\
GDD &= \frac{\lambda^3 L}{2\pi c^2}\frac{d^2 n}{d\lambda^2} && \text{2nd order dispersion} \\
TOD &= \frac{-\lambda^4 L}{4\pi^2 c^3}[3\frac{d^2 n}{d\lambda^2} + \lambda\frac{\delta^3 n}{\delta\lambda^3}] && \text{3rd order dispersion}
\end{aligned} \tag{44}$$

If the wavelength and the refractive index are known, the GDD, group-velocity and TOD can be quickly calculated. For an ultrashort pulse, the bandwidth of the pulse is huge and therefore to know the shape of the GDD or the group-velocity, a cycle of calculations must be done for a number of wavelengths. Moreover, the well-defined GDD and TOD of the materials can be used for ultrashort pulse compression to a duration-bandwidth limited product of 0.441 for a Gaussian pulse shape. For this purpose, angular dispersive elements such as prisms or diffraction gratings can be used for dispersion compensation [12, 13].

In the work presented here, we used dielectric mirrors containing multiple thin layers of optical materials. By changing the low and high refractive indices (usually by introducing TiO_2 and SiO_2 materials), mirrors operating over a certain wavelength range can be designed [14, 15]. Each layer thickness of the material must be a quarter of the local wavelength. The thickness of the layers is increased in deeper regions so that a group delay is generated: dispersion of these chirped mirrors is adjustable so that faster propagating longer wavelengths are reflected from the deeper mirror layers whereas the shorter wavelengths are reflected from the closer to the surface layers. In this way we can compensate the positive chirp which is incurred when propagating in normal dispersion materials by using chirped mirrors to introduce negative dispersion. Chirped mirrors are manufactured quite routinely and most importantly the supplier can provide well-defined dispersion curves [14]. Since each chirped mirror has a modulation of the GDD, these mirrors are implemented in pairs with matched coatings. The modulation of the GDD is cancelled and remains flat over required wavelength region. The chirped mirror structure is shown in Figure 3.

For the GDD compensation Gires-Tournois interferometer (GTI) mirrors were used too. These mirrors introduce several times higher negative GDD at the cost of a narrower reflectivity bandwidth. The GTI mirror structure comprises a partially reflective mirror, an etalon-like

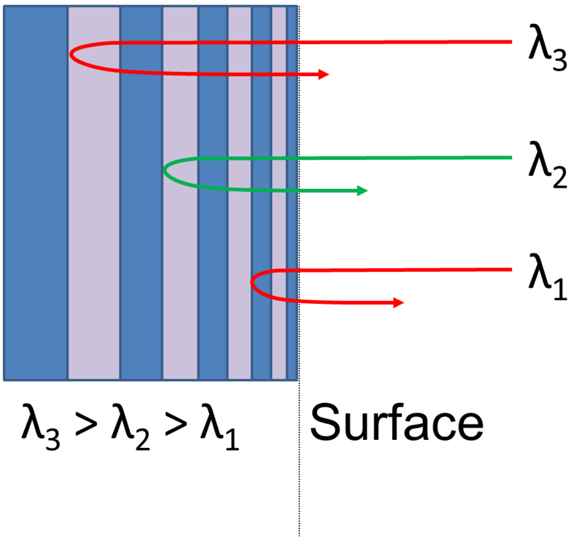

Figure 3. The principle of a chirped mirror. The longer wavelength light penetrates deeper into the mirror structure experiencing larger group delay v_G where the shorter wavelengths experience a smaller group delay. The difference leads to anomalous chromatic dispersion where GDD is negative.

resonant cavity and a highly reflective Bragg mirror. The GTI mirror utilises the natural dispersion of a Fabry-Pérot etalon to develop greater values of GDD than are typically available from chirped mirror designs [16].

2.5 Conclusions

In this chapter I have presented the fundamentals of nonlinear optics together with a mathematical description of ultrashort pulse propagation. The linear and nonlinear effects introduced here form the basis of the OPO systems described in the following chapters, and are also fundamental to the measurement methods which are essential for frequency comb stabilisation.

References

[1] R. W. Boyd, Nonlinear Optics, 3rd ed., (Academic Press, 2008).

[2] A. Yariv, Quantum Electronics, 3rd ed., (John Wiley and Sons, 1988).

[3] M. Conforti, F. Baronio, and C. De Angelis, "Nonlinear envelope equation for broadband optical pulses in quadratic media," Phys. Rev. A 81, 053841 (2010).

[4] G. P. Agrawal, Nonlinear Fiber Optics, 3rd ed. (Academic, San Diego, 2001).

[5] J. M. Dudley, G. Genty, S.Coen, "Supercontinuum generation in photonic crystal fiber," Reviews of Modern Physics 78, 1135-1184 (2006).

[6] J.Lagsgaard, "Mode profile dispersion in the generalised nonlinear Schrodinger equation," Optics Express 15, 16110-16123 (2007).

[7] W. Koechner, Ch. 11, Damage of Optical Elements, in Solid-State Laser Engineering, 6th Edn., (Springer, 2006), pp. 680-701.

[8] G. J. Hall, M. Ebrahimzadeh, A. Robertson, G. P. A. Malcolm, and A. I. Ferguson, "Synchronously pumped optical parametric oscillators using all-solid-state pump lasers," J. Opt. Soc. Am. B 10, 2168–2179, (1993).

[9] D. T. Reid, C. McGowan, W. Sleat, M. Ebrahimzadeh, and W. Sibbett, "Compact, efficient 344-MHz repetition rate femtosecond optical parametric oscillator," Opt. Lett. 22, 525–527 (1997).

[10] J. Jiang and T. Hasama, "Harmonic repetition-rate femtosecond optical parametric oscillator," Appl. Phys, B Lasers Opt. 74, 313–317 (2002).

[11] I.Walmsley, L.Waxer, and C.Dorrer, "The role of dispersion in ultrafast optics," Rev. Sci. Instrum. 72, 1-29 (2001).

[12] R.Fork, O.Martinez, and J.Gordon, "Negative dispersion using pairs of prisms," Optics Letters 9, 150-152 (1984).

[13] E.Treacy, "Compensation of picosecond light pulses,"Physics Letters A 28, 34-35 (1968).

[14] R.Szipocs, K.Ferencz, C.Spielmann, and F.Krausz, "Chirped multilayer coatings for broadband dispersion control in femtosecond lasers," Optics Letters 19, 201-203 (1994).

[15] R. Szipocs, "Invited paper Theory and design of chirped dielectric laser mirrors," Applied Physics B: Lasers and Optics 135, 115–135 (1997).

[16] G. R. Holtom, "Mode-locked Yb:KGW laser longitudinally pumped by polarization-coupled diode bars," Optics letters 31, 2719–2721 (2006).

Chapter 3. Design and characterisation of a Ti:sapphire pumped optical parametric oscillator

3.1 Introduction

Here I present details of the Ti:sapphire laser and the OPO sources. We aimed for a high repetition rate, high average power frequency comb, which was pumped by a repetition-frequency stabilised Laser Quantum 333 MHz Ti:sapphire laser. In Section 3.2, the Ti:sapphire laser is described, while in Section 3.3 the OPO design is presented. The OPO was the frequency comb source for which stabilisation procedures and results are detailed in Chapters 4 and 5.

3.2 Ti:sapphire pump laser

High quality frequency combs were achieved by designing our synchronously pumped OPO around a commercial femtosecond Ti:sapphire pump laser (Laser Quantum). The Ti:sapphire laser produced 30-fs duration pulses with 1.45 W of average power centered at 800-nm central wavelength. The self-mode-locking regime in the Ti:sapphire laser is mediated by the optical Kerr effect. Following its original demonstration [1], the Ti:sapphire laser quickly become the most popular laser for generating femtosecond pulses because of the Ti:sapphire gain medium's excellent thermal conductivity, large gain bandwidth, wide wavelength tunability, variety of pumping wavelengths and short upper-state lifetime making it possible to extract high average powers. In these days the pulse durations achievable directly from commercial Ti:sapphire lasers are less than 10-fs if the intracavity dispersion is carefully optimised. I will briefly introduce the mode-locking regime for generating femtosecond pulses and characterise the pulses achieved from the 333-MHz Ti:sapphire pump laser.

3.2.1 Ultrashort pulse generation

Several different approaches can be applied to generate ultrashort pulses. Normally, high peak power pulses are extracted from the laser cavity through an output coupler (OC) after every round trip, where the repetition rate of the laser is determined by its round-trip cavity length L

$$f_{rep} = \frac{c}{L} \tag{45}$$

If phase or amplitude modulation is applied inside the cavity during continuous wave (CW) operation a modelocking regime can be activated. In the frequency domain modelocked pulses contain thousands of longitudinal modes. All of them are experiencing more gain than loss after every round trip and these longitudinal modes have a fixed relative phase relationship. In phase oscillating modes can constructively interfere with each other and form broadband ultrashort pulses whose durations are inversely proportional to the bandwidth of the pulses [2].

3.2.2 Active and passive modelocking regimes

Modelocking can be achieved with an active or passive element [3, 4]. In the case of active modelocking an additional optical element is placed inside the laser cavity for phase or amplitude modulation. The introduced amplitude or phase modulator changes the intra-cavity loss (transmission) or intra-cavity phase respectively and can be implemented by either an acousto- or electro-optic modulator [5]. Sinusoidal loss or phase modulation causes phase coupling between neighbouring cavity modes, causing the formation of pulses. The drawback of active modelocking is its limited modulation bandwidth which limits the minimum possible pulse duration.

The passive modelocking regime does not require an actively driven element and therefore the modulation bandwidth can be much greater. Passive modelocking is activated through the use of intensity dependent loss or gain. The most common example is the semiconductor saturable absorber mirror (SESAM), which introduces a reflectivity coefficient which depends on the intensity [6, 7]. Low intensity waves experience high intra cavity loss while high intensity waves propagate with relatively low loss. This loss saturation gives more loss for lower intensity light (CW light) while the loss is decreased or reduced to zero for higher intensity light (typically meaning shorter pulses) [8]. When random noise is present in the cavity, any higher intensity light experiences lower loss while passing through the saturable absorber in comparison with the average background level of CW light. This noise peak will see lower loss and therefore will get stronger after every round trip. The more intense this light becomes the more transparent the SESAM becomes. In this way, light initiated from a random noise spike will get stronger every time it passes the SESAM whereas the CW light will decay since all the energy will be taken by this intense pulse. During such a buildup phase there may be many noise peaks travelling around the cavity, but eventually , following the action of intra-cavity dispersion and self-phase modulation, only one pulse will be left oscillating inside the cavity with minimal loss.

As was first shown in Ti:sapphire [1], a laser can be passively modelocked without the need for any additional element. In all materials third order χ^3 nonlinear effects including the Kerr effect are obtained. As a strong electric field is propagating through the Kerr medium, the refractive index n is changed. The time-dependent refractive index for a Kerr medium can be expressed as

$$n(t) = n_0 + n_2 I(t) \tag{46}$$

where n_0 is the refractive index of the material, $n_2 = \frac{\chi^3}{n_0^2 c \epsilon_0}$, the nonlinear index dependent on the material and $I(t)$ is the laser intensity. The Kerr effect results in self focusing and self phase modulation (see Chapter 2) [9].

In this case we have a much faster modulation bandwidth even compared with SESAMs. SESAMs are in common use in many solid-state femtosecond lasers, but Kerr lens modelocking is even better since it supports sub-10-fs pulse durations [10, 9].

Kerr lens modelocking is achieved through self focusing. Because the refractive index in χ^3 materials depends on the intensity, the more intense central part of the pulse will propagate with a slower phase velocity in comparison with the boundaries of the pulse since the intensity on the edges is much lower. A transverse phase velocity gradient will be established, which creates a virtual lens within the gain material (in our case Ti:sapphire) which is an effect called self focusing (see Figure 1).

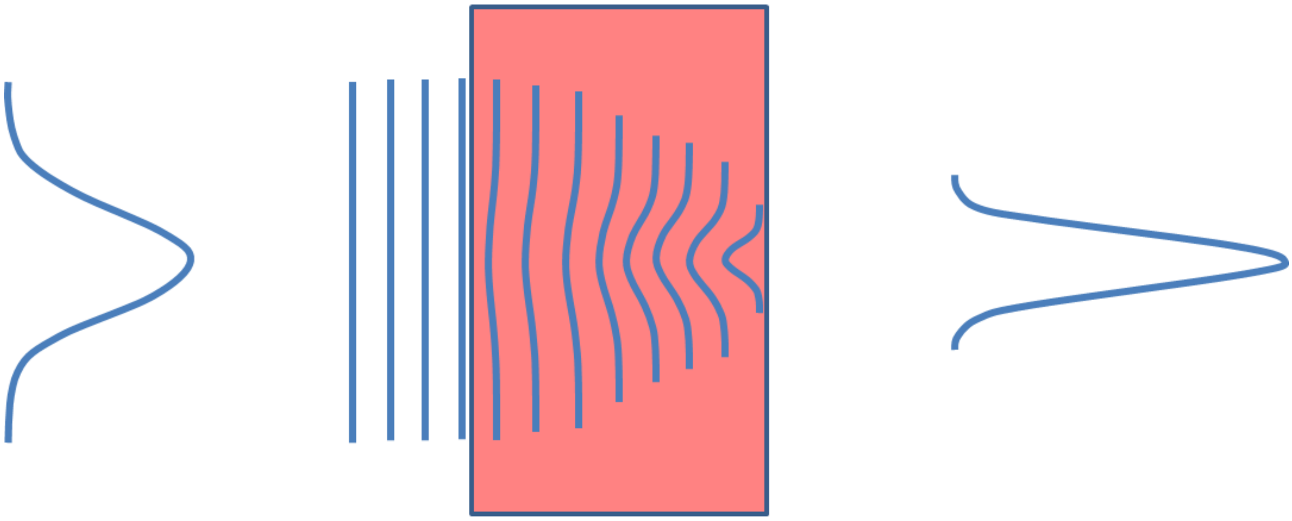

Figure 1. Self-focusing in a nonlinear medium.

To enable modelocking, this Kerr lens must be exploited to cause self-amplitude modulation, so that more intense pulses or noise peaks see less loss or more gain than less intense light. The so called soft aperture arranges the beam alignment inside the cavity so that in the presence of the Kerr lens the pulsed light experiences better overlap with the intra-crystal pump mode (in our case from a 532-nm Finesse laser) [9]. Another case of self modelocking is the so called hard-aperture modelocking. In this case a physical aperture is placed inside the laser cavity so that the loss depends on the intracavity mode. The less focused CW light will experience greater loss than the more focused intense light, favouring modelocked operation.

3.2.3 The Laser Quantum modelocked laser

The Laser Quantum modelocked laser was based on a titanium-doped sapphire (Ti:Al_2O_3) crystal. This crystal is one of the most common gain media for ultrashort pulse generation. It has broad wavelength tunability from 650-1100 nm [11], a large gain cross section, and excellent thermal conductivity. The absorption spectrum starts at 400 nm and extends up to 650 nm. Our commercial Laser Quantum Ti:sapphire laser was pumped by a Finesse Pure 10-W pump laser which emitts frequency doubled Nd^{3+}:YVO_4 laser light at 532 nm wavelength. The solid state laser is pumped by diodes located inside the controller. The light from these diodes is transmitted to the Nd^{3+}:YVO_4 laser using fibres. An image of the Ti:sapphire laser cavity is shown in Figure 2.

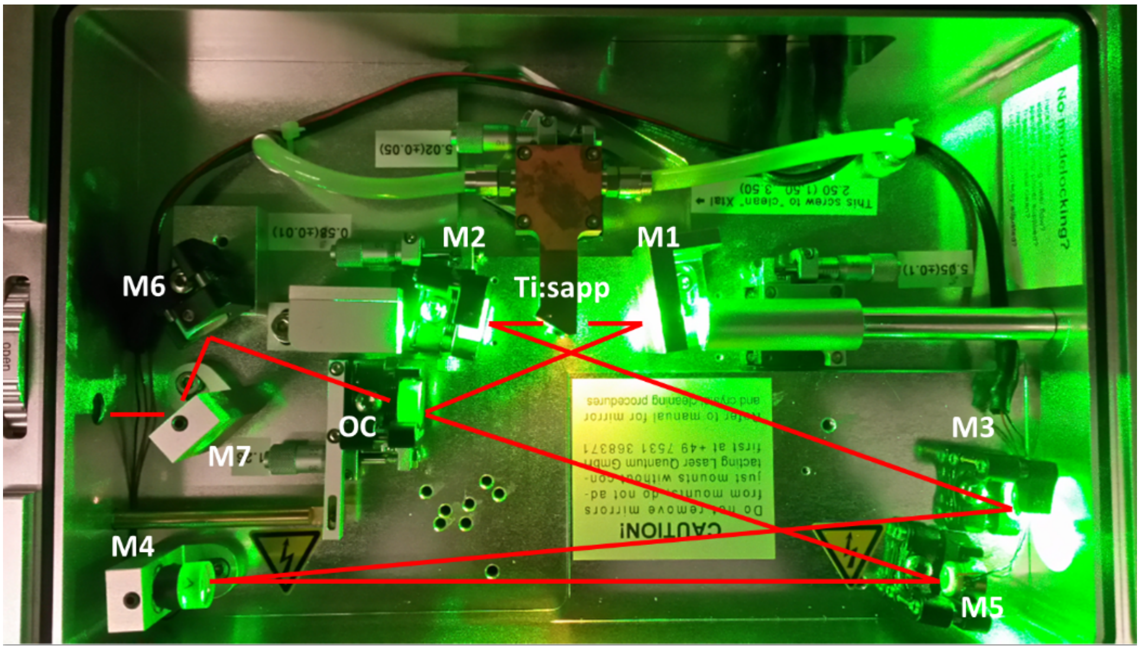

Figure 2. The Laser Quantum Ti:sapphire cavity design.

The six mirror ring-type cavity was based on a 5-mm-long Brewster angled Ti:sapphire crystal placed between two curved mirrors. Both curved mirrors, the focusing lens for the Finesse CW light and the Ti:sapphire crystal itself were screwed onto micrometer translation stages. The distance between each element could be changed if necessary. The 532-nm CW light pumped the Ti:sapphire crystal, causing light at 800-nm wavelength to be generated. The emitted light propagates around the cavity a total of 901-mm length before again reaching the Ti:sapphire crystal. This cavity length corresponds to a 333-MHz repetition rate. The mechanical stability was improved by using a temperature controlled breadboard, cooled by using a chiller set at 22 celsius temperature. The cooled water from the chiller flowed through the breadboard on which the Ti:sapphire and green Pure Finesse pump lasers were fixed. Both lasers shared the same breadboard in order to improve the overall stability of the system. For achieving a suitable modelocking regime, the laser cavity dispersion must be taken into account; normally the high reflectivity mirrors add group delay dispersion (GDD) and inside the Ti:sapphire crystal there is self-phase modulation (SPM) because of the Kerr effect. In our laser, all this additional dispersion is compensated by using specially optimised negative dispersion mirrors inside the cavity [9]. The average power measured after the output coupler outside the laser cavity was 1.45 W at 800-nm central wavelength. With a repetition rate of 333 MHz, this corresponded to a pulse energy of 4.35 nJ. Inside the femtosecond laser cavity two piezo electric transducers (PZTs) were included for repetition rate locking on which high reflectivity mirrors were glued. One piezo had a much higher modulation bandwidth than the other one. The faster one was attached to M5 and could change f_{REP} by 2-Hz V^{-1} while the slower one attached to M4 could change f_{REP} by 20-Hz V^{-1}. The range of the input voltage for both PZTs was from -200 V up to +200 V. The bandwidth of the faster PZT was around 1-kHz frequency. The slower PZT had a resonance at around 150-Hz frequency which was identified during experiments at Neuchatel which will be presented later on in this thesis.

3.2.4 Characterisation

Outside the cavity several irises were used to maintain the alignment of the ultrashort pulse beam into the OPO and PCF. Part of the laser light was reflected with a wedge for pulse characterization. As mentioned earlier, the average output power when the laser was modelocked was 1.45-W, centered at 800-nm wavelength (750-mW in CW regime). The output in the radio-frequency (RF) domain recorded with an RF spectrum analyser is shown in Figure 3.

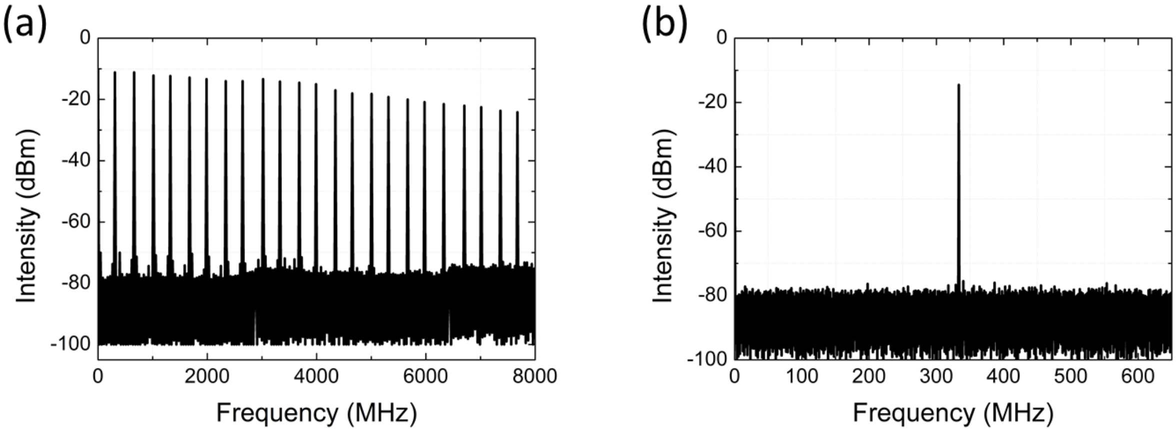

Figure 3. The repetition rate f_{REP} of the 333-MHz Ti:sapphire laser measured with a high speed InGaAs photodiode (DSC40S) photodiode: (a) Radio-frequency (RF) spectrum of the repetition frequency up to 23rd harmonic; (b) RF spectrum of the fundamental 333-MHz repetition rate. The data were recorded using a resolution bandwidth of 100 kHz.

The RF observations of the modelocked laser suggest that stable Kerr lens modelocking is ensured since there are no sidebands indicating Q-switching apparent around the main 333-MHz frequency. The RF spectrum from 0 Hz to 8 GHz shows clean modelocking with the only frequencies being f_{REP} and its harmonics. No multiple pulsing was observed. The repetition rate could be slightly tuned with the translation stage located inside the laser cavity. The spectrum of the pulses measured using an Ocean Optics spectrum analyser is presented in Figure 4.

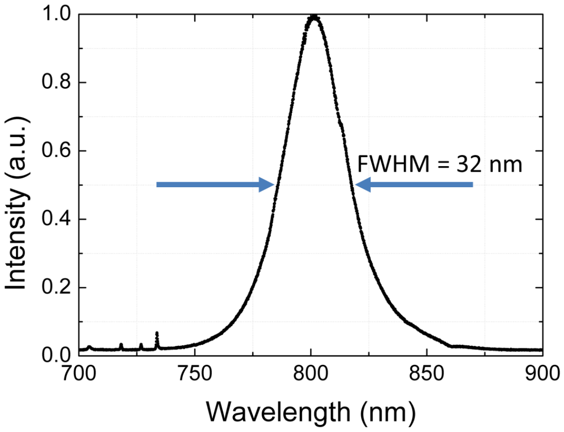

Figure 4. The 32-nm bandwidth of the modelocked femtosecond Ti:sapphire laser.

The time-bandwidth product is the product of pulse duration and spectral width in frequency domain ($\Delta\tau\Delta f$ = TBP). Since the frequency f is related to the speed of light and the wavelength as $c = \lambda f$, the Δf can be replaced by $\frac{\Delta\lambda c}{\lambda_0^2}$. We can directly relate the pulse duration to the measured spectral FWHM in nm: $\Delta\tau_p = \frac{TBP\lambda_0^2}{c\Delta\lambda}$. The minimum possible TBP depends on the pulse shape. The TBP for sech^2 shape pulses is 0.315, while for Gaussian-shaped pulses it is 0.44. There is a pulse duration limit for any given spectral width. The measured full width at half maximum (FWHM) bandwidth of the pulses was 32-nm and corresponded to a time-bandwidth product limited pulse duration of 29 fs (26 fs) for Gaussian (sech^2) shape pulses.

Since we did not observe any CW spectral component we could conclude that the laser cavity was optimised for the modelocking regime. The peak power of the pulse $P_{peakpower}$ can be calculated by dividing the average power $P_{average}$ by the repetition rate f_{REP} and pulse duration τ ($P_{peakpower} = \frac{P_{average}}{F_{REP} * \tau_{pulse}}$). The average output power was 1.45 W, repetition rate 333 MHz and the minimum possible pulse duration 29 fs for the Gaussian-shaped pulse. Therefore the calculated peak power for the shortest pulse duration was 0.14 MW. Since the femtosecond pulses leave the laser cavity through an output coupler (OC), the dispersion of the output coupler must be taken into account when characterising the pulses. The first measurement of the autocorrelation with the Timewarp (E-750) gave a pulse duration of 32 fs (see Figure 5) which is not the shortest possible duration since the spectrum of 32-nm supports bandwidth-limited pulse duration of 29 fs. The pulse duration defined at half intensity point.

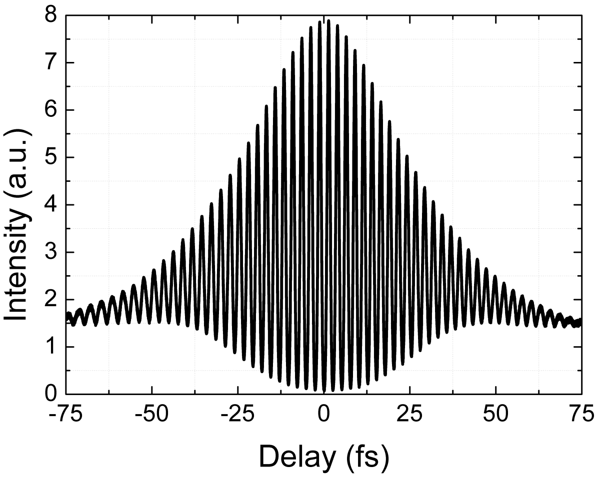

Figure 5. The autocorrelation of the Ti:sapphire pump pulse measured by two-photon absorption in a Timewarp autocorrelator immediately after the OC of the Ti:sapphire laser.

The pulse was temporally chirped since it was passing the OC placed inside the laser cavity and the fused silica window to separate the laser system from the environment. In total about 8 mm length of fused silica was introduced which corresponds to a GDD of 290 fs. To compensate the chirp, we used a pair of chirped mirrors having -100-fs^2 GDD per double reflection was implemented after the OC over the 0.75-0.95 µm wavelength region. Three pairs of reflections were sufficient to compress the pulses to their shortest durations (in total -400-fs^2 GDD compensation), but I added one more bounce for the compensation of additional optics placed before the OPO and photonic crystal fiber. The autocorrelation of the compressed pulse after the GTI mirrors is shown in Figure 5 which is still a bit chirped, but it was done in general to improve the broadening of the pump spectrum in the PCF. The bounce number was changed and the supercontinuum measured until the broadest spectrum was achieved.

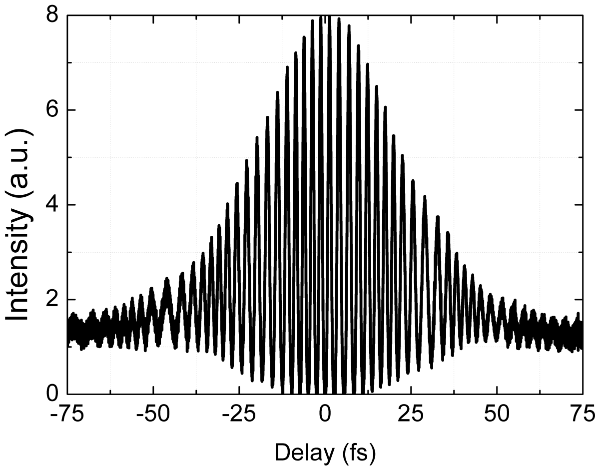

Figure 6. The autocorrelation of the Ti:sapphire pump pulse measured by two-photon absorption in a Timewarp autocorrelator after -400 fs^2 GDD was added.

After compression, a pulse duration of 29-fs was achieved. These compressed ultrashort pulses were used to synchronously pump an optical parametric oscillator based on a PPKTP crystal and to generate locked frequency combs from 1.0-4.0 µm. A repetition rate increase by a factor of three was also demonstrated by harmonically pumping this OPO. These results are presented in Chapters 4 and 5.

3.3 PPKTP optical parametric oscillator

After the laser was characterized a synchronously pumped femtosecond OPO generating pulses in the infrared region was constructed. The experiments presented in this thesis were done by employing ring-geometry type OPOs. In this section I now present the design and the characterisation of the synchronously pumped OPO.

3.3.1 Introduction

Synchronously pumped OPOs have the same cavity length as their pump laser. When the OPO cavity length is changed, the OPO output wavelength changes due to the intracavity dispersion. The OPO maintains synchronism with the pump laser but is oscillating at a slightly different wavelength [12].

3.3.2 PPKTP crystal design

We chose to build a ring type OPO cavity based on a periodically poled potassium titanyl phosphate (PPKTP) crystal. Since the Ti:sapphire pump pulses were broadband, we aimed to generate broadband signal and idler pulses too. The use of the quasi phase matching (QPM) technique allowed us more flexibility in the output wavelengths than would be possible using birefringent phasematching. The most common nonlinear crystals used for QPM are periodically poled lithium niobate (PPLN) and periodically poled potassium titanyl phosphate (PPKTP). In comparison, both are transparent from 330 nm to 4.5 µm, the target range for our OPO frequency comb. PPLN has a greater effective nonlinear coefficient than PPKTP, but PPKTP has a nonlinear gain comparable to PPLN once the refractive index contribution to the figure of merit is taken into consideration. PPKTP can operate at room temperature without photorefractive damage [13] and has 3-4 times lower second-order dispersion (GDD) at the same wavelength in comparison with PPLN (see Chapter 4), so pulse broadening and pulse walk-off effects are reduced. The net GDD of an OPO must be compensated for the simultaneous generation of broadband signal and idler pulses. Most of the dispersion is due to the nonlinear crystal. Our PPKTP crystal was 1.2 mm in length. While a longer crystal length may increase the gain and therefore might produce more power, it may not ultimately be efficient due to group delay walk-off. Using too long a crystal length will reduce the bandwidth of the generated pulses since the parametric gain bandwidth depends inversely on crystal length. All of these factors were considered when selecting the crystal length for the OPO.

Our goal was to generate a broadly tunable frequency comb in the mid-IR region from 1-4 µm covered by the signal and idler pulses. Since our pump laser central wavelength was fixed at 800 nm, the signal and idler wavelengths could be calculated using

$$\frac{1}{\lambda_{pump}} = \frac{1}{\lambda_{signal}} + \frac{1}{\lambda_{idler}} \tag{47}$$

Signal frequency combs spanning from 1-1.6 µm correspond to an idler wavelength shift from 1.6-4µm. A phasematching simulation for PPKTP was done in order to determine the appropriate QPM grating period. In this way the grating periods necessary to cover a broad range of the signal wavelengths can be determined. The signal and therefore the idler wavelengths generated in an OPO depend on the grating period Λ. Our PPKTP crystal had multiple gratings which allowed the tunability of the central signal wavelength by moving the crystal in the vertical direction. In total 10 different grating periods were implemented from 25.4-27.25 µm. A crystal length of 1 mm was used for the parametric generation of a signal field which could efficiently generate signal wavelengths from 1-1.6 µm (see Figure 7). Here we consider a practical pump pulse has 32 nm bandwidth from 784-816 nm. Figure 8 shows that the phasematching is efficient for a signal wavelengths from 1.05-1.6 µm when the grating period is 26.75 µm. Grating periods from 25.4-27.25 µm can be adjusted in order to accurately shift the central signal wavelength according to the central pump wavelength (800 nm). The central signal wavelength could be tuned with a stage or PZT across a broad range of wavelengths. The broadband tunability of the phasematching condition is determined by the pump pulse bandwidth and the grating period. If the pump pulse is femtosecond, it allows broad signal tunability by using the same grating period when the crystal is short. The grating period change is not necessary which is not as critical for tuning, unlike the case for ps or ns pump pulses.

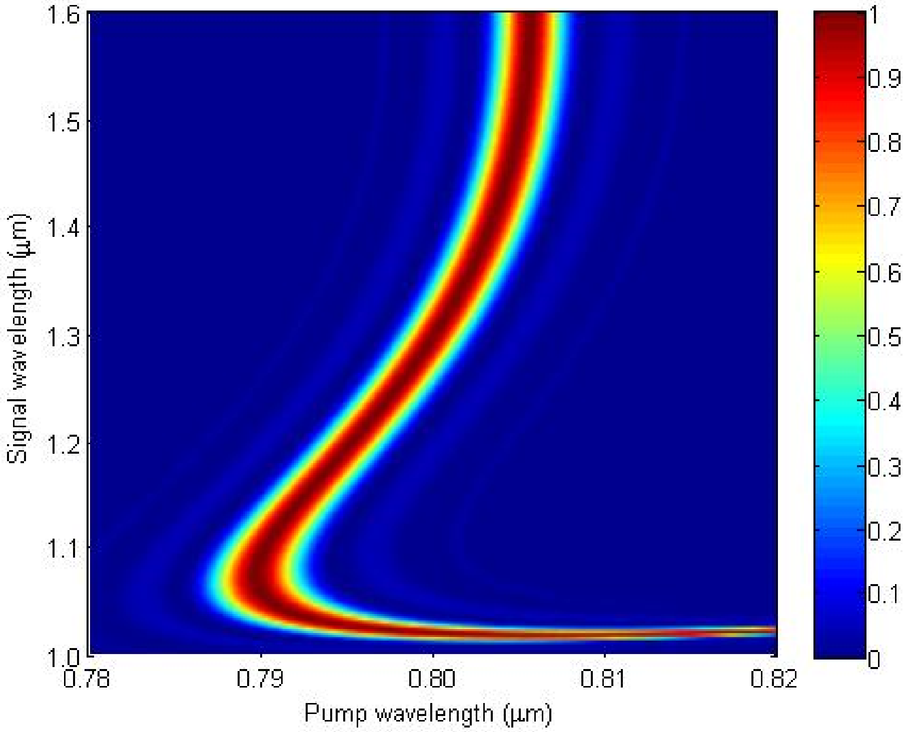

Figure 7. Phasematching condition for a 1 mm length PPKTP crystal with a grating period of 26.75 μm.

The detailed PPKTP crystal design which included OPO, SHG, blank and SFM sections is presented in Figure 8. The PPKTP crystal was used for a number of different experiments which will be presented in later chapters. The crystal was AR coated for the wavelengths from 750-850 nm (pump) and from 980-1620 nm for the signal. The multiple grating periods made it possible to generate signal pulses in a broad range of wavelengths from 1-1.6 μm. The resulting idler field was generated from 1.6-4 μm. Since our experiments involved locking the f_{CEO} of the idler or signal pulses, the additional gratings for pump+idler SFM and second-harmonic (SHG) of the signal pulses were implemented so as to provide strong visible outputs which were necessary in order to obtain a low-noise f_{CEO} heterodyne beat.

The crystal was mounted in an aluminium holder with an adapter. The mount ensured maximum space for the beam going through the crystal which was attached to an optical mount (see Figure 9). The vertical and horizontal tilting was important for ensuring that the pump light from the crystal surface could be reflected back to the Ti:sapphire laser. For the purpose of alignment the reflected light from the PPKTP crystal had much lower power than the pump beam and was followed around the OPO cavity in the opposite direction. The alignment of

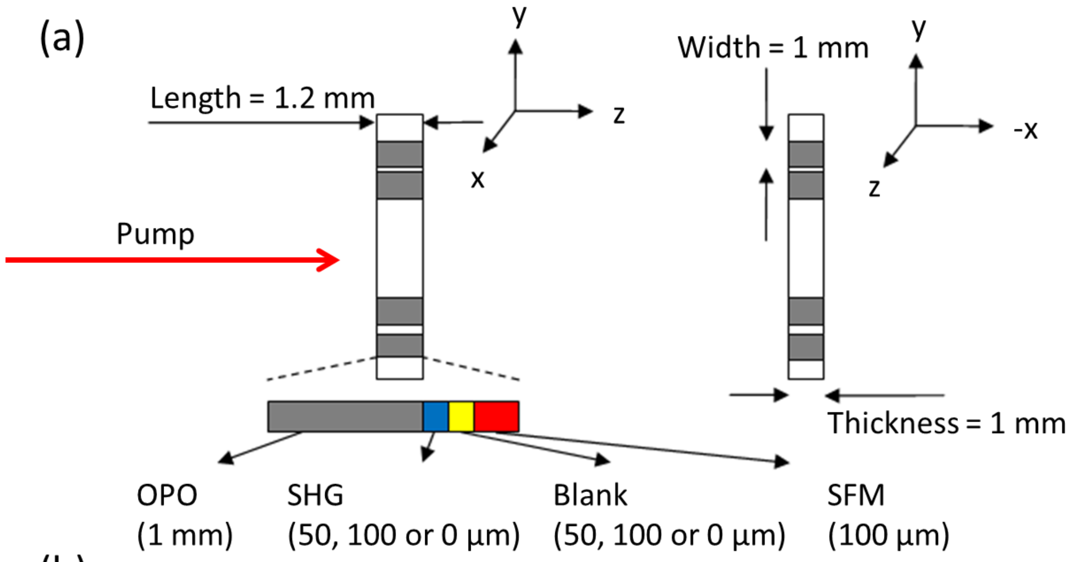

(b)

No.	OPO grating (um)	SHG grating (µm)	Blank section	SFM grating (µm)
1	Λ = 25.4 (1mm)	Λ = 6.8 (50µm)	50µm	Λ = 21.1 (100µm)
2	Λ = 25.9 (1mm)	Λ = 7.1 (50µm)	50µm	Λ = 21.0 (100µm)
3	Λ = 26.4 (1mm)	Λ = 7.5 (50µm)	50µm	Λ = 20.5 (100µm)
4	Λ = 26.9 (1mm)	Λ = 8.2 (50µm)	50µm	Λ = 20.0 (100µm)
5	Λ = 27.15 (1mm)	Λ = 9.0 (50µm)	50µm	Λ = 19.0 (100µm)
6	Λ = 27.25 (1mm)	Λ = 10.0 (50µm)	50µm	Λ = 18.0 (100µm)
7	Λ = 27.1 (1mm)	Λ = 11.8 (50µm)	50µm	Λ = 16.4 (100µm)
8	Λ = 26.85 (1mm)	No SHG grating	100µm	Λ = 14.5 (100µm)
9	Λ = 26.6 (1mm)	Λ = 18.2 (100µm)	0	Λ = 12.5 (100µm)
10	Λ = 26.5 (1mm)	Λ = 23.0 (100µm)	0	Λ = 10.5 (100µm)

Figure 8. (a) The general structure of a grating section of the PPKTP crystal. It contains OPO, SHG, blank and SFM sections. The section structure is the same for all 10 grating periods from 25.4-27.25 µm; (b) The grating periods of the PPKTP.

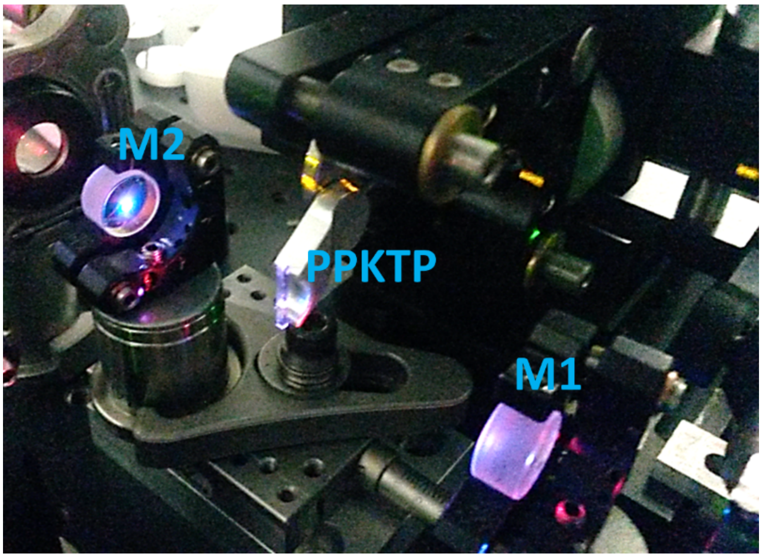

Figure 9. PPKTP crystal holder: the crystal was glued on an aluminium plate which was attached to a Newport optical mount by using an adapter. The mirror mount could be moved by an x-y-z translation stage.

the reflected beam ensured that the phasematching condition was satisfied as we expected from calculations. On other hand, the light must not be exactly reflected back to the Ti:sapphire crystal, since it can disturb and stop the modelocking regime of the laser. The translation stage which held the mirror and the crystal was used to change the grating periods without re-aligning the OPO cavity. Nevertheless, since the OPO was tuned across a broad range of the wavelengths, the alignment had to be repeated for each oscillating wavelength especially if it was changed from 1.5-1.1 μm.

3.4 Ti:sapphire pumped OPO

The OPO was synchronously pumped by a 333-MHz Ti:sapphire laser (Gigajet, Laser Quantum) producing 30-fs duration pulses with an average power of 1.45 W. Ninety-percent of the output power was used to pump a 4-mirror ring type OPO oscillator based on a PPKTP crystal (Raicol Crystals), which contained multiple cascaded gratings (see Figure 10).

3.4.1 OPO cavity design

The OPO design is presented in Figure 10. The 1.2 mm length PPKTP crystal was coated with an AR coating from 0.75-0.85 μm for the pump (T>95%) and from 0.98-1.62 μm for the signal (R>99.8%). Mirrors M1-M4 were coated for the same wavelengths and additionally were highly transmitting for the idler pulse from 1.7-4.5 μm (T>80 %).

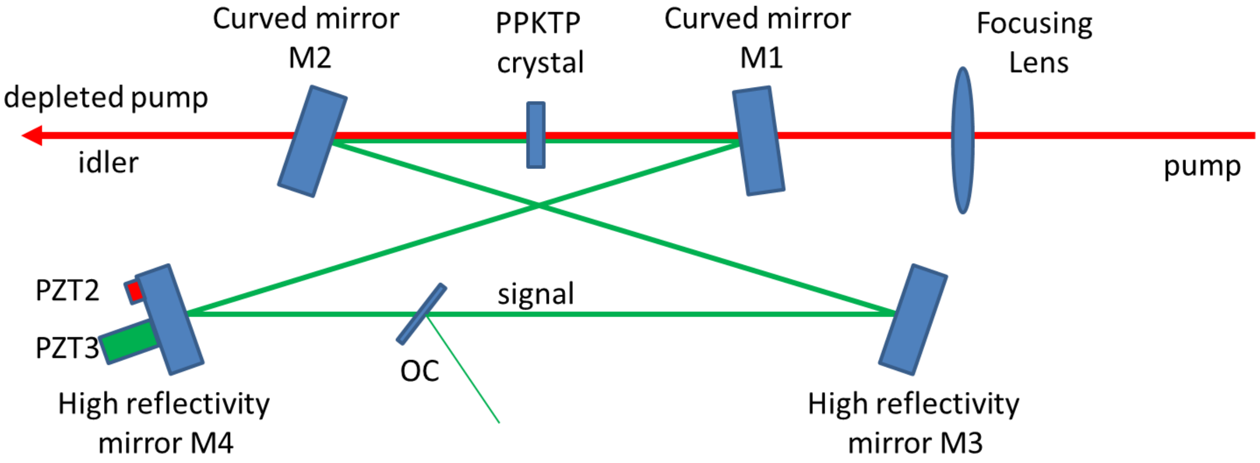

Figure 10. The OPO cavity design: PZT2 and PZT3 are piezoelectric transducers, OC is the output coupler, M1 and M2 are -75 mm curvature mirrors and M3, M4 are flat dielectric mirrors. The OC was AR coated on one surface for signal wavelengths from 1-1.6 μm and had no coating on the other one.

The pump light was focused with a f=63 mm focal length lens. The 17 μm focal spot radius gave a peak power of 0.14 MW. The damage threshold of the PPKTP crystal is much higher (about 1-2 MW) and therefore if some damage occurs it is associated with the crystal surface damage (the coating). The PZT2 (Thorlabs, AE0203D04F) used for the OPO f_{CEO} locking was mounted on a plane mirror M4. For the rough adjustment of the cavity length, a second piezo (PZT3, Thorlabs AE0505D08F) was placed inside a translation stage on which M4 mirror was attached. It was connected to a Newport Microdrive Controller (ESA-C) for manual f_{CEO} and wavelength tuning.

The optimum OPO cavity design was found in LCav (in house program). LCav used "ABCD" ray matrices to calculate the distances between optical elements, calculate the spot size at the focus, and the stability region. The PPKTP in the modelling was placed perpendicularly to the pump beam and assigned a refractive index of 1.8253. The distance between one of the curved mirrors and the PPKTP crystal was changed together with the folding angle in order to calculate the stability of the OPO cavity [14]. In the modelling a 6 degree folding angle was used. The same angle which was used in the real experiment. The smaller the angle was, the smaller the astigmatism that was introduced into the system, but we were limited by the mirror holders, and other mechanical constraints. The estimated stability region of the OPO cavity at different folding angles is presented in Figure 11. As the folding angle was increased, the stability zone of the cavity narrowed because the separation between the vertical and horizontal stability zones widened, indicating astigmatism. The cavity was less stable for bigger folding angles because of the increasing astigmatism. The distance D shown in Figure 11 represents the distance at which the cavity was still stable for the curved mirror M2.

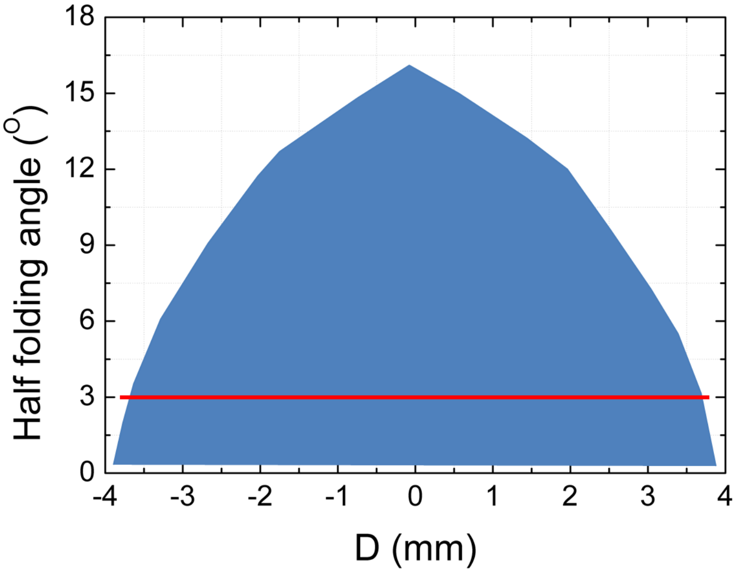

Figure 11. The stability region of the OPO cavity when the folding angle was changed from 0 to 18 degrees for the same distance between the curved mirror (R=-75 mm) and the PPKTP crystal. The line in red indicates the OPO operating angle.

At a folding angle of 0 degrees the curved mirror M2 could be placed at a distance from the PPKTP crystal of between -2 mm to 2 mm from the zero position, whereas for a folding angle of 15 degrees the distance could be changed only by 0.25 mm. In this case the cavity had a much smaller stability range and, if constructed, the OPO would be less stable and more sensitive to external perturbations. The intracavity spot radius of the oscillating signal beam was calculated in LCav. It varied from 25-30 µm ($1/e^2$ radius) depending on the central wavelength of the signal oscillating in the OPO cavity. Mirrors M2 and M3 were concave with -75-mm radius of curvature while mirrors M3 and M4 were planar. The ring cavity confined the oscillating wave to a 27-µm beam radius inside the PPKTP crystal at a signal wavelength of 1.25 µm. The pump laser beam was focused with an f = 63-mm lens through M1 to produce a beam waist radius of 17 µm, as required by the Boyd-Kleinman condition [15]. The pump spot size corresponded to an intensity of 0.14 MWcm^{-2}, which is limited by the PPKTP coatings damage threshold. A stable regime of the OPO was achieved when the distances between the PPKTP crystal and curved mirrors were set to 39.07 mm. The beam propagation inside the cavity is presented in Figure 12.

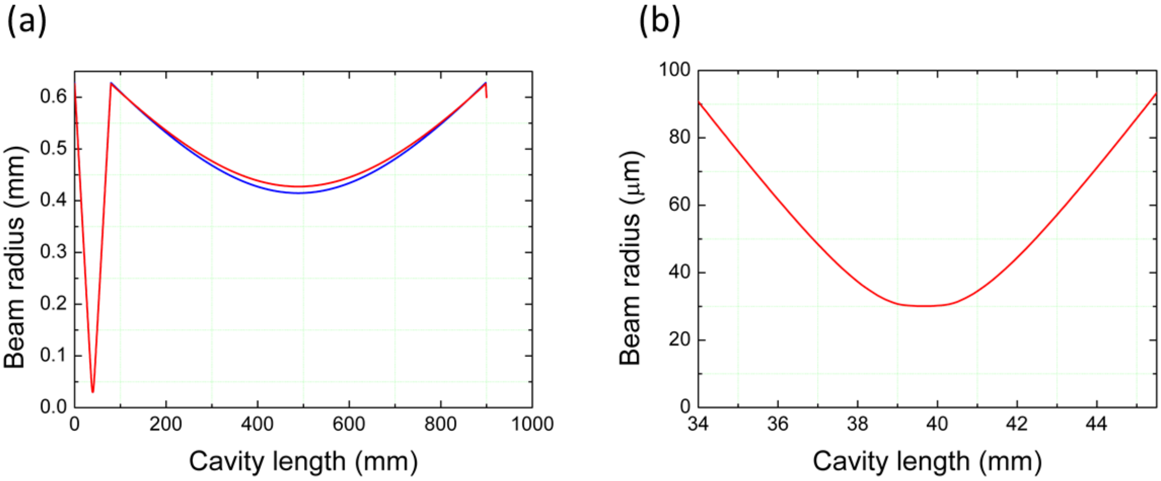

Figure 12. The beam profile of the signal pulse oscillating in the 333-MHz OPO cavity (a) full path; (b) around the nonlinear crystal.

The smallest possible half-folding angle for the OPO was 3 degrees. The detailed final configuration of the 333-MHz OPO oscillating from 1-1.6 µm for the signal pulses is presented in Figure 13. A fused silica window was used as an OC and the output power depended on the angle of that window, according to the Fresnel loss. We used a 40 degree angle which gave us power in the signal pulse as high as 60 mW. A reflectivity of 2 % at this angle should be possible, which suggests the internal power of the signal to be as high as 3 W. On the output we could see two beams leaving the OPO cavity since the other surface AR coated for the signal, which was still reflecting the signal light.

The working OPO is shown in the photograph reproduced in Figure 14. In this picture we can notice a lot of visible color in the OPO cavity. The OPO was built for signal oscillation from 1-1.6 µm, but other frequencies also appear. As the pump propagates in the PPKTP crystal, not only signal, but also idler pulses are generated. Other nonlinear processes including SFM of the pump and signal, pump and idler, and SHG of the pump and signal also take place. Even SHG of the idler occurs but we cannot see this with the eye.

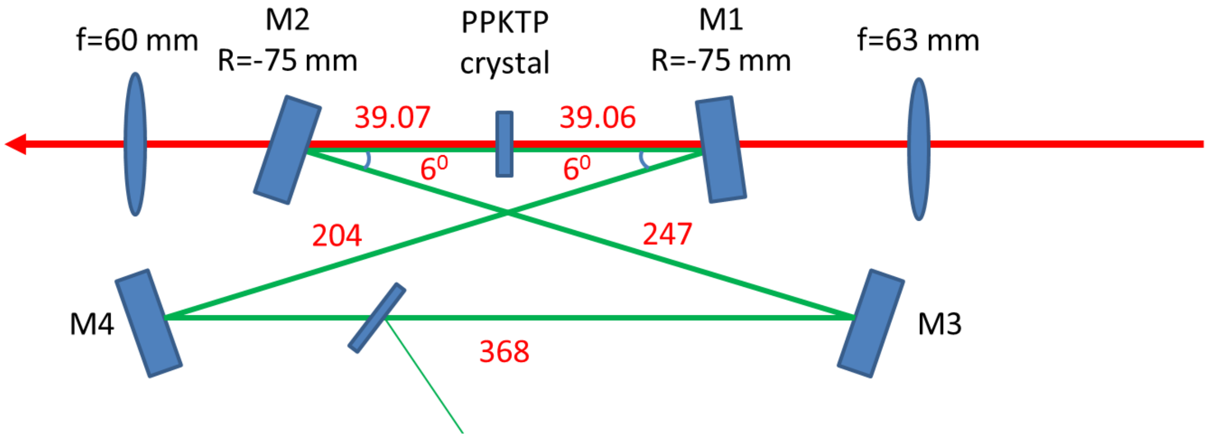

Figure 13. The final OPO cavity configuration where the folding angle of 6 degrees was used and the positions of the optical elements calculated to ensure a stable OPO operation. All units in mm.

To ensure efficient generation of different nonlinear processes the ring type OPO must be properly aligned. The distances between elements were determined before the final alignment. At the beginning the pump beam focused into the PPKTP crystal must be overlapped with itself for as many round trips as possible. This was done by using a second-harmonic beam of the pump which is in the visible at 400 nm. The 400 nm beam could be seen on the curved mirror M1 which was the initial point for the alignment. The beam travelling around the cavity twice was visible on the mirror M1 surface. When those two beams were overlapped and the cavity length was the same as the pump laser, oscillation was observed and the OPO could generate a broad range of visible wavelengths. The pump power for the initial alignment was limited to avoid damage until oscillation was found. The power and the beam shape of the signal was observed by moving the focusing lens position, the PPKTP crystal and the cavity length together with the distance between the curved mirror M2 and PPKTP crystal. All these parameters must be changed step by step by observing the signal output power reflected from the OC and the beam shape.

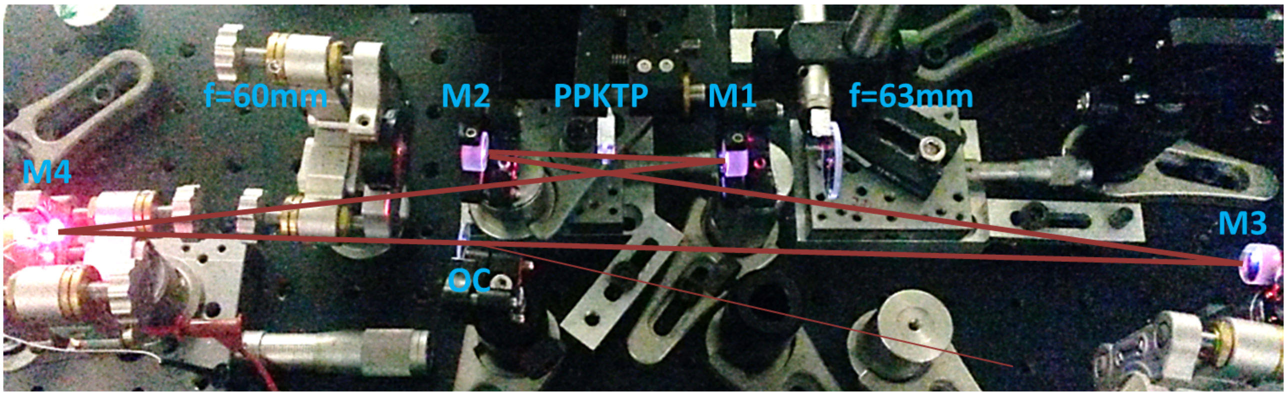

Figure 14. Photograph of the 4-mirror OPO cavity pumped by the Ti:sapphire laser.

3.4.2 Characterization

The OPO cavity length was about 900 mm. The largest separation between the mirrors was 368 mm. Any large separation means higher instability due to cavity length drift and air currents, therefore the OPO stability was ensured by boxing it. Once the OPO was finally running in a stable configuration, a full characterisation was performed. Figure 15 shows the depleted pump which was measured after the light passed through the curved mirror M2.

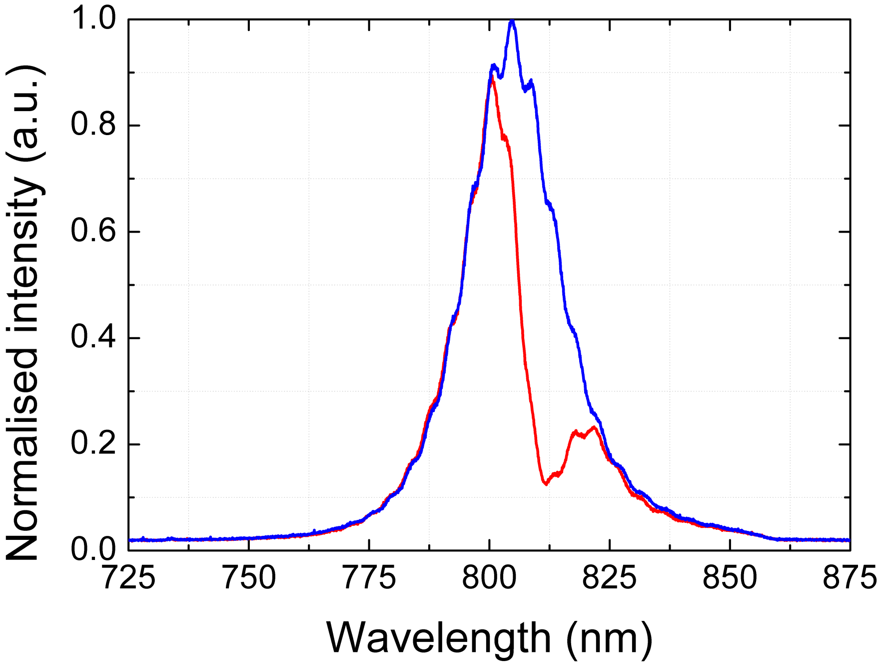

Figure 15. The pump pulse spectrum before the OPO was running (blue) and when the OPO oscillated (red) at 1450 nm. The spectra were recorded after the curved mirror M2.

The presented spectrum was measured for the grating period of 27.25 µm. For this grating period an efficient phasematching condition was ensured for the pump wavelength at 812 nm. At this pump wavelength the pump power is most depleted and the central signal wavelength was 1.46 µm. The calculated pump depletion expressed as a percentage from areas of the plots presented in Figure 15, was 25%. It means that we are not using all the pump power. We are limited by the phasematching for a relatively narrow wavelength window in comparison with the ultrashort pulse bandwidth. Details of the OPO characterization such as its tuning, pulse durations and cavity dispersion are presented in Chapter 4 and Chapter 5. We used this OPO design for the demonstration of the repetition rate multiplication of a locked frequency comb from 333 MHz to 1 GHz frequency by synchronously pumping a three times shorter OPO cavity. The OPO design also formed the basis for the demonstration of tuning covering the mid-IR region from 1.95-4.0 µm.

3.5 Conclusions

This chapter has presented details of how a Laser Quantum 333-MHz repetition rate Ti:sapphire laser was used to pump a 4-mirror ring-geometry OPO. The conditioning of the pump pulses prior to the OPO using GTI mirrors was described and a subsequent characterisation of the pump laser was presented. The rationale for the selection of a PPKTP OPO crystal was discussed and the details of its design and phasematching presented. The OPO resonator design and alignment were described, and were followed by some initial characterizations of the working OPO. The following chapters present investigations carried out using this OPO, extending its operation to 1 GHz repetition frequency (Chapter 5) and to a fully tunable frequency comb from 1.95-4.0 μm (Chapter 4).

References

[1] D. E. Spence, P. N. Kean, and W. Sibbett, "60-fsec pulse generation from a self-mode-locked Ti:sapphire laser," Opt. Lett. 16, 42–44 (1991).

[2] M. Fox, Ch. 4 "Radiative transitions in atoms," in Quantum Optics: An Introduction (Oxford University Press, 2007), pp. 48-71.

[3] L. E. Hargrove, R. L. Fork, and M. A. Pollack, "Locking Of He-Ne Laser Modes Induced By Synchronous Intracavity Modulation," Appl. Phys. Lett. 5, 4-5 (1964).

[4] E. P. Ippen, C. V. Shank, and A. Dienes, "Passive mode locking of the cw dye laser," Appl. Phys. Lett. 21, 348-350 (1972).

[5] A. E. Siegman, Ch. 27 "Active Laser Mode-Coupling," in Lasers (University Science Books, 1986), pp. 1041-1103.

[6] N. Sarukura and Y. Ishida, "Pulse evolution dynamics of a femtosecond passively mode-locked Ti:sapphire laser," Opt. Lett. 17, 61–63 (1992).

[7] U. Keller, K. J. Weingarten, X. K. Franz, D. Kopf, B. Braun, I. D. Jung, R. Fluck, H. Clemens, N. Matuschek, and J. A. Der Au, "Semiconductor saturable absorber mirrors (SESAM's) for femtosecond to nanosecond pulse generation in solid-state lasers," IEEE J. Quantum Electron. 2, 435–453 (1996).

[8] U. Keller, "Recent developments in compact ultrafast lasers," Nature 424(6950), 831-838 (2003).

[9] R. Paschotta and U. Keller, Ch. 1 "Ultrafast Solid-State Lasers," in Ultrafast Lasers: Technology and Applications, M. E. Fermann, A. Galvanauskas, and G. Sucha, eds. (Marcel Dekker, Inc, 2003), pp. 1-60.

[10] W. Koechner, Ch. 9 "Mode Locking," in Solid-State Laser Engineering, 6th Edn. (Springer, 2006), pp. 534-586.

[11] P. F. Moulton, "Spectroscopic and laser characteristics of Ti:Al_2O_3," J. Opt. Soc. Am. B 3, 125-133 (1986).

[12] D. C. Edelstein, E. S. Wachman, and C. L. Tang, "Broadly tunable high repetition rate femtosecond optical parametric oscillator," Appl. Phys. Lett 54, 1728-1730 (1989).

[13] W. Koechner, Ch. 10 "Nonlinear Devices," in Solid-State Laser Engineering, 6th Edition (Springer, 2006), pp. 587-679.

[14] A. E. Siegman, Ch. 15 "Ray Optics and Ray Matrices," in Lasers (University Science Books, 1986), pp. 581-625.

[15] G. D. Boyd and D. A. Kleinman, "Parametric Interaction of Focused Gaussian Light Beams," J. Appl. Phys. 39, 3597 (1968).

Chapter 4. Mid-IR 333-MHz frequency comb continuously tunable from 1.95-4.0 µm

This chapter reports a fully stabilized idler comb from a 333-MHz femtosecond optical parametric oscillator in which carrier envelope offset frequency (f_{CEO}) stabilization was implemented by using a versatile locking technique that allowed the idler comb to be tuned continuously over a mid-infrared range from 1.95-4.0 µm. We designed a multi-section and multi-grating PPKTP crystal which provided phasematched parametric generation, amplification and efficient pump+idler sum-frequency generation (SFG). The pump+idler SFG light from 570-670 nm heterodyned with the pump supercontinuum resulted in a strong signal across the tuning range of the OPO. The idler comb f_{CEO} was stabilized to a 10-MHz external frequency. A cumulative phase noise from 1 Hz–64 kHz of <1.3 rad was measured across the full comb operating range. Average idler output powers of up to 50 mW were obtained.

4.1 Introduction

Many molecules exhibit vibrational absorptions in the mid-infrared (mid-IR) spectral region where each molecule has a characteristic absorption spectrum which can be used for 'molecular fingerprinting'. This chapter is focused on the generation of a continuously tunable frequency comb in the mid-IR region since such combs are promising sources for dual-comb [1], coherent FTIR spectroscopy [2] and for molecular spectroscopy, trace gas detection [3, 4]. Combs producing longer wavelengths could have applications in laser-driven particle acceleration [5] or as sources of carrier-envelope-phase (CEP) stabilized seed pulses for injection into high power amplifiers [6, 7] for extreme ultraviolet (XUV) high harmonic generation [8, 9]. Frequency comb based techniques can provide hundred-fold improvements in acquisition rates, high spectral resolutions and broad spectral bandwidths limited only by the femtosecond laser. Conventional mid-IR Fourier-transform infrared (FTIR) spectrometers have limited acquisition times and their spectral resolutions are limited by the mechanical motion of the Michelson interferometer and the available displacement of the scanning system. Frequency combs comprise many equally spaced lines in frequency and periodically repeating trains of pulses in time and therefore are perfect candidates for high resolution spectroscopy.

There are several methods to achieve frequency combs in the mid-IR region. Extremely tunable combs extending from 3-17 µm can be generated via difference frequency generation (DFG) but the DFG nonlinear process is not efficient [10, 11, 12]. This method is most efficient only for high peak power pulses since the interacting pulses travel through the material only once. Frequency combs can be generated in high-Q-factor optical micro-resonators [13, 14]. In these microscale resonators four-wave mixing and Raman gain generates combs from an intense CW pump. Wavelengths to 3.1 µm in silicon have been produced in this way [15]. Practical micro-resonators are still on the horizon since a lot of investigations must be done in order to understand how the comb is generated, and control its exact structure and dynamics.

Nonetheless this is still one of the most promising methods to generate combs in the mid-IR region. Femtosecond lasers emitting light directly in the mid-IR have also been reported, notably Cr^{2+}:ZnSe [16, 17], Cr^{2+}:ZnS [18] and Tm-/Ho-co-doped fiber lasers [19] operating from 2.0-2.4 µm, and such systems have been demonstrated as fully stabilized frequency combs [20, 21]. The highest average power combs with the best conversion efficiency in the mid-IR region are achieved from optical parametric oscillators (OPOs) [22]. Wavelength coverage of up to 4.8 µm has been generated [22, 23] with f_{CEO} beat linewidths limited to the instrument resolution of 15 Hz [24]. Such Hz-level linewidths [24] are much better than those obtained from other mid-IR combs [25, 26]. Degenerate OPOs have been reported which can emit spectra covering 900 cm^{-1} at 3 µm [27].

Building broadband frequency combs in the mid-IR region is a challenging task involving precise dispersion and reflectivity control together with sophisticated design of the nonlinear crystal over a broad range of wavelengths. In this chapter I describe an approach which allows the generation of a broadly tunable and locked frequency comb in the mid-IR region from 1.95-4 µm, in which the pump repetition rate f_{REP} and the carrier-envelope offset f_{CEO} frequency of the idler pulses are locked to a traceable radio-frequency reference. This work proved that the frequency comb in the mid-IR region was preserved by some careful power spectral density and cumulative phase noise measurements. Two-sample frequency deviation data are also presented.

4.2 Concepts in phase and frequency control of femtosecond lasers

4.2.1 Repetition rate f_{REP}

A modelocked laser produces pulses which are separated in the time-domain by a fixed spacing. In the frequency-domain these pulses form a comb: a number of longitudinal modes, separated by a fixed spacing. Unfortunately, this spacing is not truly fixed because of temperature fluctuations, vibrations and electronic noise. These perturbations couple into the optical system and effectively modulate the time-dependent output intensity, whose variations can be measured via a relative intensity noise (RIN) measurement. Moreover, these perturbations change the repetition rate f_{REP} of the laser system and the difference between the group and phase velocities (f_{CEO}). Both frequencies must be stabilized to a well known reference, if we want to achieve a truly stabilized frequency comb.

4.2.2 Carrier-envelope-offset f_{CEO} frequency

Definition of the f_{CEO} frequency

The second-parameter which must be stabilized to achieve a locked frequency comb is the f_{CEO} frequency. The femtosecond pulses oscillating inside the Ti:sapphire or OPO cavity are transmitted and reflected from different optical elements. Usually these optical elements are dispersive and cause the group and phase velocities to be different. This results in a change of the f_{CEO} frequency. The ultrashort pulse envelope travels at the group velocity, while the carrier wave travels with the phase velocity. The difference between the carrier-wave of a pulse and the maximum point of its envelope is the carrier-envelope-phase (f_{CEP}). The ultrashort pulse electric field can be written

$$E(t) = E_0(t)\exp[i\omega t + i\phi_{CEP}] \tag{48}$$

Because of the difference between group and phase velocities in THE presence of dispersion, the ϕ_{CEP} is changing continuously from pulse to pulse. Usually ϕ_{CEP} is not controlled, but if we want to have the same ϕ_{CEP} (or f_{CEO}=0 since $f_{CEO} = f_{REP}\frac{\Delta\phi_{CEP}}{2\pi}$) for each pulse leaving the laser system, the difference between carrier and envelope must be fixed.

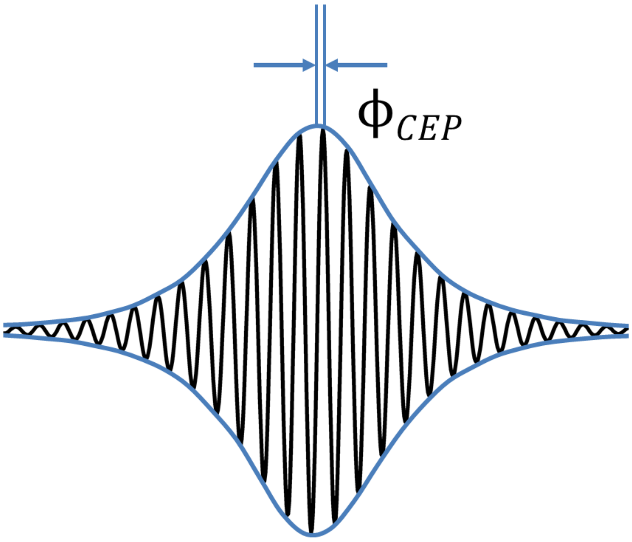

Figure 1. The pulse carrier is offset from the pulse envelope by ϕ_{CEP}. In a modelocked oscillator, after each cavity roundtrip, ϕ_{CEP} changes by $\Delta\phi_{CEP}$.

In the frequency domain the pulse train contains a number of longitudinal modes separated by the repetition frequency, where the ensemble of modes has an offset from zero hertz of an amount equal to the f_{CEO} frequency. If we lock the repetition rate or the mode spacing f_{REP} and the longitudinal modes offset f_{CEO}, we achieve a truly stabilised frequency comb whose stability is only limited by the reference source. The structure of the locked comb is presented in Figure 2.

f_{CEO} detection

There was no straightforward method for measuring the f_{CEO} until 1999 when microstructure fibers, today known as photonic crystal fibers (PCF), appeared. These fibers containing air-holes surrounding a silica core were used to demonstrate supercontinuum generation in 1999 by Ranka et al. [28]. The PCF structure gives a large core-cladding index difference which results in strong mode confinement, single-mode operation over an exceptionally wide wavelength range and a large effective nonlinearity. Moreover, the air-hole pattern determines the dispersion of the fiber and therefore the GVD can be easily controlled. The optical nonlinearities in the PCF ensure efficient pulse broadening leading to supercontinuum generation. A variety of

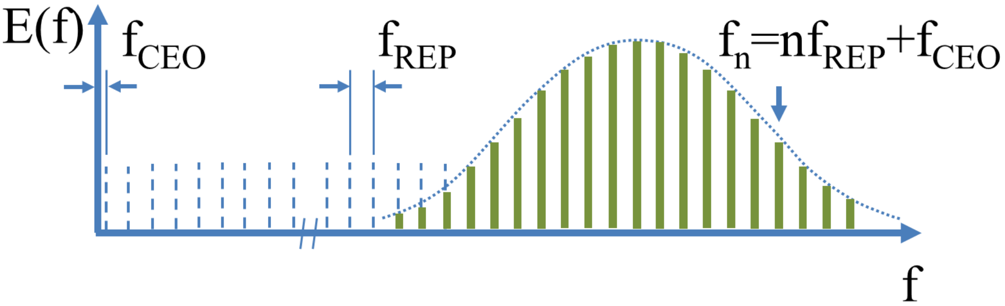

Figure 2. Evenly spaced modes of an ultrashort pulse train forming a frequency comb which f_{REP} and f_{CEO} are locked.

applications were presented where one of them was the optical frequency comb stabilization [29]. Jones et al. in 2000 demonstrated f_{CEO} stabilization of an ultrashort pulse modelocked Ti:sapphire laser by using a PCF.

The method for detecting the f_{CEO} frequency was called the f-2f self-referencing technique [30]. The idea of detecting f_{CEO} is simple: the comb must be broadened to become octave spanning. This can be achieved in a PCF in which self-phase modulation, Raman and four-wave mixing effects can broaden the spectrum so much that the second-harmonic of the long-wavelength end can spectrally coincide with the shorter wavelengths in the spectrum (see Figure 3). The frequency doubled comb has an offset of $2f_{CEO}$ while the original comb at the same wavelength has an offset of only f_{CEO}. As a result, by heterodyning the frequency doubled light with the original comb, we can detect the f_{CEO} of the laser pulse if the phase relationship between the longer and shorter wavelengths/frequencies is maintained during the comb broadening. For this technique to be possible, the supercontinuum must be octave spanning and coherent. This technique is now the common method used to measure f_{CEO} of a laser frequency comb.

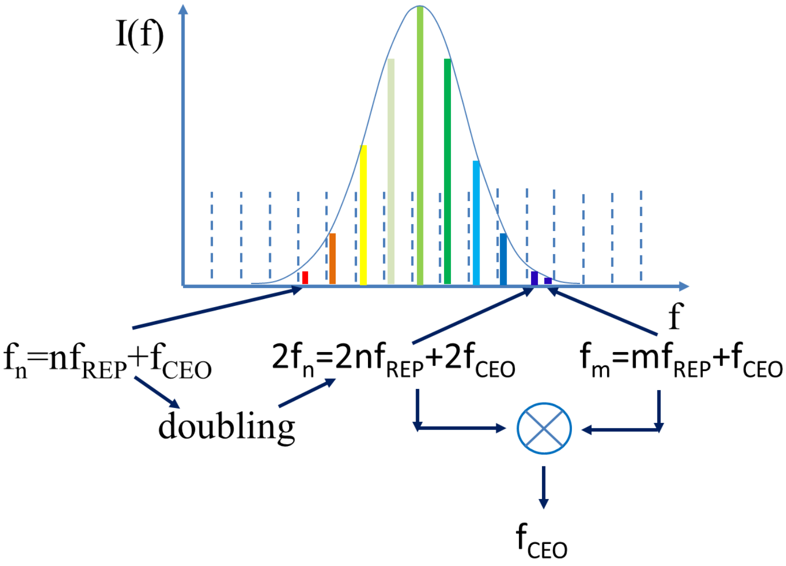

Figure 3. Measurement of f_{CEO} by the f-2f self-referencing method using an octave spanning pump spectrum.

The shorter and longer frequencies of an octave spanning comb can be expressed as

$$\begin{aligned} f_1 &= f_{CEO} + n f_{REP} \\ f_2 &= f_{CEO} + m f_{REP} \end{aligned} \tag{49}$$

where n and m are mode numbers. If f_1 is frequency doubled in a nonlinear crystal then it will contain

$$2f_1 = 2f_{CEO} + 2n f_{REP} \tag{50}$$

As we can see, when $2n \approx m$ we have two combs in a common spectral region but whose offsets are different by f_{CEO}. Therefore by heterodyning these two combs on an avalanche photodiode we can detect only harmonics of the f_{REP} and the desired f_{CEO}. The obtained f_{CEO} signal may vary between 0 Hz and $\frac{f_{REP}}{2}$.

Other self-referencing methods have been used for f_{CEO} detection. In the case of fs OPOs we heterodyned non-phasematched SHG or SFM visible wavelengths with the coherent pump supercontinuum light. There are three waves interacting with each other: pump, signal and idler. They possess a fixed phase relationship between the pump, signal and idler ϕ_{CEP}. In the frequency domain it can be expressed as

$$f_{CEO}^{pump} = f_{CEO}^{signal} + f_{CEO}^{idler} \tag{51}$$

From this equation we can state that all frequency combs are stabilised, when at least two out of three f_{CEO} are locked. If the repetition rate f_{REP} of the pump laser is also referenced, then we have fully stabilised frequency combs from an OPO too. After the f_{CEO} has been detected, it must be compared to a reference source. We used a phase frequency detector (PFD) circuit reported by Prevedelli et al. in 1995 to measure the difference between the detected f_{CEO} frequency and a reference frequency [33]. The PFD expresses the frequency/phase difference as a voltage which we can then use as an error signal. The corresponding voltage is then applied to steer the f_{CEO} via any element that controls the difference between the group and phase velocities. In our OPO we used a piezoelectric-transducer (PZT), on which was attached a cavity end mirror.

Controlling f_{CEO}

There are several methods by which we can control the detected f_{CEO}. The common methods modulate the pump power [31, 32] or change the nonlinear refractive index of the laser medium via acousto-optic modulators (AOM) placed in the pump beam. The parameters of the fs laser are the same, but due to diffraction effects the power is reduced. More efficient control of f_{CEO} can be achieved by directly modulating the pump diode current [34].

We used piezo-electric transducers (PZTs) for the f_{CEO} control in our synchronously pumped

OPOs. The central wavelength of the OPO was tunable with cavity length [35]. Since the OPO uses only dispersive mirrors, the cavity round trip time/cavity delay is fixed

$$\tau(\omega) = \frac{\delta\phi}{\delta\omega} = constant \tag{52}$$

This means that the group delay must change accordingly to the change of the cavity length L. Therefore the group delay dispersion is:

$$\frac{\delta\tau}{\delta\omega} = \frac{\delta^2\phi}{\delta\omega^2} = -\frac{1}{c}\frac{\delta L}{\delta\omega} \tag{53}$$

or

$$\frac{\delta\omega}{\delta L} = \frac{-\frac{1}{c}}{[\frac{\delta^2\phi}{\delta\omega^2}]} \tag{54}$$

From the equation above we can see that the cavity central wavelength will tune quickly for a low GDD cavity and slower for a high GDD cavity.

The spectral phase is given by (see Chapter 2)

$$\phi_{CEP} = \phi(\omega) - \omega\frac{\delta\phi(\omega)}{\delta\omega} \tag{55}$$

Then the change with frequency can be expressed as

$$\frac{\delta\phi_{CEP}}{\delta\omega} = -\omega\frac{\delta^2\phi(\omega)}{\delta\omega^2} \tag{56}$$

The equations (54) and (56) can be compared to give

$$\frac{\delta\phi_{CEP}}{\delta\omega} = \frac{\omega}{c}\frac{\delta L}{\delta\omega} \tag{57}$$

or

$$\frac{\delta\phi_{CEP}}{\delta\omega} = \frac{\frac{\omega}{c}}{\frac{\delta\omega}{\delta L}} \tag{58}$$

From Equations (54) and (58) it can be shown that the phase will shift much faster than the oscillating pulse central frequency. Therefore the f_{CEO} can be controlled by adjusting the OPO cavity length without significantly affecting the oscillating pulse central wavelength. This is done by a PZT via a feedback loop for f_{CEO} stabilization.

4.2.3 Phase-noise

Phase-noise measurements were performed for the purpose of determining the noise of the locked f_{CEO} and repetition rate f_{REP} frequencies. The laser produces pulses whose phase and amplitude can be described as

$$E(t) = E_0 \exp^{[i\omega_0 t + i\phi(t)]} \tag{59}$$

We can measure the noise of the locked f_{CEO} and determine the frequencies at which the noise is strongest and has the most impact on the linewidth of the comb tooth. For this measurement we used the output from a PFD circuit and the output from a mixer in the case of the repetition rate. The PFD output was calibrated in order to calculate the power spectral density (PSD) of the locked signal. The cumulative phase noise PSD was calculated by summing the noise across the recorded frequency range.

The phase noise was presented by using a power spectral density (PSD) plot. It describes the noise power per unit frequency interval relative to the mean rad^2 Hz^{-1}. The equation for the PSD calculation can be found in [39]. The Fourier transform for a function $h(t)$ can be expressed as

$$H(f) = \sum_{-\infty}^{\infty} h(t) \exp^{[2\pi i f t]} dt \tag{60}$$

$$h(t) = \frac{1}{2\pi} \sum_{-\infty}^{\infty} H(f) \exp^{[-2\pi i f t]} df \tag{61}$$

According to Parseval's theorem, the contained signal energy in time and frequency domains is the same. Therefore the total power

$$E_{total} = \sum_{-\infty}^{\infty} |H(f)|^2 df = \sum_{-\infty}^{\infty} |h(t)|^2 dt \tag{62}$$

The power spectral density (power in a frequency interval) can be calculated as

$$P_h(f) = |H(f)|^2 + |H(-f)|^2 \tag{63}$$

for $0 \leq f \leq \infty$. We used a discrete Fourier transform for the PSD calculation since we have a finite number of points. The discrete Fourier transform containing N points is written as

$$H_k = \sum_{j=0}^{N-1} h_j \exp^{[\frac{2\pi i j n}{N}]} \tag{64}$$

Then the phase noise PSD can be normalised using the mean-squared-amplitude. The integral of the PSD over the range from 0 Hz to the Nyquist frequency is equal to half the mean-squared-amplitude and this was used to normalise the PSD for each frequency [39]. The resulting phase noise PSD against frequency is given for the characterization of the locked heterodyne beat. The cumulative noise is calculated by integrating the normalised PSD over the frequency range

$$RMS_{PSD} = [\sum_{0}^{f_{Nyquist}} P_{norm}(f) df]^{\frac{1}{2}} \tag{65}$$

where $f_{Nyquist}$ is the Nyquist frequency and P_{norm} is the normalised PSD.

4.2.4 Two-sample frequency deviation

The next important method for the noise characterization of the locked f_{CEO} and repetition rate f_{REP} is the two-sample frequency deviation measurement [36]. The Allan or two-sample variance is a measure of the stability of an oscillator in the time domain. A frequency counter is used to count the mean value of a frequency over a several different gate times. It is the variance of the difference of two fractional frequencies f_{i+1} and f_i (see Figure 4). The fractional frequency f_i was measured at time $t_0 + i\tau$ while frequency f_{i+1} was measured at a later time of $t_0 + (i+1)\tau$. The Allan variance depends on the gate time τ and expresses the mean-square of all frequency counter samples separated in time by τ. The Allan variance can be expressed as

$$\sigma_f(\tau) = \sqrt{\frac{1}{2(N-1)} \sum_{i=1}^{N-1} (f_{i+1} - f_i)^2} \tag{66}$$

where $N - 1 = [\frac{T}{\tau}] - 1$ and

$$f_i = \frac{f_1(t_0 + i\tau) - f_0}{f_0} \tag{67}$$

f_i is the fractional frequency at sample time $t_0 + i\tau$ and $f_1(t)$ represents the current frequency averaged over a time interval of τ. f_0 is the frequency of the reference. It is a variance of N-1 pairs of frequency measurements taken at time t and $t+\tau$. The Allan variance calculated values depend on the accuracy of the counters used for the measurement and on the timing precision between any two measurements.

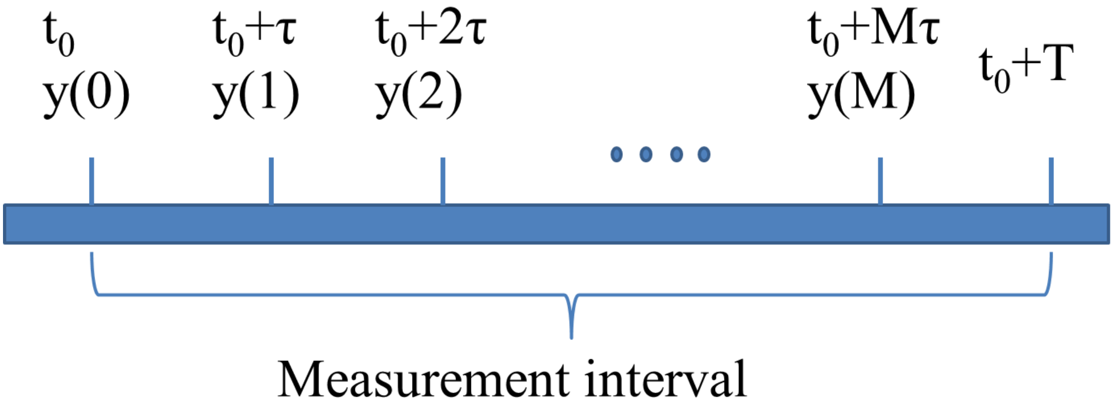

Figure 4. Time line for frequency counter measurements.

There are two methods of measuring the frequency stability referred as Π and Λ counters [37, 38]. Both counters provide one value every τ seconds when programmed to measure over the time τ. This can lead to assumption that the estimation is always of the Π type. The internal estimation for the frequency error are of the form:

$$\begin{aligned} \sigma_y(\tau) &= \frac{1}{\tau}\sqrt{2(\delta t)^2_{trigger} + 2(\delta t)^2_{interpolator}} && \text{for } \Pi \text{ counter} \\ \sigma_y(\tau) &= \frac{1}{\tau sqrtn}\sqrt{2(\delta t)^2_{trigger} + 2(\delta t)^2_{interpolator}} && \text{for } \Lambda \text{ counter} \end{aligned} \tag{68}$$

where for Λ counter

$$\begin{aligned} n &= f_0\tau \quad \text{when } f_{00} \leq f_1 \quad \text{and} \\ n &= f_1\tau \quad \text{when } f_{00} \geq f_1 \end{aligned} \tag{69}$$

where f_1 is of the order of 200 kHz. The two terms inside the square root correspond to independent white noise processes. In the Π counter, the measurement stops at the first zero crossing as the measurement time elapses. We have uniform average in the presence of white phase noise. In case of Λ counter, it consists of a triangular-weight average. The counter takes a series of n measurements of f_i and expects value of f by averaging. Therefore by using a Λ counter we can not calculate the frequency stability for other gate times than we set gate time of the measurement. The Allan variance for different gate times can be extracted only by using Π counter.

4.3 Ti:sapphire pumped OPO

The OPO was synchronously pumped by a 333-MHz Ti:sapphire laser (Gigajet, Laser Quantum). Details of the OPO design were presented in Chapter 3.

4.3.1 Cascaded-grating PPKTP crystal

In order to achieve comb locking over a broad wavelength range, a strong enough heterodyne possible for a variety of OPO operating wavelengths. As introduced already in Section 3.3.3 for this reason we used a new design of PPKTP crystal. The PPKTP crystal was 1.2 mm thickness with an aperture of 1 x 13 mm. It contained a 1-mm section phasematched for signal generation from 1.0-1.6 µm, a 50 µm section for second-harmonic generation (SHG) of the signal and a 100-µm section for pump+idler sum frequency generation (SFG) (see Figure 5).

This crystal design enabled the efficient production of pump+idler SFG light, which was heterodyned with common wavelengths in a pump super-continuum (SC) generated in a 30-cm length of photonic crystal fiber (PCF) to yield the idler f_{CEO} frequency employed for comb stabilization. The introduction of the 100 µm thickness additional quasi-phasematched pump+idler SFG sections was critical for generating a sufficiently strong heterodyne beat signal for idler f_{CEO} stabilization. Our electronics required a >30-dB S/N beat between the pump supercontinuum and the SFG light. In previously reported examples of OPO frequency-comb locking schemes, parasitic SFM has served this purpose, however it cannot be relied on to be generated with uniform efficiency across a broad tuning range, because it typically originates either from the last coherence length of the crystal or from high-order phasematching, which is strongly wavelength dependent.

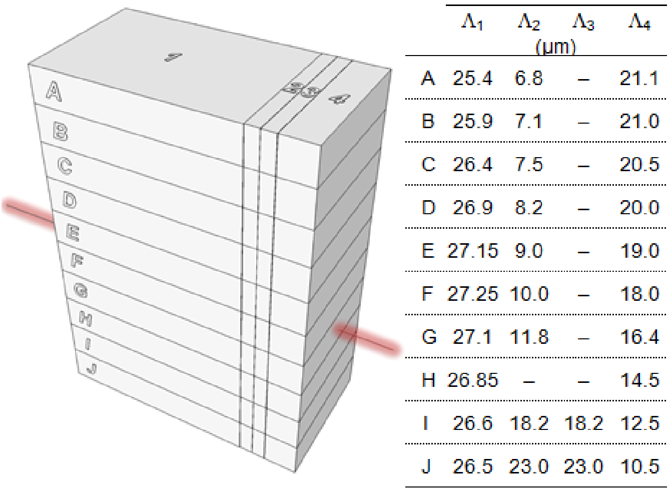

	Λ_1	Λ_2 (μm)	Λ_3	Λ_4
A	25.4	6.8	–	21.1
B	25.9	7.1	–	21.0
C	26.4	7.5	–	20.5
D	26.9	8.2	–	20.0
E	27.15	9.0	–	19.0
F	27.25	10.0	–	18.0
G	27.1	11.8	–	16.4
H	26.85	–	–	14.5
I	26.6	18.2	18.2	12.5
J	26.5	23.0	23.0	10.5

Figure 5. PPKTP crystal design, comprising four sections with lengths of 1 mm, 50 μm, 50μm and 100 μm. Sections 1, 2 and 4 were phasematched for OPO, signal SHG and pump + idler SFG respectively, with Section 3 being unpoled except for Gratings I and J, in which it was phasematched for signal SHG.

To illustrate the importance of phasematched SFG section in the crystal for ensuring efficient pump+idler frequency mixing we present here a simulation for section G using a nonlinear envelope equation model [40] introduced in Section 2.2.3. The simulation presented in Figure 6 reached steady state after 80 roundtrips. Figure 6 presents the evolution of the p+i mixing field as the pump and idler propagate through the 1.2-mm length PPKTP crystal. As we can notice, at the beginning the pump+idler field is weak. The light is weakly generated in the 1000μm OPO section of the crystal. We can notice a forward and backward pump+idler field energy exchange which happens over one coherence length. The pump+idler SFG starts to grow rapidly in the 50-μm SHG section and in the 100-μm SFG section at 1100 μm. Between the SHG and SFG sections a 50-μm blank section does not change the strength of the pump+idler field. Once we start introducing gratings, the crystal is better phase-matched for frequency mixing and it gives an advantage as the power goes up by nearly two orders of magnitude compared to the parasitic SFG which is sufficient to ensure a strong heterodyne beat for f_{CEO} locking across a broad range of wavelengths in the mid-IR region.

4.3.2 OPO tunability in the mid-IR region

The idler pulses were output coupled through cavity mirror M3 and their tunability was evaluated by directing the collimated idler beam into a Fourier-transform spectrometer. A second beam from a 632.8 nm HeNe laser was coupled into the interferometer for absolute delay calibration. Mid-IR and HeNe calibration interferograms were recorded, with idler spectra measured as the OPO cavity length was tuned. Operation close to degeneracy was unstable and unsuitable for comb stabilization. We note however that, with suitable intracavity dispersion control and cavity stabilization, degenerate femtosecond OPOs can operate stably over a broad instan-

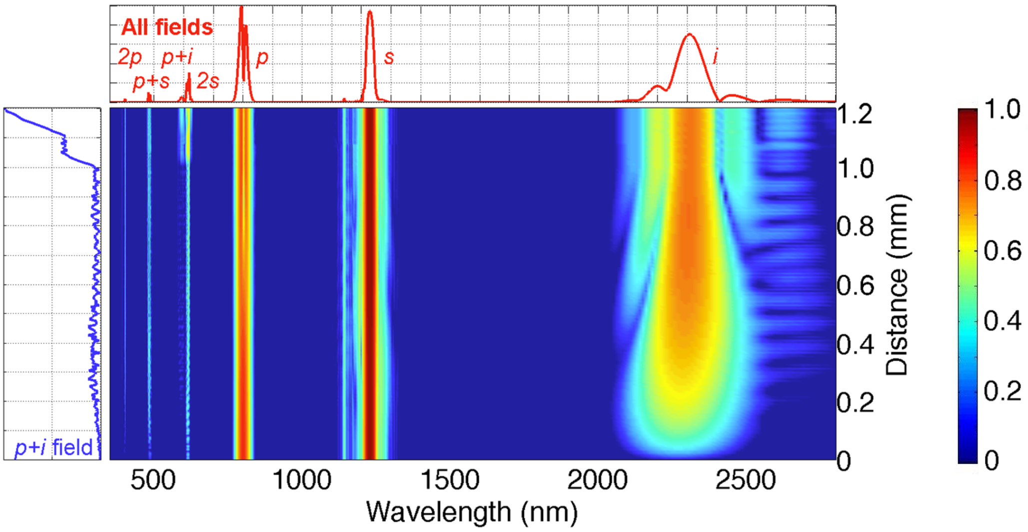

Figure 6. Simulated OPO output spectrum for Grating G, expressed as a logarithmic density plot, showing its evolution through the crystal once steady-state has been reached. The upper line plot shows, on a linear scale, the fundamental, second-harmonic and sum-frequency fields of the pump (p), signal (s) and idler (i) waves. The line plot left of the main figure shows the evolution of the p + i sum-frequency field, illustrating how its amplitude is enhanced substantially by the inclusion of both the SHG and SFG gratings.

taneous bandwidth [41, 42]. Figure 7 shows the idler spectra and corresponding average power for the 1.95–4.0 μm tuning range over which frequency-comb stabilization was possible.

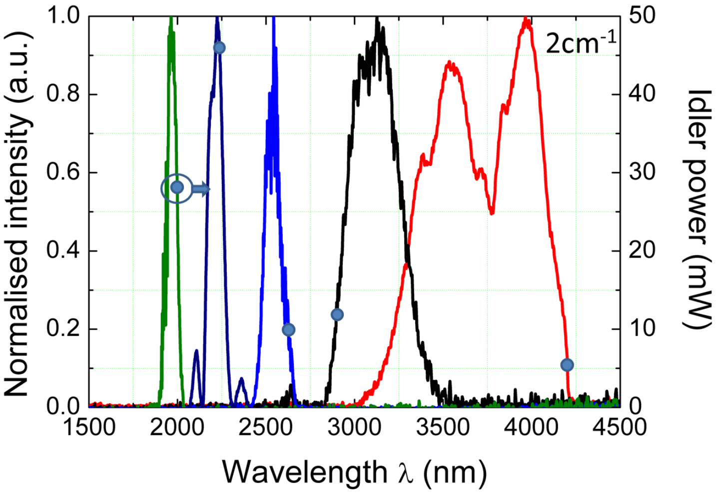

Figure 7. Cavity-length-tuned OPO idler spectra measured using a Fourier-transform spectrometer. Symbols specify average output coupled idler power. The resolution of the FTIR interferometer was 2 cm^{-1}.

As the idler wavelength was changed from 1.95-4 μm, the wavelength of the pump+idler light was changed from 570-670 nm accordingly (see Figure 8). The new design of cascaded-grating PPKTP crystal could easily generate a strong pump+idler field across the full tuning range of idler. A strong f_{CEO} heterodyne beat note was obtained for every idler wavelength. The heterodyne beat signal was maintained at a sufficiently strong level as the idler wavelength was tuned from 1.95-4 µm. Selection of a common wavelength on the photodiode over such a broad wavelength range was ensured by introducing a monochromator. There was no need to use optical filters in order to overlap the same wavelengths from the PCF and OPO, allowing the f_{CEO} signal-to-noise ratio to be maintained at a high level (>35 dB at 100kHz RBW) across the OPO tuning range.

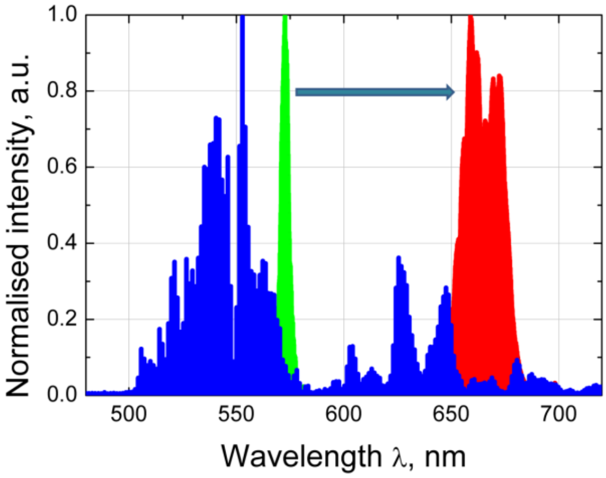

Figure 8. Spectral overlap of the pump+idler SFG light (green to red) and the pump super-continuum (blue). The 570-nm SFG light (green) was overlapped with the super-continuum light component on one edge giving the f_{CEO} frequency of the idler pulse at 1.95 µm. Similarly, the 670-nm SFG light (red) on the other edge was overlapped with the super-continuum component for f_{CEO} stabilization of the idler at 4.0 µm.

The full spectrum recorded from 417-1600 nm for the pump supercontinuum from the PCF is presented in Figure 9. The data are plotted from the measurements taken by two Ocean Optics visible spectrometers and an optical spectrum analyser (OSA). The pump supercontinuum generated in the photonic crystal fibre spanned from wavelengths as low as 510 nm and as high as 1200 nm.

4.4 Stabilization of the mid-IR frequency comb continuously tunable from 1.95-4.0 µm

Stabilisation of the OPO was done by stabilising the f_{REP} of the Ti:sapphire laser and then with a nonlinear interferometer locking the signal or idler f_{CEO} by interfering the pump supercontinuum with pump+idler or signal SFM pulses [43]. For example, the interference of the pump+signal SFM pulses with the pump supercontinuum results in the f_{CEO} of the signal pulses since the noise of the pump pulses vanish because of common-mode rejection [43]. In this chapter I focus on the stabilisation of the idler comb and therefore only the idler pulses are considered. Here we have only one nonlinear interferometer for heterodyning the pump supercontinuum with the pump+idler SFM pulses from the OPO.

An optical scheme for detecting the f_{CEO} of the idler pulses is presented in Figure 10. The

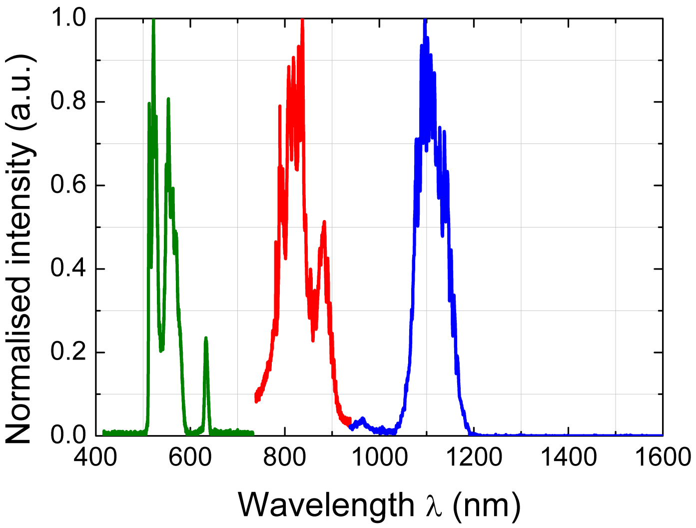

Figure 9. Spectrum of coherent pump supercontinuum from the photonic-crystal-fiber (PCF). The wavelengths from 417-732 nm (in green) were recorded with an Ocean Optics visible spectrometer (Ocean Optics, USB4000-UV-VIS) while the wavelengths from 732-937 nm (in red) were recorded using a second Ocean Optics spectrometer which covered the range from 661-937 nm (Ocean Optics, USB4000-VIS-NIR). The near-infrared spectrum spanning from 937-1600 nm (in blue) was recorded with an OSA (Ando AQ6317B Optical Spectrum Analyzer).

333-MHz Ti:Sapphire pump laser produced 30-fs pulses with 1.45-W average power centered at 800 nm. The Ti:sapphire pump pulse was divided at a 90 % reflecting beamsplitter (BS1) into two channels. The majority of the power (90 %) was used to synchronously pump the OPO while the remaining 10 % was launched it into 30-cm length of photonic crystal fibre with a core diameter of 2 μm and zero dispersion at 740-nm wavelength (NKT, NL-2.0-740) for supercontinuum generation. The nonlinear crystal was placed perpendiculary to the pump beam.

Before transmission through BS1 the light was bounced off a pair of GTI mirrors for a dispersion compensation (-200 fs^2). The light transmitted through BS1 was propagated through a half-wave plate before being focussed into the PCF. The spectrum from the PCF was optimised by adjusting the average power and the chirp of the pump pulses to give the shortest wavelengths in the supercontinuum. The strength of the heterodyne beat was improved by small half-waveplate adjustments. In addition a number of different focal length aspheric lenses were tested to improve the coupling efficiency into the PCF. A transmission efficiency of up to 60 % was achieved. After the fiber, the output coupled light's polarization was rotated with quarter- and half-wave plates which changed the polarization from circular to horizontal. The use of wave-plates made it possible to maximise the light transmitted through the polarising cube (PBS) and increased the strength of the heterodyne beat detected at the avalanche photodiode (APD). On the other arm the pump+idler SFM pulses passed through OPO cavity mirror M3 since it was not coated for the visible range. For the collimation of the beam, a 60-mm focal length lens was placed after mirror M3. To ensure the same beam sizes from the OPO and PCF, +50-mm (f3) and -20-mm (f4) lenses were placed before the half-wave plate.

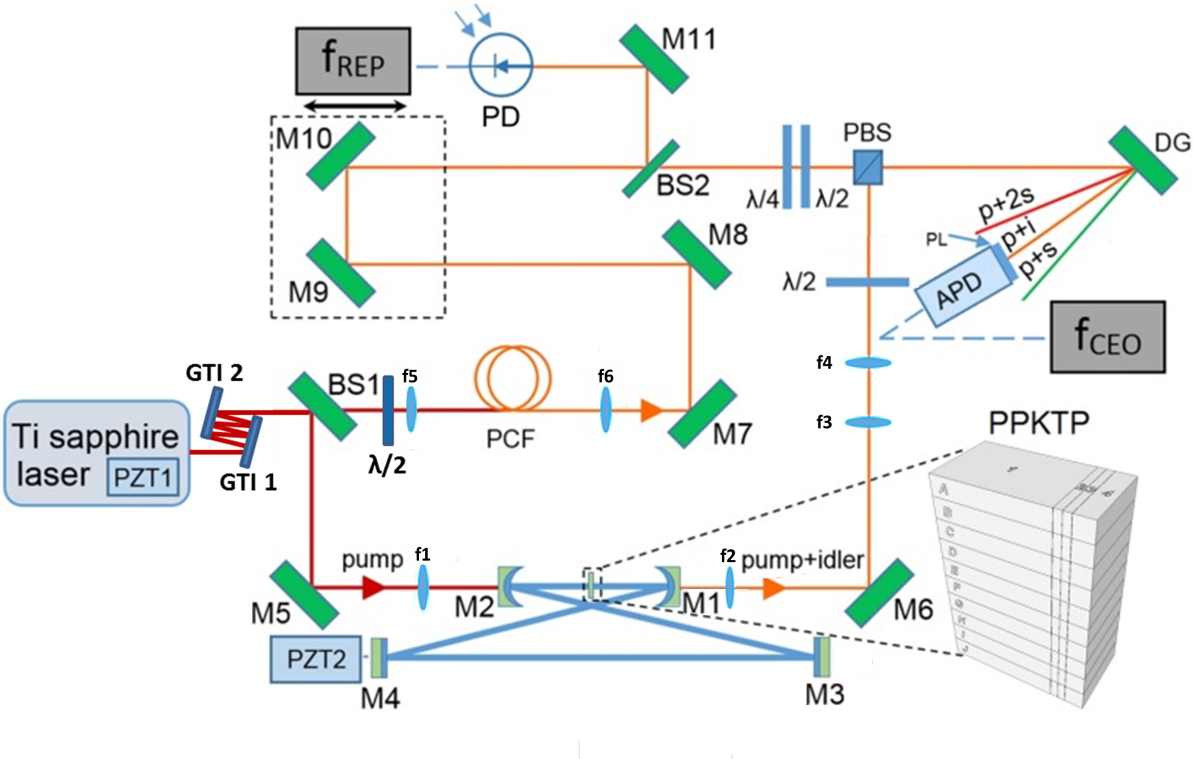

Figure 10. Layout of the PPKTP OPO: PD, photodiode; PBS, polarizing beam splitter; DG, diffraction grating; APD, avalanche photodiode; PCF, photonic crystal fiber; BS, beam splitter.

The light polarization was optimised with a half-waveplate which improved the transmission of the pump+idler light through the beamslitter (PBS). After it the pump+idler beam was overlapped with the supercontinuum beam, and the common wavelengths were isolated with a diffraction grating (Thorlabs, 1800 lines per mm, 12.7x12.7x6 mm). This ensured that only a narrow-bandwidth of light reached the APD. A polariser was rotated in front of the APD to maximise the S/N ratio of the heterodyne beat for f_{CEO} detection. It balanced the two arms of the interferometer, ensuring that the strengths of the two signals at the APD were the same. Finally, the alignment of the beams was ensured over several meters distance to ensure a strong beat. The path difference between them was optimised with a delay-line.

The f_{CEO} of the pulses was acquired by heterodyning non phase-matched light from the OPO with the coherent pump supercontinuum light from PCF. As presented in Figure 8, the lowest pump+idler wavelength was 570 nm which could be quite easily acquired from the PCF. As the OPO was tuned, we acquired f_{CEO} of the idler pulses by heterodyning the phasematched pump+idler light tuned from 570-670 nm with the coherent pump supercontinuum light. A typical heterodyne beat obtained at the APD is presented in Figure 11. As we acquired a heterodyne beat from the 333-MHz OPO, we could detect the f_{CEO} drift. The f_{CEO} of the idler typically would drift by 100 MHz in several tens of seconds. With a fast Si photodiode the repetition rate of the 333-MHz Ti:sapphire was detected. As a result, the frequency comb was fully stabilised by locking the f_{REP} and the f_{CEO} frequencies. The feedback loops for the comb stabilization are illustrated in Figure 12.

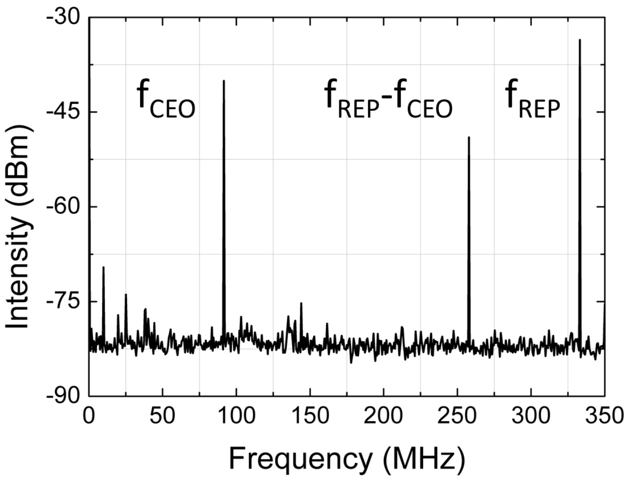

Figure 11. f_{CEO} of the idler was maintained at a high level (>35 dB) across the entire tuning range from 1.95-4 µm. RBW=100 kHz.

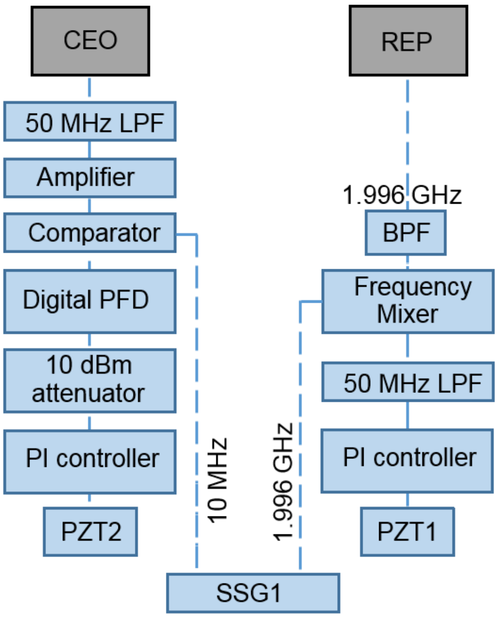

Figure 12. Comb stabilization scheme, showing the separate control loops used for f_{CEO} and f_{REP} locking. LPF stand for low-pass-filter, BPF is band-pass-filter, PFD is phase-frequency detector, PI controller is proportional-integral controller, SSG1 is synthesized signal generator.

4.4.1 Repetition rate stabilization

Firstly the f_{REP} of the Ti:sapphire laser was stabilized. If the pulse repetition rate is stabilized, the mode spacing between each pair of neighbouring comb modes will be exactly the same. For this purpose a small fraction of light, leaving the photonic crystal fiber (PCF) was reflected from BS2 to photodiode (PD) (see Figure 10). This fast Si photodiode acquired the 333-MHz repetition rate and moreover, gave higher order harmonics of f_{REP} up to the 6th harmonic (2 GHz). The detected 2-GHz frequency was isolated with a band-pass filter (BPF) and mixed-down with a 2-GHz reference frequency obtained from a synthesized signal generator (SSG1).

The difference frequency output of the mixer was low-pass-filtered (LPF) at 50-MHz and entered a proportional-integral (P-I) amplifier as an error signal. The output from the P-I controller was used to actuate a piezoelectric transducer (PZT1) in the Ti:sapphire laser. The active tracking of f_{REP} with PZT1 made it possible to stabilize the repetition rate which could remain locked for several hours without additional cavity length adjustments. The implemented feedback loop locked f_{REP}. The best phase noise PSD measurement of the locked repetition rate was obtained when the P-I amplifiers parameters were set to $\mathrm{LF}_{gainlimit}$= 30 dB, Gain = 5.0 and $\mathrm{f}_{Cornerfrequency}$= 3 kHz. We used both PZTs available inside the laser cavity (see Chapter 3). The results are presented in Figure 13. The phase noise measurements were done in-loop. The limitation is that in in-loop measurement the phase noise of the locking loop is measured. It is relative measurement since the noise of the reference source is not taken into account. The overal phase noise performance is better or the noise is lower in comparison with out-of-loop phase noise measurement.

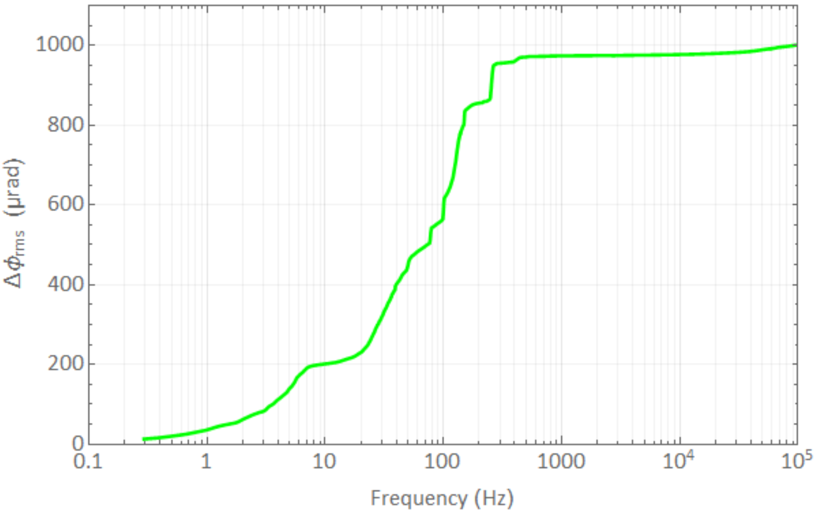

Figure 13. Cumulative phase noise of the locked f_{REP}.

The Allan deviation was also measured for the locked repetition rate. A frequency counter (Hameg Instruments, HM8123) recorded the instabilities of the locked f_{REP} over different gate times. The two sample frequency .deviation was calculated. A 10 MHz Rubidium (Rb) clock provided reference to SSG1, SSG2 and the frequency counter (see Figure 14).

The f_{REP} stability was measured after a BPF which removed the 333-MHz and other harmonics of it transmitting only 1.996 GHz frequency, and provided one input for the frequency mixer. The results are presented in Figure 15. When the Ti:sapphire cavity length is fixed, f_{REP} cannot change due to temperature drifts or mechanical perturbations and therefore the frequency is stable. The Allan deviation of the locked repetition rate for a 1-second gate was 1.5 mHz which results in a fractional stability of $4.5\mathrm{e}^{-12}$. Before the repetition rate was locked, it could drift by several hundreds of Hz in frequency. The locking improved the repetition rate stability by a factor of more than 10,000. For a synchronously pumped OPO, if the repetition rate f_{REP} of the fs laser is stabilised, the repetition rate f_{REP} of the optical parametric oscillator (OPO) is stabilised too.

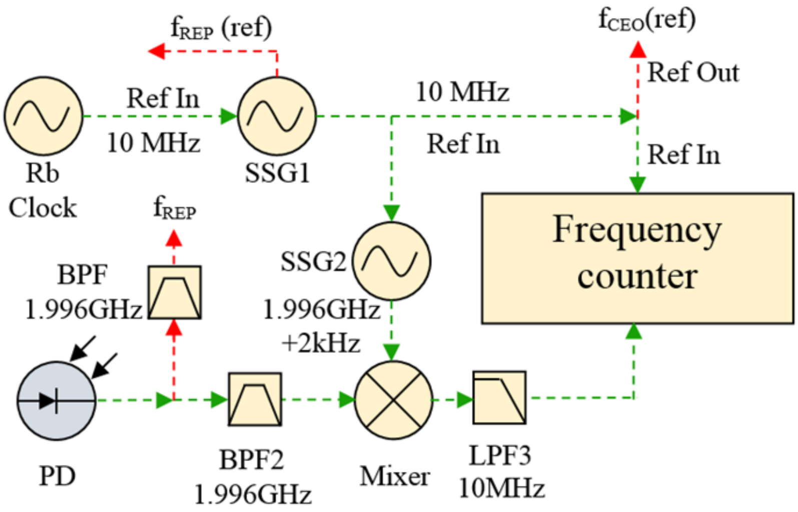

Figure 14. Configuration for recording the f_{REP} stability data.

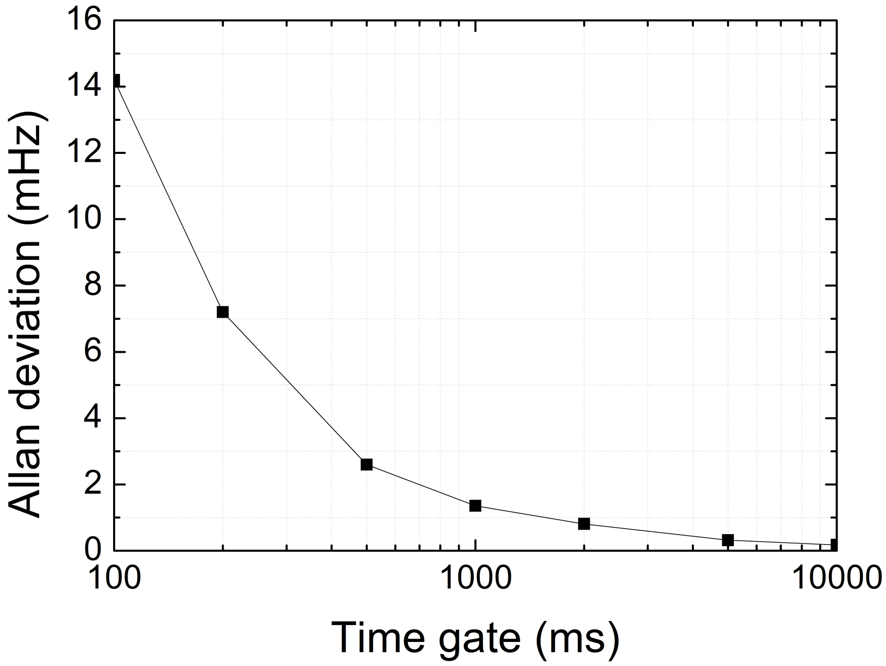

Figure 15. Allan deviation of locked Ti:sapphire repetition rate f_{REP}.

4.4.2 Carrier envelope offset f_{CEO} frequency stabilization

The detection and amplification of the f_{CEO} frequency

After the heterodyne beat between the pump supercontinuum and the pump+idler SFM light was detected with a APD (Hamamatsu C5331-11s, f_c=100 MHz), it was stabilised to a reference. The detected signal from the APD was monitored with an RF spectrum analyser (Rigol, DSA1030A, 9 kHz-3 GHz) when the f_{CEO} of the idler pulse was tuned from 0-333 MHz with a Newport Microdrive Controller (Model ESA-C) via PZT3. The detected frequency spectrum contained f_{REP} and $f_{CEO} - f_{REP}$ frequencies (see Figure 11). The absolute strength of the detected heterodyne beat signal was about -25 dBm. The detected f_{CEO} frequency was low-pass-filtered (LPF) at 50-MHz frequency to attenuate the f_{REP} signal and amplified to increase the detected signal power level up to -10-dBm with at least a 30-dB S/N ratio (at 100 kHz RBW) which is necessary for our analog to digital converter (Pulse Research Lab L-350 TTL Dual-Channel Converter). A THS3202 RF amplifier module was modified to increase the strength of the signal from the APD. The modified circuits could increase the signal level by +20 dB and +40 dB. The cut-off frequency of the amplifiers was about 500 MHz. Into the second channel we introduced a 10-MHz frequency signal from a synthesized signal generator (Agilent synthesized signal generator 8664A, 0.1-3000 MHz). The synthesizer was referenced to a Rb-clock. The comparator output was a TTL signal with a voltage of 0 or 5 V (see Figure 16).

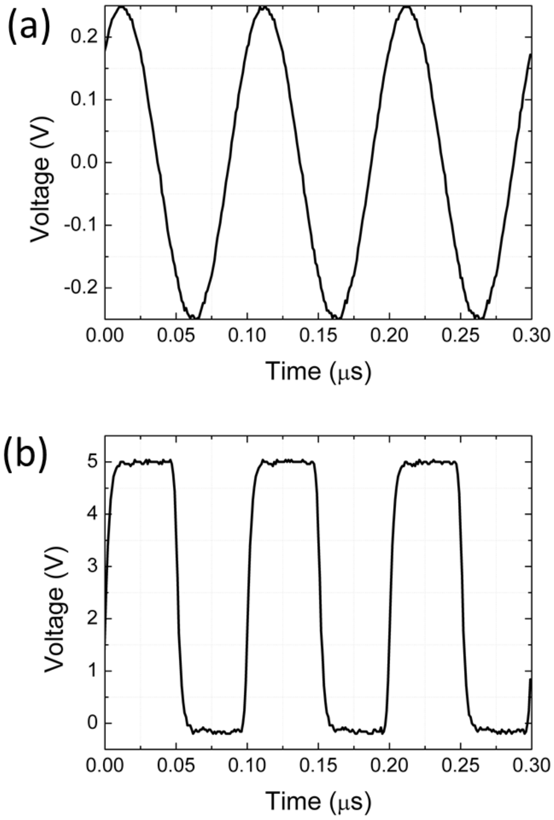

Figure 16. (a) A 10 MHz signal from the APD; (b) The TTL signal from the comparator.

f_{CEO} stabilisation

The detected, amplified heterodyne beat after the comparator was introduced into a phase frequency detector (PFD). The digital phase-frequency detector (PFD) takes TTL signals of the heterodyne beat and the reference, and outputs a DC voltage depending on the frequency difference of the introduced signals. The PFD circuit had a linear phase range of $\pm 32\pi$ (about ± 100 rad). We could not lock the f_{CEO} of the idler pulses at higher than 32 MHz and at lower than 5 MHz frequencies. The frequency was limited by a digital to analogue signal converter functioning in the 5-32 MHz frequency range. As the analog signal was generated, it was used as an error signal to a proportional-integral (P-I) amplifier (New Focus LB1005 Servo Controller). The PZT used for the stabilisation could be driven directly by the P-I amplifier (see Figure 17) with no further amplifier between them. The P-I amplifier could output a voltage from 0-10 V which was enough for the f_{CEO} locking. The P-I amplifier provided a signal used to actuate PZT2 in the OPO cavity for f_{CEO} control.

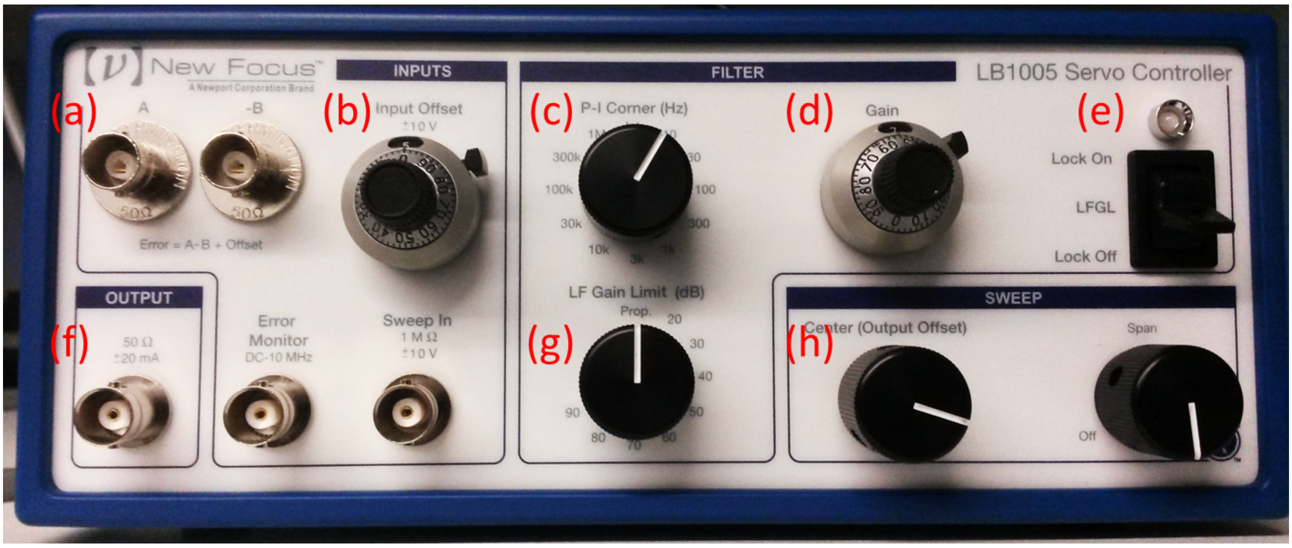

Figure 17. New Focus LB1005 P-I amplifier: (a) error input; (b) input offset control; (c) P-I corner frequency; (d) proportional gain control; (e) gain regime; (f) P-I amplifier output; (g) low frequency gain limit; (h) output offset.

Firstly, before closing the loop, the P-I amplifier was set properly. By terminating the input channel (a) the output voltage was set to zero by using the output offset control knob (on the rear side of the P-I controller). The same adjustment was done for the upper voltage limit (10 V). The voltage range from 0-10 V ensured that only a positive voltage could be applied to the PZT2. A 10 V range was sufficient to capture the fluctuating f_{CEO} frequency. After these adjustments were done, the error signal from the PFD was introduced into the P-I amplifier. In between the P-I amplifier and the PFD a 10-dB attenuator was used before the input channel -B since the signal from the PFD was too strong. Then the output channel of the P-I amplifier was connected to PZT2 (Thorlabs, AE0203D04F). The input offset was set to 5.0 which corresponds to a zero offset of the input signal. The locking of the signal was enabled by setting the gain to the LFGL regime (low frequency gain limit) which limited the DC gain.

Before the feedback loop was activated, the f_{CEO} signal was set at 10-MHz frequency by changing the cavity length with a long travel (9.1 µm) PZT3. The default P-I amplifier parameters were optimised until the f_{CEO} of the idler comb was stabilised. Figure 18 presents the stabilised f_{CEO} frequency at 10-MHz reference. As we increased the proportional gain, the lock of the heterodyne beat improved. The bandwidth of the locked signal was reduced. If the gain was too high, the output from PFD would oscillate and add additional noise. The RF spectrum analyser would measure a much broader signal locked at the 10-MHz reference. Therefore after

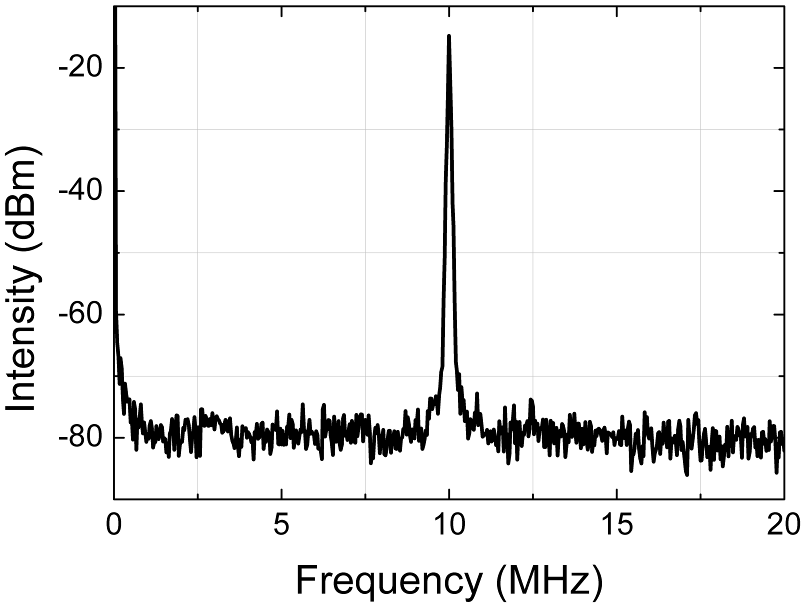

Figure 18. f_{CEO} of the idler pulses when locked to a 10-MHz external reference. RBW=10 kHz

careful optimisation of the parameters, the corner frequency, low frequency gain limit and the gain were set at 10 kHz, 90 dB and 5.15 accordingly. The f_{CEO} frequency could remain locked from several seconds to half an hour depending on the overall noise level in the laboratory. After the experiment, presented in this chapter, we introduced a second piezo into the locking loop and therefore the f_{CEO} could remain locked for more than several hours. Even so, any loud noise such as a door slam could stop the locking.

4.5 Frequency comb phase noise PSD measurements

4.5.1 Bandwidth of the locked f_{CEO}

The typical locked f_{CEO} of the idler pulses over the range from 1.95-4.0 μm in RF spectrum is presented in Figure 19. We can see a finite linewidth of a locked heterodyne beat on the RF spectrum analyser. The quality of the locking is determined by the S/N ratio and the bandwidth at the -3-dB level. Both parameters can be monitored on the frequency analyser. The stabilised signal was measured with a Rigol DSA 1030A spectrum analyser which had a resolution limit of 10 Hz. The locked signal at 10-MHz reference frequency had 10-Hz bandwidth which was limited by our spectrum analyser. The result was taken when the f_{REP} of the Ti:sapphire laser was also locked which led to an increase in the noise for the f_{CEO} frequency lock.

Figure 20 shows the RF spectrum of the stabilized f_{CEO} beat note against a 10-MHz reference frequency, recorded using an instrument limited bandwidth of 10 Hz at -3-dB level with a span of 400 Hz. The locked idler comb f_{CEO} frequency with different spans and resolution bandwidths is shown in Figure 20. As we see, there are noise peaks at 25-34 kHz and 0.5-2 kHz frequencies which can be properly identified only from phase noise PSD measurements. Those measurements are presented in the next subsection of this chapter.

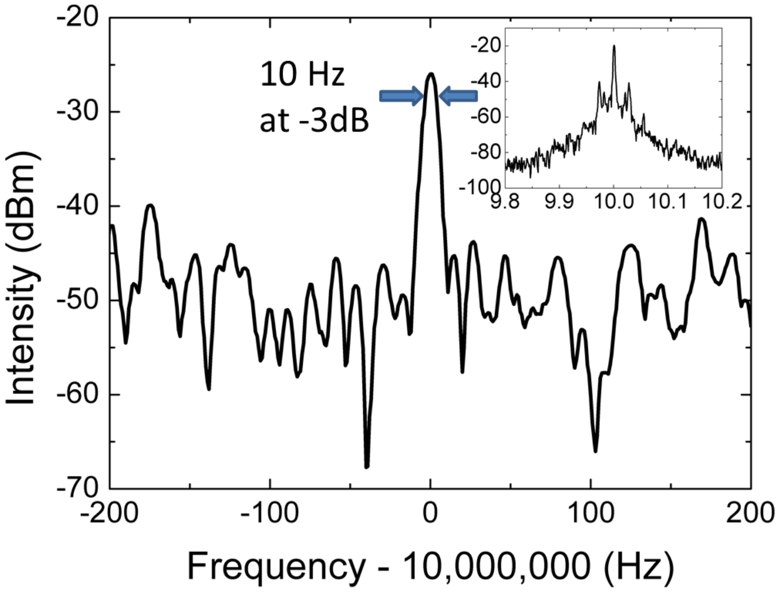

Figure 19. RF spectrum of the locked idler f_{CEO} recorded with an instrument-limited 10-Hz resolution bandwidth. Inset: 400-kHz bandwidth scan showing locked f_{CEO} with 25–35 kHz sidebands.

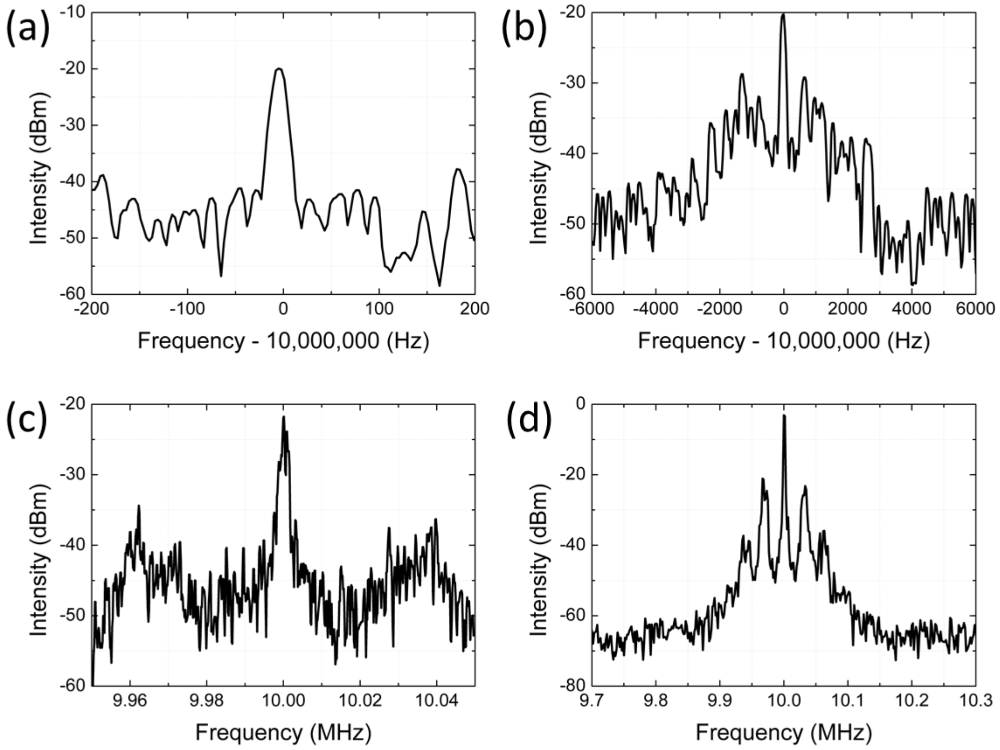

Figure 20. RF spectrums of the locked idler f_{CEO} at 10-MHz frequency: (a) span 400-Hz, resolution 10-Hz; (b) span 12 kHz, resolution 100 Hz indicating a noise at 0.5-2 kHz frequencies; (c) span 100 kHz, resolution of 300-Hz indicating a noise at 24-35 kHz frequencies; (d) span 600 kHz, resolution of 1 kHz indicating higher order harmonics of the 24-35 kHz signal.

The locked f_{CEO} of the idler indicates a very narrow bandwidth lock in comparison with other near-IR Cr:forsterite [44], Er:doped fiber laser [45] frequency combs. OPO combs can produce Hz-level heterodyne beat linewidths [46], whereas typical Cr:forsterite [47, 44] and Er:fiber [26] near-IR combs typicaly generate >100-kHz linewidths. Higher bandwidth feedback loops could reduce the locked f_{CEO} bandwidths even further.

4.5.2 Phase-noise PSD measurements

While the frequency comb was fully stabilised, in-loop phase noise PSD measurements were carried out and the cumulative phase noise calculated for the locked idler f_{CEO}. The phase noise power spectral density (PSD) data were taken when the idler comb was locked. For the phase noise PSD measurements a signal from the PFD circuit was taken. The signal was amplified and recorded with a 12-bit acquisition card. For the best possible resolution, before taking the data, the dynamic range of the acquisition card was filled. The output from the PFD was calibrated in phase in order to calculate the phase error between the locked f_{CEO} of the signal and the 10-MHz reference frequency. The calibration of the PFD circuit to the phase was done by introducing two identical 10-MHz frequencies into the circuit with an offset of 1 Hz. Then the output from PFD was changing from minimum to its maximum value. As a result, we had a slope of voltage against phase (V rad^{-1}). The knowledge of the slope let us change the recorded voltage in the phase noise PSD measurements into phase.

The f_{CEO} frequency phase-noise PSD was recorded as the idler was tuned from 1.95-4.0 μm, and representative measurements (blue) are shown in Figure 21. The integrated cumulative phase noise from 1 Hz-64 kHz was around 1.2 rad over an observation time of 1 second. The primary noise contribution appeared in the 25-35 kHz range. This noise increase was caused by intensity fluctuations in the pump source for the Ti:sapphire laser which couple into the OPO as both intensity and phase noise [40]. These fluctuations lay outside the bandwidth of our locking loop, which was limited to 1 kHz by the response of PZT2 in the OPO cavity. The noise around 1-kHz frequency is associated with environmental vibrations and acoustic noise.

The range of measured cumulative phase noises is presented in Figure 22. The upper and lower bounds of the cumulative phase noise of the idler across the entire tuning range are shown in red. The characteristic of each locked idler comb is the same: we observed dominant noise contributions at 27-kHz and 1-kHz frequencies. The noise at 27-kHz could be removed by replacing the pump source and the noise at 1-kHz frequencies could be suppressed by increasing the locking loop bandwidth. The f_{CEO} could be stabilised via pump laser diode-current adjustments. In this way a bandwidth up to 100-kHz could be achieved.

The cumulative phase noise for the repetition rate f_{REP} integrated from 1-100 kHz over a 1-second was around 1.1 mrad, which corresponds to 0.18 mHz. The cumulative phase noise for the f_{CEO} was 0.2 Hz. The repetition rate of the Ti:sapphire was 333 MHz, therefore for the optical frequency of 200 THz (about 1.5 μm) it would give us a mode number of 600,600. Now we can estimate the contribution of the noise to the comb line position. This value of f_{REP} implies an uncertainty of 108-Hz, while the f_{CEO} only increases it by 0.2 Hz. The f_{CEO} frequency phase noise measurement shows that its contribution to the uncertainty of the comb line is negligible. The uncertainty of comb line position in the frequency domain is determined by the quality of the repetition rate locking. A more detailed discussion on comb line uncertainty

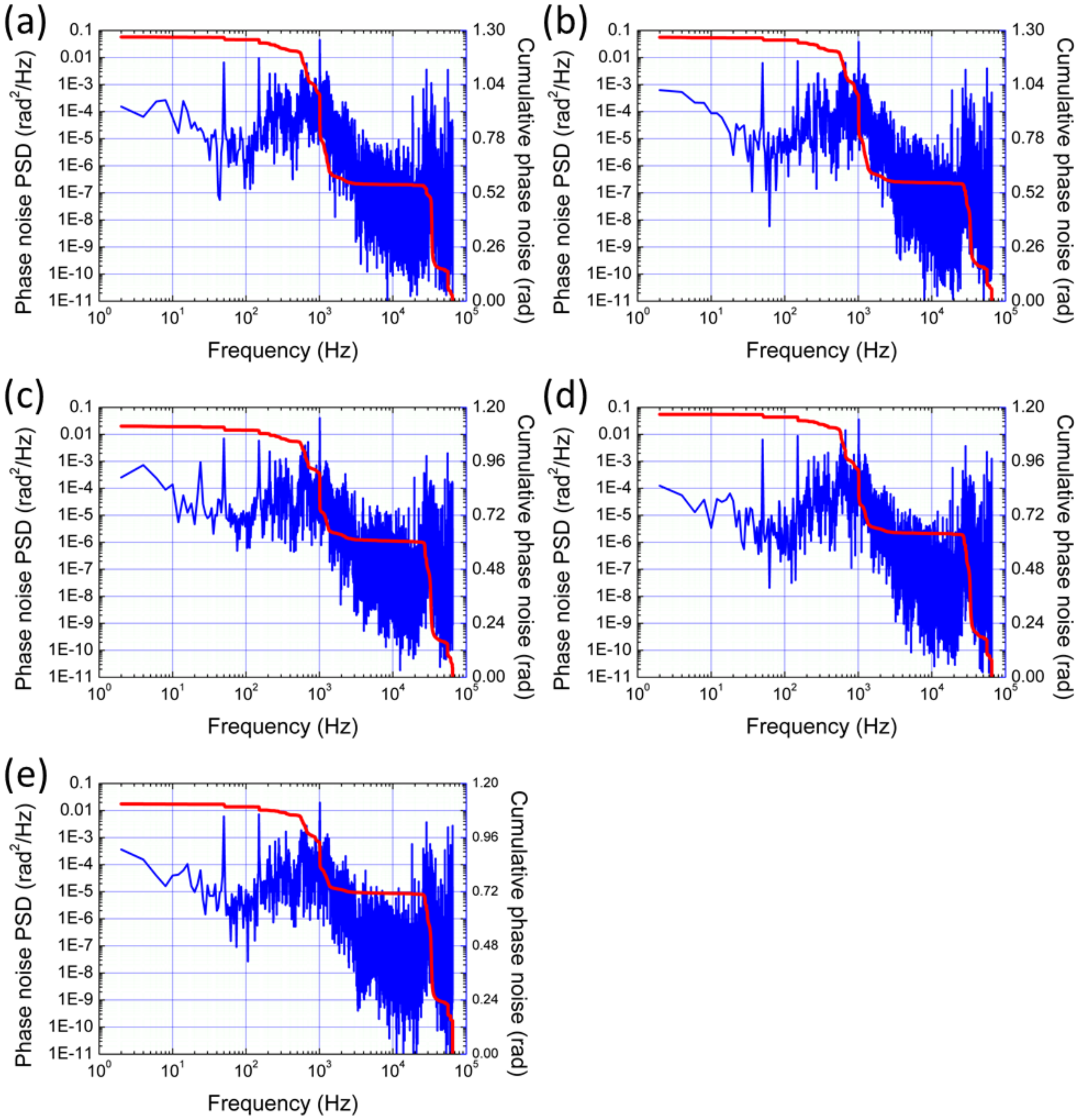

Figure 21. Characteristic in-loop phase noise PSD at every locked idler wavelength (blue) over frequency range from 1 Hz-64 kHz (1-second observation time): (a) 4000 nm; (b) 3100 nm; (c) 2600 nm; (d) 2250 nm; (e) 1950 nm.

is presented in Chapter 8.

4.6 Conclusions

The repetition rate f_{REP} and carrier-envelope offset frequency f_{CEO} frequency of the idler pulses from an OPO were stabilized to a reference source to obtain a fully locked frequency comb in the mid-IR region from 1.95-4 μm. Here I have presented a frequency comb locked across a broad range of wavelengths in the mid-IR region which was not done before. Phase noise PSD and cumulative phase noise calculations were carried out for the characterization of

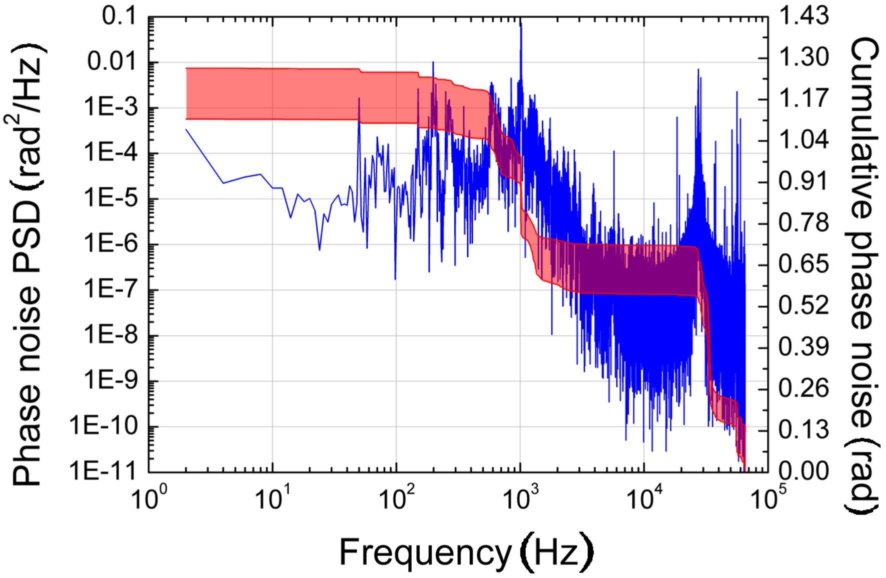

Figure 22. Characteristic in loop phase noise PSD for the idler f_{CEO} frequency (blue, left) from 1 Hz to 64 kHz (1-second observation time). Upper and lower bounds for the cumulative phase noise across the entire idler tuning are shown in red (right axis).

the frequency comb. By combining an optimized nonlinear interferometer with a multi-section PPKTP crystal we produced pump-idler SFG powers far exceeding those from parasitic SFG. The implementation of a new design of PPKTP crystal enabled us to produce continuously tunable combs operating across >2000-nm in the mid-IR, which could be used for spectroscopy/metrology in this region. The results of this work have been published in Optics Letters [48].

References

[1] Z. Zhang, T. Gardiner, and D. T. Reid, "Mid-infrared dual-comb spectroscopy with an optical parametric oscillator," Opt. Lett. 38, 3148-3150 (2013).

[2] K. A. Tillman, R. R. J. Maier, D. T. Reid, and E. D. McNaghten, "Mid infrared absorption spectroscopy across a 14.4 THz spectral range using a broadband femtosecond optical parametric oscillator," Appl. Phys. Lett. 85, 3366 (2004).

[3] F. Keilmann, C. Gohle, and R. Holzwarth, "Time domain mid infrared frequency comb spectrometer," Opt. Lett. 29, 1542-1544 (2004).

[4] F. Adler, P. Masłowski, A. Foltynowicz, K. C. Cossel, T. C. Briles, I. Hartl, and J. Ye, "Mid infrared Fourier transform spectroscopy with a broadband frequency comb," Opt. Express 18, 21861-21872 (2010).

[5] W. D. Kimura, A. van Steenbergen, M. Babzien, I. Ben-Zvi, L. P. Campbell, D. B. Cline, C. E. Dilley, J. C. Gallardo, S. C. Gottschalk, P. He, K. P. Kusche, Y. Liu, R. H. Pantell, I. V. Pogorelsky, D. C. Quimby, J. Skaritka, L. C. Steinhauer, and V. Yakimenko, "First Staging of Two Laser Accelerators," Phys. Rev. Lett. 86, 4041 (2001).

[6] E. Gagnon, I. Thomann, A. Paul, A. L. Lytle, S. Backus, M. M. Murnane, H. C. Kapteyn, and A. S. Sandhu, "Carrier envelope phase shift caused by variation of grating separation," Opt. Lett. 31, 3113-3115 (2006).

[7] A. Baltuška, T. Fuji, and T. Kobayashi, "Controlling the Carrier Envelope Phase of Ultrashort Light Pulses with Optical Parametric Amplifiers," Phys. Rev. Lett. 88, 133901 (2002).

[8] M. Hentschel, R. Kienberger, C. Spielmann, G. A. Reider, N. Milosevic, T. Brabec, P. Corkum, U. Heinzmann, M. Drescher, and F. Krausz, "Attosecond metrology," Nature 414, 509-513 (2001).

[9] R. Kienberger, E. Goulielmakis, M. Uiberacker, A. Baltuška, V. Yakovlev, F. Bammer, A. Scrinzi, T. Westerwalbesloh, U. Kleineberg, U. Heinzmann, M. Drescher, and F. Krausz, "Atomic transient recorder," Nature 427, 817-821 (2004).

[10] A. Gambetta, N. Coluccelli, M. Cassinerio, D. Gatti, P. Laporta, G. Galzerano, and M. Marangoni, "Milliwatt level frequency combs in the 8-14 µm range via difference frequency generation from an Er:fiber oscillator," Opt. Lett. 38, 1155-1157 (2013).

[11] F. Zhu, H. Hundertmark, A. A. Kolomenskii, J. Strohaber, R. Holzwarth, and H. A. Schuessler, "High power mid infrared frequency comb source based on a femtosecond Er:fiber oscillator," Opt. Lett. 38, 2360-2362 (2013).

[12] C. Erny, K. Moutzouris, J. Biegert, D. Kühlke, F. Adler, A. Leitenstorfer, and U. Keller, "Mid infrared difference frequency generation of ultrashort pulses tunable between 3.2 and 4.8 µm from a compact fiber source," Opt. Lett. 32, 1138-1140 (2007).

[13] T. J. Kippenberg, R. Holzwarth, and S. A. Diddams, "Microresonator Based Optical Frequency Combs," Science 332, 555-559 (2011).

[14] P. Del'Haye, A. Schliesser, O. Arcizet, T. Wilken, R. Holzwarth, and T. J. Kippenberg, "Optical frequency comb generation from a monolithic microresonator," Nature 450, 1214-1217 (2007).

[15] A. G. Griffith, R. K. W. Lau, J. Cardenas, Y. Okawachi, A. Mohanty, R. Fain, Y. H. D. Lee, M. Yu, C. T. Phare, C. B. Poitras, A. L. Gaeta, and M. Lipson, "Silicon-chip mid-infrared frequency comb generation," Nature Commun. 6, 6299 (2015).

[16] M. N. Cizmeciyan, H. Cankaya, A. Kurt, and A. Sennaroglu, "Kerr lens mode locked femtosecond Cr2+:ZnSe laser at 2420 nm," Opt. Lett. 34, 3056-3058 (2009).

[17] E. Sorokin, I. T. Sorokina, J. Mandon, G. Guelachvili, and N. Picqué, "Sensitive multiplex spectroscopy in the molecural fingerprint 2.4 µm region with a Cr+2:ZnSe femtosecond laser," Opt. Express 15, 16540-16545 (2007).

[18] E. Sorokin, N. Tolstik, K. I. Schaffers, and I. T. Sorokina, "Femtosecond SESAM mode-locked Cr:ZnS laser," Opt. Express 20, 28947-28952 (2012).

[19] Q. Wang, J. Geng, Z. Jiang, T. Luo, and S. Jiang, "Mode locked Tm Ho doped fiber laser at 2.06 µm," IEEE Photon. Tech. Lett. 23, 682-684 (2011).

[20] C.-C. Lee, C. Mohr, J. Bethge, S. Suzuki, M.E. Fermann, I. Hartl, and T. R. Schibli, "Frequency comb stabilization with bandwidth beyond the limit of gain lifetime by an intracavity graphene electro-optic modulator," Opt. Lett. 37, 3084-3086 (2012).

[21] K. F. Lee, J. Jiang, C. Mohr, J. Bethge, M. E. Fermann, N. Leindecker, K. L. Vodopyanov, P. G. Schunemann, and I. Hartl, "Carrier envelope offset frequency of a doubly resonant, nondegenerate, mid-infrared GaAs optical parametric oscillator," Opt. Lett. 38, 1191-1193 (2013).

[22] J. H. Sun, B. J. S. Gale, and D. T. Reid, "Composite frequency comb spanning 0.4-2.4 µm from a phase controlled femtosecond Ti:sapphire laser and synchronously pumped optical parametric oscillator," Opt. Lett. 32, 1414-1416 (2007).

[23] F. Adler, K. C. Cossel, M. J. Thorpe, I. Hartl, M. E. Fermann, and J. Ye, "Phase stabilized, 1.5 W frequency comb at 2.8-4.8 µm," Opt. Lett. 34, 1330-1332 (2009).

[24] T. I. Ferreiro, J. Sun, and D. T. Reid, "Frequency stability of a femtosecond optical parametric oscillator frequency comb," Opt. Express 19, 24159-24164 (2011).

[25] K. A. Tillman, R. Thapa, K. Knabe, S. Wu, J. Lim, B. R. Washburn, and K. L. Corwin, "Stabilization of a self-referenced, prism-based, Cr:forsterite laser frequency comb using an intracavity prism," Appl. Opt. 48, 6980–6989 (2009).

[26] T. R. Schibli, K. Minoshima, F.-L. Hong, H. Inaba, A. Onae, H. Matsumoto, I. Hartl, and M. E. Fermann, "Frequency metrology with a turnkey all-fiber system," Opt. Lett. 29, 2467–2469 (2004).

[27] N. Leindecker, A. Marandi, R. L. Byer, and K. L. Vodopyanov, "Broadband degenerate OPO for mid infrared frequency comb generation," Opt. Express 19, 6296-6302 (2011).

[28] J. K. Ranka, R. S. Windeler, and A. J. Stentz, "Visible continuum generation in air-silica microstructure optical fibers with anomalous dispersion at 800-nm," Optics Letters 25, 25-27 (2000).

[29] S. A. Diddams, D. J. Jones, J. Ye, S. T. Cundiff, J. L. Hall, J. K. Ranka, R. S. Windeler, T. Udem, and T. W. Hänsch, "Direct link between microwave and optical frequencies with a 300-THz femtosecond laser comb," Phys. Rev. Lett. 84, 5102-5105 (2000).

[30] D. J. Jones, S. A. Diddams, J. K. Ranka, A. Stentz, R. S. Windeler, J. L. Hall, and S. T. Cundiff, "Carrier-envelope phase control of femtosecond mode-locked lasers and direct optical frequency synthesis," Science 288, 635-639 (2000).

[31] A. Poppe, R. Holzwarth, A. Apolonski, G. Tempea, C. Spielmann, T. W. Hänsch, and F. Krausz, "Few-cycle optical waveform synthesis," Appl. Phys. B 72, 373-376 (2001).

[32] B. J. S. Gale, J. H. Sun, and D. T. Reid, "Towards versatile coherent pulse synthesis using femtosecond laser and optical parametric oscillators," Optics Express 16, 1616-1622 (2008).

[33] M. Prevedelli, T. Freegarde, T. W. Hänsch, "Phase locking of grating-tuned diode laser," Applied Physics B 60, S241-S248 (1995).

[34] S. A. Meyer, J. A. Squier, and S. A. Diddams, "Diode-pumped Yb:KYW femtosecond laser frequency comb with stabilized carrier-envelope offset frequency," Eur. Phys. 48, 19-26 (2008).

[35] D. C. Edelstein, E. S. Wachman, and C. L. Tang, "Broadly tunable high repetition rate femtosecond optical parametric oscillator," Appl. Phys. Lett. 54, 1728-1730 (1989).

[36] D. W. Allan, “Statistics of atomic frequency standards,” Proc. IEEE 54, 221-230 (1966).

[37] E. Rubiola, “On the measurement of frequency and of its sample variance with high-resolution counters,” Review of Scientific Instruments 76, 054703 (2005).

[38] S. T. Dawkins, J. J. McFerran, and A. N. Luiten, “Considerations on the measurement of the stability of oscillators with frequency counter,” IEEE Transactions on Ultrasonics, Ferroelectrics, and Frequency Control 54, 918–925 (2007).

[39] W. H. Press, S. A. Teukolsky, W. T. Vetterling, and B. P. Flannery, Ch. 13, "Fourier and Spectral Applications," in Numerical Recipes: The Art of Scientific Computing, 3rd Edn. pp. 640-719 (Cambridge University Press, 2007).

[40] D. T. Reid, "Ultra broadband pulse evolution in optical parametric oscillator," Opt. Express 19, 17979-17984 (2011).

[41] S. T. Wong, K. L. Vodopyanov, and R. L. Byer, "Self phase locked divide by 2 optical parametric oscillator as a broadband frequency comb source," J. Opt. Soc. Am. B 27, 876-882 (2010).

[42] S. T. Wong, T. Plettner, K. L. Vodopyanov, K. Urbanek, M. Digonnet, and R. L. Byer, "Self phase locked degenerate femtosecond optical parametric oscillator," Opt. Lett. 33, 1896-1898 (2008).

[43] J. Sun and D. T. Reid, "Coherent ultrafast pulse synthesis between an optical parametric oscillator and a laser," Optics Letters 34, 854-856 (2009).

[44] K. A. Tillman, R. Thapa, K. Knabe, S. Wu, J. K. Lim, B. R. Washburn, and K. L. Corwin, "Stabilization of a self-referenced, prism-based, Cr:forsterite laser frequency comb using an intracavity prism," Appl. Opt. 48, 6980-6989 (2009).

[45] J. K. Lim, K. Knabe, K. A. Tillman, W. Neely, Y. S. Wang, R. Amezcua-Correa, F. Couny, P. S. Light, F. Benabid, J. C. Knight, K. L. Corwin, J. W. Nicholson, and B. R. Washburn, "A phase-stabilized carbon nanoture fiber laser frequency comb," Optics Express 17, 14115-14120 (2009).

[46] T. I. Ferreiro, J. Sun, and D. T. Reid, "Frequency stability of a femtosecond optical parametric oscillator frequency comb," Opt. Express 19, 24159–24164 (2011).

[47] K. Kim, B. R. Washburn, G. Wilpers, C. W. Oates, L. Hollberg, N. R. Newbury, S. A. Diddams, J. W. Nicholson, and M. F. Yan, "Stabilized frequency comb with a self-referenced femtosecond Cr:forsterite laser," Opt. Lett. 30, 932–934 (2005).

[48] K. Balskus, Z. Zhang, R. A. McCracken, and Derryck T. Reid, "Mid-infrared 333-MHz frequency comb continuously tunable from 1.95 to 4 μm," Optics Letters 40, 4178-4181 (2015).

Chapter 5. Fundamentally and harmonically pumped femtosecond optical parametric oscillator frequency combs

In the previous chapter the OPO frequency comb was fully locked by heterodyning the phase-matched p+i SFG light from OPO with the supercontinuum light from the PCF for a broad range of idler wavelengths from 1.95-4-µm. What if we want to increase the mode spacing of the comb? Here we present for the first time a locked femtosecond frequency comb achieved from a harmonically-pumped OPO. A 333-MHz Ti:sapphire laser was used to achieve a stabilized signal comb at 1-GHz mode spacing at 1.46 µm. The f_{CEO} of the signal pulses and the f_{REP} locking of the comb resulted in uncertainties over 1s of 0.27-Hz and 5-mHz respectively, which were comparable with those of 0.27-Hz and 1.5-mHz achieved for 333-MHz fundamental pumping. The phase-noise power-spectral density of the CEO frequency integrated from 1 Hz to 64 kHz was 2.8 rad for the harmonic comb, 1.0-rad greater than for fundamental pumping. The results show that harmonic operation does not substantially compromise the frequency-stability of the comb. The results of this work have been published in Optics Express [1].

5.1 Introduction

Tunable frequency combs with a wide mode spacing [2, 3, 4, 5] are in demand for such applications as astronomical spectrograph calibration [6], optical arbitrary waveform generation [7], direct comb spectroscopy [8], microwave frequency generation [9] and optical coherence tomography [10]. The usual method to achieve multi-GHz mode spacing is by implementing Fabry-Pérot cavities. By filtering the modes of lower repetition frequency combs, mode spacings of >1-GHz have been demonstrated [11, 12]. Other approaches were implemented using a phase-matched nonlinear fibre seeded by the modulated optical carrier [13] or by using a micro-resonator [14, 15, 16], but these methods lack tunability and often require additional electronic and mechanical locking loops to achieve useful stability.

It is challenging to achieve GHz mode spacing from OPOs and the reason is that the nonlinear processes are very sensitive to the amount of pulse peak power. As we increase the repetition rate the pulse peak power falls and therefore the conversion efficiency. Moreover, there are two nonlinear processes involved which require high peak power – one is the parametric gain in the nonlinear crystal and the second one is the supercontinuum generation in the PCF used as a part of the frequency comb locking scheme. We have here two nonlinear effects involved in achieving frequency combs and obviously when we try to pump with higher repetition rate pulses the peak power falls and these nonlinear effects become more challenging. In this chapter we describe one solution to this problem, which uses a 333-MHz pump laser to produce a 1-GHz frequency comb. As I will show, it is possible to obtain similar phase noise and jitter performance from a harmonically pumped OPO compared with another, which is pumped fundamentally.

Harmonically pumping an optical parametric oscillator (OPO), makes it possible to extend the mode spacing to GHz frequencies and with broad wavelength coverage [17], short pulse durations [18] and access to low-noise frequency combs [19, 20]. As shown by other research, it is possible to operate an OPO at a harmonic when the OPO cavity length is an integer multiple [21, 22] or integer fraction [23, 24] of the pump cavity length. Specifically, in this work a 333-MHz repetition rate femtosecond Ti:sapphire laser was used to to harmonically pump a three times shorter OPO cavity resulting in a 1-GHz mode spacing. Fundamentally and harmonically pumped OPOs were characterized and the frequency comb stability compared. More details on the detection, electronics and characterization of the heterodyne signal f_{CEO} and the repetition frequency f_{REP} were already presented in Chapter 4.

5.2 Fundamentally and harmonically Ti:sapphire pumped optical parametric oscillators

Optical parametric oscillators (OPOs) are used to shift the wavelength of the pump pulse to the infrared (IR) region via photon splitting into signal and idler pulses whose wavelengths are longer. These OPOs are pumped synchronously when the OPO cavity length is the same as the pump lasers cavity length [25]. In the case of harmonically pumped OPOs, there are two routes to obtain repetition rates higher than that of the pump laser. In the following section I will explain the comb structure achievable from harmonically pumped OPOs, and explain the design of the OPO cavities and the locking scheme used for frequency comb stabilization.

5.2.1 Harmonic operation of synchronously pumped OPOs

In the synchronously pumped regime the modelocked pump laser cavity length is the same as the optical parametric oscillator cavity length. In this case we are fundamentally pumping the PPKTP based OPO. The oscillating signal pulse is amplified after every round trip (see Figure 1).

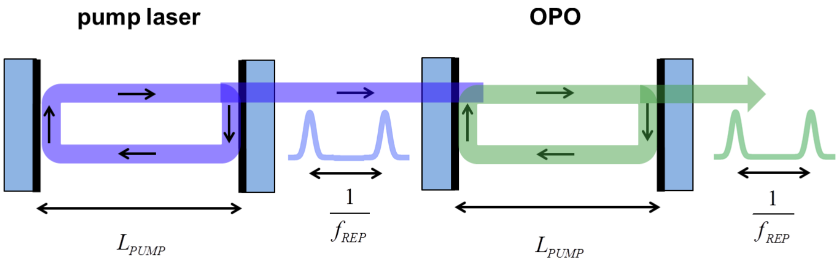

Figure 1. Fundamentally pumping the OPO.

We can also harmonically pump the OPO. Usually OPOs are synchronously pumped and therefore are limited by the repetition rate of the pump laser, but it is possible to operate the OPO at a harmonic of the pump laser when the OPO cavity length is an integer or integer fraction of the pump cavity length. Harmonic operation can be described as

$$L_{OPO} = \frac{nL_{PUMP}}{Q} \tag{70}$$

where L represents the pump and OPO cavity lengths, Q and n are positive integers, and $\frac{n}{Q}$ is an irreducible fraction. The relation describes an OPO cavity with n independent circulating pulses forming a pulse sequence Q times the repetition rate. We can achieve higher repetition rates by pumping shorter and even longer cavities (see Figure 2). The only difference is that when n is not equal to one, each set of pulses grows independently from noise leading to a random relative phase between each sequence, which is undesirable for frequency comb generation.

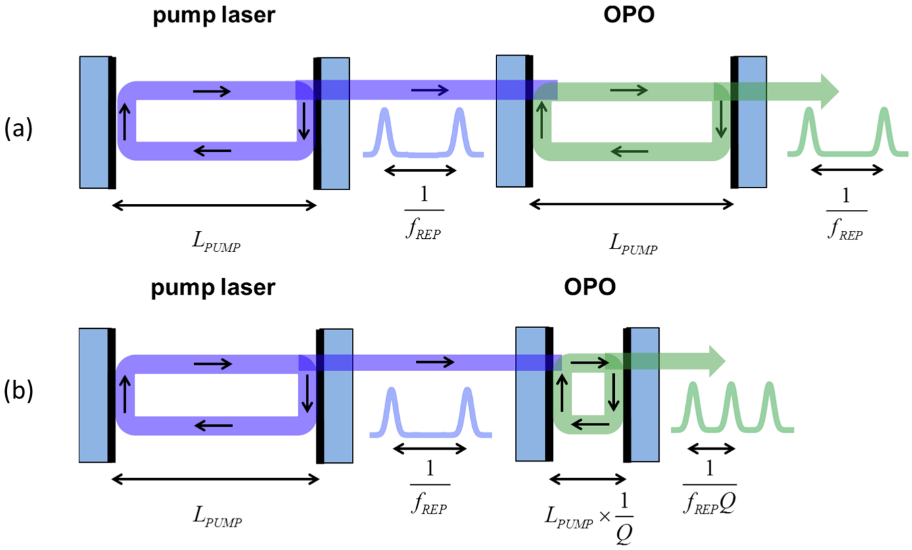

Figure 2. Harmonic operation of a synchronously pumped OPO, configured as a standing wave cavity: (a) an OPO (green) the same length as the pump cavity length (blue) (synchronous pumping); (b) an OPO (green) $\frac{1}{Q}$ times the pump cavity length (blue) (shorter cavities).

In simple harmonic pumping, when $n = 1$ and $Q > 1$ the OPO cavity length is Q times shorter than the pump laser and the signal pulses transit the cavity Q times before interacting with the next pump pulse [22, 27] (see Figure 2(a)). Shorter cavities are harder to design since smaller radius of curvature mirrors must be used for ensuring mode-matching between the pump and oscillating inside the OPO cavity beams. In the case of longer cavities (Vernier cavities), when $n \neq 1$ - each set of pulses grows independently from noise, leading to a random relative phase between each sequence, which is undesirable for frequency comb generation (see Figure 2(b)). Each pulse interacts with a pump pulse every Q round trips resulting in a pulse train with a repetition rate Qf_{REP}. If $Q > n$ the OPO is shorter than the pump cavity, but if $Q < n$ the OPO is longer. As demonstrated by Kokabee et al [24, 27], designs where both Q and n are large allow high harmonic repetition frequencies to be obtained from a cavity which is sufficiently long to permit optimum pump signal mode matching and the insertion of dispersion compensating optics.

5.2.2 Frequency comb structure in a harmonically pumped fs OPO

While attractive for these reasons, the Vernier approach (n>1) leads to the formation of n independent frequency combs of equal inter-mode spacing. The absolute phase of each comb is random, determined as the signal pulses build up from quantum noise, however the relative phase between each resonant comb is fixed as they share a common cavity. The pulses of a modelocked laser contain equally spaced frequencies separated by the repetition rate. For synchronously pumped OPOs it is the same - they produce signal and idler pulses for which the spacing between the modes is the same as the pump laser's repetition rate (see Figure 3(a)). In the case of simple harmonic pumping where n=1 and $Q > 1$, only one signal pulse oscillates in the OPO cavity and experiences gain after every round trip Q (see Figure 3(b)). Since the oscillating pulse is leaving the OPO cavity after every round trip and experiences the gain only after Q round trips, a ring-down effect writes sidebands at $\pm f_{REP}$ onto comb lines spaced at Qf_{REP}. In Vernier cavities, we have n oscillating signal pulses inside the OPO where each signal pulse experiences gain after Q round trips (see Figure 3(c)). In this case the phases of each signal pulse sequence are random since each set of signal pulses grows from quantum noise.

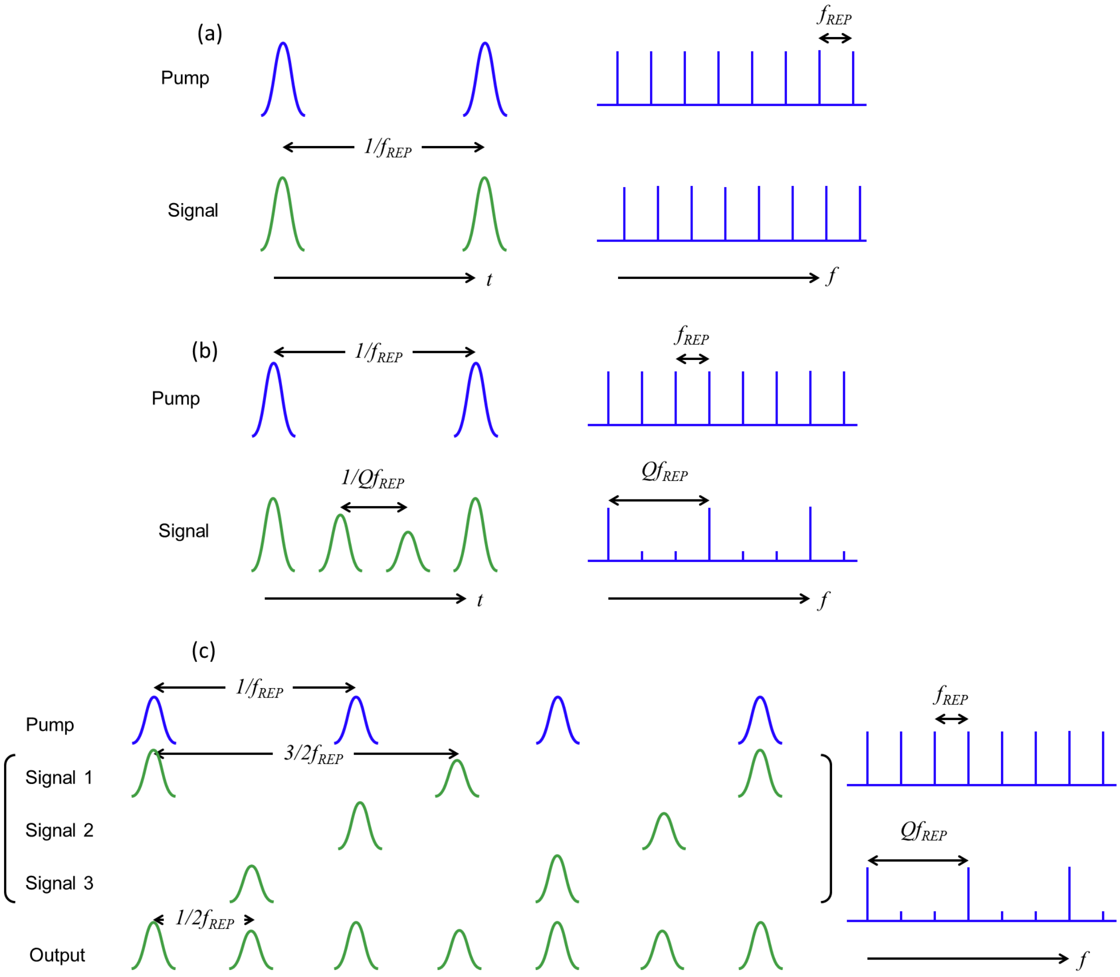

Figure 3. OPO frequency comb structure. (a) strictly synchronous pumping; (b) simple harmonic pumping; (c) Vernier harmonic pumping.

In this experiment the comparison of fundamentally and harmonically pumped OPOs, used shorter cavities where n=1 and Q=3. The OPO cavity length was three times shorter than the pump laser's cavity resulting in a three times higher repetition rate. One pulse oscillating in the cavity (n=1) experienced gain after every three round trips (Q=3).

5.2.3 Cavity design

For this study we utilized the short-cavity configuration with $Q = 3$ and $n = 1$. The 4-mirror ring OPOs were based on a 1.2-mm long periodically poled potassium titanyl phosphate (PPKTP) crystal (Raicol Crystals), which was antireflection (AR) coated at both the pump and signal wavelengths. The PPKTP crystal was attached to an XYZ translation stage. Mirrors M1, M2, M3 and M4 for the 333-MHz OPO were half-inch diameter, while for the 1-GHz OPO the M1 and M2 mirrors were quarter-inch to provide a smaller angle for the beam reflected from mirror M2. The generalized cavity design is shown in Figure 4. The Ti:sapphire pump beam was focused by a 63-mm focal length lens placed before one of the cavity mirrors, M1.

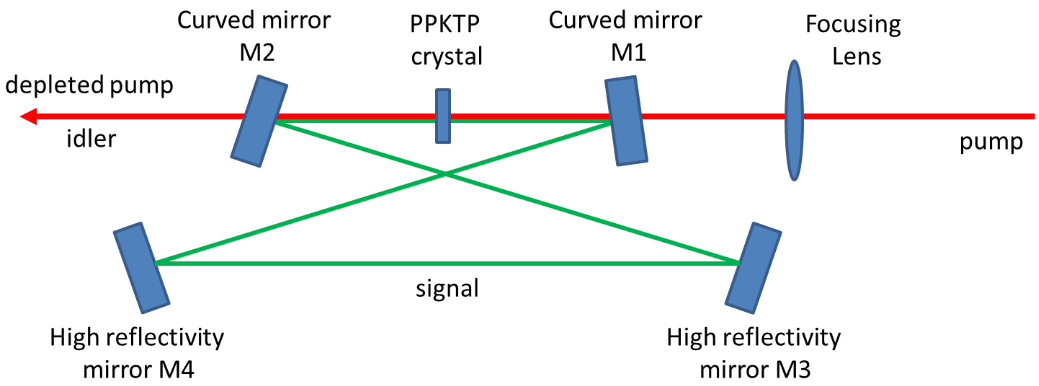

Figure 4. The optical layout of the 333-MHz and 1-GHz OPOs.

Fundamentally and harmonically pumped OPOs were modelled in LCav. The final parameters used for the OPOs are presented in Figure 5(a), (b).

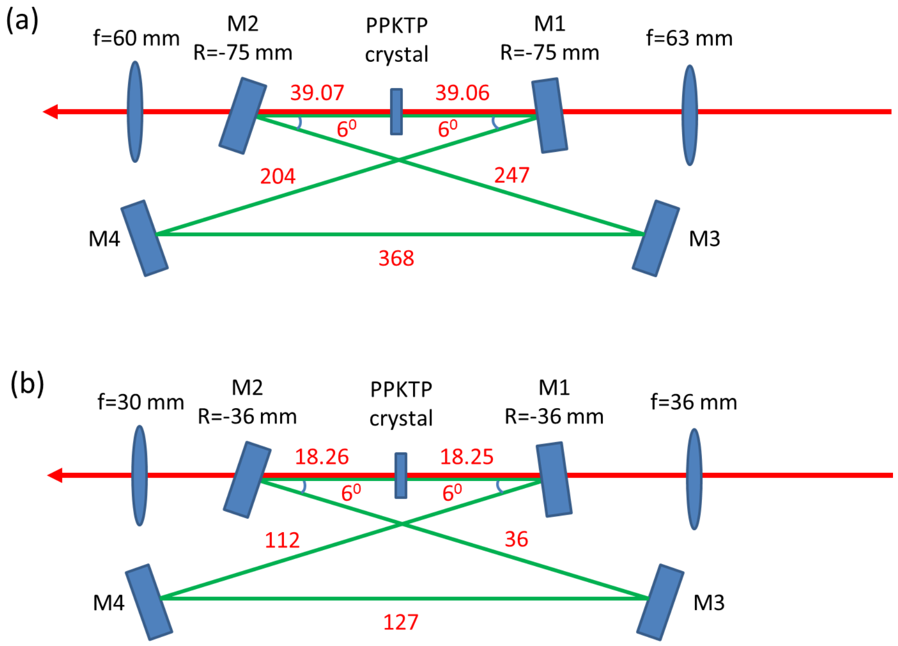

Figure 5. The initial parameters for the spot size and beam profile determination in LCav for: (a) 333-MHz OPO; (b) 1-GHz OPO. The distances are in mm.

The beam propagation inside the cavities for a fundamentally pumped OPO is presented in

Figure 6 (a), (b), while for a harmonically pumped OPO it is shown in Figure 7(a), (b). As a result, a stable regime of the OPO could be achieved when the minimum beam radii for the fundamentally and harmonically pumped OPOs were 30 μm and 21 μm respectively. We used -35-mm curvature mirrors for the three times shorter OPO cavity, because the signal pulse is traveling around the cavity three times before it gets amplified. The loss experienced in the cavity for the pulse is higher than in the case of the fundamentally pumped OPO. The threshold with the same curvature mirrors (-75-mm) for the 1-GHz OPO is also higher. In addition, the three times shorter cavity limits our design freedom, because quite small diameter holders must be used in order to ensure a sufficiently short distance between the M1 and M2 mirrors. A 1-GHz cavity corresponds to roughly 333-mm length, which limits the distance between the two curved mirrors.

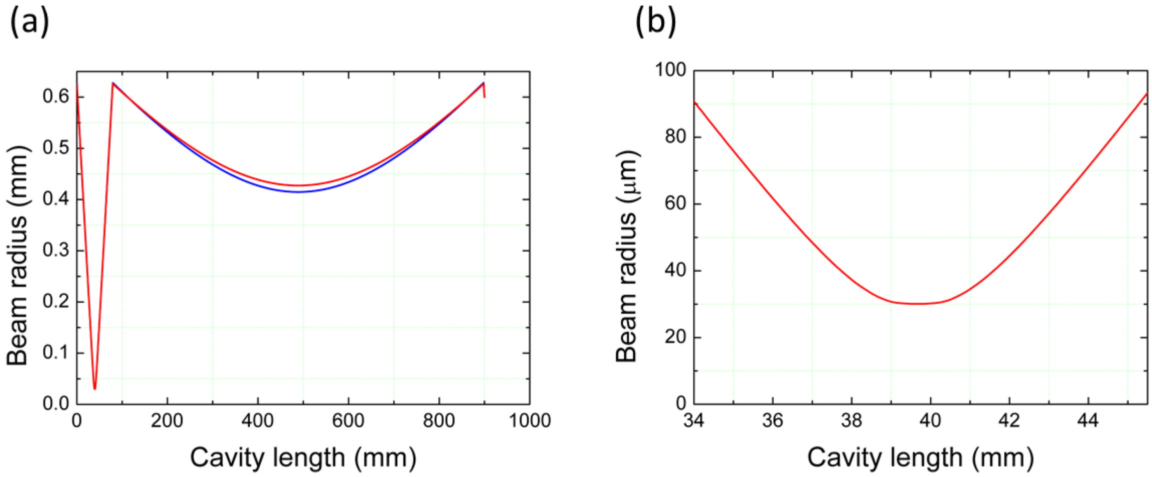

Figure 6. (a) The beam profile of the signal mode supported in the 333-MHz OPO cavity full path; and (b) through the nonlinear crystal.

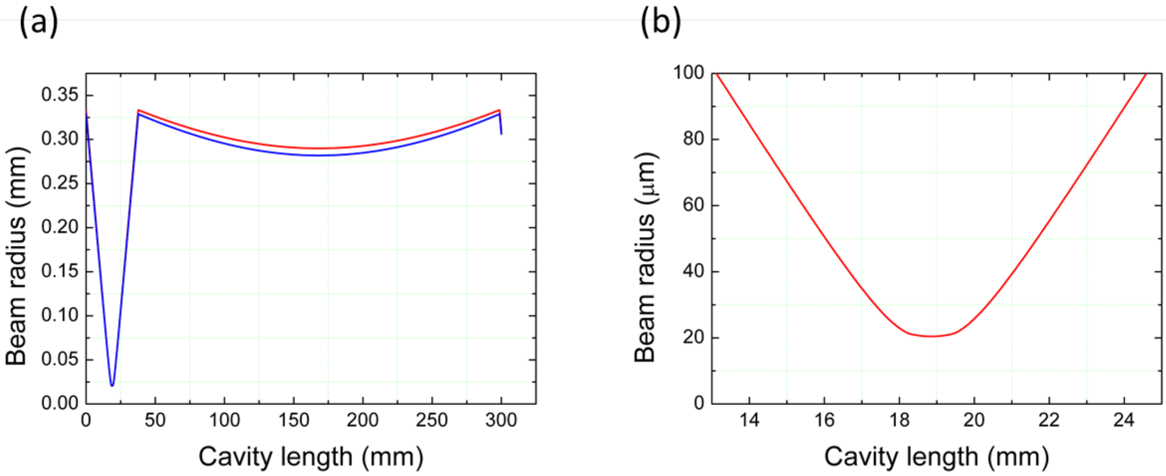

Figure 7. (a) The beam profile of the signal mode supported in the 1-GHz OPO cavity full path; and (b) through the nonlinear crystal.

5.2.4 The OPO characterization

The operating OPO is shown in Figure 8. Here 90 % of the Ti:sapphire pump laser (Gigajet, Laser Quantum) power centered at 800-nm was used to pump a 333-MHz repetition rate OPO, with 1.3 W of pump power steered into the OPO.

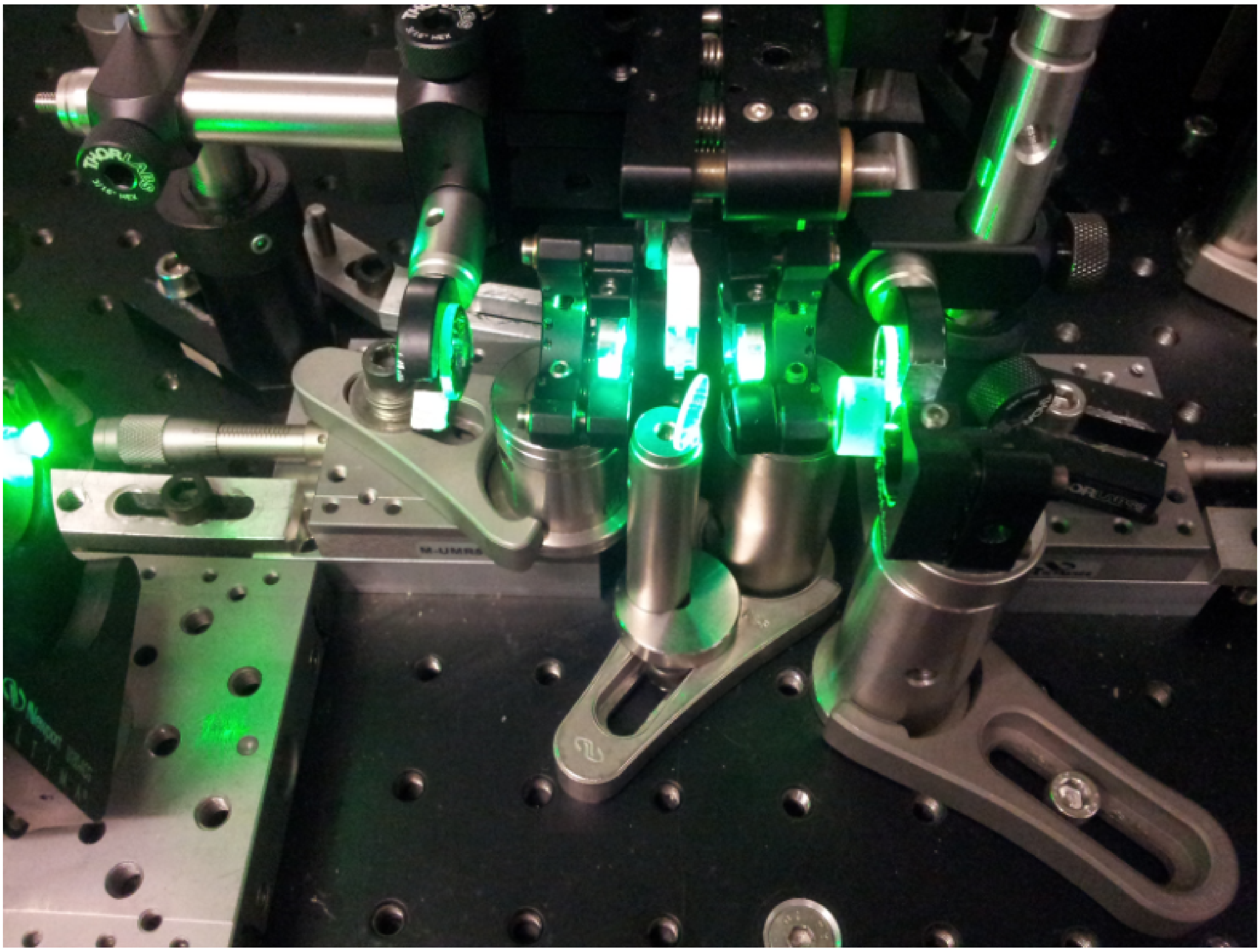

Figure 8. OPO running at 1550 nm. The green color represents the pump and signal SFG light.

Both the harmonically and fundamentally pumped 4-mirror ring OPOs (Figure 8, inset) were based on a 1.2-mm long periodically poled potassium titanyl phosphate (PPKTP) crystal (Raicol Crystals), which was antireflection (AR) coated at both the pump and signal wavelengths. In the fundamental 333-MHz configuration the OPO operated with a threshold of 250 mW and was cavity length tunable from 1100-1600-nm in the signal (Figure 9(a)). Harmonic operation was implemented by reducing the cavity length to 1/3 of the pump laser's cavity length, producing a 1-GHz output. For fundamental pumping the OPO was configured with -75-mm radius-of-curvature focusing mirrors, while for harmonic pumping this value was reduced to -32-mm to provide similar intracavity spatial mode conditions. The mirror coatings used in both cases were identical. The threshold at 1-GHz increased to 500 mW due to the increased losses from multiple cavity round trips, however the OPO tuning performance remained comparable (see Figure 9(b)). Both OPO configurations produced pulses with durations of 60–90 fs across the tuning range, depending on the cavity dispersion.

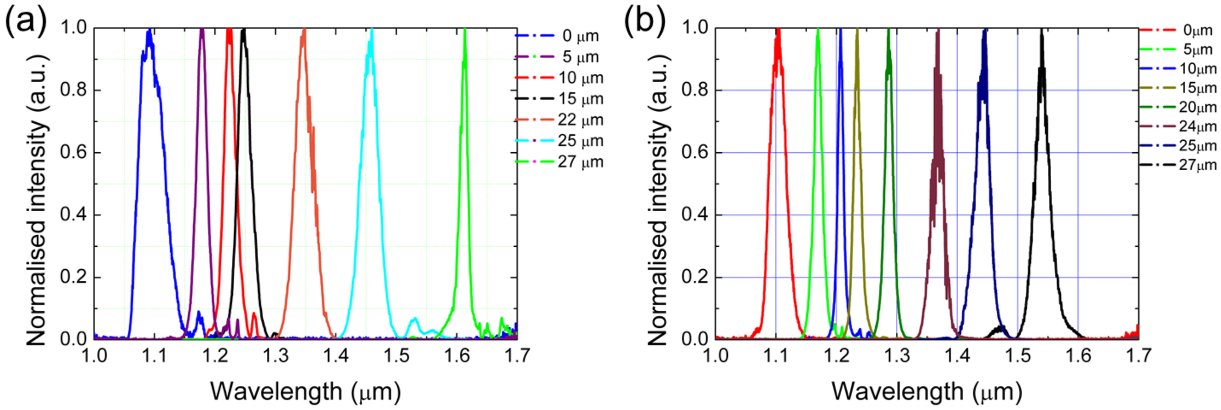

Figure 9. Signal spectra from cavity-length tuning of the (a) 333-MHz fundamental and (b) 1-GHz harmonic OPOs.

A 2-mm-thick fused silica plate, with an anti-reflection (AR) coating over the signal wavelength range on one surface, was placed in the cavity as an output coupler in order to extract some of the signal power for pulse duration, wavelength tuning and signal repetition rate measurements. This output coupler provided an average power of 10–45 mW depending on the signal wavelength. The centre wavelength of the signal could be tuned from 1.1-1.6 μm using a stage forming part of the OPO cavity. The OPO with the OC is shown in Figure 10.

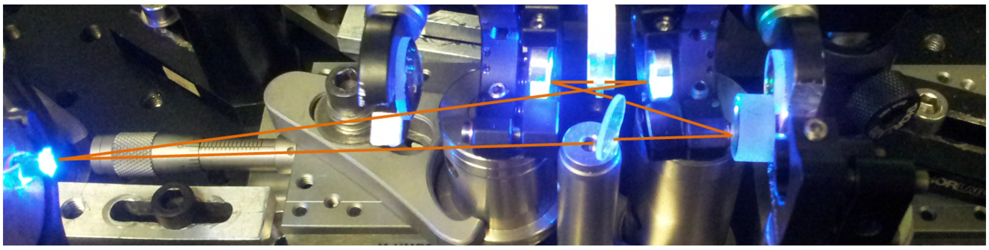

Figure 10. Harmonically pumped 1-GHz OPO cavity.

The measured central wavelength of the signal pulses did not tune smoothly with cavity length due to oscillations in the net cavity dispersion. In Figure 9 the OPO was tuned manually by a stage. The signal pulses covered the wavelength range from 1.1-1.6 μm. The bandwidth of the pulses was around 25-30 nm. The wavelength tuning was not smooth across the full range and exhibited sudden wavelength shifts around 1.425 μm and 1.55 μm. To have a more accurate tuning curve characteristic, the tunability around these wavelengths was investigated by using a PZT. Figures 11 and 12 show this tuning behaviour of the 1-GHz and 333-MHz OPOs along with the calculated net dispersion for the cavities respectively.

The PZT voltage was changed from 70-160 V and with that change in cavity length, the output wavelength shifted from 1.3-1.6 μm. On the lower side of the wavelengths the tuning was slow, a 70 V change on the PZT from 160-90 V shifted the output wavelength only by 150 nm while a further decrease of the voltage on the PZT by 20 V from 90-70 V shifted the wavelength by almost 250 nm (see Figure 11(a)). This behaviour is related to the net cavity dispersion. Figure 11(b) presents the net cavity dispersion for the 1-GHz OPO. The dispersion is not flat across all of the tuning range. It is positive at 1.0 μm and falls below zero for wavelengths above 1.1 μm. It stays negative until the OPO wavelength is tuned to 1.425 μm. Here we have the first region where the OPO does not oscillate at 1.425 μm. Instead of oscillating at 1.425 μm the OPO jumps to 1.45 μm. Beyond this we see a narrow 30-40 nm window where the OPO tunes smoothly and then jumps again.

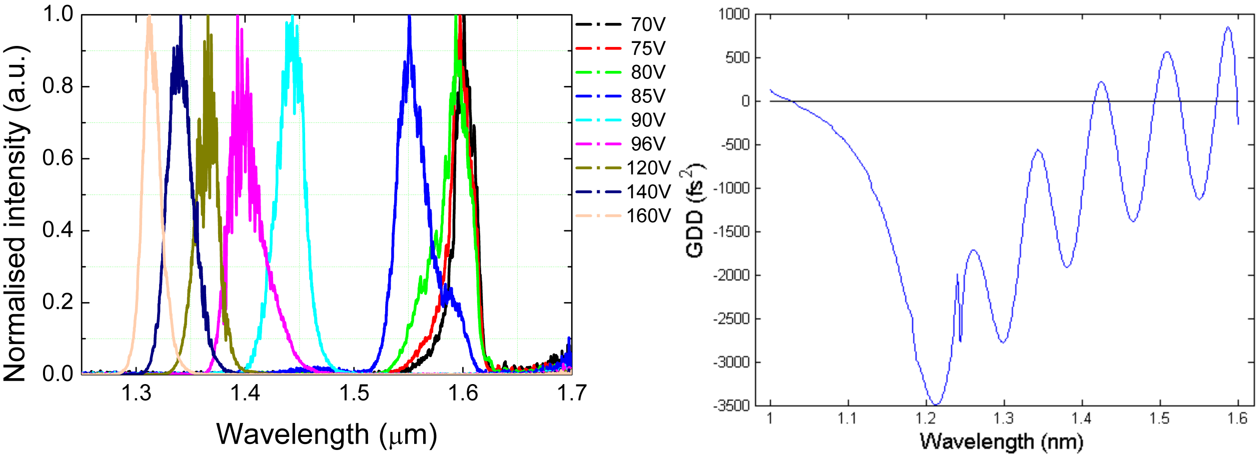

Figure 11. (a) Tuning curve of the 1-GHz harmonic OPO, showing a similar a distinct gap over the 1.4-1.6μm range. (b) Dispersion curve of the 1-GHz OPO.

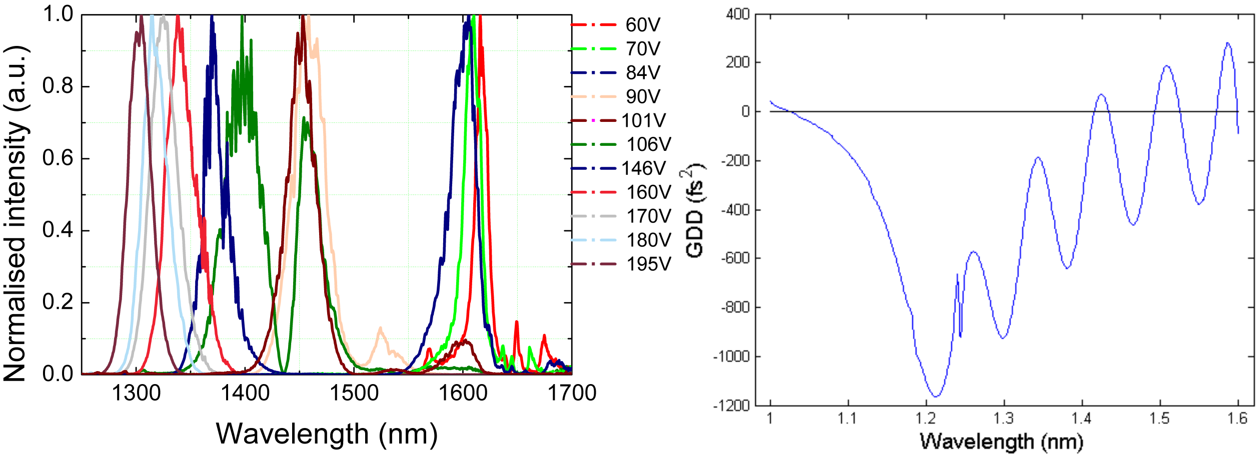

Figure 12. (a) Tuning curve of the 333-MHz OPO, showing the distinct gap over the 1.4 -1.6-μm range. (b) Dispersion curve of the 333-MHz OPO.

The tunability of the 333-MHz OPO was similar. The output wavelength covered the range from 1.1-1.6 μm. We noticed the same pattern: the PZT voltage was changed from 60-195 V (see Figure 12(a)). The OPO again did not oscillate at wavelengths where the net cavity dispersion was positive. Figure 12(b) presents the net cavity dispersion for the 333-MHz OPO. In this case we have three times smaller positive/negative dispersion for the same wavelength because the signal pulses travel only once around the cavity while in the 1-GHz OPO the signal pulse propagates three times around the cavity until it sees the next pump pulse and is amplified.

The net cavity GDD for the 1-GHz OPO at 1.22 μm was -3000 fs^2 while for the 333-MHz OPO it was only -1000 fs^2. The tunability of the cavity could be improved by introducing additional optics inside the OPO for net cavity dispersion reduction. In Figure 13 I show the net cavity dispersion calculated if two 6-mm thickness BK7 windows are introduced into the OPO cavity. In this case the positive dispersion at most wavelengths is suppressed down to zero. This was implemented and improved the OPO tuning. The tuning was much smoother, but apparently not negative enough since a wavelength jump in the tuning from 1.42-1.5 μm was still observed.

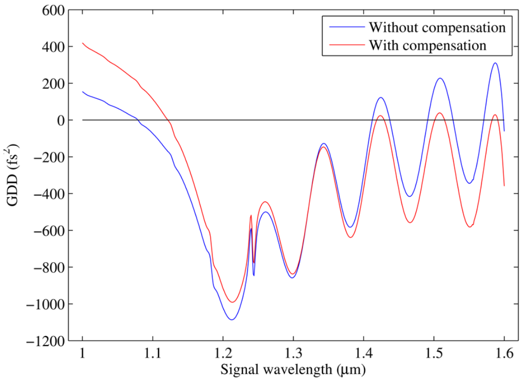

Figure 13. Net cavity dispersion after introducing 2 x 6-mm thickness BK7 windows.

Pulse duration measurements were taken as the OPO cavity length was tuned for both fundamentally and harmonically pumped OPOs. The autocorrelation traces are shown in Figure 14.

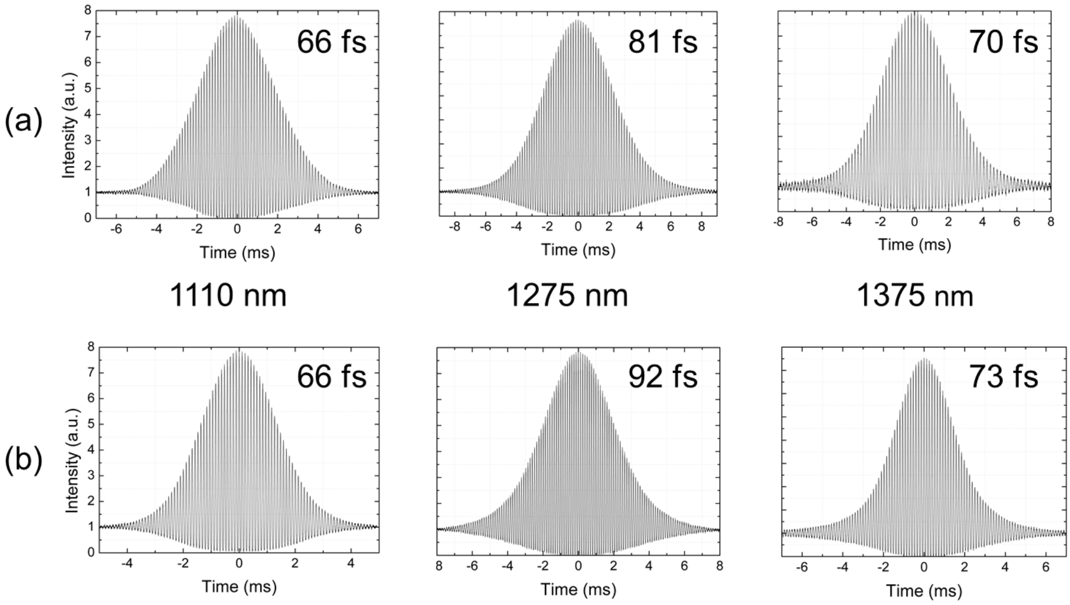

Figure 14. Pulse duration measurements of the signal pulses at different wavelengths: (a) 333-MHz OPO, (b) 1-GHz OPO.

The pulse durations varied from 66-92 fs depending on the net cavity dispersion. At 1.11 μm the net cavity dispersion was close to zero and therefore the pulse durations for both OPOs were the same. At 1.275 μm the dispersion is much bigger for the 1-GHz OPO and as result the pulse duration was longer in comparison with that measured for the 333-MHz OPO. There is a 10-fs difference in pulse duration at 1275 nm. When the net cavity dispersion decreased again at 1375 nm, the pulse durations became closer to each other. The 1-GHz OPO emitted signal pulses which were longer in duration by several fs.

5.3 Stabilization of a harmonically pumped femtosecond OPO comb

The exact experimental configuration is shown in Figure 15. A Ti:sapphire pump laser (Gigajet, Laser Quantum) produced 30-fs pulses with 1.45-W average power centered at 800-nm with a full-width half-maximum (FWHM) bandwidth of 32 nm and a repetition rate of 333-MHz. A 90 % reflector was used to steer 1.3-W of pump power into the OPO, with the remaining 10 % coupled into a photonic crystal fibre (PCF) for supercontinuum generation.

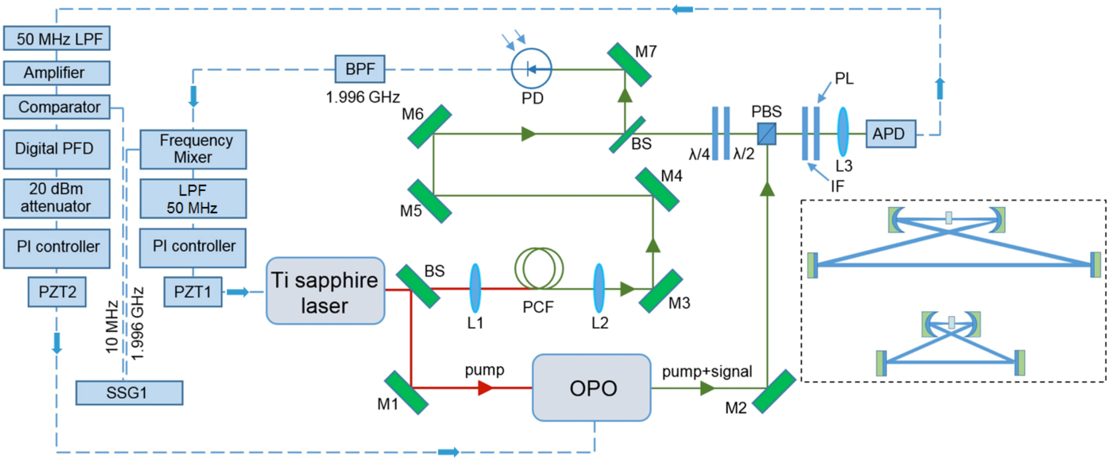

Figure 15. Stabilization layout and (inset) cavities of fundamental / harmonically-pumped OPO combs. OC, output coupler; M, dielectric mirrors; PCF, photonic crystal fiber, BS, beam splitter; PBS, polarizing beam splitter; IF, interference filter; PL, polarizer; L, focusing lenses; PD, photodiode; APD, avalanche photodiode; LPF, low pass filter; PFD; phase frequency detector; BPF, bandpass filter; PZT, piezo-transducer; SSG, synthesized signal generator.

Both f_{REP} and f_{CEO} must be detected and stabilized in order to achieve fully stabilized frequency combs. The electronic feedback loops were the same for both the fundamentally and the harmonically pumped OPOs. More details on the locking of the f_{REP} and f_{CEO} frequencies were presented in Chapter 4.

5.3.1 Repetition rate stabilization

The pump repetition rate (f_{REP}) was sampled with a fast Si photodiode (PD) and its sixth harmonic (2-GHz) isolated with a bandpass filter (BPF) then mixed with a 2-GHz reference from a synthesized signal generator (SSG1, Agilent 8664A). The low-pass-filtered error signal from the mixer entered a proportional-integral (P-I) controller, generating a control signal which was used to actuate PZT1 in the Ti:sapphire laser. The repetition rate remained locked for about 2 hours without adjustments. The f_{REP} stabilization was quite straight forward.

5.3.2 Carrier envelope offset f_{CEO} stabilization

Carrier-envelope offset (f_{CEO}) frequency stabilization of the OPO signal pulses was implemented by heterodyning light from the pump supercontinuum with non-phasematched pump-signal sum-frequency light from the OPO, as described in [28] and selected using a diffraction grating (DG). The CEO frequency, f_{CEO}, was filtered, amplified and passed through a comparator to provide an input to one channel of the phase-frequency detector (PFD) [29]. The 10-MHz clock output from SSG1 was used as the CEO reference frequency and served as the second PFD input. The PFD output provided an error signal to a second P-I controller, the output of which was connected to PZT2 in the OPO cavity to control f_{CEO}. The OPO wavelength and f_{CEO} could be manually tuned using a long-travel PZT stage, allowing the f_{CEO} to be brought into the locking-loop capture range.

Beat note survey for 333-MHz OPO

Before choosing the locking wavelength, a beat note survey over a broad range of wavelengths was carried out. In the PPKTP crystal different frequencies can be mixed and therefore different heterodyne beats can be acquired: we have signal pulses oscillating in the cavity; we have the idler wave which is the product of pump and signal waves and also the pump pulses from Ti:sapphire laser. Our 1.2-mm length crystal had special sections (detailed in Chapter 4) for sum frequency mixing for p+i and second harmonic generation of signal pulses. We can expect many different interactions but at the end we are interested only in obtaining a beat strong enough for locking.

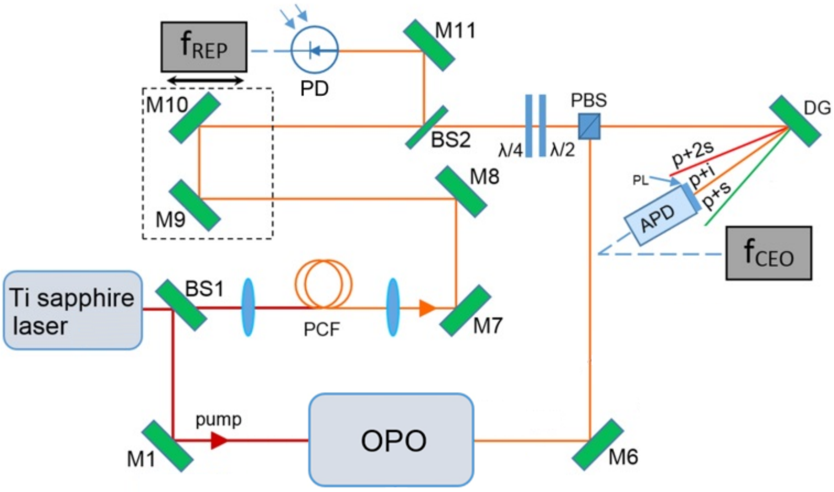

Figure 16. A diffraction grating was used for the beat-note survey as signal, idler and p+2s f_{CEO} frequencies were obtained at different wavelengths.

For that reason we decided to measure the beat strength for different interactions at different wavelengths. The generated p+i, 2s and p+s waves were overlapped with the light from the PCF. The beats were acquired by spectrally selecting common wavelengths of light propagating from the OPO and PCF with a diffraction grating (DG) (see Figure 16).

The results for different f_{CEO} frequencies are shown in Figure 17–19. To trigger our electronics, the f_{CEO} S/N ratio must be at least 30 dB (at RBW=100 kHz). Figure 17 shows the interference between the pump supercontinuum and the p+i pulses. From the measured beat strengths (data recorded by Mr. Stewart Leitch, a summer student whom I supervised), we can see that the beat at 1.13 µm is not strong enough for f_{CEO} locking. On other hand, the measured heterodyne beats reached a 40-dB SNR between 1.15-1.5 µm. The beat was weaker only at 1.35 µm because of the water absorption in the band from 1.3-1.4 µm. In case of the 2s and pump supercontinuum beat, the results were similar: we observed weak beats on the edge of the lower wavelengths and also around 1.3-1.4 µm (see Figure 18). The last results for the p+s and supercontinuum heterodyne beats acquired on the APD are presented in Figure 19. We detected lockable beats in the region around 1.4-1.55 µm. Below 1.4 µm there was no efficient p+s mixing inside the PPKTP crystal since the crystal only had additional sections for p+i and 2s generation but not for p+s. We measured strong beats above 1.4 µm only because at these wavelengths a strong parasitic interaction between the pump and signal pulses appeared.

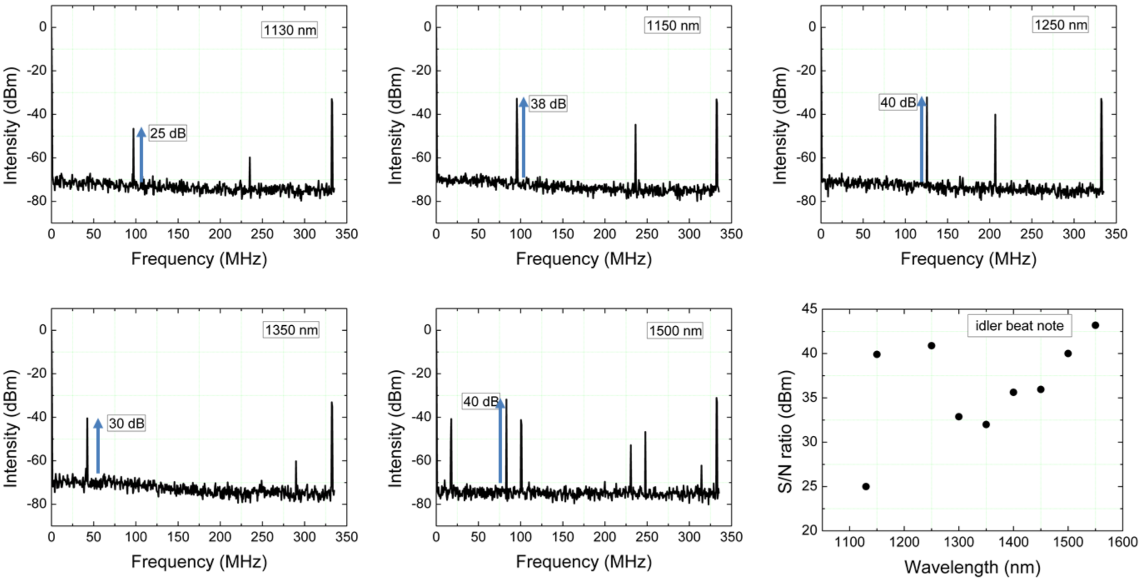

Figure 17. Heterodyne beats between pump+idler SFG and the pump supercontinuum light from the PCF. The acquired beats represent the actual f_{CEO} frequency for the idler pulses. Using these beats we could lock the idler f_{CEO} in broad wavelength range from 1.9-3.0 µm. RBW=100 kHz.

In Figure 20 an overall survey map of beat notes for all three heterodyne signals is presented. From these results we can claim that a heterodyne beat across the full tuning range of the OPO can be acquired for p+i and 2s nonlinear interactions. This survey shows the quality of the heterodyne beats which can be acquired for each interaction. The strength of the beats could always be improved by some careful adjustments and optimisations. The size of the circle represet the strength of the obtained heterodyne beat at certain wavelength for different interactions.

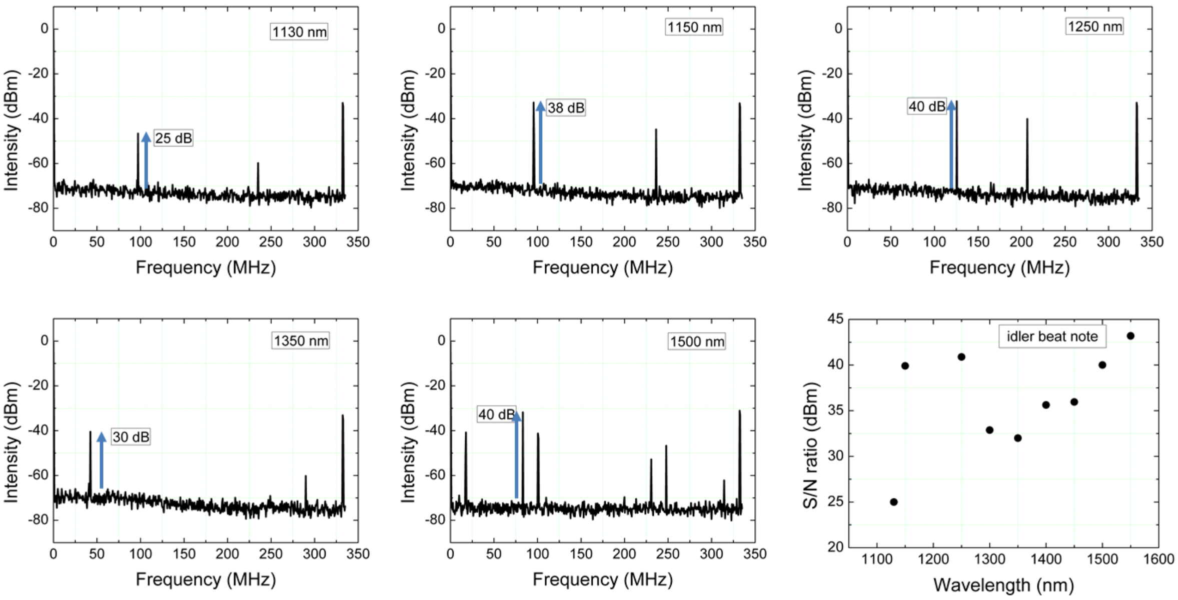

Figure 18. Heterodyne beats between the second harmonic (SHG) of the signal and the pump supercontinuum light from the PCF. The acquired beats represent the f_{CEO} difference between the pump and 2s pulses. Using only this beat we cannot directly lock any pulses, however if the pump laser is self-referenced then this beat can be used to lock the OPO signal pulses. RBW=100 kHz.

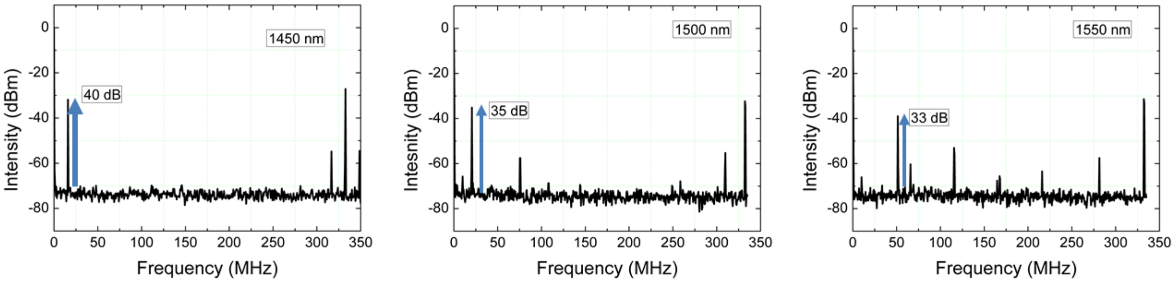

Figure 19. Heterodyne beats between the pump + signal sum-frequency light from OPO and the light from the PCF. The acquired beats represent the f_{CEO} frequency for the signal pulses. Using this beat frequency we can directly lock the f_{CEO} of the signal pulses. RBW=100 kHz.

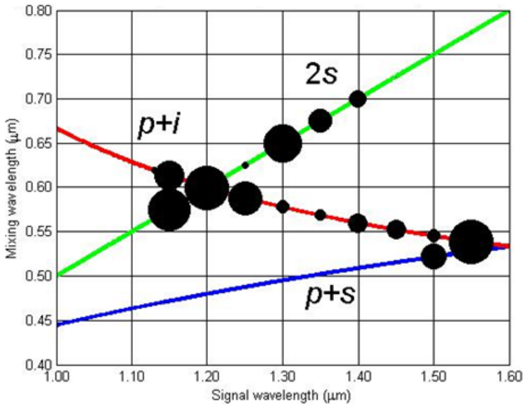

Figure 20. Results of the heterodyne beat note survey over a broad tuning range.

f_{CEO} of the signal pulses stabilization

Following the beat note survey, we concentrated on evaluating the frequency comb locking for the signal pulses at 1.45-µm. The p+s wavelength at 515-517 nm from OPO was heterodyned with the same wavelength from the PCF (see Figure 21), to give a beat note containing only the signal pulse f_{CEO} frequency fluctuation. Another limitation for f_{CEO} locking was the PCF. It was challenging to extend the supercontinuum broadening below 500 nm and with our PCF we could reach 490-nm at the most. An example of this limitation would be if we wanted to lock the signal f_{CEO} at 1.2 µm, we would need to have supercontinuum light from a fibre around 460 nm, which in our case would be impossible.

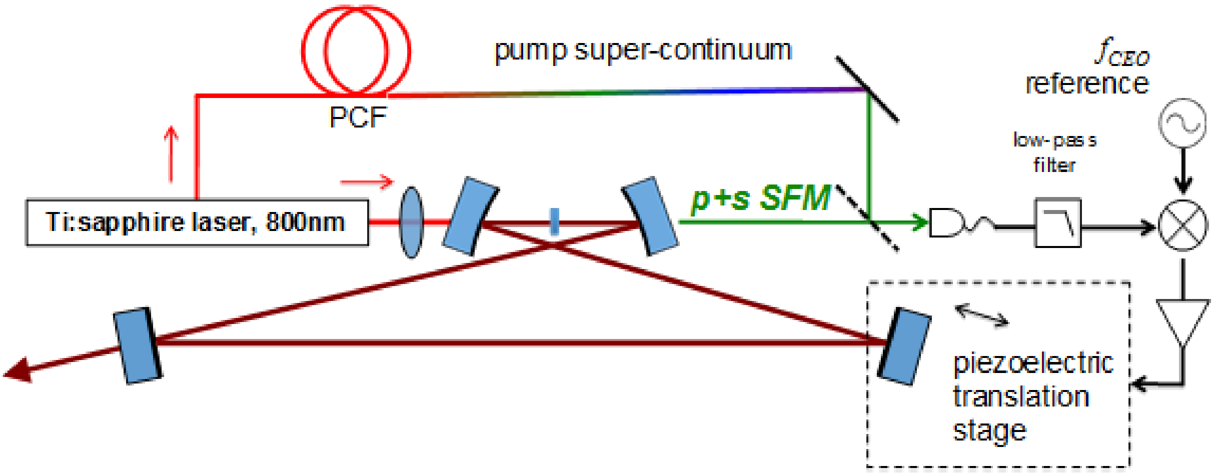

Figure 21. f_{CEO} detection and locking to an external reference approach.

For the comparison of fundamentally and harmonically pumped OPOs the wavelength does not matter. In both configurations we measured 35-40 dB beat notes for the signal f_{CEO} from 1.45-1.55 µm. For a comparison of the two OPOs at 333-MHz and 1-GHz we locked the signal f_{CEO} at 1.46 µm. The characteristic RF spectrum of the heterodyne beat after filtering by a 50-MHz low pass filter and then amplification is shown in Figure 22(a). The beat was then passed through a dual channel comparator to provide a TTL signal to one channel of a phase-frequency detector (PFD). To the second channel of the PFD a 10-MHz reference from SSG1 was introduced. The PFD output was used as an error signal to a P-I controller whose output provided a signal to PZT for f_{CEO} locking. The locked heterodyne beat at 10-MHz frequency is presented in Figure 22(b).

The f_{CEO} frequency could remain locked for several minutes, however any sudden noise increase such as a knock on the optical bench or door slamming made the locking drop out. We expect that engineering improvements would considerably improve this long term stability. Results presented later in this thesis which report using a divide-by-N circuit to improve the locking capture range have also suggested that locking over hours could be achievable.

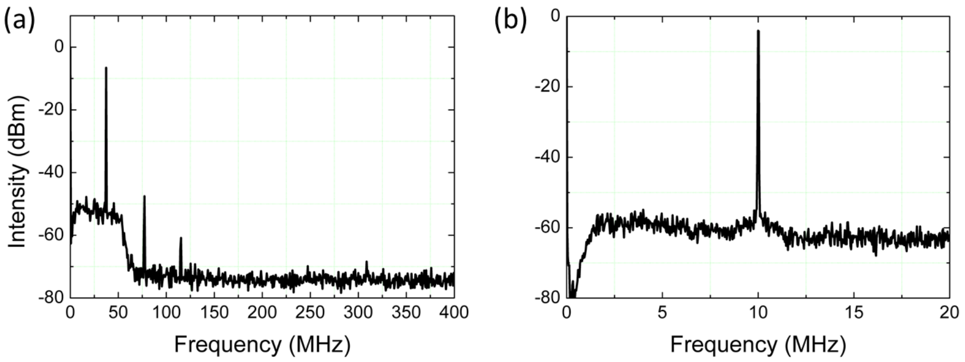

Figure 22. (a) The detected signal f_{CEO} of 1-GHz OPO was low-pass filtered. RBW=100 kHz; (b) and locked to 10-MHz reference. RBW=10 kHz.

5.4 Frequency comb instability and phase noise measurements

Harmonically and fundamentally pumped OPOs were characterized by measuring the two sample frequency deviation (the Allan variance) and and in loop phase noise PSD of the locked f_{CEO}. From these measurements the repetition rate and f_{CEO} fractional instabilities were calculated. Separate measurements of the phase noise PSD provided information about which frequencies contributed most to the instability of the comb.

5.4.1 Two sample frequency deviation

A frequency counter (HM8123) recorded the instabilities of the locked f_{REP} and f_{CEO} over different gate times, and their two sample frequency deviation was calculated. In our locking loops a 10 MHz Rubidium (Rb) clock [30] provided an external reference to SSG1, SSG2 and the frequency counter (see Figure 23(a)). The f_{CEO} signal after a low pass filter (LPF1) was split into two channels to lock it to the 10-MHz reference frequency and at the same time sample its fluctuations. The f_{REP} stability was measured after a BPF which removed the 333-MHz or 1-GHz harmonics depending on the OPO configuration, and provided one input for the frequency mixer. The other frequency from SSG2 was introduced into the mixer with a 2-kHz offset frequency to enable counting at high resolution (see Fig.23(b)).

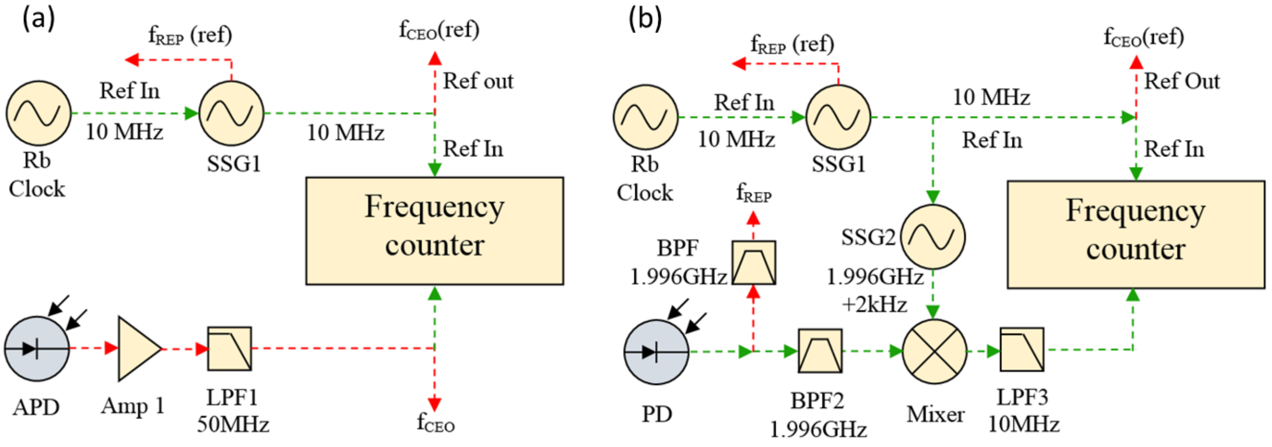

Figure 23. Configuration for recording the frequency stability data for (a) f_{CEO} and (b) f_{REP}.

First I present the frequency stability measurements of f_{CEO} and f_{REP} for a 1 second gate time. The Allan variance in f_{CEO} when locked to a 10-MHz reference was close to 0.27-Hz for both the fundamental and harmonically pumped OPOs (see Figure 24(a,b)). This result is comparable with the one achieved by Ferreiro et al [28] where for a 280 MHz OPO a value of 0.17 Hz was obtained. The calculated instabilities in f_{REP} were 1.5-mHz and 5-mHz for the 333-MHz and 1-GHz harmonic OPO respectively (see Figure 24(c),(d)). The noise limit of the locking loop was measured by replacing the photodiode in Figure 23(b) with a synthesized signal from SSG1. The resulting frequency fluctuations gave a $5e{-}12$ fractional instability for a 1-second gate time, which is in this case limited by our locking loop. The measured instabilities of the Rb referenced synthesized frequencies at 333-MHz and 1-GHz were 1.5-mHz and 4.5-mHz respectively, confirming that the stability of the OPO repetition frequency was limited by the locking loop itself since clock source gave the same Allan deviation for different gate times. In-loop measurements were done by referencing the SSG and frequency counter to the same clock. The increase of the repetition frequency by three times resulted in a three times higher frequency fluctuations. We therefore conclude that the repetition rate instability of the harmonically pumped OPO increases proportionally with f_{REP} due to an increase in the fractional change in the cavity length of the OPO relative to the pump laser.

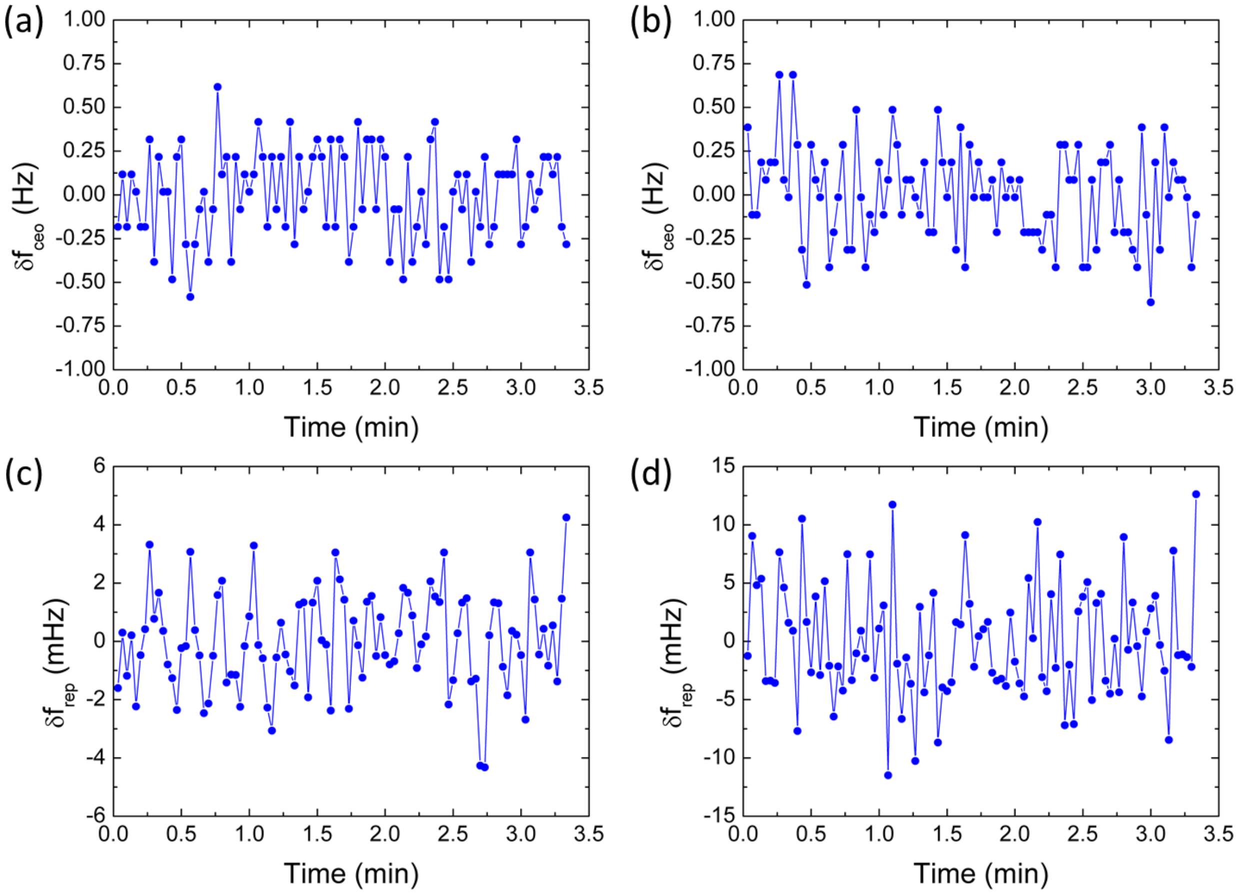

Figure 24. f_{CEO} frequency instability measurements around 10-MHz over a 1-second gate time for the (a) 333-MHz and (b) 1-GHz OPO. Repetition frequency instability measurements over a 1-s gate time for the (c) 333-MHz and (d) 1-GHz harmonic OPO.

The f_{CEO} and f_{REP} fractional frequency comb instabilities for different gate times are presented in Figure 25. The fractional stability data calculated from the raw data for the Rb clock are also plotted for comparison. The fractional instability of the locked f_{CEO} for both the fundamentally and harmonically pumped OPOs over a 1-second gate was $1.35e{-}15$. The fractional instability of f_{REP} over a 1-second gate time was $4.5e{-}12$ for 333-MHz OPO and $5.0e{-}12$ for the 1-GHz harmonic OPO. These results demonstrate that the frequency stability obtained from the harmonically pumped OPO comb is comparable with that from the fundamentally pumped OPO, despite the fact that the signal pulses are making multiple round trips around the OPO cavity, which might be expected to enhance the contribution of environmental effects to the repetition rate f_{REP} phase noise.

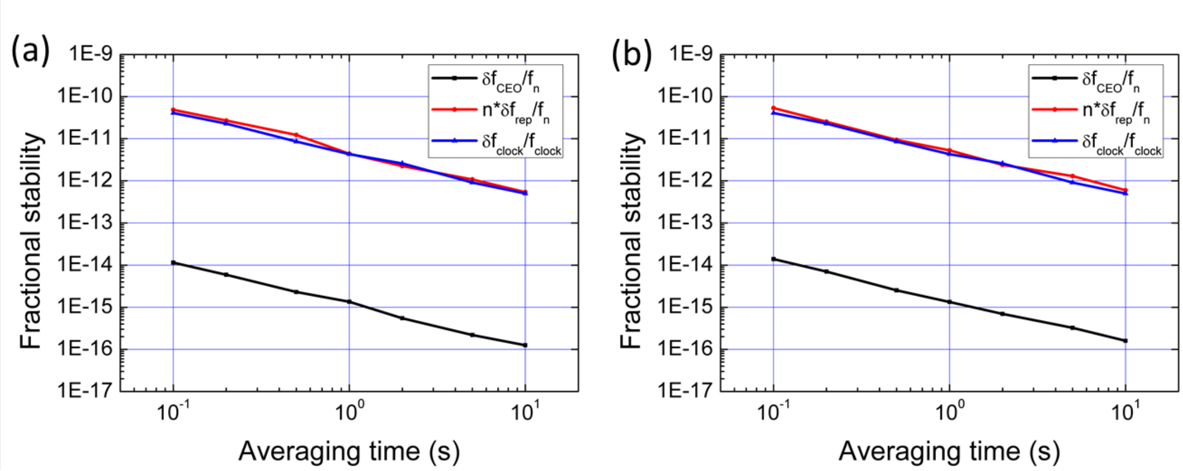

Figure 25. Fractional frequency comb stability from the in-loop f_{REP} and f_{CEO} signals. The data for the Rb clock show the limiting instability in the f_{REP} locking. Frequency comb instability is shown for: (a) the 333-MHz OPO ($f_n = 200$ THz, $n = 600000$) and (b) the 1-GHz harmonic OPO ($f_n = 200$ THz, $n = 200000$).

5.4.2 In loop phase noise PSD measurements

The RF spectrum of the stabilized f_{CEO} frequency for the 1-GHz harmonically pumped OPO was recorded using a 400-Hz span and 10-Hz resolution bandwidth (RBW), showing an instrument limited bandwidth of 10 Hz at the 3 dB level (Fig. 26(a)), which is comparable to the performance reported in [28]. In loop phase noise measurements of f_{CEO} were carried out when f_{REP} was locked by acquiring the PFD output signal with a 12-bit DAQ card. The output from the PFD was split into two channels. One of them was used for the PSD measurements. The signal before the 12-bit acquisition card was first amplified to fill the dynamic range of the DAQ card. PSD phase-noise plots for the fundamental and harmonic OPOs are shown in Figure 27. The integrated phase noise from 1 Hz–64 kHz was 1.8 rad and 2.8 rad for the 333-MHz and 1-GHz harmonically pumped OPOs respectively. Both PSD plots show increased phase noise in the 25–32 kHz range, which arises from 27-kHz intensity fluctuations in the pump laser (see Figure 26(b)). This noise caused the cumulative phase noise to increase by 1 rad for both the fundamentally and harmonically pumped OPOs. These fluctuations couple into the

Ti:sapphire laser as RIN and into the OPO as both RIN and phase noise [31]. Noise above 1 kHz lay outside our locking loop bandwidth, which was limited by the response of the fast PZT in the OPO cavity (PZT2). The noise contribution around the 1 kHz frequency increased from 0.8 rad for the 333-MHz OPO to 1.8 rad for the 1-GHz OPO. Frequencies around 1 kHz are usually related to acoustic or electrical noises source which can couple into the feedback loop or the OPO itself. For a shorter cavity, the impact of acoustic noise and thermal vibrations is more obvious in comparison with the 333-MHz OPO. For the feedback loop in the 1-GHz OPO it is harder to stabilize the f_{CEO} drift caused by vibrations since the repetition rate of the shorter OPO cavity will change faster and further. Not only must the bandwidth of the PZT be increased, but also capture the range of the PFD for f_{CEO} stabilization. If the pump noise could be reduced then the f_{CEO} PSD for the 333-MHz OPO would be comparable to previously published results [28].

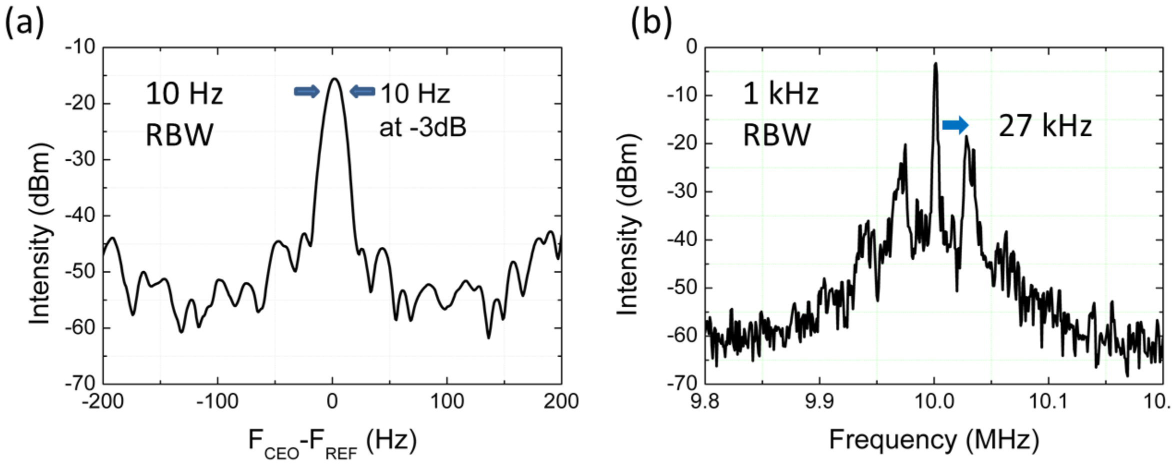

Figure 26. RF spectra of the locked f_{CEO} signal recorded with (a) 400-Hz span, 10-Hz resolution bandwidth; (b) 400-kHz span, 1-kHz resolution bandwidth, for 1-GHz OPO.

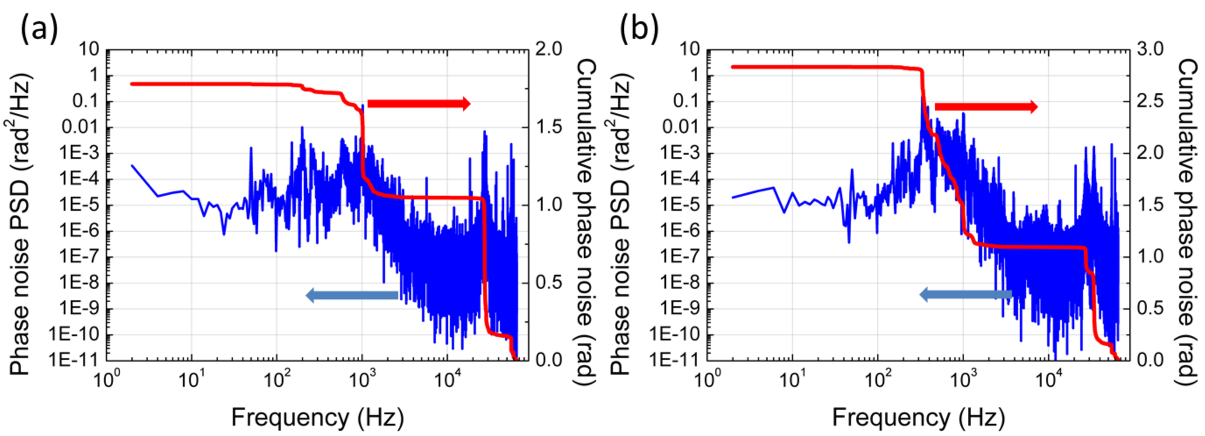

Figure 27. In loop 1-second observation time of the phase noise PSD for f_{CEO} of the (a) 333-MHz and (b) 1-GHz harmonically pumped OPO, for which the cumulative phase noise values from 1-Hz to 64-kHz are 1.8-rad and 2.8-rad respectively.

From the 333-MHz and 1-GHz OPOs phase noise PSD measurements we locked with PZT2 we could suppress the noise only if its frequency was below or close to 1-kHz. We were able by some careful optimization to suppress the noise at 1 kHz down to 0.4 rad, but the 27-kHz noise never changed: it always increased the cumulative phase noise by 1-rad. We were able to prove this by changing the so called "Pure Gain" parameter of the Ti:sapphire pump laser (Laser Quantum Finesse) controller. According to the manufacturer, the increase of the Pure Gain parameter shifts the frequency noise floor from low to high frequencies which can be seen from its effect on the locked f_{CEO} heterodyne beat. The noise at certain frequencies can be suppressed or increased. This setting was changed manually. By default the Pure Gain was set to 22.1 % which we used for all the experiments presented earlier. It gave us the lowest RIN in range from 1 Hz to 1 MHz according to the detector placed inside the pump laser. As a demonstration that the noise around 27-kHz could be changed, the Pure Gain parameter was changed from 0.1-32 % when the 333-MHz OPO was completely locked (see Figure 28). The locked beat shape changed together with the Pure Gain parameter. The beat note was noisy when the Pure Gain was close to 0 % and decreased when it was changed from 0-32 %. Therefore the optimum Pure Gain setting was found to be 32 %, because it gave the best SNR between the middle peak (10 MHz) and the sidebands sitting at 27-kHz frequency. The best phase noise PSD measurement with the optimised Pure Gain setting is presented in Chapter 8, in which we report a cumulative phase noise of less than 300 mrad.

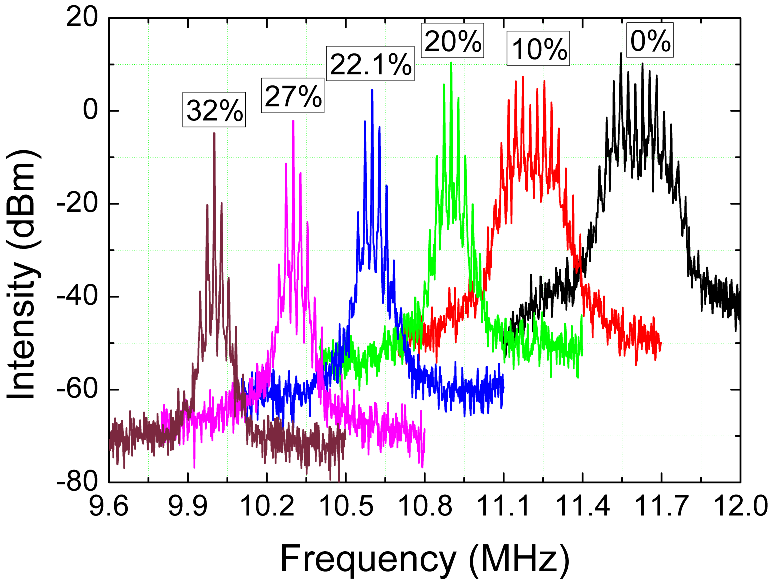

Figure 28. Locked f_{CEO} beat at 10-MHz reference dependence on Pure Gain parameter.

Table 1. Comparison of the fundamentally and harmonically pumped OPOs.

	333 MHz	1 GHz
Tuning range	1.1-1.6 µm	1.1-1.6 µm
Pulse duration	66-81 fs	66-92 fs
f_{CEO} noise (1 second, 0-64 kHz)	1.8 rad	2.8 rad
f_{CEO} stability (1 second, 0-64 kHz)	$1.35 * 10^{-15}$	$1.335 * 10^{-15}$
f_{REP} stability (1 second, 0-64 kHz)	$4.38 * 10^{-12}$	$5.3 * 10^{-12}$

5.5 Conclusions

The results presented in this chapter demonstrate for the first time a femtosecond OPO frequency comb exploiting harmonic pumping to multiply its repetition frequency by a factor of three (1 GHz) compared to that of its Ti:sapphire pump laser (333 MHz). Allan variance measurements of the fully phase-stabilized signal pulses from both the fundamentally-pumped and harmonically-pumped OPOs showed that the use of harmonic pumping does not substantially degrade the frequency stability of the comb. The integrated phase noise (1 Hz–64 kHz) of the f_{CEO} frequency increased by around 1-rad under harmonic pumping, with the increase arising in the 300–1000 Hz band associated with acoustic noise contributions to the resonator stability, which couples directly to f_{CEO} in a femtosecond OPO. The f_{CEO} phase noise was reduced by optimising the setting of the internal gain of the pump laser. Extension of this technique to higher repetition rates should be possible by using cavities with higher values of Q.

References

[1] K. Balskus, S. M. Leitch, Z. Zhang, R. A. McCracken, and D. T. Reid, “1-GHz harmonically pumped femtosecond optical parametric oscillator frequency comb," Optics Express 23, 1283-1288 (2015).

[2] R. Holzwarth, T. Udem, T. W. Hänsch, J. C. Knight, W. J. Wadsworth, and P. S. J. Russell, “Optical frequency synthesizer for precision spectroscopy," Phys. Rev. Lett. 85, 2264–2267 (2000).

[3] D. J. Jones, S. A. Diddams, J. K. Ranka, A. Stentz, R. S. Windeler, J. L. Hall, and S. T. Cundiff, "Carrier-envelope phase control of femtosecond mode-locked lasers and direct optical frequency synthesis," Science 288, 635–639 (2000).

[4] T. Udem, R. Holzwarth, and T. W. Hänsch, "Optical frequency metrology," Nature 416, 233–237 (2002).

[5] S. T. Cundiff and J. Ye, "Colloquium: femtosecond optical frequency combs," Rev. Mod. Phys. 75, 325–342 (2003).

[6] T. Steinmetz, T. Wilken, C. Araujo-Hauck, R. Holzwarth, T. W. Hänsch, L. Pasquini, A. Manescau, S. D’Odorico, M. T. Murphy, T. Kentischer, W. Schmidt, and T. Udem, "Laser frequency combs for astronomical observations," Science 321, 1335–7 (2008).

[7] F. Ferdous, H. Miao, D. E. Leaird, K. Srinivasan, J. Wang, L. Chen, L. T. Varghese, and A. M. Weiner, "Spectral line-by-line pulse shaping of on-chip microresonator frequency combs," Nat. Photonics 5, 770–776 (2011).

[8] S. A. Diddams, L. Hollberg, and V. Mbele, "Molecular fingerprinting with the resolved modes of a femtosecond laser frequency comb," Nature 445, 627–30 (2007).

[9] A. A. Savchenkov, A. B. Matsko, V. S. Ilchenko, I. Solomatine, D. Seidel, and L. Maleki, "Tunable optical frequency comb with a crystalline whispering gallery mode resonator," Phys. Rev. Lett. 101, 093902 (2008).

[10] D. Huang, E. A. Swanson, C. P. Lin, J. . S. Schuman, W. G. Stinson, W. Chang, M. R. Hee, T. Flotte, K. Gregory, C. A. Puliafito, and J. G. Fujimoto, "Optical coherence tomography," Science 254, 1178–1181 (1991).

[11] T. Sizer, "Increase in laser repetition rate by spectral selection," IEEE J. Quantum Electron. 25, 97–103 (1989).

[12] T. Udem, J. Reichert, R. Holzwarth, and T. W. Hänsch, "Absolute optical frequency measurement of the Cesium D1 line with a mode-locked laser," Phys. Rev. Lett. 82, 3568–3571 (1999).

[13] E. Myslivets, B. P. P. Kuo, N. Alic, and S. Radic, "Generation of wideband frequency combs by continuous-wave seeding of multistage mixers with synthesized dispersion," Opt. Express 20, 3331–44 (2012).

[14] P. Del'Haye, A. Schliesser, O. Arcizet, T. Wilken, R. Holzwarth, and T. J. Kippenberg, "Optical frequency comb generation from a monolithic microresonator," Nature 450, 1214–7 (2007).

[15] P. Del'Haye, O. Arcizet, A. Schliesser, R. Holzwarth, and T. J. Kippenberg, "Full stabilization of a microresonator-based optical frequency comb," Phys. Rev. Lett. 101, 053903 (2008).

[16] T. J. Kippenberg, R. Holzwarth, and S. A. Diddams, "Microresonator-based optical frequency combs," Science 332, 555–9 (2011).

[17] D. C. Edelstein, E. S. Wachman, and C. L. Tang, "Broadly tunable high repetition rate femtosecond optical parametric oscillator," Appl. Phys. Lett. 54, 1728–1730 (1989).

[18] G. M. Gale, M. Cavallari, T. J. Driscoll, and F. Hache, "Sub-20-fs tunable pulses in the visible from an 82-MHz optical parametric oscillator," Opt. Lett. 20, 1562–1564 (1995).

[19] B. R. Washburn, S. E. Ralph, J. K. Ranka, and R. S. Windeler, "Controlling the phase of a femtosecond optical parametric oscillator via coherent mixing of the pump-generated supercontinuum and an OPO subharmonic," in IEEE Lasers and Electro-Optics Society - 13th Annual Meeting (IEEE, 2000).

[20] D. T. Reid, B. J. S. Gale, and J. Sun, "Frequency comb generation and carrier-envelope phase control in femtosecond optical parametric oscillators," Laser Phys. 18, 87–103 (2008).

[21] D. T. Reid, C. McGowan, W. Sleat, M. Ebrahimzadeh, and W. Sibbett, "Compact, efficient 344-MHz repetition-rate femtosecond optical parametric oscillator," Opt. Lett. 22, 525–7 (1997).

[22] B. Ruffing, A. Nebel, and R. Wallenstein, "All-solid-state cw mode-locked picosecond $KTiOAsO_4$ (KTA) optical parametric oscillator," Appl. Phys. B Lasers Opt. 67, 537–544 (1998).

[23] J. Jiang and T. Hasama, "Harmonic repetition-rate femtosecond optical parametric oscillator," Appl. Phys. B Lasers Opt. 74, 313–317 (2002).

[24] A. Esteban-Martin, O. Kokabee, K. Moutzouris, and M. Ebrahim-Zadeh, "High-harmonic-repetition-rate, 1-GHz femtosecond optical parametric oscillator pumped by a 76 MHz Ti:sapphire laser," Opt. Lett. 34, 428–430 (2009).

[25] D. C. Edelstein, E. S. Wachman, and C. L. Tang, "Broadly tunable high repetition rate femtosecond optical parametric oscillator," Appl. Phys. Lett. 54, 1728–30 (1989).

[26] J.Jiang and T.Hasama, "Harmonic repetition-rate femtosecond optical parametric oscillator" Appl. Phys. B Lasers Opt. 74, 313-317 (2002).

[27] O. Kokabee, A. Esteban-Martin, and M. Ebrahim-Zadeh, "Extended-cavity, tunable, GHz-repetition-rate femtosecond optical parametric oscillator pumped at 76 MHz," Opt. Express 17, 15635–15640 (2009).

[28] T. I. Ferreiro, J. Sun, and D. T. Reid, "Frequency stability of a femtosecond optical parametric oscillator frequency comb," Opt. Express 19, 24159–64 (2011).

[29] M. Prevedelli, T. Freegarde, and T. W. Hänsch, "Phase locking of grating-tuned diode lasers," Appl. Phys. B Lasers Opt. 60, S241–S248 (1995).

[30] "iSource +TM Ultra LCR-900 Spec High Precision Source", spectratime.com.

[31] T. D. Mulder, R. P. Scott, and B. H. Kolner, "Amplitude and envelope phase noise of a modelocked laser predicted from its noise transfer function and the pump noise power spectrum," Opt. Express 16, 14186–14191 (2008).

Chapter 6. Atomically referenced 1-GHz optical parametric oscillator frequency comb

OPO frequency combs covering the near- to mid-infrared (mid-IR) region are promising sources for high-resolution spectroscopy and astrophotonic spectrograph calibration. These applications require wide mode spacing and absolute frequency traceability. This chapter reports the demonstration of a fully stabilized 1-GHz OPO frequency comb for the signal, idler and pump pulses by locking the repetition rate and the carrier-envelope-offset (f_{CEO}) of the Ti:sapphire laser, and the frequency of an OPO internal f_{CEO} beat. In this way all the outputs from the OPO and the pump laser were locked and fully stabilized frequency combs for the signal, idler and pump pulses achieved. The novelty of this work is a promising alternative locking scheme which uses an absolute optical reference at 780.2 nm for the Ti:sapphire laser f_{CEO} locking. The frequency comb of the Ti:sapphire laser is phase locked to the absolute optical frequency of the Doppler-free ^{87}Rb D$_2$ F=2-2 transition line. By referencing it to a Rb-stabilised external cavity diode laser (ECDL), we demonstrated a fully stabilized Ti:sapphire and OPO comb stable over several hours. Carrier-envelope-offset frequencies were locked within the sub-MHz linewidth of the Rb transition and more importantly without the need for supercontinuum generation.

I personally made a final design of the ECDL and improved the stability of this system which was used for the experiments presented in this chapter. The description of the Rb-locking to the D_2 transition crossover resonance of ^{87}Rb is given. In collaboration with Thomas Christian Schratwieser we were able to lock the f_{CEO} of the Yb-doped fibre laser directly to a ^{87}Rb transition line. We built the nonlinear interferometer which was used for the f_{CEO} detection and locked. Subsequently a frequency comb of an OPO was fully referenced to the Rb transition line. Together with Richard A. McCracken an atomically referenced 1-GHz optical parametric oscillator frequency comb was developed. The results were published in Optics Express [1].

6.1 Introduction

In this chapter we present an alternative approach to OPO comb stabilization, where the OPO comb was fully-stabilised when a single-tooth of the pump comb was locked to an atomically referenced single-mode CW laser (ECDL) referenced to the well-known ^{87}Rb $_2$ F=2-2 transition line. The absolute optical frequency of the ^{87}Rb D_2 F=2-2 transition is well-defined and therefore represents a traceable reference. The use of this system allows the carrier-envelope-offset (f_{CEO}) of the pulse to be acquired and locked without the need for supercontinuum generation, since nonlinear interferometer for f_{CEO} detection is not needed.

As mentioned earlier, high-repetition-rate frequency combs are becoming more in demand due to the emergence of new application fields such as spectroscopy [2, 3] and astrophotonics [4, 5], where wide mode-spacing is preferred. In these areas individual comb modes must be resolved. As we demonstrated earlier, optical parametric oscillators [6] can be used for nonlinear down-conversion into the mid-IR spectral region [7, 8]. A number of OPO combs have been experimentally demonstrated [9, 10, 11]. Normally, f_{CEO} detection of the pump pulses requires an octave spanning supercontinuum, typically generated in photonic crystal fibre (PCF [12]) [13]. In a nonlinear interferometer a second-harmonic or sum-frequency generation (SHG, SFG) light from the OPO is heterodyned with the pump supercontinuum providing a f_{CEO} beat frequency that is used for OPO stabilization [14, 10]. For this reason generating a coherent supercontinuum generation in the blue-green wavelength region is the limiting factor for achieving stabilized high repetition rate frequency combs. A sufficient peak power for the octave spanning supercontinuum generation is needed for carrier-envelope-offset (f_{CEO}) detection [15, 13]. This limitation becomes more critical at higher repetition frequencies [16]. High repetition rate modelocked lasers are available, but to achieve pulses with sufficiently short durations and high peak powers for a coherent octave-spanning spectrum becomes more challenging. On the other hand the power per comb mode increases with the repetition rate, therefore a linear based approach for f_{CEO} stabilization becomes more appropriate. The offset frequency of a Ti:sapphire laser has been locked to a CW laser via a 1064 nm iodine-referenced Nd:YAG laser [17]. Similar techniques were presented for Er:fibre comb stabilization where researchers used a 780-nm Rb stabilized ECDL [18]. In our case, the 1-GHz repetition rate Ti:sapphire laser output couples 1.4-W average power. For the f_{CEO} detection almost half of the available pump power is needed to pump the PCF and therefore the pump power focused into the OPO is reduced significantly, and consequently the tunability as the threshold stays at the same peak power level. For these reasons the use of a nonlinear interferometer becomes more difficult but the wider mode spacing ensures a higher power-per-mode which means a linear optical heterodyning becomes easier.

The chapter is organised as fallows. The experimental configuration and locking results of the ECDL are presented in the first part. An initial attempt to use an ECDL as a reference for frequency comb locking was performed with a 1030 nm Yb:fibre frequency comb operating at a pulse repetition rate of 375 MHz without using a nonlinear interferometer. Following this, I present a fully stabilized OPO comb: the pump comb is directly locked to a Rb-stabilized ECDL where the f_{CEO} of signal and idler pulses are fixed by locking their internal beat frequency [19, 20].

6.2 Rubidium stabilized external cavity diode laser

6.2.1 Locking the frequency of the external cavity diode laser

The emission line of a free running diode laser is too wide for accurate frequency locking. Moreover, the free-running diode laser is unstable in terms of its optical frequency and power. In our case this is a good thing, because this gives us the possibility to construct a tunable laser. The diode laser emission wavelength can be controlled through the temperature and current of the laser. In order to increase the wavelength selectivity, we introduced a diffraction grating

(DG), which provided considerable control of the diode-laser emission wavelength [21, 22, 23]. This additional optical element in the diode laser gives us a so called external cavity diode laser. The extension of the cavity provides wavelength selective optical feedback into the diode laser with a quality factor higher than that of the external cavity. Moreover, diode lasers have a high sensitivity to optical feedback, and their gain is only weakly dependent on wavelength. Consequently, the laser frequency can be easily steered by the injection of a few photons in the cavity. This gives us the possibility to use an ECDL for probing atomic energy states. By slightly turning the diffraction grating (DG), we can tune the diode-laser output wavelength [24]. The steering of the diffraction grating is done by a piezoelectric transducer (PZT). We can also change the temperature and current, which in conjunction with grating tuning may provide wavelength tuning over many nm.

With an active feedback loop we can control the output and stabilize the wavelength of the diode laser. For the wavelength stabilisation we used a Doppler-free absorption technique in Rubidium gas. The ^{87}Rb isotope provides well defined absorption lines, which are perfect for ECDL frequency locking and therefore can provide a stable optical frequency reference ensuring high quality f_{CEO} frequency locking.

Operating principles of external cavity diode lasers

For a diode-laser to be useful for frequency comb stabilisation, it must be single-mode and tunable. The laser must be capable of operating at a single frequency and it must be possible to vary the frequency by a certain amount. There are a lot of tunable lasers [25], but diode lasers are the best for frequency locking due to their broad gain profile and therefore tunability. They are perfect for spectroscopy applications and also cheap, small and have high gain.

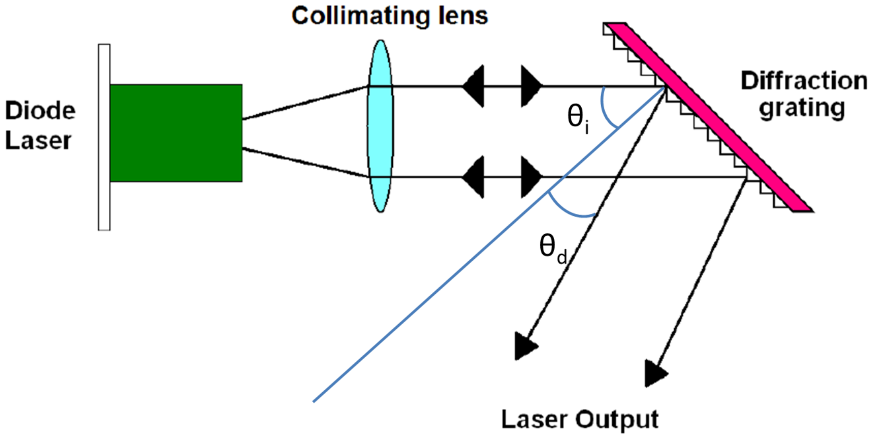

Figure 1. The ECDL design.

To make a tunable diode-laser, we need to extend the optical cavity of the laser and use optical feedback for mode selection. This is done in a Littrow configuration by using a DG placed at one end of the external cavity (see Figure 1). The DG spatially separates the light based on wavelength. The wavelength, which is sent back to the laser diode, can be varied by adjusting the angle of the diffraction grating relative to the light in the cavity. Modes coupled back into the lasing cavity interfere with each other and form standing waves. These modes in the extended cavity are enforced and other modes are suppressed. This gives us a tunable single-mode laser [26]. Moreover, the DG is oriented so that the polarisation it receives from the diode-laser is diffracted with a relatively low efficiency (<50%), leaving the zero-order beam as the useful output for f_{CEO} locking [27].

The broad semiconductor laser emission spectrum gives us the possibility to create a tunable wavelength source. The diffraction grating selects the lasing cavity wavelength, which is critical for the performance of the laser. The grating equation is [24]

$$D(sin\theta_i + sin\theta_d) = m\lambda \tag{71}$$

where λ is the wavelength, θ_i is the incident angle of the laser beam, θ_d is angle of the diffracted laser beam, $D = \frac{1}{N}$ is the distance between slits, if N is the number of lines per unit length and m is the order of the DG. In order for a light to be reflected back into the lasing cavity, the angles θ_i and θ_d have to be equal, which is known as the "Littrow configuration"

$$\frac{\lambda}{D} = 2sin\theta_i \tag{72}$$

The diffracted wavelength depends on the incident angle of the laser beam. By changing the diffraction grating angle θ_i, we select a desired wavelength to be injected back into the diode laser (see Figure 2). The external cavity diode laser amplifies only the diffracted wavelength, which gives us a much narrower linewidth of the emission spectrum than the free-running diode-laser provides itself. In the Littrow configuration the first order diffraction is coupled back into the diode laser to provide optical feedback. The diode laser output wavelength was adjusted to be around 780.24 nm and the diffraction grating had 1800 lines per mm.

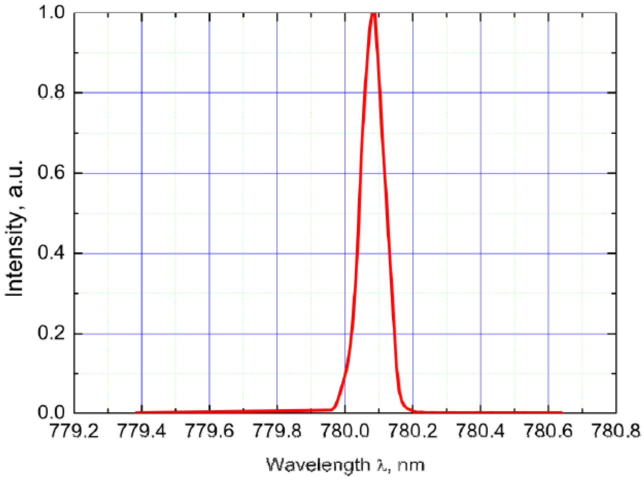

Figure 2. The spectrum of the ECDL light, showing the free-running output of the ECDL adjusted to a wavelength close to the transition of ^{87}Rb.

Frequency selective optical feedback

The most important laser characteristics determining the operating wavelength are the laser's cavity modal properties, the bandwidth and the gain of the semiconductor material. Mode properties in general are described in terms of longitudinal and transverse modes. Longitudinal modes refer to the discrete frequencies in the laser cavity. All of these modes compete with each other for gain dominance. Each mode has a Lorentzian intensity distribution with the given frequency bandwidth characterized by the full width at half maximum (FWHM) of the peak. The laser cavity free spectral range (FSR) describes the frequency spacing between these neighboring peaks.

Interacting gain and loss mechanisms determine the operating wavelength of an ECDL (see Figure 3). The semiconductor material contributes a broad gain bandwidth, while the loss is modulated by the modes of the short internal cavity formed by the semiconductor die facets and the long external cavity formed by the DG and the end facet. Single-mode operation is possible when the gain and loss curves combine to provide net gain at a single, well defined wavelength.

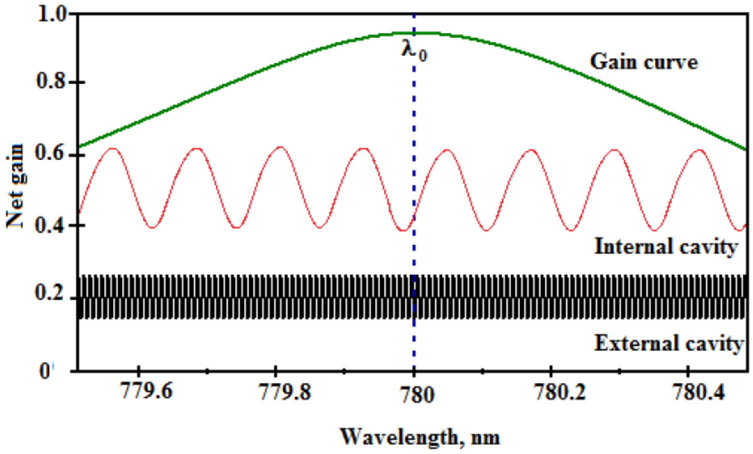

Figure 3. Schematic representation of different contributions to the net diode laser gain.

Temperature and current tuning

In addition to grating tuning, other tuning parameters are the diode laser temperature, injection current and the band-gap of the chip. The band-gap can be changed by changing the device temperature. An increasing temperature causes an expansion of the semiconductor lattice constant and slightly modifies the band-gap. The band-gap is responsible for determining the centre wavelength of the gain profile of the laser medium. When we change the diode laser temperature, we are shifting the entire gain profile by modifying the band-gap

$$E_g(T) = E_g(0) - \frac{aT^2}{T+q} \tag{73}$$

where the $E_g(0)$ is the band-gap at absolute zero, a and q are the constants for given semiconductor, T is diode laser temperature. We know that $E = h\nu$ and then

$$\lambda_0 = \frac{hc}{E_g} \tag{74}$$

where h is the Planck constant and λ_0 is the peak laser wavelength. So, by changing the band-gap, we can change the output wavelength of the diode laser.
A temperature variation may also change the optical path length (nL) of the laser cavity

$$\delta L(T) = xL(0)\delta T \tag{75}$$

where x is the thermal coefficient of linear expansion. The refractive index n also depends on the temperature

$$n(T) = n(0) + pT \tag{76}$$

where $n(0)$ is the refractive index at absolute zero and p is constant of proportionality. The last tuning parameter is the current, which alters the temperature of the laser chip through the Joule heating

$$P(I) = IR^2 \tag{77}$$

where R is the effective resistance of the laser chip and I is the injected current. By changing the injection current, we can indirectly change the temperature of the diode laser. The increased injection current also increases the carrier density within the lasing medium, affecting the refractive index. When the current reaches threshold (in our case around 40 mA), it impacts the laser only through the temperature. As the injection current changes the temperature internally, this gives us a much faster response than other tuning parameters. The injection current also changes the gain profile.

From Eq. (73) - Eq. (75) we notice that these tuning variables affect the wavelength differently, but act together. As current, temperature and grating position are varied we observe stepwise wavelength tuning – mode hopping. The laser longitudinal modes change from time to time as the laser heats up or cools down. Mode hopping appears after every degree, because the optical path length changes by about 0.06 nm/K, while the gain curve changes by about 0.3 nm/K [29]. When the diode laser temperature is changed, the gain curve and the lasing cavity modes shift at different rates. Each hop represents the slow tuning rate of the optical cavity path length over a single cavity mode or/and the hops represents the quicker tuning rate of the gain curve, which occurs through the hopping effect from one longitudinal mode to another.

The transitions of the Rubidium atom

Rubidium (Rb) is the chemical element with atomic number 37 and belongs to the alkali metal group with an atomic mass of 85.4678. It is a highly oxidizing element in air and because of that Rubidium has only one stable ^{85}Rb isotope. Another – ^{87}Rb – composes almost 28% of naturally occurring rubidium [30]. For ECDL frequency locking we used a quartz reference cell (Thorlabs GC19075-RB) containing both Rb isotopes. The ground state electronic configuration of Rubidium is $1s^22s^22p^63s^23p^63d^{10}4s^24p^6\ 5s^1$. Rubidium has only one electron in the valence shell ($5s^1$), which can interact with the light. When the valence electron jumps from one level to another, energy is released. There are two possible energy levels $P_{1/2}$ and $P_{3/2}$ [31]. This splitting into the two levels appears because of the magnetic field. The ground state has $(5p)^2P_{1/2}$ quantum numbers. The second energy level has $(5p)^2P_{3/2}$ quantum numbers. This splitting of the S=1/2 and L=1 state into two states is known as the magnetic fine structure states of the atom (J=1/2 and J=3/2). The J=1/2 represents the transition from the ground state with the wavelength of 794.9788509 nm and the J=3/2 represents the transition from the ground state with the wavelength of 780.241209686 nm [32]. The transition from the ground state to the excited state takes place only when the electron absorbs photons with right amount of energy. Our diode laser works around 780.24 nm wavelength, so we are interested only in the D_2 transition (see Figure 4). These well known lines can be used as a reference for ECDL frequency locking. In reality to lock the wavelength at the level mentioned before is extremely opsimistic since the sensitivity of the locking loop or the stability of the wavelength can be adjusted about 4 digits after point. The reproduction of the ECDL is also quit challenging since it depends on for example magnetic fields, locking loops, signal strengts, active elements used in locking loop.

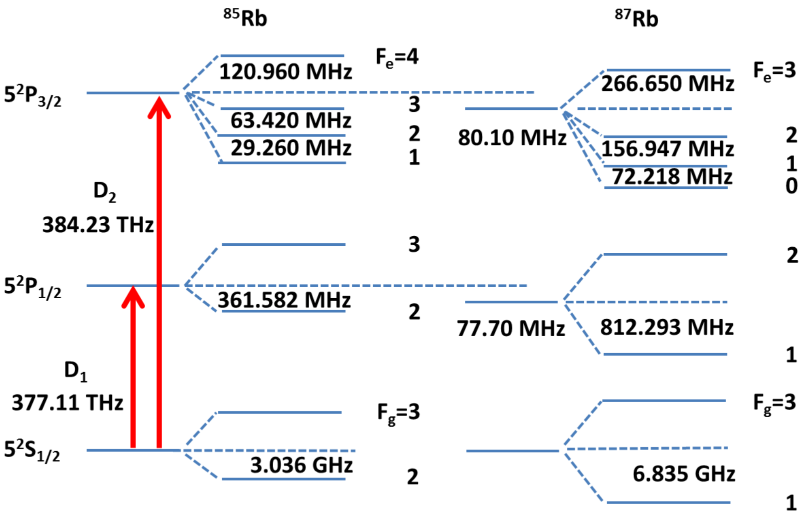

Figure 4. The hyperfine structure for the spectroscopic lines of Rb.

Moreover, the energy of the nuclear magnetic dipole moment in the magnetic field generated by the electrons and the energy of the nuclear electric quadrapole moment in the electric field gradient due to the distribution of charge within the atom causes an additional splitting of the energy levels [33]. This is the so called atomic hyperfine structure. The ground state splits into two energy levels and the excited state splits up into four hyperfine energy levels. There are only six possible transitions in each Rubidium isotope, because not every transition from ground states to an excited state is allowed. The transition rule is that quantum number F can change only by 0, +1 and -1. Some transitions are prohibited by a quantum mechanical selection rule. Figure 4 shows the hyperfine structure for absorption in Rb. When the transition from a ground state to an excited state exists an absorption spectrum may be observed. The transition in Rb vapour (^{85}Rb 72%, ^{87}Rb 28%) occurs at 780.24 nm wavelength. In the 780 nm D_2 transition we should see four peaks [31]. In order to observe these peaks, we need to continuously tune the ECDL and sweep quickly across the range of these peaks, which can be done by driving the diffraction grating angle using a piezoelectric transducer (PZT).

In Figure 5 we see four peaks known as the Doppler broadened spectrum which represent transition for both Rb isotopes. In our case we are interested only in the D$_2$ transition. There are six possible transitions from the ground states to excited states, because not every transition from ground states to an excited state is allowed. All of them consist of two sets of transitions, because we have two isotopes – ^{87}Rb and ^{85}Rb. Within each peak we have three excited states. These peaks broaden, because the Rubidium atoms are moving randomly. If Rb atoms are travelling towards an observer with velocity v_1, then the frequency, at which the transition actually occurs, f, can be calculated from the frequency at which it is observed, f_1 [34]:

$$f_1 = f[1 - \frac{v_1}{c}]^{-1} \tag{78}$$

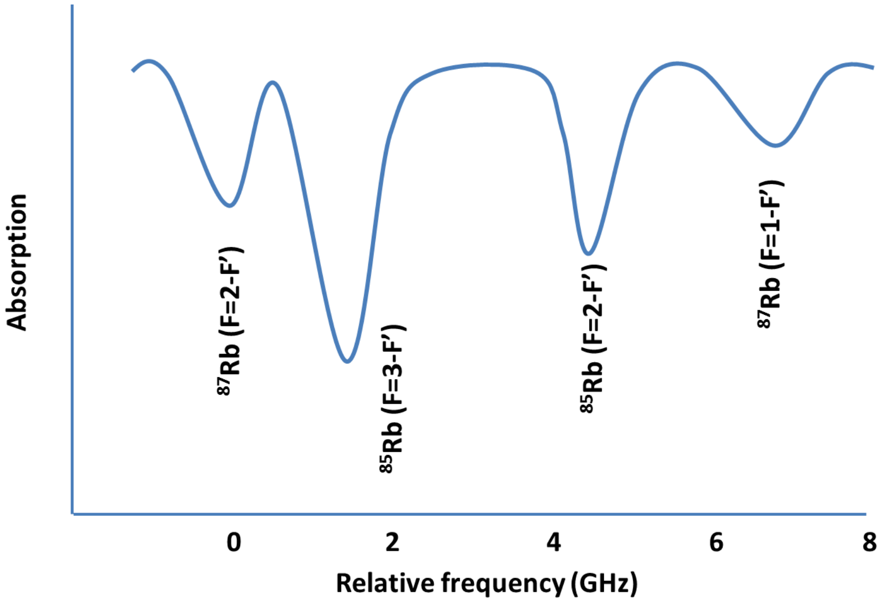

Figure 5. Doppler-free absorption spectrum of Rb D_2 transition.

This is the Doppler Effect. Rb atoms are moving in a cell and these atoms have a Maxwell velocity distribution. This results in Doppler line broadening [34]:

$$\Delta f = \frac{f}{c}[\frac{2kT\ln 2}{m}]^{1/2} \tag{79}$$

where m is atomic mass, T is temperature and k is the Boltzmann constant. This means that for some atoms the frequency of the laser light will be blue or red shifted. This causes the absorption frequency to occur either a little bit above or below the natural absorption frequency. Because the atoms are moving back and forward, there will be an absorption line broadening, which is caused by the Doppler effect.

For accurate f_{CEO} frequency locking the transition bandwidth must be as small as possible. Therefore the saturation spectroscopy has to come into play, which reduces the FWHM of the Doppler broadened peaks. This is done by reflecting the laser beam back along its incident path. The incident beam is called pump beam. It produces the Doppler broadened peaks and the counter-propagating beam is called probe beam, which samples the saturated absorption. The pump and probe beams interact at the same time in the Rubidium vapour cell with zero velocity atoms. These beams are counter-propagating to each other and the light interacts with the atoms, whose velocities are also opposite to each other. So each beam interacts with opposite sides of the Doppler profile – with the blue-shifted or red-shifted light. It depends on the propagation direction of the beam. When the probe and pump beams interact with different sets of atoms at the same time, they do not have an effect on each other. But not all the atoms move. Some of the atoms have zero velocity for both beams. Then the probe and pump beams interact with the same set of atoms. As the result, the probe beam absorption is reduced at one frequency along the Doppler broadened peak. The photodiode will indicate that the absorption of the light is reduced and the intensity will go up as the scan reaches the transition of the zero velocity atoms. This happens, because the stronger pump beam will excite zero speed atoms and the absorption of the probe beam will be reduced and the photodiode (PD) will see a stronger signal at certain frequencies. On the screen we will see small dips called Lamb dips, which corresponds to the absorption frequencies of the zero velocity atoms. This gives us the natural linewidth of the atomic transition, which has a Lorentzian lineshape. The Lamb dips are much narrower and more suitable for precise frequency locking [34].

The average frequency for the D_2 transition is 384.23 THz (780.24 nm). All other hyperfine peaks will have an offset from this one. The ^{87}Rb excitation from the F=2 ground state was used to lock the external cavity diode lasers wavelength at 780.24 nm [35].

Cross-over resonances

It is important to notice, that in a saturated absorption spectrum, a sharp signal increase is obtained at frequencies halfway between two different hyperfine transitions (see Figure 6). Those cross-over peaks appear between each real absorption peak and arise when there is more than one hyperfine transition. The cross-over resonances are obtained, because the laser beam has the possibility of interacting with two different velocity atoms at the same time. The diode laser frequency will be Doppler shifted to both transitions of the atom at the same time. The spacing between the hyperfine transitions results in the possibility for the single beam to interact with atoms moving in the opposite direction for the cross-over peak to appear. It means that the light is blue shifted and red shifted depending on the propagation direction of the atoms. We can excite two different hyperfine transitions with the same pump beam at the same time. We have two different hyperfine transitions, but it is impossible for single mode diode laser to be red shifted and blue shifted to the same transition frequency. Moreover, we have not only the probe beam, but also the saturating beam. Each of them will interact with two groups of atoms moving in opposite directions. As a result, we have four groups of atoms since probe beam interacts with +v_1 and -v_2 velocity atoms, while saturating beam with -v_1 and +v_2 velocity atoms. Here -v_1=-v_2 and v_1=v_2 since the frequency of the probe and saturating beam is the same. We have a situation where the probe and saturating beam interact with the same set of velocity atoms. As a result a cross-over occurs when a single mode laser frequency interacts with -v velocity atoms (red shifted, $f_1 = \frac{f_L}{1-\frac{v}{c}}$) and with +$v$ velocity atoms (blue shifted, $f_1 = \frac{f_L}{1-\frac{v}{c}}$) at the same time. The measured frequency of the diode laser will be $f_L = \frac{f_1+f_2}{2}$, which results in a cross-over peak placed halfway between each hyperfine transition.

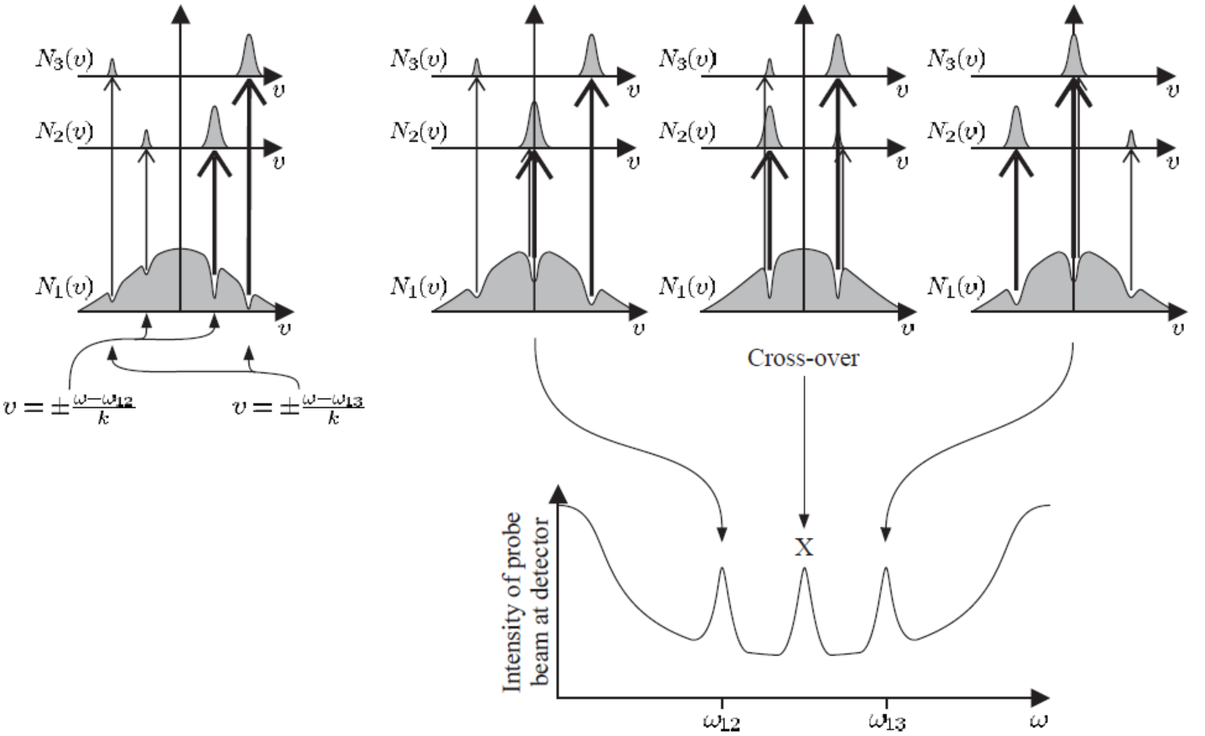

Figure 6. A cross-over resonance occurs at X which is the midway between two saturated absorption peaks. At the cross-over the hole burnt by the pump beam acting on transition 1-2 reduces the probe beam absorption on transition 1-3, and vice versa [37].

The pump beam has two sharp decreases depending on the velocity. This corresponds to an appearance of two peaks in the pump spectrum when the laser frequency overlaps with those two transitions. This is what we expect to happen. In reality, an additional peak appears. A hole caused by one transition reduces the absorption for the other transition. The symmetry of this situation means a cross-over. It occurs exactly midway between two saturated absorption transitions. When data are taken, we are measuring the crossover resonance.

Dither locking of the ECDL

The dither locking technique allows us to lock the laser output power or in our case the output frequency of the external cavity diode laser. The ECDL frequency was locked to the ^{87}Rb D_2 transition. In order to lock it, first we must monitor the frequency change and then control it to ensure the stability of the variable [36, 38, 39].

Dither locking is based on modulation by a signal with a known amplitude, phase and frequency. This modulation signal is transferred into the output signal obtained from PD. In our case this low amplitude modulation signal introduces a small voltage amplitude modulation on the PZT. Therefore we can see a small amplitude modulation on top of the Rb gas absorption spectrum. In this way this modulation signal is directly transferred into the output signal on top of the Rubidium absorption line. This is the key for frequency locking. On other hand this introduced modulation signal must be as small as possible, because using a small amplitude modulation ensures the smallest possible frequency noise in the system.

In our external cavity diode laser the PZT is attached to the DG and the modulation signal to the PZT is provided through a frequency generator (FG). The diode laser output spectrum is monitored with a Si photodiode (PD). The diode laser beam goes through the Rb gas cell and therefore is absorbed by Rb gas. On the oscilloscope we see six absorption peaks (see Figure 7).

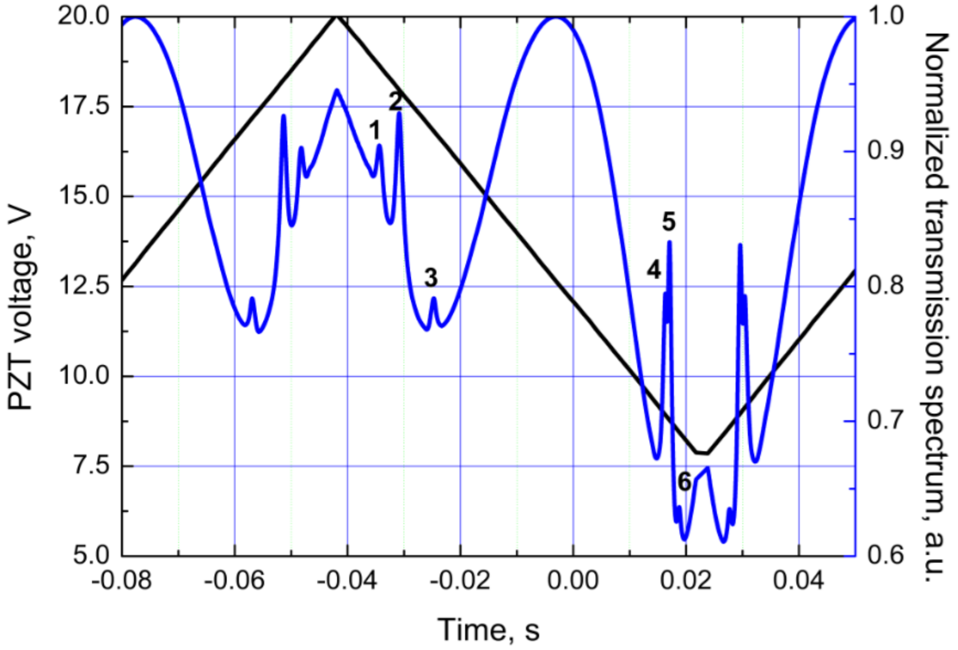

Figure 7. Measured absorption peaks of ^{87}Rb from the F=2 ground state (left) and ^{85}Rb from the F=3 ground state (right): (1) corresponds to the transition F=2-1; (2) F=2-2; (3) F=2-3; (4) F=3-2; (5) F=3-3; (6) F=3-4.

When the dither locking technique is used for frequency locking, a clear error signal is needed. Let's say we have Gaussian-form absorption lines:

$$P_z = \exp^{\frac{-(z-z_0)^2}{2v^2}} \tag{80}$$

where z_0 is the PZT position at zero point, z is the offset of the frequency from zero position and v is the variance. As we can imagine, the diode laser output signal is not stable in frequency – the output frequency is always moving around zero. This zero position of the frequency is marked by a Rb gas absorption line at 780.241209686 nm. When the temperature in the room is changing, the laser diode temperature changes too and then we can see a slow output wavelength drift from zero position. The feedback loop locks and actively corrects the frequency drift by the PZT. The voltage variation changes the wavelength returned by the DG to the laser cavity and therefore it amplifies photons at this zero position. All other photons except photons at 780.241209686 nm are suppressed. The required wavelength will occur at the voltage setpoint level and will increase or decrease as the output wavelength tries to drift from the zero position (780.241209686 nm). In this way, spectral or temperature fluctuations of the ECDL are compensated to maintain maximal possible accuracy of the output wavelength.

Once the PZT displacement is brought within the locking range of a feedback loop, locking to the zero of the signal derivative will always coincide with the edge of the output intensity (see Figure 8). The locking range will be limited by the amplitude of the dither signal, but the smaller modulation amplitude minimizes the frequency fluctuation, resulting in lower frequency noise. Any temperature or air current fluctuations must be minimised to maintain passive frequency stability of the external cavity diode laser.

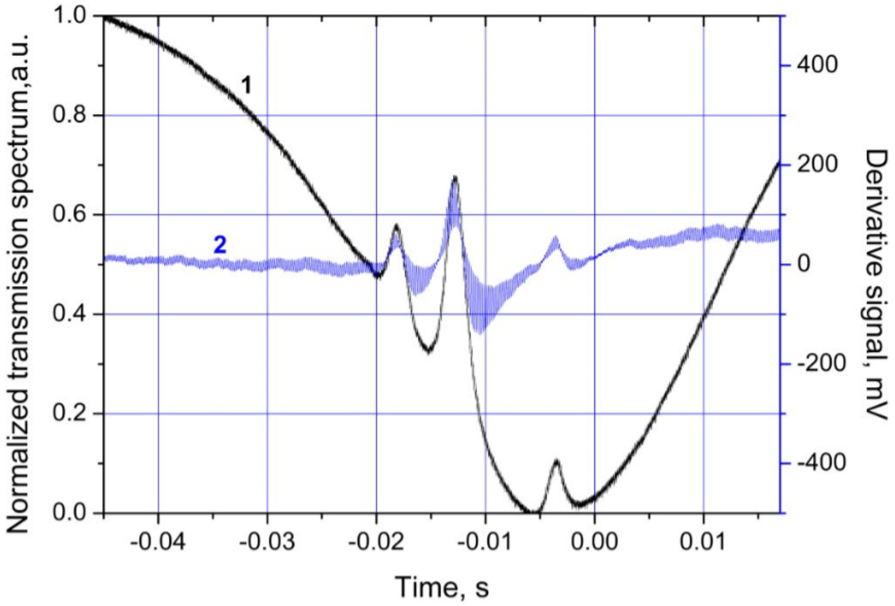

Figure 8. Transmission peak (1) with the low pass filtered derivative signal (2) from the mixer.

The applied dither frequency voltage was about 240 mV. A higher amplitude signal with lower frequency – in our case 8 Hz – was applied on the PZT in order to resolve the absorption peaks. The applied low frequency voltage amplitude on the PZT was 15 V to be sure that the right absorption line of the Rb gas was selected for dither locking. When the right peaks have been identified, the 8 Hz frequency signal amplitude was reduced from 15 V to 0 V until the locking to the exact peak could be ensured. A small drawback of dither locking is that there always will be some fluctuations in the intensity of the peak used for locking.

6.2.2 Experimental configuration of the ECDL

Optical design

The light source in the ECDL system was an AlGaAs diode laser which operated at around 780.2 nm wavelength. For this diode laser the Thorlabs LD1255R driver was used as a low noise power supply. Also 200μ F and 100 nF capacitors were placed in parallel to the diode laser to reduce any fluctuations in the injection current. The 200 μF capacitor acts as a charge reservoir, ensuring that if the current demand is high and or sudden then this can be provided without being limited by the power supply. The 100 nF capacitor works as a high-pass filter. If there is high frequency noise from the power supply, it will not reach the diode. Therefore the capacitors improve the diode laser stability and can ensure the performance of the ECDL. The injected current was adjustable and monitored by the voltage across a 10 ohm resistor (see Figure 9).

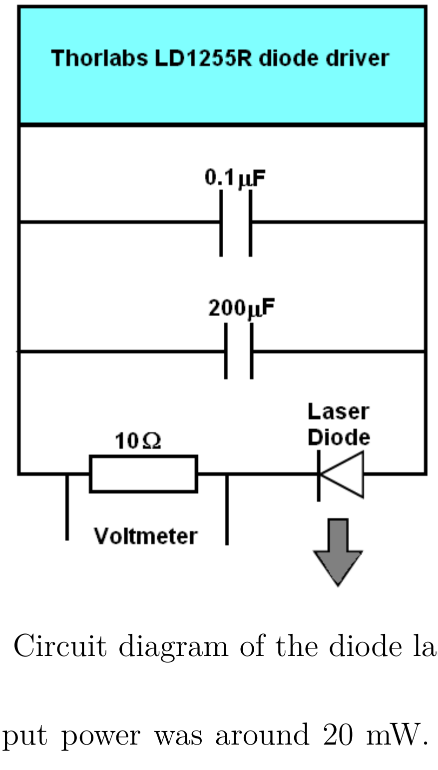

Figure 9. Circuit diagram of the diode laser driver.

The diode laser maximum output power was around 20 mW. The light from diode laser was collimated using an aspheric lens and the polarization was oriented in the vertical axis. The polarization of the diode laser light was parallel to the lines of the DG to maximise the reflection efficiency and the wavelength tunability [24]. The kinematic mount, which consisted of the diode laser, collimator and DG, was placed onto a Peltier element to improve heat conduction and stabilise the temperature of the ECDL (see Figure 10). By changing the temperature we could control the diode laser emission spectrum. The temperature was optimised to give the smoothest tuning over the 780.2 nm wavelength and at the same time the most stable output.

For the temperature monitoring we used a thermistor. The thermistor and Peltier element were connected to an Arroyo Instruments temperature controller. With the controller we changed the temperature of the mount and stabilised the temperature at 24.88 celsius.

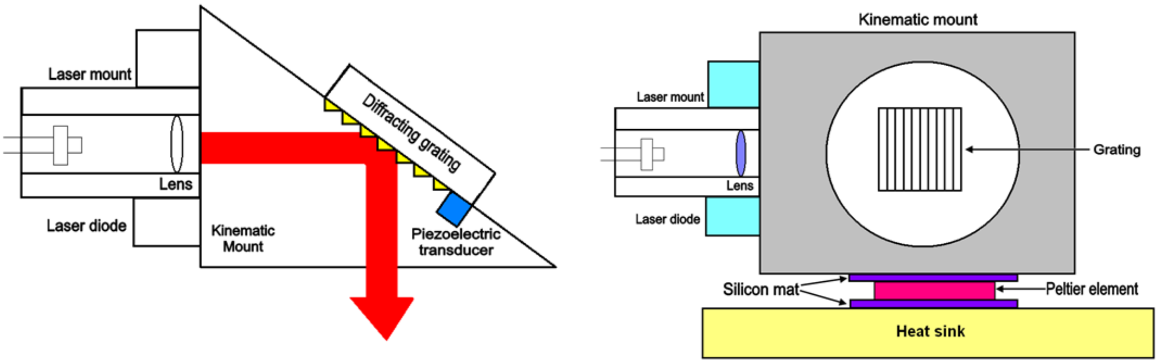

Figure 10. ECDL design.

The DG had 1800 lines per mm and was glued into the kinematic mount. There were two adjustment screws which provided rough adjustment of the DG position. For fine adjustment we used a piezoelectric transducer (PZT), which allowed a maximum of 9.1 μm displacement of the grating. This allowed us to change the diffracted wavelength back into the diode laser to lock the output frequency of the diode laser. By varying the voltage on the PZT, we were able to change the output wavelength untill it overlapped with the Rubidium gas absorption lines. Then the dither signal for the frequency locking on the PZT was introduced by the P-I controller. Because the voltage from P-I controller can be negative, an additional positive voltage source was connected. This ensured that the PZT would never receiver an overall negative voltage. This is important, because a PZT can be damaged by a negative voltage. This positive low noise offset voltage was introduced by a Tektronix PWS 4323 power supply. All voltage sources were connected into series to provide a net positive voltage to the PZT.

Zero-order reflected light from the DG passed through a LINOS isolator. This optical element blocks light which is reflected back into the ECDL, which could damage the diode laser or destabilize the frequency locking. After the isolator the output entered a half-wave plate $\frac{\lambda}{2}$. This wave plate rotates the light's polarization and reduces the intensity of light which is used for the observation of the absorption lines. Only a small fraction of the light is needed for saturation in the Rb gas cell. The majority of the laser output was transmitted. We used a glass window with reflectivity of around 1%. The rest of the light is transmitted by the glass and can be used for f_{CEO} locking. After the Rubidium gas cell the light hits the beamsplitter (BS). This BS reflects half of the light back into the Rb gas cell. The path of the incident and reflected beams are the same. Only then we can see Rb gas absorption lines on the oscilloscope. The remaining part of the light after the BS is reflected on to the Si photo detector (see Figure 11). After optical optimisation, the ECDL frequency locking was achieved. By observing the Rb gas absorption spectrum peak, the ECDL frequency was stabilized. We used an 8 Hz

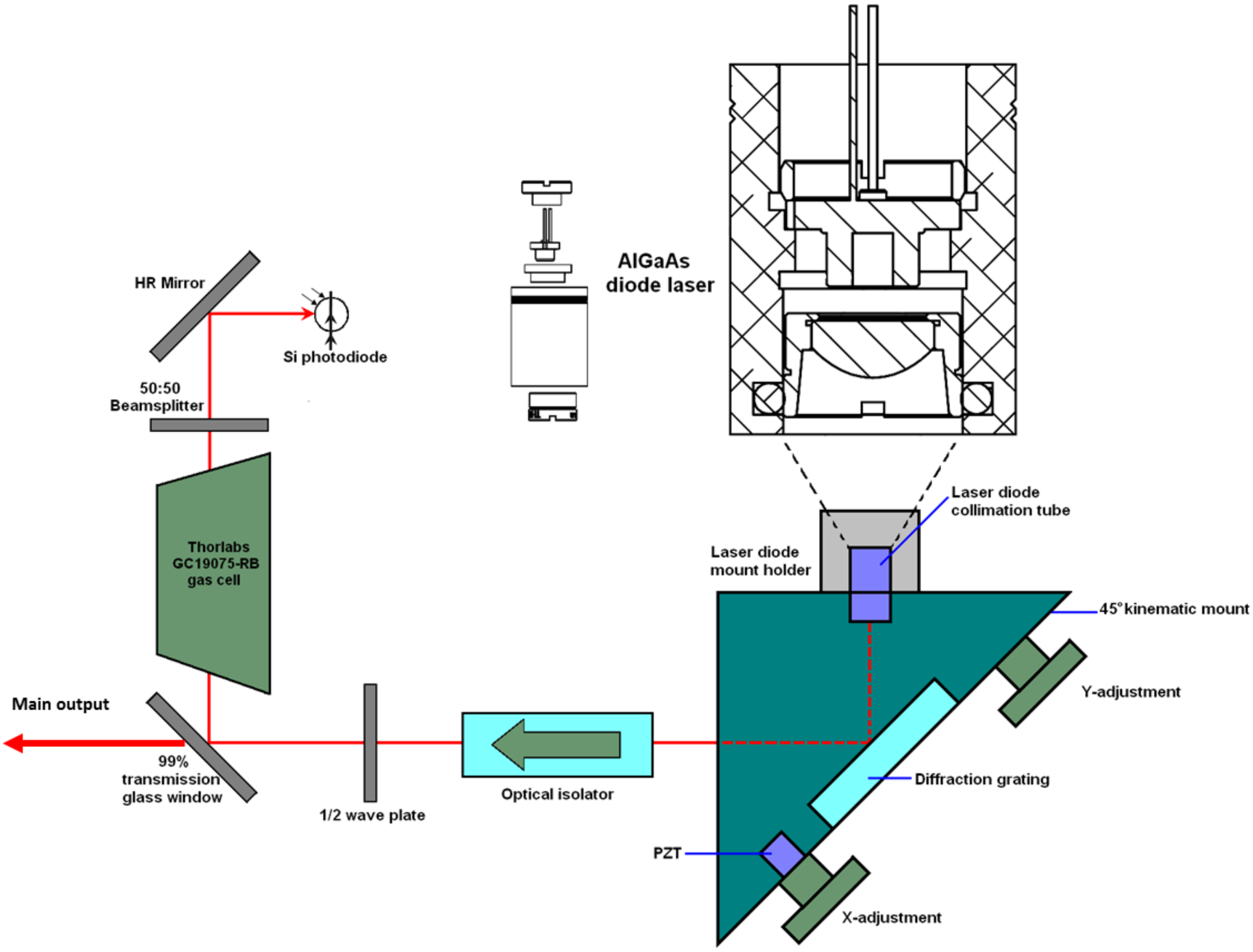

Figure 11. Optical configuration for frequency locking of the ECDL.

frequency and 15 V amplitude triangular signal to scan the voltage on the PZT. This slow scan helped to find the right absorption lines. The current of the diode laser was also varied to find the absorption lines. Finally the system was enclosed with a box in order to increase the temperature stability of the ECDL and protect it from air currents (see Fig.12).

Frequency locking

The frequency locking of the ECDL was achieved by using a New Focus LB1005 Servo Controller. This is a proportional-integral (P-I) amplifier. It has a slow sweep, an input for the derivative signal from the mixer and a modulation input on the back for the modulation frequency. For the slow sweep we used a TG215 function generator. The triangular (8 Hz frequency and 15 V amplitude) signals were used for the initial observation of the Rb gas absorption lines, but were turned off for locking. A 7455-Hz modulation signal was generated in a low noise SRS lock-in amplifier (SR810 DSP) and introduced into the P-I controller through the modulation input channel on the back of the controller. The fast modulation signal amplitude was 0.24 V. This modulation signal could be seen on the top of the slow scan frequency from the P-I controller (see Figure 13).

We can see the 7455-Hz frequency modulation on top of a slow 8-Hz frequency scan. This low

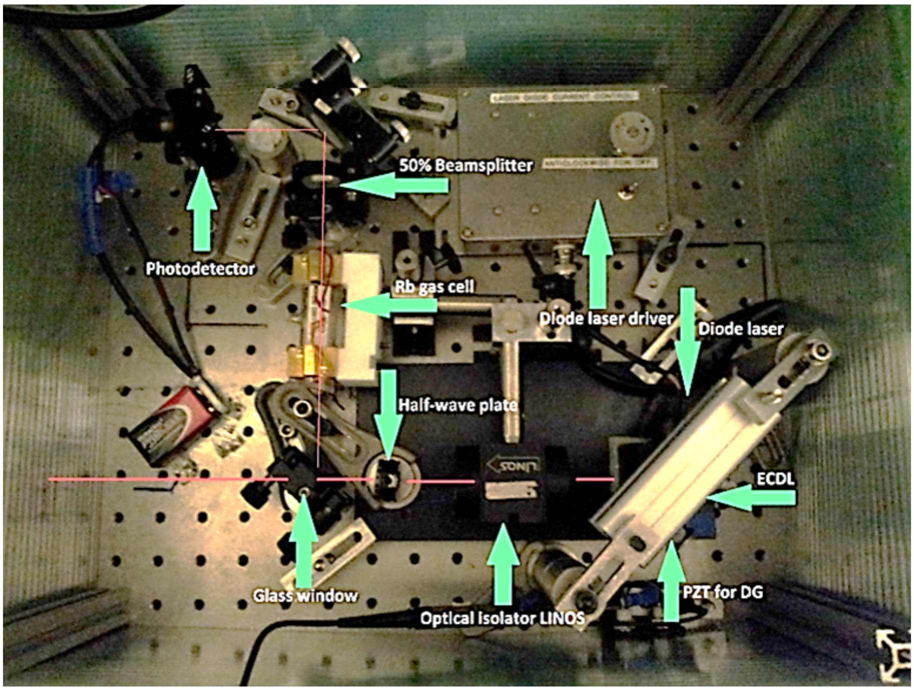

Figure 12. ECDL system from top.

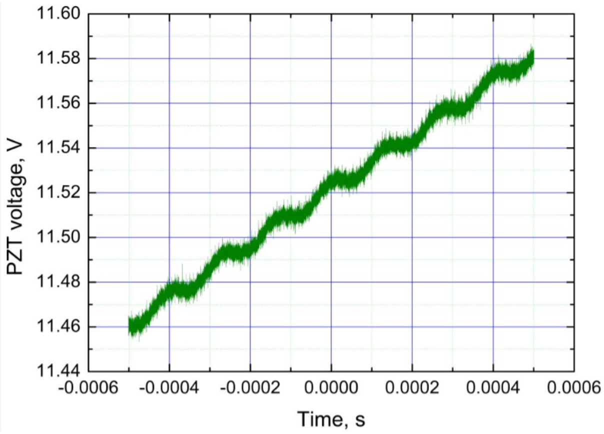

Figure 13. 7455 kHz modulation signal on top of the slow scan.

amplitude modulation signal is the main key to achieving the frequency locking. This signal from the lock-in amplifier was split into two channels – one of which was directed into the P-I controller and another which was used as an input for a mixer. Before mixing both signals, they were high-pass filtered (HPF), to get rid of the low frequency signal. To ensure that the strongest derivative signal was achieved, the gains for both inputs in the mixer were adjusted. We also used inverting amplifiers to match the phases of these two modulation signals before they were mixed. After the mixing a low-pass filter (LPF) was used to get only the error signal with no modulation frequency. The derivative signal was used as the input into channel –B on the P-I controller. The output voltage from the P-I controller was used for the ECDL frequency locking. The feedback loop for ECDL frequency locking is shown in Figure 14.

When the Rubidium gas absorption peak was in the middle of the scan, the sweep was smoothly turned down till only the peaks from ^{87}Rb were monitored (see Figure 15). Then the offset from

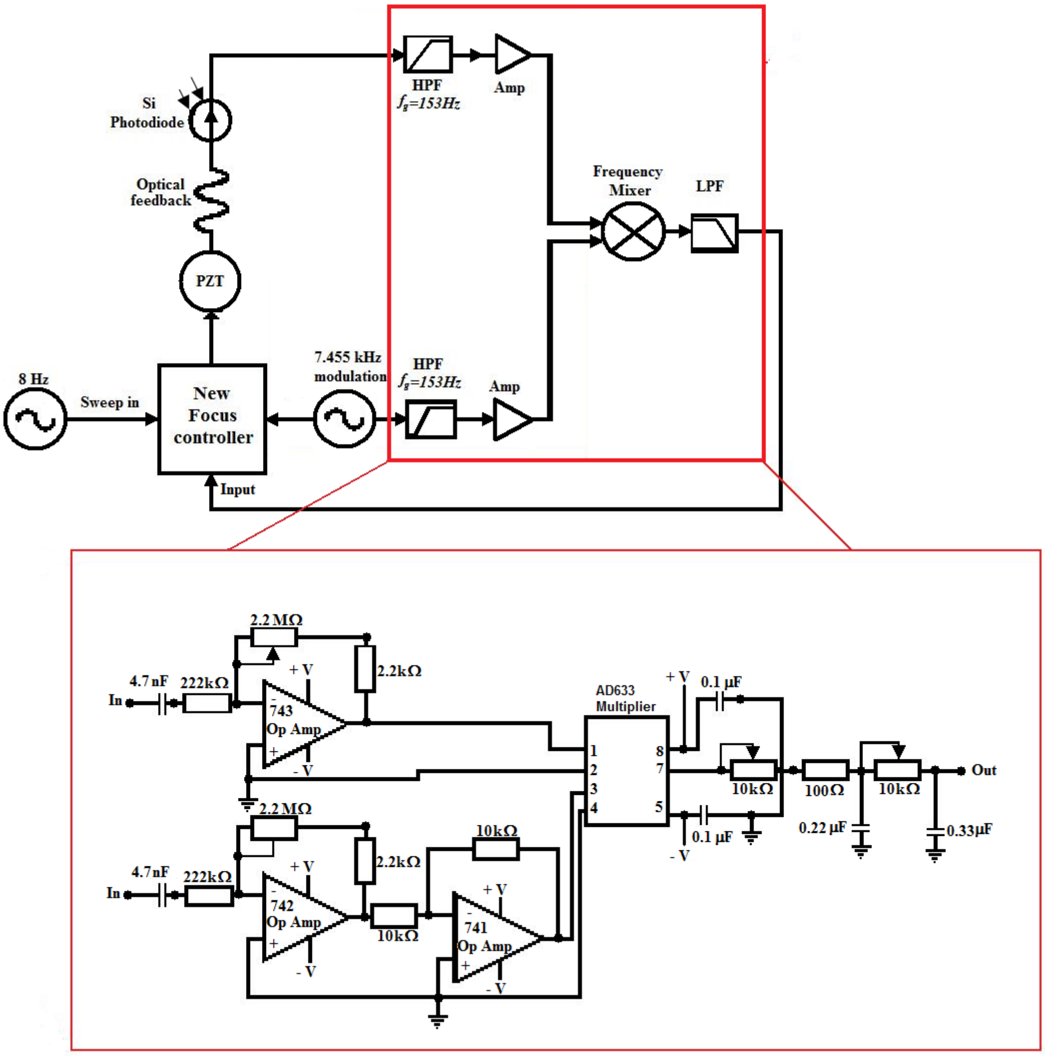

Figure 14. Feedback loop for ECDL frequency locking.

low noise DC power supply was adjusted to bring the strongest peak into the middle position of the scan. The scan was further reduced until only the derivative of the observed Rb gas absorption peak was in the middle of the scan. At that moment the offset on the P-I controller could be used to adjust the position of the derivative signal.

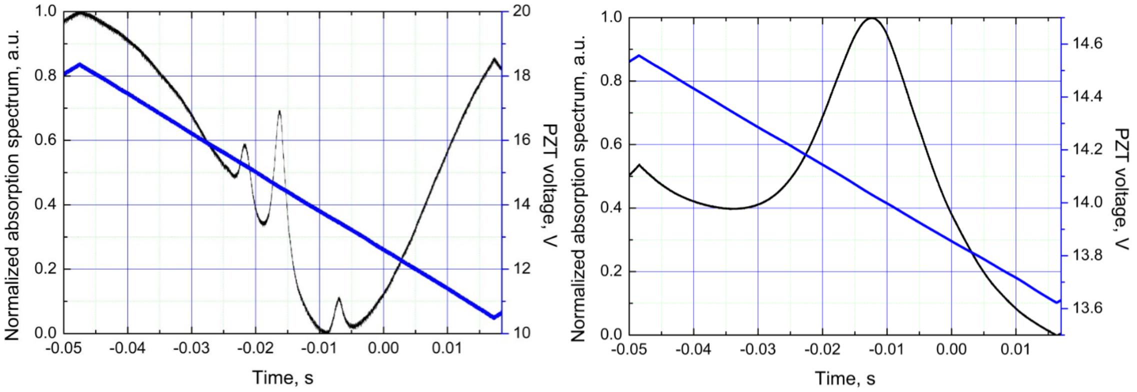

Figure 15. The observed Rb gas absorption peaks, when the scan amplitude was 8 V (left) and 1 V (right).

The scan was reduced further on the oscilloscope until there was only a small fraction of the absorption peak observed. Then the feedback loop was closed by switching the P-I controller to the LFGL position to initiate frequency locking. When the P-I corner frequency and the gain are optimal, the P-I controller locks the frequency of the diode laser immediately. The scan was fully turned down and the P-I controller switched into the "Lock-On" mode. Once locked on the oscilloscope we could see a stable flat line at the same level where the maximum of the absorption peak was observed. This indicated that we locked at the right absorption peak. By knocking on the table we could easily see that the ECDL system remained locked. A disturbance can be seen, but the system adjusts accordingly (see Figure 16). The feedback loop is able to hold the frequency locking properly without any jumps from one peak to another. When the system is not properly adjusted mode hopping can be observed.

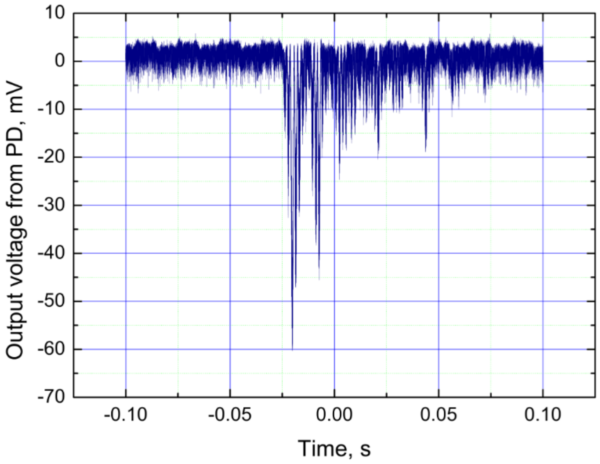

Figure 16. Output voltage from PD showing that the system can easily absorb an external disturbance without losing the locking.

6.2.3 ECDL locking results

When the ECDL frequency was locked, it could remain locked for at least 24 hours. The main reason why we cannot increase the locking time is the wavelength drift caused by the temperature drift in the laboratory. The temperature should stay always at 20 C, but the temperature stabilisation system is imperfect. The real temperature can fluctuate by around 1-2 C. By using the PZT we can stabilize the wavelength, but the P-I controller was limited by its voltage range, which was 10 V. The ECDL system was much more stable in terms of frequency during the weekends. At that time there is less equipment which is turned on than during the weekends increases much more slowly. In order to maintain the temperature at 20 C the temperature stabilisation system turns on less frequently than during working days. This gives us longer time periods before the cooler comes into play. It is pretty convenient, because during working days the wavelength of the diode laser always moves to one side of the frequency and in the morning the wavelength is on the other side of the 780.2 nm wavelength central position. During weekends the wavelength varies much less. The quality of the frequency locking was determined by recording the relative intensity noise (RIN) and cumulative standard deviation measurements. The cumulative standard deviation reflects the locking stability at certain frequencies. For proper ECDL frequency locking the standard deviation should be as small as possible, which is particularly important for the f_{CEO} locking, because the noise from the ECDL frequency locking can be transferred to f_{CEO} locking noise. High RIN and high cumulative standard deviation increase the noise of the f_{CEO} locking. The instability of the diode laser frequency increases the uncertainty in f_{CEO}. We have two different feedback loop controllers. The LaseLock is a digital one and the New Focus one is analog. The Laselock gives us the possibility to change the modulation signal frequency and amplitude. LaseLock also contains a function generator for a slow loop scan. It even has a mixer and low pass filter, which provide us with the derivative signal for ECDL frequency locking. Moreover, the LaseLock gives us the possibility to vary independently proportional P, integral I and derivative D coefficients. This is an advantage compared with the analog New Focus LB1005 servo controller. By introducing an external disturbance into the locking loop, we can find the best PID parameters. This is the reason why first we tried the digital controller. We used a 4 degree wedged mirror and a 40 mm focal length lens to focus part of the light into the Si photo detector. The recorded light was observed on an Agilent Infiniium 54833A oscilloscope. Time spans of 1 to 200 seconds were used to calculate the RIN and the cumulative standard deviation (Figure 17).

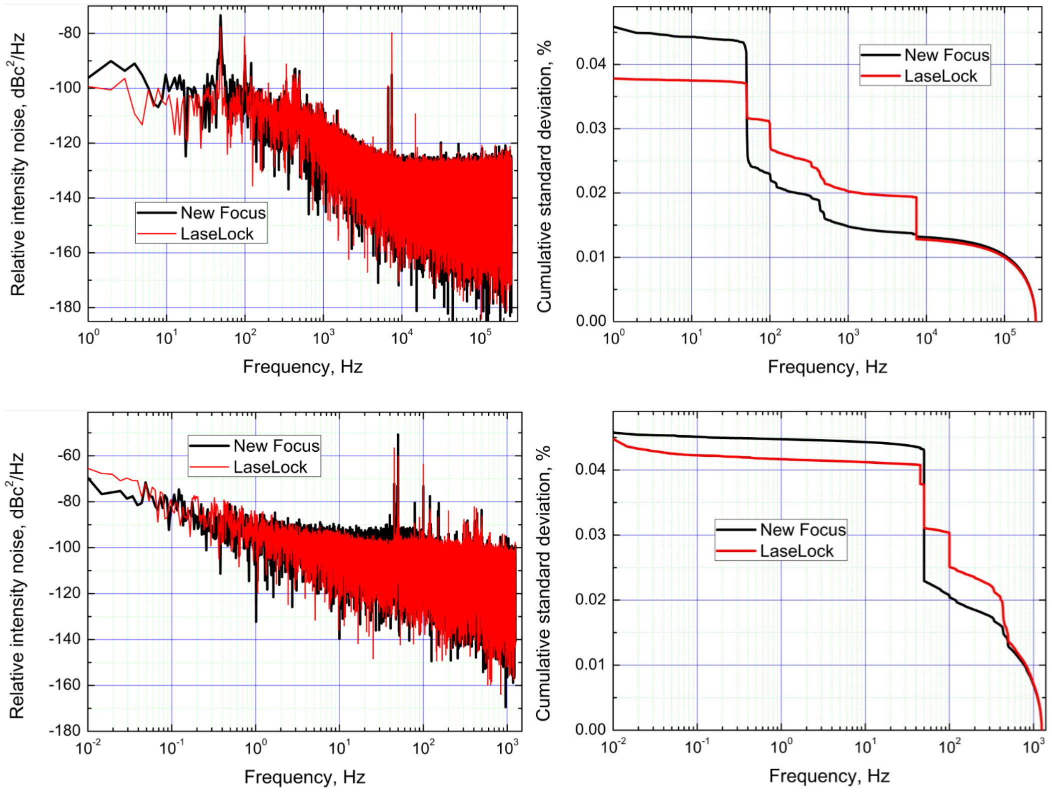

Figure 17. The RIN measurements from locked ECDL. The left axis shows frequency-dependent relative intensity noise to the frequency and the right axis shows the cumulative standard deviation of the RIN data. (top) Results for a 1 second data acquisition. (bottom) Results for a 200 second data acquisition.

When the frequency of the ECDL system was locked, we changed the modulation frequency till we found the strongest derivative signal. The strongest derivative signal was observed at 7455 Hz frequency and this frequency value was used for frequency locking with the analog New Focus LB1005 servo controller. The relative intensity noise and the cumulative standard deviation were the same. The 1 second data acquisition shows us that the biggest noise peaks arise in both cases from the mains at 50 Hz and 100 Hz, and at the modulation frequency of 7455 Hz. With both controllers the measured cumulative standard deviation for 1 second and 200 seconds data acquisition time was 0.04 %. When longer data acquisition times were used, other noise peaks at lower frequencies than 100 Hz were observed. The noise at 50 Hz could be suppressed by using batteries. The only bad thing is that the batteries do not last forever.

The ECDL system was located on a table which was not an optical bench. It was easy to see that the locked system was very sensitive to mechanical vibrations. There was a working air conditioner over the ECDL system all the time. These air currents also had an effect on the quality of the frequency locking as the temperature varied in the laboratory. Still, it was a convenient way to compare analogue and digital controllers.

After some time the ECDL system was placed on the optical bench. This suppressed mechanical vibration and the system was better protected from direct air currents. Moreover, further PZT improvements were implemented. We used a small piece of steel to increase the PZT resistance from the screw tip. This slowed down the response time of the PZT, but increased the PZT lifetime. By the use of screw we ensure that the PZT is always in contact with the diffraction grating. We also increased the overlapping area between the PZT and the DG. On the other end of the PZT we placed double-sided sticky tape and a washer. All these small improvements increased the ECDL frequency locking quality in terms of mechanical vibrations and temperature fluctuations (see Figure 18).

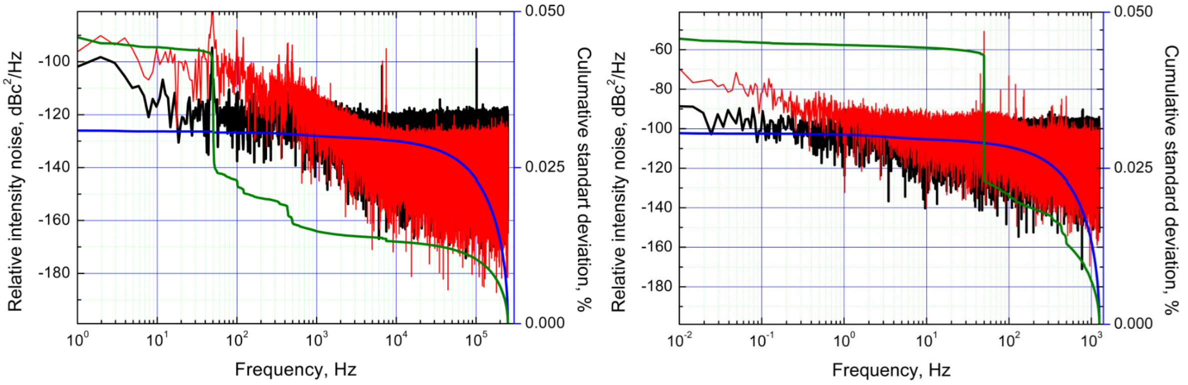

Figure 18. Results for a 1 second data acquisition. (Right) Results for a 200 second data acquisition. Black and blue colors represents RIN and deviation measurements after improvements. Red and green represent data before improvements.

The ECDL frequency locking could not be maintained for a longer time than before. On the other hand we increased the noise at higher frequencies, but this is not so critical in our case. For us the biggest problem was the locking sensitivity to mechanical vibrations and temperature fluctuations, which we suppressed. The diode laser output wavelength was always less sensitive to the diode current variations or noise from the mains. Instability was always more associated with the temperature fluctuations and mechanical vibrations. These small improvements led to better long term frequency locking stability. The relative intensity noise at lower frequencies was reduced by sacrificing lower noise at higher frequencies.

Once the frequency of the ECDL system was locked an external disturbance was implemented into the locked system. This gave the possibility to find the best parameters of the controllers for proper frequency locking. For this we used a GW Instek GFG-8015G signal generator. We used a 17 Hz square-wave signal to disturb the ECDL frequency locking through the PZT. The disturbance signal amplitude was increased up to 300 mV. When the disturbance of the PZT was in place, the signal from controller output was monitored on the oscilloscope. The disturbance was implemented for both feedback loop controllers. For LaseLock and New Focus controllers the PID parameters were changed directly till the best response was achieved. In Figure 19 we see a disturbance signal and the response for an analogue New Focus LB1005 servo controller.

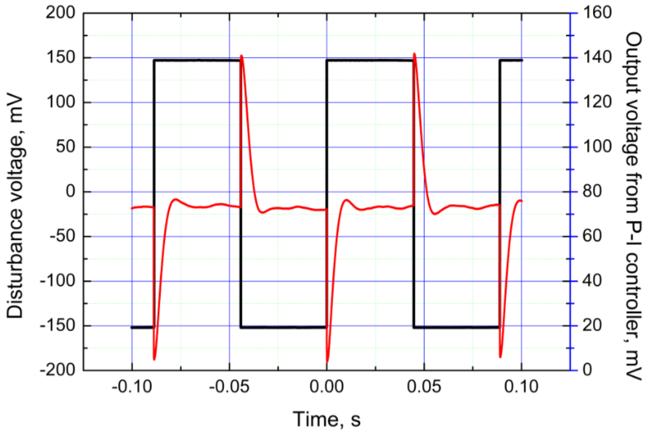

Figure 19. ECDL frequency locking optimisation by using external disturbance. Black line represents external disturbance signal and red line – output voltage from New Focus controller.

The response of the PZT depends on the proportional P, integral I and derivative D coefficients. These three coefficients were changed in the LaseLock separately till the best response was achieved. In the case of the New Focus LB1005 servo controller, we have only two options - P-I corner frequency and the gain. If the P-I corner frequency was too high the PZT response had more fluctuations, because the voltage on PZT has been increased too quickly. The response lasted for a shorter time period but with oscillations. If the P-I corner frequency was too low, the response was too slow – it was hard for the New Focus controller to maintain the frequency at zero position. The response of the P-I controllers was found to be much slower. The response curve covers a much longer time period and it was not good for proper frequency locking. This could cause a bigger f_{CEO} phase noise. On other hand we have the gain coefficient. If the gain was too low the disturbance signal causes the P-I controller to increase the voltage on PZT by a much bigger value. Slower response is again not a good thing for proper locking.

Then the system has bigger frequency drift and it can more easily lose the frequency locking. The best results were achieved by leaving P-I corner frequency at 1000 Hz, LF gain limit at 20 dB, the gain at 5.55 and the input offset at 4.82. The output from the New Focus controller was optimized for stable ECDL frequency locking. The ECDL system could easily stabilize the frequency even after a hard knock on the table without losing the locking. The modulation signal amplitude from the lock-in amplifier was as small as 240 mV. The ECDL stability was confirmed by heterodyne beating two ECDL lasers light on the APD. The acquired signal was stable within 1 MHz region at RBW=100 kHz.

6.2.4 ^{87}Rb stabilized 375-MHz Yb:fibre femtosecond frequency comb

When the ECDL was ready, an alternative to the nonlinear self-referencing method for f_{CEO} locking was investigated. A femtosecond 375 MHz Yb:fibre laser comb was referenced to the Rb stabilized ECDL [40]. The experimental configuration of the experiment is presented in Figure 20. The Yb:fibre laser was built by Dr. Thomas Schratwieser and Dr. Cal Farrell.

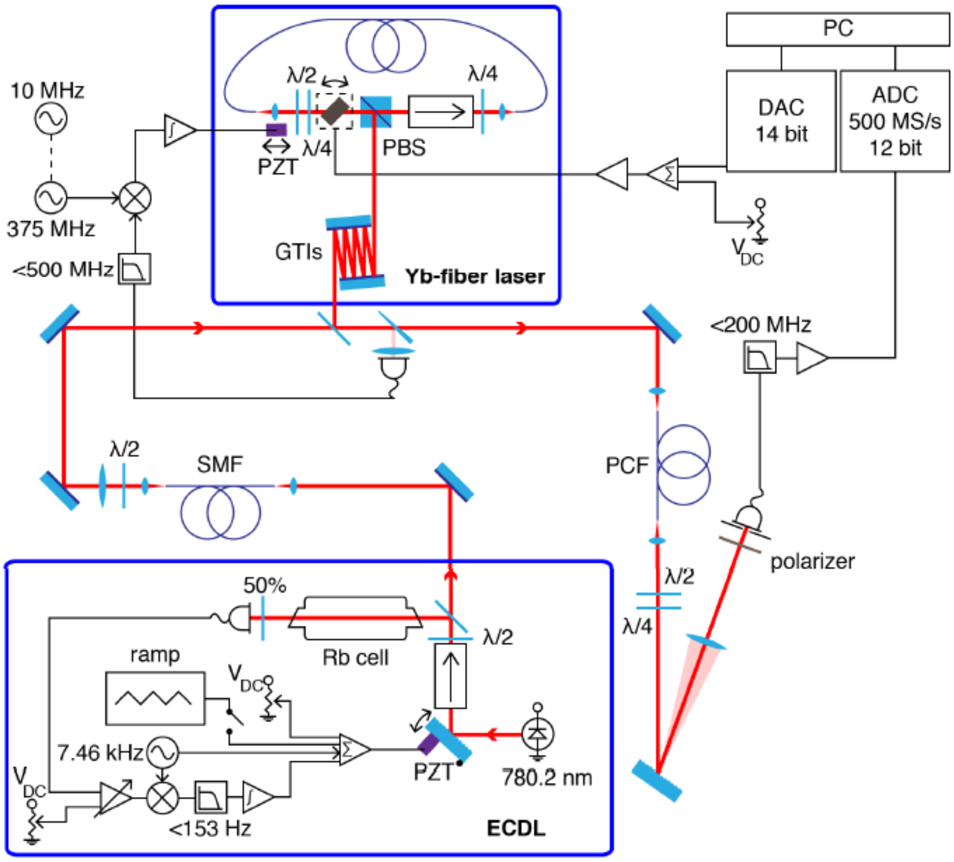

Figure 20. Configurations of the Yb:fibre laser and Rb-referenced ECDL (upper and lower blue boxes) and the comb stabilization scheme. PBS, polarizing beamsplitter; PC, personal computer; DAC, digital to analog converter; ADC, analog to digital converter [40].

The sampled repetition frequency f_{REP} was low-pass filtered (LPF) and mixed with a 375 MHz signal from a synthesized signal generator to give an error signal for the PI controller whose output was connected to a piezo-electric transducer (PZT). In this way the repetition rate was stabilized. A 5.8 mHz Allan deviation was measured for a 50-second averaging time (in-loop measurement). For full frequency comb stabilization, the f_{CEO} of the pump laser also had to be locked. The ECDL presented earlier was locked to the ^{87}Rb D_2 F=2-2 transition line at 780.2 nm by using the dither locking technique. The absolute frequency of the transition is 384,227,981.9 MHz [35]. The Rb stabilized ECDL light was combined with the Yb:fibre laser light in a 1.5 m photonic crystal fibre (NKT SC-3.7-975) via a dichroic beamsplitter (HR 1030 nm, HT 780 nm).

High peak power fs pump pulses at 1030 nm were extended using supercontinuum generation to the visible generating a coherent 10 nm bandwidth component at 780 nm. With this laser it was too challenging to generate an octave spanning and coherent spectrum for f_{CEO} to be stabilised using self-referencing. By implementing an ECDL, a coherent beat between the sub-octave supercontinuum and the ECDL could be acquired. An efficient heterodyne beat was ensured by implementing quarter- and half-wave plates before a monochromator containing an 1800 lines mm^{-1} diffraction grating and 500 mm focal lens. A heterodyne beat was detected using an avalanche photodiode (APD) placed in the focal spot of the lens. The detected f_{CEO} of the Yb:fibre laser was isolated with a 200 MHz LPF, amplified and acquired by a 12-bit analogue-to-digital converter sampling 2048 points at 500 MS/s resulting in 244 kHz frequency resolution. An algorithm compared the acquired frequency with a set-point and accordingly provided an error signal through a 14-bit digital-to-analogue converter. This signal was used to actuate the angle of the intracavity dielectric filter placed inside the Yb:fibre laser. A galvomotor tuned the filter angle causing a carrier-envelope-offset f_{CEO} frequency change at a rate of 150 MHz mrad^{-1}. The stability of the locked frequency comb f_{CEO} is presented in Figure 21. The locking the f_{CEO} of the pump obtained by heterodyne beating the Rb-ECDL with the comb, which contained not only f_{CEO}, but also and uncertainty in f_{REP}. The heterodyne beat contains not only the $_{CEO}$ of the pump as it was done earlier. Still, since the f_{REP} is locked, the biggest impact comes from the f_{CEO} uncertainty which was locked to the Rb-ECDL.

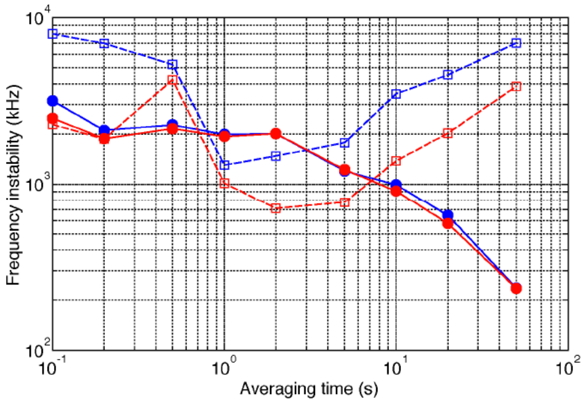

Figure 21. The RMS deviation (blue) and two-sample frequency deviation (red) of the comb-offset beat signal for comb-offset stabilization turned on (filled symbols) and turned off (open symbols). The data were recorded while the repetition frequency of the Yb:fibre was stabilized [40].

The Allan deviation and RMS deviation for multiple averaging times were calculated when f_{REP} was locked. We measured better frequency stability at longer averaging times and poorer at shorter time gates. The noise at lower averaging times appeared because the galvanometer motor experiences 100 µrad level disturbance due to internal noise. This periodic modulation introduced an additional noise to f_{CEO}.

In Figure 22 we present a long term stability measurement of the locked frequency comb. The blue symbols corresponds to the fluctuations of the unlocked f_{CEO} while the green symbols correspond to the locked comb heterodyne frequency fluctuation relative to the mean of f_{CEO}. The air conditioning cycling was responsible for the unlocked heterodyne beat oscillation. As we locked the system, the f_{CEO} could remain stabilized about a set-point for at least 60 minutes. An Allan deviation of 235 kHz was calculated where the RMS was 236 kHz. In comparison the unlocked heterodyne beat was fluctuating by up to 10 MHz. The fractional frequency stability with a 50 second gate time was $6.1e{-}10$ which is by one order of magnitude greater than presented in a previously reported Rb stabilized Er:fibre system [18]. The f_{CEO} of the pump was measured in-loop which is relative phase noise measurement since it does not take into account the reference instabilities.

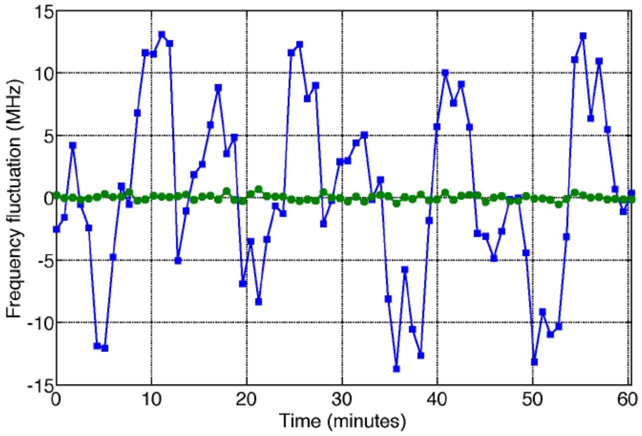

Figure 22. Comparison of the fluctuations in the beat frequency relative to the mean with comb offset stabilization turned on (green symbols) and turned off (blue symbols) for averaging times of 50 s over a period of 60 minutes. All data were recorded while the repetition frequency of the Yb:fibre was stabilized [40].

6.3 Atomically referenced 1-GHz optical parametric oscillator frequency comb

With the ECDL stabilized to a Rb transition line, a well-defined optical frequency was available which could be directly heterodyned with the 1-GHz Ti:sapphire laser comb. The acquired beat frequency was stabilized resulting in a locked Ti:sapphire OPO pump frequency comb. The locking scheme and results are described below. The characteristic noise of the locked carrier-envelope-offset (f_{CEO}) frequency is also presented.

6.3.1 A Rb-stabilized Ti:sapphire frequency comb

An interferometer was constructed in order to obtain the f_{CEO} beat frequency between the Ti:sapphire laser and the Rb stabilized ECDL. Before locking the f_{CEO} of the comb, the f_{REP} was stabilized and the ECDL locked to Rb transition. Therefore by beating the comb with ECDL, we are obtaining the fluctuations of f_{CEO}. The experimental configuration is shown in Figure 22. In order to lock the f_{CEO} of the pump pulse, a beat frequency between a pump comb line and single mode diode laser locked to the F=2-2 transition (384,227,981.9 MHz [35]) must be acquired. For this reason an interferometer was developed. A partial reflector was used to synchronously couple 95% of the pump power (Gigajet, Laser Quantum, 1 GHz, 1.4 W, 30 fs) into an OPO based on a 1.2 mm PPKTP crystal (Raicol Crystals). The OPO output was tunable from 1.1-1.6 μm producing 80-fs pulse duration signal pulses. The remaining 5% (0.07 W) of the power was coupled into a 2-m length of FC/APC single-mode patch core fibre (P3-630AR-2). The Rb stabilized ECDL light was coupled into the same type of fibre. The fibre had an angled input facet since it was necessary to avoid feedback to ensure stable diode laser performance. The beams were combined using a 50/50 beam-splitter (BS). After the light reached a DG (Thorlabs, GH25-24V), it was spectrally dispersed. To ensure efficient diffraction and a suitable power balance between the two arms, half-wave plates were introduced into the two channels before the BS. A 750-mm focal length lens focused the beams onto the APD (APD210). A slit placed before the APD was used to ensure a maximum of 30 modes beating on the APD.

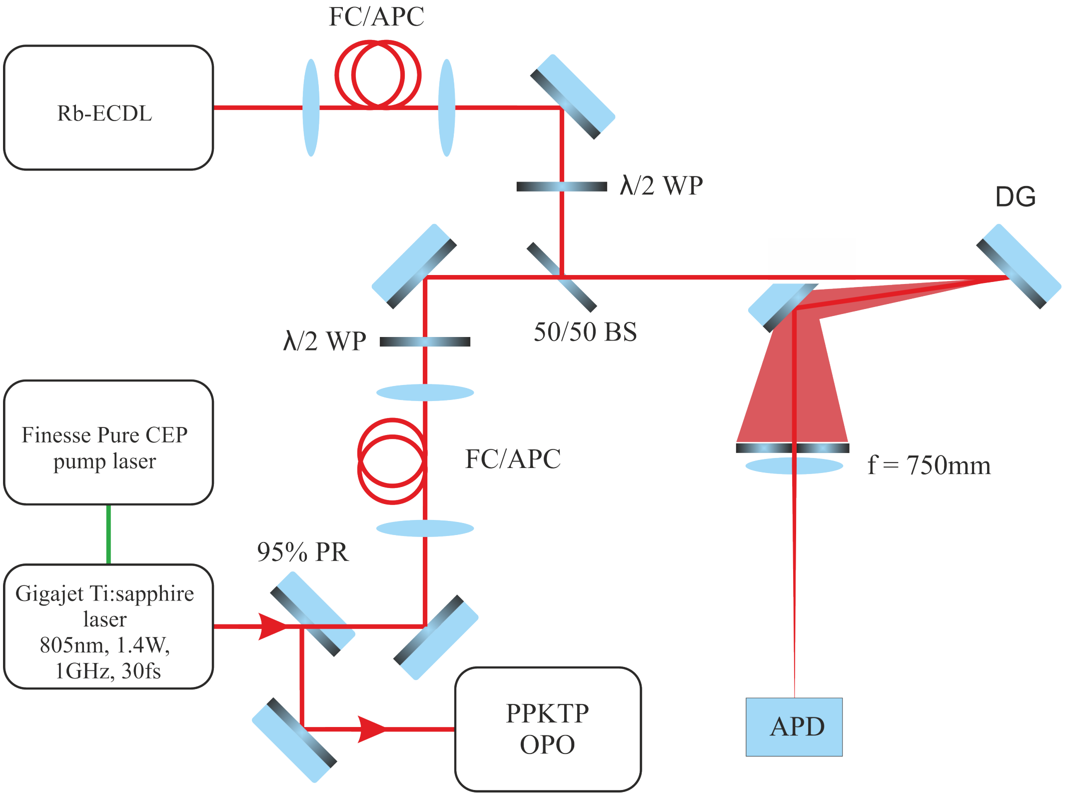

Figure 22. Optical schematic of the Ti:sapphire and Rb-ECDL interferometer. APD, avalanche photodiode; BS, beam spliter; DG, diffraction grating; FC/APC, angled fibre patch cord; PR, partial reflector; WP, waveplate.

Figure 23 presents the electronic locking loop for f_{CEO} frequency locking of the Ti:sapphire laser. The signal from the APD was low-pass filtered (Minicircuits, VLF-400+) to remove frequencies above $f_{REP}/2$. The filtered signal was amplified by 20 dB (Farnell, THS3202EVM) and mixed (in a Minicircuits ZP-3) with a strong (+10 dBm) signal from a synthesized signal generator (SSG, Agilent 8664-A) to produce a frequency at around 10 MHz. This 10 MHz difference frequency was amplified by 20 dBm and low-pass filtered (Minicircuits, BLP-30+). This LPF signal was introduced into one channel of a comparator (Pulse Research Labs, PRL-350TTL) to produce the square wave signal which is necessary for the phase frequency detector (PFD). The reference 10 MHz signal was taken from the same SSG and passed through a comparator to provide a reference frequency for the PFD. As a result, the output from the PFD was varied according to the frequency difference between two signals. The output from the PFD was plugged into a proportional-integral amplifier (Newport, New Focus LB1005) which provided the error signal for the Ti:sapphire f_{CEO} comb stabilization. The f_{CEO} was locked via diode current modulation of the Finesse Pure pump laser.

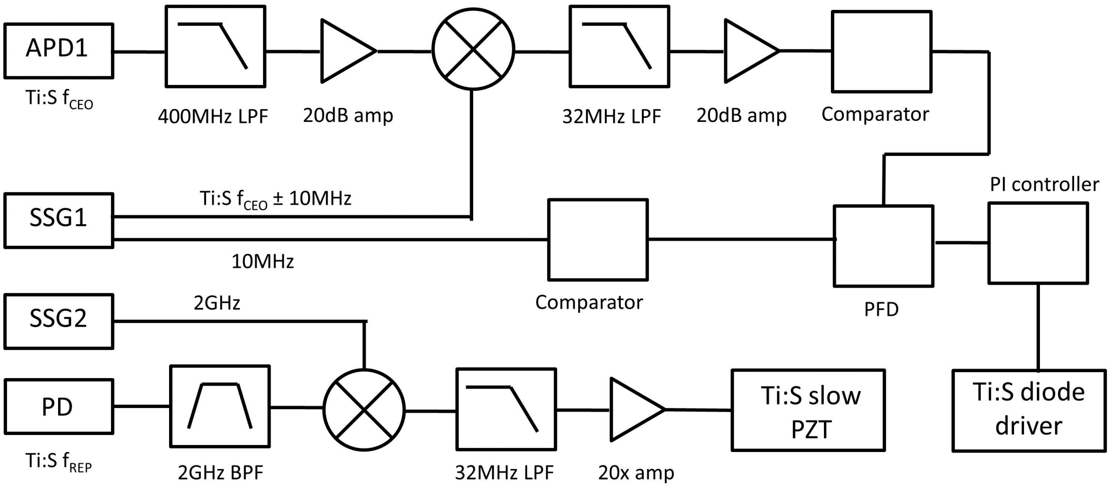

Figure 23. Locking loop for Rb-ECDL stabilization of the Ti:sapphire laser frequency comb. APD, avalanche photodiode; BPF, band-pass filter; LPF, low-pass filter; PD, photodiode; PFD, phase frequency detector; PZT, piezo-electric transducer; SSG, synthesized signal generator.

6.3.2 Stabilization of an optical parametric oscillator frequency comb

After the f_{CEO} of the Ti:sapphire laser was locked to a Rb transition line, we attempted to lock the 1 GHz OPO in a similar way. As we demonstrated earlier, for the f_{CEO} locking of the OPO we do not need a PCF. We simply need to generate an output from the OPO at 780 nm wavelength so that we can detect the beat between the OPO and the ECDL locked to the Rb transition line. If the signal wavelength of the OPO is oscillating at 1560 nm, parasitic or phase-matched SHG can be generated in the PPKTP crystal. The only problem is that the Ti:sapphire pump pulse bandwidth also reaches 780 nm, which means we cannot separate SHG and pump light since they share the same wavelength. We tried to output couple the signal pulse and externally frequency double it to 780 nm, but these attempts were unsuccessful due to the low average powers achievable at 1560 nm (<20 mW). An alternative approach was therefore employed.

An investigation was launched into whether a beat between the Rb stabilized ECDL and the OPO SHG (f_{CEO-2S}) could be achieved. Light exiting an OPO folding mirror was focused into the FC/APC fibre previously used for the Ti:sapphire beat detection, as shown in Figure 24. A second APD2 (Hamamatsu, APM-400, 0.042 mm^2 active area) was placed in the spectrometer so that both beats could be locked simultaneously by employing different RF filtering processes.

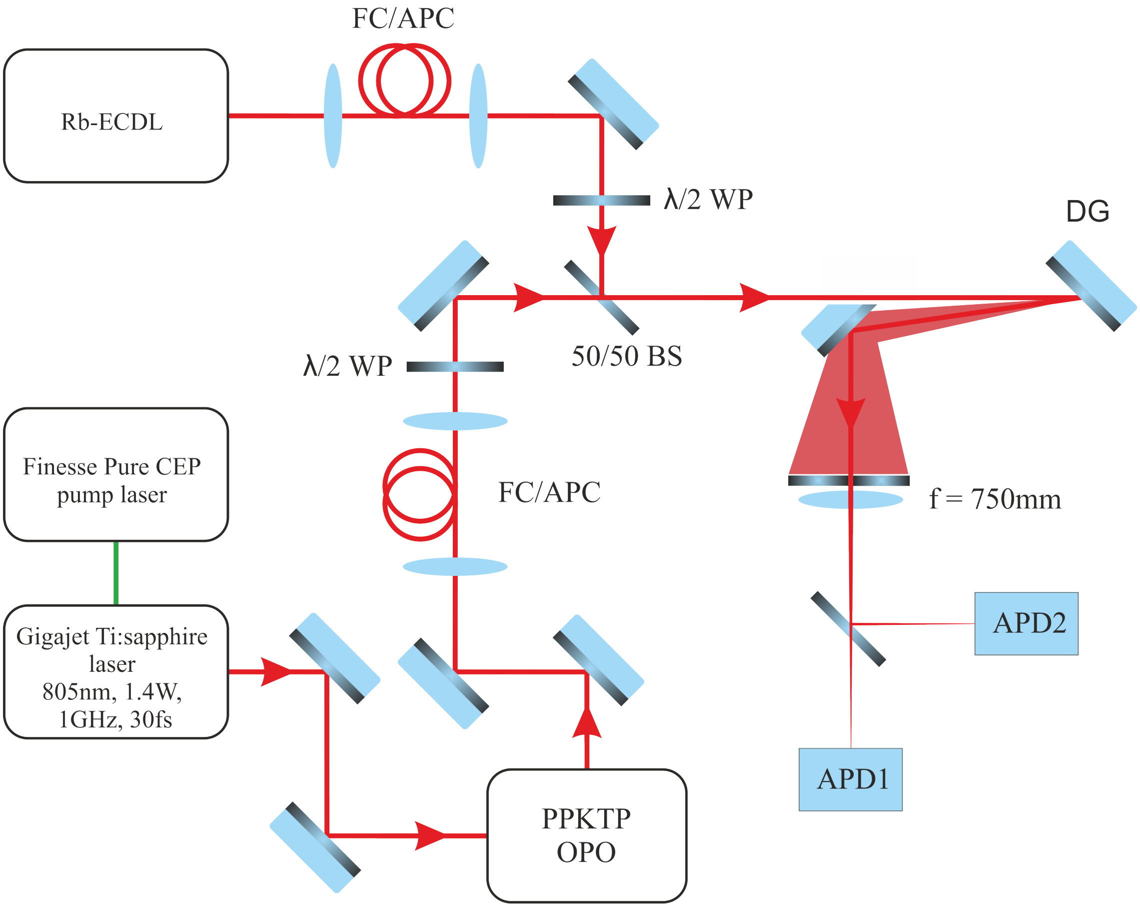

Figure 24. Modified spectrometer configuration for simultaneous Ti:sapphire and OPO locking to the Rb-ECDL.

The signals on both APDs were optimized by changing the OPO cavity length. When there was no oscillation in the OPO, only pump light left the OPO and entered the mode-matching fibre. The same beat strength was detected as demonstrated with one APD (see earlier sub-section). After this, the OPO cavity length was tuned to a signal wavelength of 1560 nm. The resulting RF trace is shown in Figure 25(a). There are two pairs of beat frequencies - one stable (the Ti:sapphire laser f_{CEO}) and one very mobile (the OPO f_{CEO-2S}). Moreover, even by blocking the Rb stabilized ECDL light we could not get rid of the mobile beat (see Figure 25(b)). The mobile beat arises due to a spectral overlap between the idler and signal wavelengths close to 1560 nm. Near 1560 nm both waves can oscillate in the OPO cavity resulting in an internal beat which is evident on the APD. A small change in cavity length ΔL causes a Δf_{CEO} change. If the $f_{CEOpump}$ of the pump pulse is stabilized, the conservation of energy [41] requires that the non-resonant idler $f_{CEOidler}$ frequency must shift by $-\Delta f_{CEO}$. This means that the internal beat is changing by $2\Delta f_{CEOinternal}$. Therefore our acquired heterodyne beat shift is mobile. Moreover, near degeneracy the resonant signal and non-resonant idler pulses are frequency doubled in the PPKTP crystal and the overlap in wavelength results in an internal beating at 780 nm wavelength ($f_{CEO(SHsignal)}$-$f_{CEO(SHidler)}$). Frequency doubling means that $f_{CEOinternal}$ changes twice as fact. It means that the ΔL change in the cavity length will result in a $4\Delta f_{CEOinternal}$ change at 780 nm. The acquired internal beat prevents the detection of a separate beat against the Rb stabilized ECDL. On other hand, this beat can be used for the stabilization of the entire system. By locking the Ti:sapphire laser to the Rb stabilized ECDL and separately stabilizing the internal beat of the OPO, we could stabilize the $f_{CEOpump}$ of the pump, signal and idler pulses without the need for a PCF.

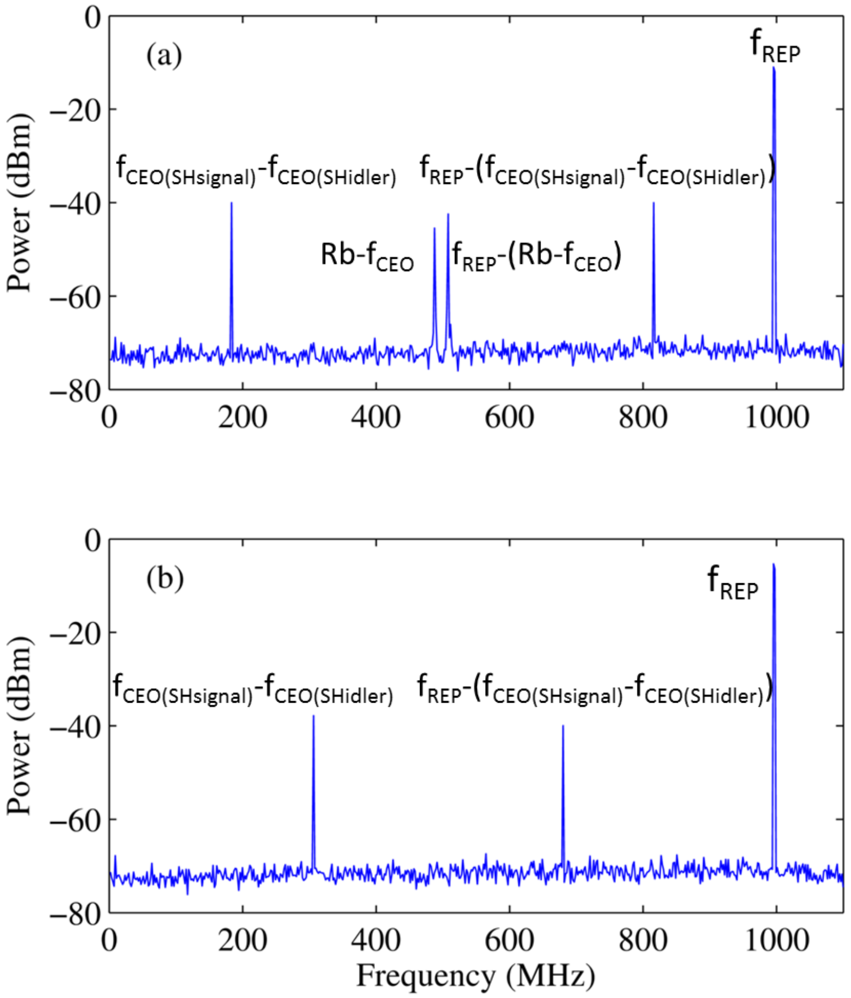

Figure 25. (a) Beat between Rb-ECDL and collinear pump and SHG signal beam; (b) Collinear pump and SHG signal beam only, with the remaining beats at 300 MHz and 700 MHz due to an OPO internal beat between signal and idler pulses.

This rapidly moving internal beat, while strong, moved too fast to be captured by the locking electronics. A frequency divider (HMC394LP4) was used to increase the capture range of the locking circuitry by reducing the frequency excursions by a factor of n=8. This divider greatly improved the stability of the locking, which could be maintained for many hours at a time without loss due to the 8x increase in the capture range of the locking loop. The stability of the heterodyne beat improved by several orders of magnitude.

6.3.3 Locking quality and noise characterization

After the repetition rate of the Ti:sapphire laser was stabilized, the detected f_{CEO} beat was passively stable. The slowly drifting beat frequency was mixed down below 30 MHz, because of the operational region of our electronics. The locked beat is presented in Figure 26. The bandwidth of the locked beat note was about 1 MHz, which is what we expected since the linewidth of the Rb transition is around 500 kHz. The quality of the Ti:sapphire comb lock was investigated via a phase noise power spectral density (PSD) measurement at the output of the PFD (Figures 26 and 28). The stability of the locked comb was determined by taking Allan deviation measurements [42] over several different gate times (Hameg, HM8123). The calculated Allan deviations are presented in Figure 29.

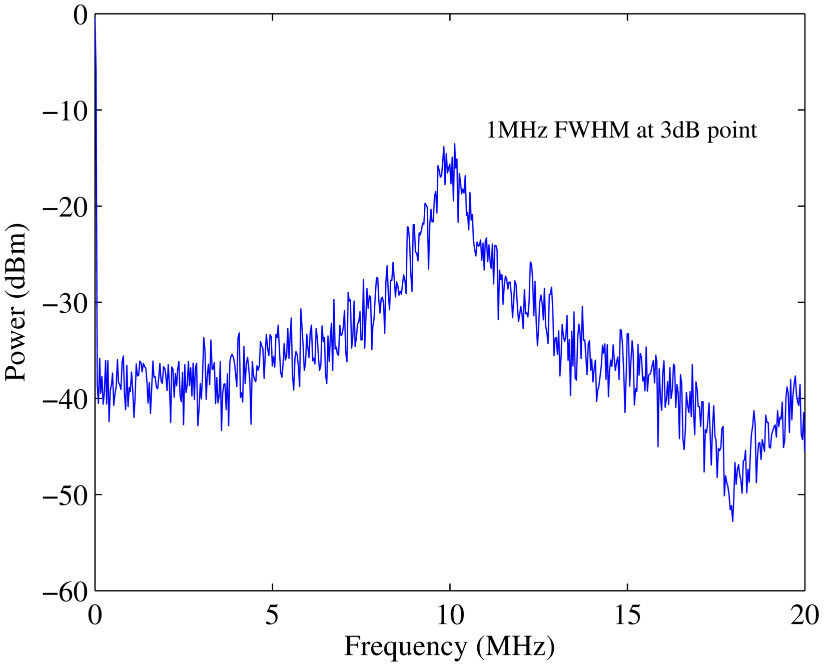

Figure 26. Locked beat note between the Ti:sapphire laser and the Rb-ECDL.

The PSD plot in Figure 27 shows a cumulative phase noise of 3.67 rad over 1 second, when we integrated over a frequency range from 1-64 kHz. Most of the noise came at >10 kHz frequencies. The corner frequency of the PI-controller used for locking was 10 kHz. The theoretical bandwidth of the Ti:sapphire locking loop was about 1 MHz (since we were using diode current control), but the bandwidth of the beat signal prevented better locking at higher corner frequencies. We can notice a great increase in the noise at 7.5 kHz frequency, which can be traced back to the dither frequency used for stabilization of the Rb stabilized ECDL. We used the smallest possible voltage amplitude for the dither signal, but this frequency was still present in the locked loop. With quieter electronics the dither signal could be removed and the cumulative phase noise could be reduced down to 2.85 rad (see Figure 28). In addition the use of a piezo with a higher resonance frequency could allow the use of a higher dither frequency.

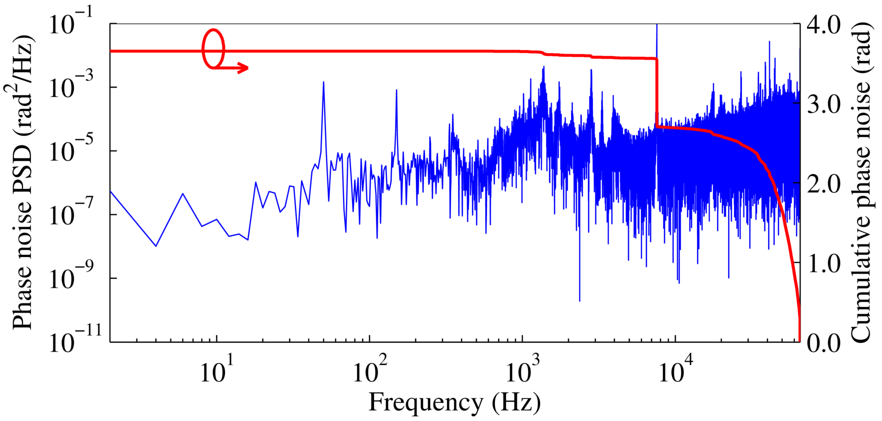

Figure 27. Phase noise PSD plot of the Rb-Ti:sapphire lock.

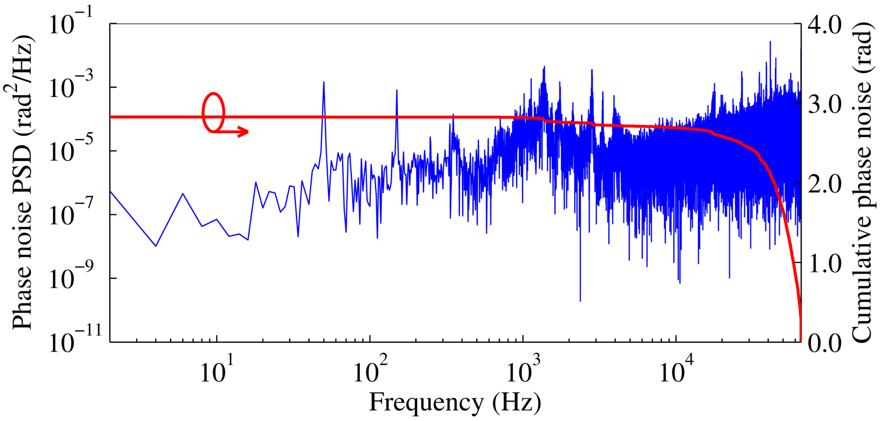

Figure 28. Phase noise PSD plot of the Rb-Ti:sapphire lock filtered to remove the strong 7.5-kHz contribution from the dither lock.

The calculated Allan deviations shown in Figure 29 illustrate the improved stability of f_{CEO} by nearly four orders of magnitude when locked to the Rb stabilized ECDL over a range of different gate times. The passive stability of the 1-GHz Ti:sapphire laser is also shown for comparison. We are actively stabilizing the f_{CEO} frequency, but over longer time periods the beat frequency could deviate out of the range of the locking electronics. The reason is that the repetition rate of the Ti:sapphire laser is slowly drifting due to thermal drift. This shift changes the comb lines relative position. The slow drift of f_{CEO} can be traced back to small changes in the f_{REP} of the Ti:sapphire laser when its repetition rate is not locked. As presented in Figure 23, the second order of the detected Ti:sapphire repetition rate was referenced to 2 GHz frequency taken from the SSG. The cavity length of the Ti:sapphire laser and therefore the repetition rate was stabilized by a PZT placed inside the cavity. A corner frequency of 10 Hz was used. As can be observed in Figure 29, the repetition rate locking improved the stability of the f_{CEO} locking in a long term measurement. We are suppressing the slow drift of the f_{REP} which improved the long-term stability. A fractional stability of $5e{-}15$ was achieved in a 10-s gate time.

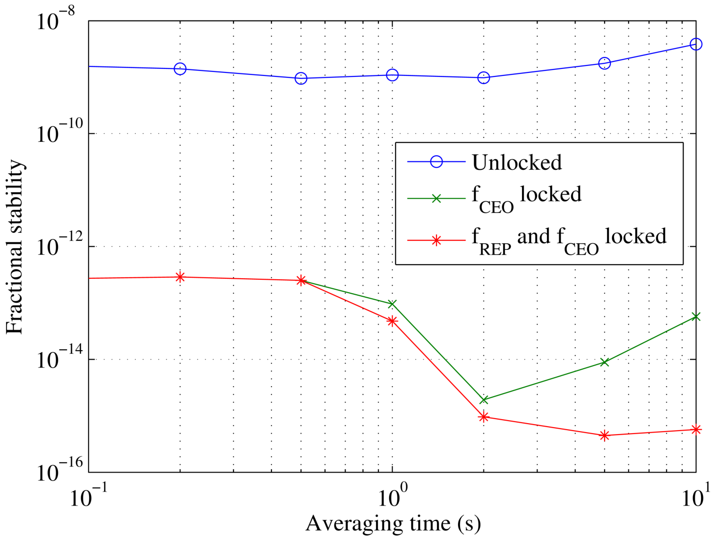

Figure 29. Allan deviation measurements of Rb stabilized ECDL locking of the 1-GHz Ti:sapphire laser.

The linewidth of the locking signal is wider in comparison to a supercontinuum based f-2f locking scheme, but the comb could remained locked for hours. The reason is the high-quality locking of the ECDL which could remain locked to the Rb transition line for 24 hours without any adjustments. On other hand we also benefited from a passively stable pump laser. The Allan deviation results show a comparable performance with self-referenced systems, but here we are getting rid of PCF from the system. We can lock the f_{CEO} of the pump pulse without the need for nonlinear fibre, and without the need for supercontinuum generation. This means we can lock higher repetition rate frequency combs much more easily than we could by using PCF.

Phase noise PSD measurements of the internal heterodyne beat locking are presented in Figure 30. The calculated cumulative phase noise from the phase noise PSD profile resulted in 1.6 rad in range from 1 Hz – 64 kHz over a 1-second observation time. The quality of the locking is limited by the bandwidth of the electronics (through the signal formatting stages) or physically (by the travel range and resonance frequency of the PZT used for cavity length control).

The noise data presented in Figure 31 and Allan variance data presented in Figure 32 were measured in-loop after the frequency divider. The in-loop phase noise PSD of the locked internal f_{CEO} showed a cumulative phase noise of 1.59 rad in a 1 second acquisition time integrated from 1-64 kHz. The corner frequency of the PI-controller was set to 3 kHz. The limiting factor was the resonance of the PZT used for the cavity length stabilization in the OPO. The real bandwidth of the PZT was in the 500-1000-Hz frequency range. The Allan deviation

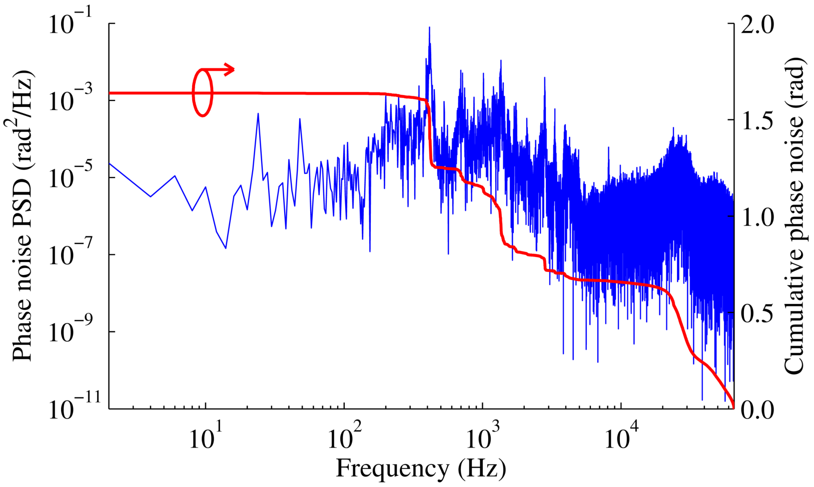

Figure 30. PSD spectrum from the 1-GHz OPO locked to the divided internal beat frequency.

calculations of the frequency divided and locked internal f_{CEO} are shown in Figure 32. The fractional stability slightly was slightly noisier than what was reported for the 333 MHz OPO [11]. The presented Allan deviation was measured for the frequency-divided 10-MHz signal. The division of the acquired frequency increased the capture range of the locking allowing an excellent long term stability to be obtained.

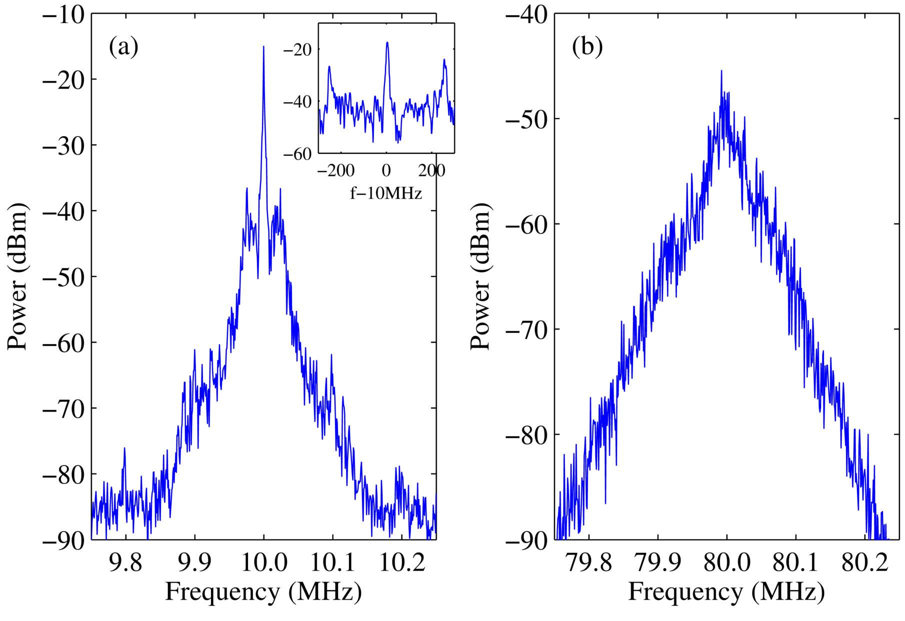

Figure 31. Locked beat frequency measured: (a) after, and (b) before the $\frac{f}{8}$ divider.

An out-of-loop measurement of the phase noise PSD was done by splitting the amplified signal before the frequency divider (80 MHz when locked) and mixing with a 70 MHz RF signal to generate a new 10 MHz beat frequency. This new frequency was passed through a comparator and into a second PFD along with a second 10 MHz reference signal, generated by the same RF source as the reference signal for the locking loop. The output from this out-of-loop PFD was used to measure the PSD of the undivided signal, which is shown in Figure 33, after a

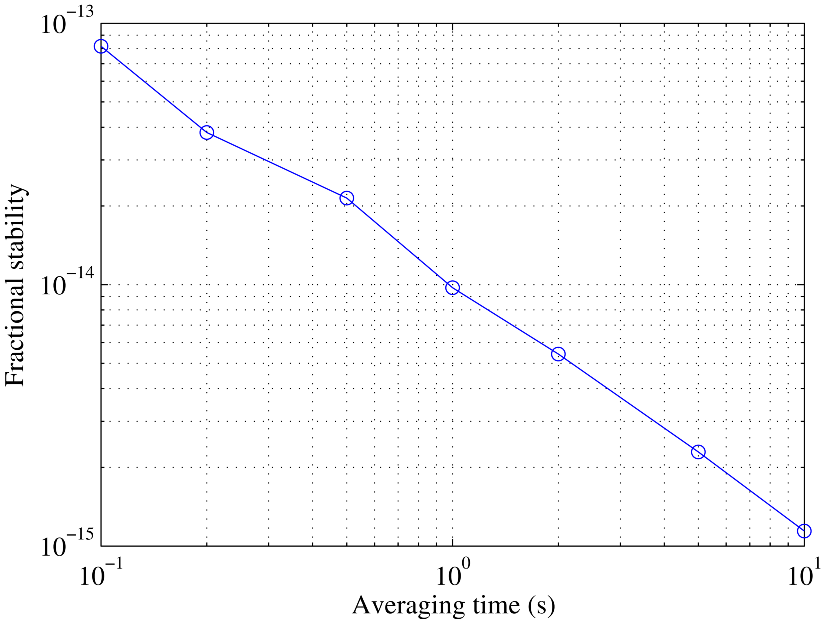

Figure 32. Allan deviation measurements of the locking stability of the 1-GHz OPO when stabilized to an internal beat frequency.

scaling consideration that accounts for the divider used for locking [43, 44]. As was discussed previously, the detected and locked internal beat frequency corresponds to a change in signal carrier-envelope offset frequency of $4\Delta f_{CEO}$. The noise data presented in Figure 33 represent a worst-case scenario for the locking stability of the OPO, as there is also a noise contribution from the Rb-locked Ti:sapphire f_{CEO}. The measured value of 3.4 rad can be considered as an upper limit on the phase noise of the OPO frequency comb.

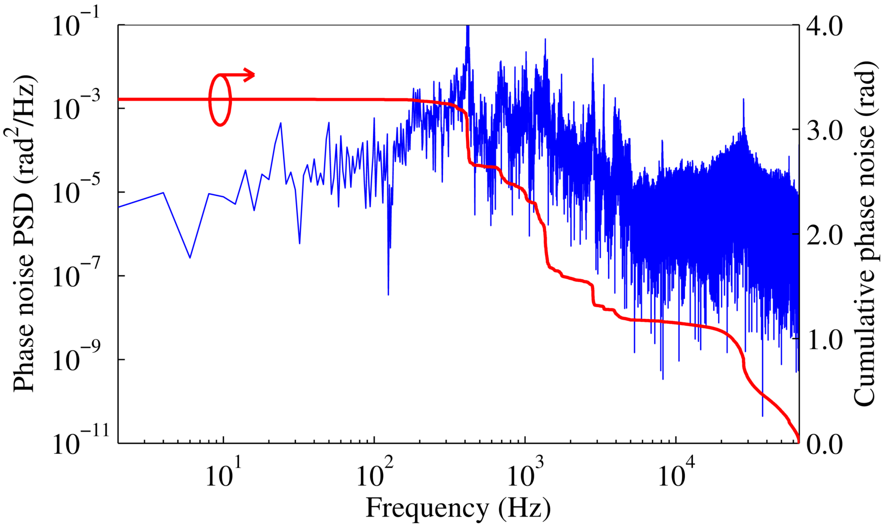

Figure 33. Out-of-loop phase noise PSD measurement of the internal beat lock for the 1-GHz OPO. The cumulative phase noise has been divided by 4, as discussed in the text. Observation time was 1s.

6.4 Conclusions

A Rb gas absorption line was used for ECDL frequency locking at 780.24 nm. The ultimately achieved frequency locking had low noise, was quite stable and could persist for at least 24 hours. The limitation of the locking time was that the New Focus LB1005 servo controller had a voltage range from -10 V to +10 V. The temperature in the laboratory is varying quite substantially for the ECDL and in order to increase the locking time further we need to increase the voltage output range or increase the temperature stability in the laboratory. Apart from these limitations, the frequency locking was stable and it could last long enough to be useful it for other experiments.

We have presented a new method for stabilizing the offset frequency of a 1030 nm Yb:fibre laser comb. When the comb was locked to a Rb transition line, the f_{CEO} exhibited an Allan deviation of 235 kHz at a 50-s gate time. A software-based feedback loop actuating the intracavity filter enabled a wide capture range and therefore f_{CEO} could remain locked for hours. The locking performance could be improved by implementing a hardware-based approach and by replacing a quite noisy galvanometer motor with a PZT actuator.

We have decribed a linear f_{CEO} stabilization method for a 1-GHz OPO synchronously pumped by a Ti:sapphire laser. An ECDL was developed and characterized which was used as an optical reference in an f_{CEO} locking scheme for the pump pulses. An additional locking of the internal heterodyne beat of the OPO resulted in a fully stabilized frequency comb spanning from the visible to the mid-IR region. This method bypasses the nonlinear interferometer limitations related to pump-supercontinuum generation in a PCF as the repetition rate increases, which is important because operation at 1-GHz frequency begins to reach a limit at 1 GHz in the conventional OPO comb locking scheme. The direct comb stabilization to an optical standard (^{87}Rb D_2 F=2-2 transition line) is promising as the repetition rate of the pump laser increases even further. In our demonstration the 1-GHz OPO comb was locked to a Rb stabilized ECDL and could remain locked up to several hours. The phase noise PSD measurements revealed a poorer locking in comparison with when a supercontinuum based lock was used due to the MHz-level linewidth of the ECDL used as the optical reference. Nevertheless, the demonstrated stability of the comb is sufficient for many spectroscopy applications. By implementing a low-finesse Fabry-Pérot cavity a multi-GHz mode spacing could be achieved.

References

[1] Richard A. McCracken, Karolis Balskus, Zhaowei Zhang, and Derryck T. Reid, “Atomically referenced 1-GHz optical parametric oscillator frequency comb," Optics Express 23(12), 16466-16472 (2015).

[2] S. A. Diddams, L. Hollberg, and V. Mbele, “Molecular fingerprinting with the resolved modes of a femtosecond laser frequency comb,” Nature 445, 627–630 (2007).

[3] A. Bartels, D. Heinecke, and S. A. Diddams, “10-GHz self-referenced optical frequency comb,” Science 326, 681 (2009).

[4] T. Steinmetz, T. Wilken, C. Araujo-Hauck, R. Holzwarth, T. W. Hänsch, L. Pasquini, A. Manescau, S. D’Odorico, M. T. Murphy, T. Kentischer, W. Schmidt, and T. Udem, “Laser frequency combs for astronomical observations,” Science 321, 1335–1337 (2008).

[5] F. Quinlan, G. Ycas, S. Osterman, and S. A. Diddams, “A 12.5 GHz-spaced optical frequency comb spanning >400 nm for near-infrared astronomical spectrograph calibration,” Rev. Sci. Instrum. 81, 063105 (2010).

[6] D. C. Edelstein, E. S. Wachman, and C. L. Tang, “Broadly tunable high repetition rate femtosecond optical parametric oscillator,” Appl. Phys. Lett. 54, 1728–1730 (1989).

[7] G. M. Gale, M. Cavallari, T. J. Driscoll, and F. Hache, “Sub-20-fs tunable pulses in the visible from an 82-MHz optical parametric oscillator,” Opt. Lett. 20, 1562–1564 (1995).

[8] K. L. Vodopyanov, I. Makasyuk, and P. G. Schunemann, “Grating tunable 4-14 μm GaAs optical parametric oscillator pumped at 3 μm,” Opt. Express 22, 4131–4136 (2014).

[9] F. Adler, K. C. Cossel, M. J. Thorpe, I. Hartl, M. E. Fermann, and J. Ye, “Phase-stabilized, 1.5 W frequency comb at 2.8-4.8 μm,” Opt. Lett. 34, 1330–1332 (2009).

[10] T. I. Ferreiro, J. Sun, and D. T. Reid, “Frequency stability of a femtosecond optical parametric oscillator frequency comb,” Opt. Express 19, 24159–24164 (2011).

[11] K. Balskus, S. M. Leitch, Z. Zhang, R. A. McCracken, and D. T. Reid, “1-GHz harmonically pumped femtosecond optical parametric oscillator frequency comb,” Opt. Express 23, 1283–1288 (2015).

[12] J. M. Dudley, G. Genty, and S. Coen, “Supercontinuum generation in photonic crystal fibre,” Rev. Mod. Phys. 78, 1135–1184 (2006).

[13] D. J. Jones, S. A. Diddams, J. K. Ranka, A. Stentz, R. S. Windeler, J. L. Hall, and S. T. Cundiff, “Carrier envelope phase control of femtosecond mode-locked lasers and direct optical frequency synthesis,” Science 288, 635–639 (2000).

[14] J. H. Sun, B. J. S. Gale, and D. T. Reid, “Composite frequency comb spanning 0.4-2.4 μm from a phasecontrolled femtosecond Ti:sapphire laser and synchronously pumped optical parametric oscillator,” Opt. Lett. 32, 1414–1416 (2007).

[15] H. R. Telle, G. Steinmeyer, A. E. Dunlop, J. Stenger, D. H. Sutter, and U. Keller, “Carrier-envelope offset phase control: A novel concept for absolute optical frequency measurement and ultrashort pulse generation,” Appl. Phys. B 69, 327–332 (1999).

[16] P. Li, G. Wang, C. Li, A. Wang, Z. Zhang, F. Meng, S. Cao, and Z. Fang, “Characterization of the carrier envelope offset frequency from a 490 MHz Yb-fibre-ring laser,” Opt. Express 20, 16017–16022 (2012).

[17] S. A. Diddams, D. J. Jones, J. Ye, S. T. Cundiff, J. L. Hall, J. K. Ranka, R. S. Windeler, R. Holzwarth, T. Udem, and T. W. Hansch, “Direct link between microwave and optical frequencies with a 300 THz femtosecond laser comb,” Phys. Rev. Lett. 84, 5102–5105 (2000).

[18] D. Hou, B. Ning, J. Wu, Z. Wang, and J. Zhao, “Demonstration of a stable erbium-fibre-laser-based frequency comb based on a single rubidium atomic resonator,” Appl. Phys. Lett. 102, 151104 (2013), doi:10.1063/1.4801996.

[19] J. Sun, B. J. S. Gale, and D. T. Reid, “Coherent synthesis using carrier-envelope phase-controlled pulses from a dual-color femtosecond optical parametric oscillator,” Opt. Lett. 32, 1396–1398 (2007).

[20] D. T. Reid, B. J. S. Gale, and J. Sun, “Frequency comb generation and carrier-envelope phase control in femtosecond optical parametric oscillators,” Laser Phys. 18, 87–103 (2008).

[21] R. Lang and K. Kobayashi, ”External optical feedback effects on semiconductor injection laser properties,” IEEE J. Quantum Electronics QE-16, 347-355 (1980).

[22] K. MacAdam, A. Steinback and C. Wieman, ”A narrow-band tunable diode laser system with grating feedback, and a saturated absorption spectrometer for Cs and Rb,” Am. J. Phys. 60, 1098-1110 (1992).

[23] C. E. Wieman and L. Hollberg, ”Using diode lasers for atomic physics,” Rev. Sci. Instrum. 62, 1-21 (1991).

[24] L. Ricci, M. Weidemuller, T. Esslinger, A. Hemmerich, C. Zimmermann, V. Vuletic, W. Konig and T. W. Hansch, ”A compact grating-stabilized diode laser system for atomic physics,” Opt. Commun. 117, 541-549 (1995).

[25] M. J. Colles and C. R. Pidgeon, ”Tunable lasers,” Rep. Prog. Phys. 38, 329 (1975).

[26] M. W. Fleming and A. Mooradian, ”Spectral characteristics of external-cavity controlled semiconductor lasers,” IEEE J. Quantum Elect. 17(1), 44-59 (1981).

[27] S. D. Saliba and R. E. Scholten, ”Linewidths below 100 kHz with external cavity diode lasers,” Appl. Opt. 48, 6961 (2009).

[28] F. L. Pedrotti, L. S. Pedrotti and L. M. Pedrotti, ”Introduction to Optics,” Pearson, 3rd edition 51 (2007).

[29] T. Acsente, ”Laser diode intensity noise induced by mode hopping,” Romanian Report in Physics 59, 87-92 (2007).

[30] Handbook of Basic Atomic Spectroscopic Data: Rubidium (The National Institute of Standards and Technology, 2005), retrieved 15 July 2013, http://physics.nist.gov/PhysRefData/Handbook/Tables/rubidiumtable1htm.

[31] P. Siddons, C. S. Adams, G. Chang Ge and I. G. Hughes, ”Absolute absorption on the rubidium D lines: comparison between theory and experiment,” J. Phys. B: At. Mol. Opt. Phys. 41, 155004 (2008).

[32] Rubidium (87) D Line Data, retrieved 15 July 2013, http://steck.us/alkalidata/rubidium87numbers.pdf and Rubidium (85) D line Data, retrieved 15 July 2013, http://steck.us/alkalidata/rubidium85numbers.pdf.

[33] I. I. Sobelman, Ch. 6 ”Hyperfine Structure of Spectral line,” in ”Atomic Spectra and Radiative Transitions,” pp.156-170 (1992).

[34] J. M. Hollas, Ch. 2 ”Electromagnetic radiation and its interaction with atoms and molecules”, in ”Modern Spectroscopy,” 3rd Edition (John Wiley and Sons, 1997).

[35] J. Ye, S. Swartz, P. Jungner and J. L. Hall, ”Hyperfine structure and absolute frequency of the ^{87}Rb $5P_{3/2}$ state,” Opt. Lett. 21, 1280-1282 (1996).

[36] P. Gascoyne and H. Rutt, ”An opto-acoustic frequency lock system for pulsed lasers,” Journal of Physics E: Scientific instruments 16, 31 (1983).

[37] C. J. Foot, Ch. 8, Atomic Physics, (Oxford, 2005), pp. 160. W. Koechner, Ch. 11, Damage of Optical Elements, in Solid-State Laser Engineering, 6th Edn., (Springer, 2006), pp. 680-701.

[38] K. Volopyanov, W. Hurlbut and V. Kozlov, ”Photonic THz generation in GaAs via resonantly enhanced intracavity multispectral mixing,” Applied Physics Lett. 99, 041104 (2011).

[39] T. I. Ferreiro, J. Sun and D. T. Reid, ”Frequency stability of a femtosecond optical parametric oscillator frequency comb,” Optics Express 19, 24159-24164 (2011).

[40] T. C. Schratwieser, K. Balskus, R. A. McCracken, C. Farrell, C. G. Leburn, Z. Zhang, T. P. Lamour, T. I. Ferreiro, A. Marandi, A. S. Arnold, and D. T. Reid, “^{87}Rb-stabilized 375-MHz Yb:fibre femtosecond frequency comb,” Opt. Express 22(9), 10494–10499 (2014).

[41] J. Sun, B. J. S. Gale, and D. T. Reid, “Testing the energy conservation law in an optical parametric oscillator using phase-controlled femtosecond pulses,” Opt. Express 15, 4378–4384 (2007).

[42] D. W. Allan, "Statistics of atomic frequency standards," Proc. IEEE 54, 221–230 (1966).

[43] L. Dickstein, “Introduction to phase noise in signal generators,” http://www.gigatronics.com/uploads/document/AN-GT140A-Introduction-to-Phase-Noise-in-Signal- Generators.pdf.

[44] C. J. Grebenkemper, “Local oscillator phase noise and its effect on receiver performance,” Watkins-Johnson Co. Tech-notes (1981).

Chapter 7. Generation of 10.66-GHz frequency combs by Fabry-Pérot filtering

One of the most promising applications of the locked frequency comb is high resolution spectroscopy. If the comb mode spacing is sufficiently wide, a high resolution Fourier-transform infrared (FTIR) spectrometer can resolve the individual comb lines, with potential applications in comb-line spectroscopy. In this chapter I describe, a fully stabilized Fabry-Pérot (FP) cavity used for the generation of a 10-GHz frequency comb where the initial mode spacing was 333-MHz (see Chapter 4, 5). Firstly, a passively stable FP cavity was locked to a Rb-stabilized CW laser and could be controlled in length so that efficient 10-GHz frequency comb filtering was achieved. Later we locked the FP cavity length directly to the comb where the ECDL light was used only for the FP cavity alignment so that the comb was filtered efficiently to 10.3 GHz. Here I will present the construction of a stabilized FP cavity and demonstrate 10-GHz longitudinal mode spacing using a 1-GHz spectral resolution FTIR spectrometer operating near a wavelength of 1.5 μm. The demonstration of this narrow linewidth and well defined frequency comb confirms FP filtering as an effective option for high resolution spectroscopy or precise frequency metrology.

7.1 Introduction

Multi-GHz frequency combs are in demand for applications such as spectroscopy [1, 2], astrophotonics [3, 4, 5], calibration for spectrographs [6], microwave frequency generation [7] or optical coherence tomography [8]. The individual modes of a higher mode spacing comb can be more easily resolved which enables techniques like direct comb spectroscopy. For most of the applications, optically coherent sources covering the wavelength range from the visible up to the far-infrared region are required which is not readily achievable from laser combs. Therefore OPOs represent a convenient alternative route via frequency conversion from the visible to the mid-IR region [9]. Femtosecond OPOs are tunable [10, 11], generating narrow linewidth combs [12], but the mode spacing increase to multi-GHz frequencies was always limited by the pump laser's repetition rate. OPOs are synchronously pumped devices and therefore their repetition rate is limited by the repetition rate of their pump laser. It is possible to generate 1-GHz OPO frequency combs [13, 14, 15], but higher repetition rates becomes much more challenging. The mode spacing can be also increased by using cascaded Mach-Zehnder interferometer [16]. We decided to use a routine route to achieve multi-GHz mode spacing. Frequency combs with higher than 1-GHz mode spacing have been demonstrated by Fabry-Pérot filtering of lower repetition rate frequency combs [17, 18, 19]. From the low repetition rate frequency comb a high repetition rate frequency comb can be generated where the mode spacing of mf_{REP} is determined by the free spectral range (FSR) of the Fabry-Pérot cavity.

Our aim was to demonstrate a stabilized Fabry-Pérot cavity which could be used to filter a 333-MHz repetition rate frequency comb of the OPO up to a 10-GHz comb. This approach of generating high repetition rate frequency combs requires a lot of additional electronics for direct stabilization of FP cavity length to the incident fundamental comb. The length of the FP cavity was dither locked to a single-frequency ECDL and later on directly to the OPO frequency comb. For the direct locking to the comb, the ECDL light was used for the alignment of the comb: a Rubidium (Rb) stabilized CW laser emitting at 780.2-nm wavelength was overlapped with the comb before the FP cavity. The ECDL design was presented in Chapter 6. The dither locking technique was the same as we used for the ECDL wavelength locking [20, 21, 4, 22]. The work presented in this chapter was partly carried out by Dr. Zhaowei Zhang. My personal contribution was to ensure that the 333-MHz frequency comb was fully stabilized before the FP filtering and the ECDL maintained a stable lock to the Rb-transition line during the experiments. I was involved together with Dr. Zhaowei Zhang in aligning the ECDL and comb into the FP cavity, and locking the FP to the ECDL, and directly to the comb, resulting in a 10.3-GHz mode spacing. The filtered comb was resolved by a Fourier transform spectrometer with a spectral resolution of 0.83 GHz, which was constructed by Dr. Zhaowei Zhang.

7.2 Fabry-Pérot filtering theory

The FP filtering method was proposed by Charles Fabry and Alfred Pérot at the University of Marseille in 1897 [23]. It is the most common method used for optical filtering. A Fabry-Pérot interferometer produces an interference pattern when a number of beams are in coherence with each other. Here I will describe the physics of FP filtering and introduce the Airy formula [24]. The Airy function presents the relationship between the power and phase containing multiple resonances spaced by 2π, which are produced due to interference of the wave with itself. Attenuated copies of the wave are reflected back and forward between the two FP mirrors (see Figure 1).

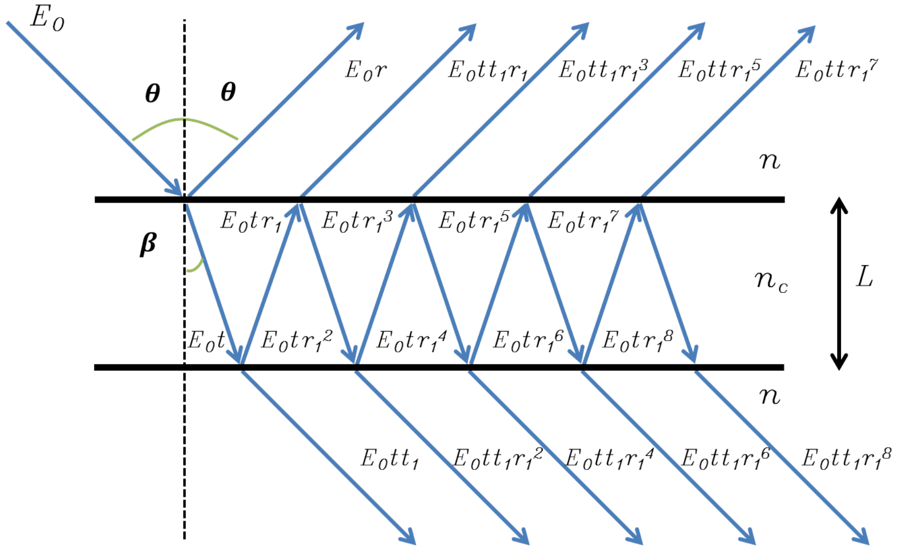

Figure 1. Multiple reflections in a FP etalon from two plane parallel mirrors resulting in interference.

As shown in Figure 1, two mirrors are placed parallel to each other with a spacing L between them. The medium between the two mirrors may have a refractive index n_c which must be taken into account. When the beam reaches one of two mirrors the incident light is partially reflected and transmitted to form an infinite series since each mirror has a reflection coefficient r. The transmitted and reflected beams interfere constructively or destructively depending on their phases and frequencies to produce a periodic transmission function which can be changed depending on the FP cavity construction. The FP cavity separation between the two mirrors can be varied resulting in a tunable optical filter.

Even after one round trip, the internal waves between the FP mirrors are interfering. Depending on how many reflections any wave experiences, it will be attenuated more or less strongly than other waves, but it will always participate in the interference process. For example, after propagating four distances of L, the reflected waves E_0r, $E_0tt_1r_1$ and $E_0tt_1r_1^3$ will interfere. The transmitted $E_0tt^{'}$ and $E_0tt_1r_1^2$ waves also interfere with each other. The electric field of the transmitted waves can be expressed as

$$\begin{aligned} E_1 &= E_0T \\ E_2 &= E_0TR\exp^{i\delta} \\ E_2 &= E_0TR^2\exp^{i2\delta} \\ &\cdots \\ E_m &= E_0TR^m\exp^{im\delta} \end{aligned} \tag{81}$$

where $T = tt_1$ is the transmittance, $R = r^2 = r_1^2$ is the reflectivity of one partially reflecting optical surface (mirror) and r and r_1 are the amplitude reflection coefficients where t and t_1 are the amplitude transmission coefficients. Here we assumed that both mirrors are the same ($r = r_1$). As the incident wave is reflected between two FP cavity mirrors, it travels a distance of $2mL$ travel distance (m is the round trip number). The total electric field of the reflected wave can be expressed in a geometric series with the ratio $R\exp^{i\delta}$ based on the identity

$$\sum_{m=0}^{\infty} r^m = \frac{1}{1-r} \quad \text{if } |r| < 1 \tag{82}$$

to obtain

$$E_{trans} = \frac{E_0T}{1 - R\exp^{i\delta}} \tag{83}$$

The incident beam reduces in amplitude after each interaction with the mirrors. The electric field reduces to zero as the field is reflected an infinite number of times. The intensity transmitted by the PF etalon is

$$I_{trans} = \frac{I_0T^2}{|1 - R\exp^{i\delta}|^2} \tag{84}$$

where

$$I_0 = |E_0|^2 \tag{85}$$

Since $\exp^{i\delta} + \exp^{-i\delta} = 2cos\delta$ and $sin^2\frac{\delta}{2} = \frac{1}{2}(1 - cos\delta)$, Equation (81) can be simplified to

$$I_{trans} = I_0 \frac{T^2}{(1-R)^2} \frac{1}{1 + \frac{4R}{(1-R)^2} sin^2\frac{\delta}{2}} \tag{86}$$

Real optical surfaces are not only transmitting and reflecting, but also absorbing and therefore $A + T + R = 1$. If wave absorption is small enough the second term can be neglected

$$\frac{T^2}{(1-R)^2} = [\frac{1 - A - R}{(1-R)}]^2 = [1 - \frac{A}{1-R}]^2 \tag{87}$$

equation (84) can be rewritten to

$$I_{trans} = I_0 \frac{1}{1 + Fsin^2\frac{\delta}{2}} \tag{88}$$

where

$$F = \frac{4R}{(1-R)^2} \tag{89}$$

The cavity transmission is therefore

$$T = \frac{1}{1 + Fsin^2\frac{\delta}{2}} \tag{90}$$

and the intensity of the reflected wave can be written as

$$I_{reflected} = I_0 \frac{Fsin^2\frac{\delta}{2}}{1 + Fsin^2\frac{\delta}{2}} \tag{91}$$

with the cavity reflectivity being

$$R_{cav} = \frac{Fsin^2\frac{\delta}{2}}{1 + Fsin^2\frac{\delta}{2}} \tag{92}$$

In a system with no absorption, energy conservation is valid for the reflectivity R and the transmittivity T (R+T=1). Equation (90) is called the Airy function and it expresses the total reflected power dependence on the phase, which in turn depends on the path difference, δ. We can calculate the optical path difference δ between two beams transmitted by the FP cavity from the geometry in Figure 2.

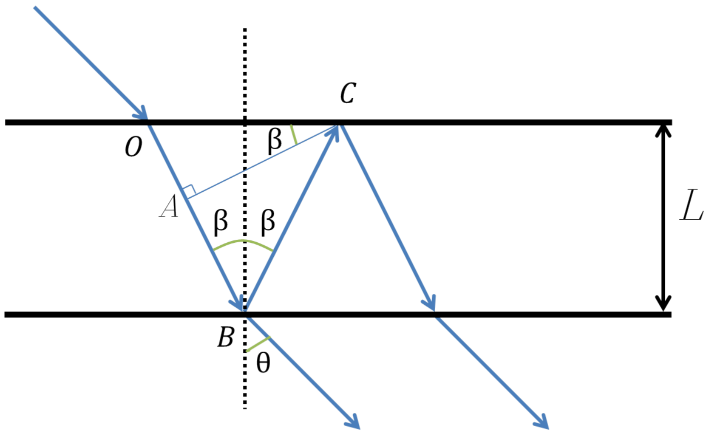

Figure 2. The optical path difference between the two beams.

$$
\begin{aligned}
&A\vec{B}C = A\vec{B} + B\vec{C}\\
&B\vec{C} = s = \frac{L}{cos\beta}\\
&A\vec{B} = O\vec{B} - O\vec{A}\\
&O\vec{A} = \sqrt{O\vec{C}^2 - A\vec{C}^2}\\
&O\vec{C} = 2ssin\beta\\
&O\vec{A} = \sqrt{4s^2sin^2\beta - s^2sin^2(2\beta)} = 2ssin\beta\sqrt{1-cos^2\beta} = 2ssin^2\beta\\
&A\vec{B}C = 2s - 2ssin^2\beta = 2scos^2\beta = 2Lcos\beta
\end{aligned}
\tag{93}
$$

The path length difference is associated with the phase shift according to

$$\delta = \frac{2\pi}{\lambda}n_c2Lcos\beta \tag{94}$$

The Fabry-Pérot mirrors must be chosen to contribute low (ideally zero) dispersion because every reflection from the optical surface adds an additional phase shift β_{add}. The sum of the phase difference is

$$\delta = \beta + \beta_{add} \tag{95}$$

which means if the dispersion of the mirrors is not flat across the full spectrum, the mode filtering is not efficient for all of the pulse. Different comb modes will therefore experience different phase shifts leading to a spectral narrowing since only part of the spectrum will experience efficient filtering. Let's go back to Equation (86). At certain phase differences, interference peaks appear. From Equation (86) it is obvious that interference is constructive if $\frac{\delta}{2} = \pi$ or an integer multiple of π

$$
\begin{aligned}
&\frac{2\pi}{\lambda}n_c2Lcos\beta = 2m\pi\\
&\frac{2n_c}{\lambda}Lcos\beta = m
\end{aligned}
\tag{96}
$$

In this case maximum intensity is equal to

$$I_{maximum} = \frac{T^2}{(1-R)^2} \tag{97}$$

For minimum transmission, the phase difference must be $\frac{\delta}{2} = \frac{\pi}{2}$ or an odd integer multiple of it. Then $sin^2\frac{\delta}{2} = 1$ resulting in

$$I_{minimum} = \frac{T^2}{(1+R)^2} \tag{98}$$

The full-width at half maximum ($FWHM$) intensity, can be expressed as

$$\delta = 2m\pi \pm \frac{\sigma}{2} \tag{99}$$

From Equation (86)

$$\begin{aligned} &\frac{1}{1+Fsin^2\frac{\sigma}{4}} = \frac{1}{2} \\ &sin\frac{\sigma}{4} \approx \frac{\sigma}{4} \\ &F\frac{\sigma^2}{16} = 1 \\ &\sigma = \frac{4}{\sqrt{F}} \end{aligned} \tag{100}$$

When we compare this extracted relation with the 2π separation of the maximum peaks, the FP cavity finesse can be expressed as

$$\mathcal{F} = \frac{2\pi}{\sigma} = \frac{\pi\sqrt{F}}{2} = \frac{\pi\sqrt{R}}{1-R} \tag{101}$$

We can notice that the FP cavity transmission and reflection is a function of wavelength (see Equation (91)). The transmission profile contains multiple fringes which depend on the reflectivity R (see Equation (83)).

There are several other important features of the Fabry-Pérot cavity. The first one is the capability to resolve two very similar wavelengths. The resolving power (RP) can be defined as

$$RP = \frac{\lambda}{\Delta\lambda} \tag{102}$$

Two wavelengths are resolved if the curves of two transmission fringes meet each other at their $FWHM$. In this case the sum of the two intensities of the fringes is equal to the intensity of a single fringe. This can be related with the interval Δ. First we differentiate Equation (89)

$$|\Delta\delta| = \frac{4\pi n_c Lcos\beta}{\lambda^2}\Delta\lambda = 2\pi m\frac{\Delta\lambda}{\lambda} \tag{103}$$

from Equation (95) and if $|\Delta\delta| = \sigma$

$$
\begin{aligned}
2\pi m\frac{\Delta\lambda}{\lambda} &= \frac{4}{\sqrt{F}} \\
\frac{\lambda}{\Delta\lambda} &= \frac{m\pi}{2}\sqrt{F}
\end{aligned}
\tag{104}
$$

Since $\frac{\pi\sqrt{F}}{2} = \mathcal{F}$ and for $\theta = 0$

$$
\begin{aligned}
\frac{\lambda}{\Delta\lambda} &= \frac{2n_cL\mathcal{F}}{\lambda} \\
\Delta\lambda &= \frac{\lambda}{\mathcal{F}m} = \frac{\lambda^2}{\mathcal{F}2n_cLcos\beta}
\end{aligned}
\tag{105}
$$

Another important parameter of the FP cavity is the free spectral range (FSR). This is the frequency difference between two maxima in the transmission profile of the FP interferometer. In order to calculate the FSR, the difference in phase is taken as 2π. Then

$$FSR = \Delta\lambda(FSR) = \frac{\lambda^2}{2n_cLcos\theta} = \frac{\lambda}{m} \tag{106}$$

The FSR, $FWHM$ and finesse $\mathcal{F}$ are related according to

$$FSR = \mathcal{F} \times FWHM \tag{107}$$

The characteristics of the FP cavity are defined by the parameter m (see Equation (94)) and the finesse $\mathcal{F}$. Once we have defined the wavelength and the incident angle, the only parameter which can be varied is the spacing L. After the spacing is chosen, the FSR is fixed. In our experiment we want to increase the mode spacing from 333 MHz up to 10 GHz frequency. The $FWHM$ is then determined by the ratio between the FSR and the finesse $\mathcal{F}$. The higher the reflectivity of the mirrors, the higher is the finesse $\mathcal{F}$. This results in narrower peaks and a higher resolving power for the FP cavity.

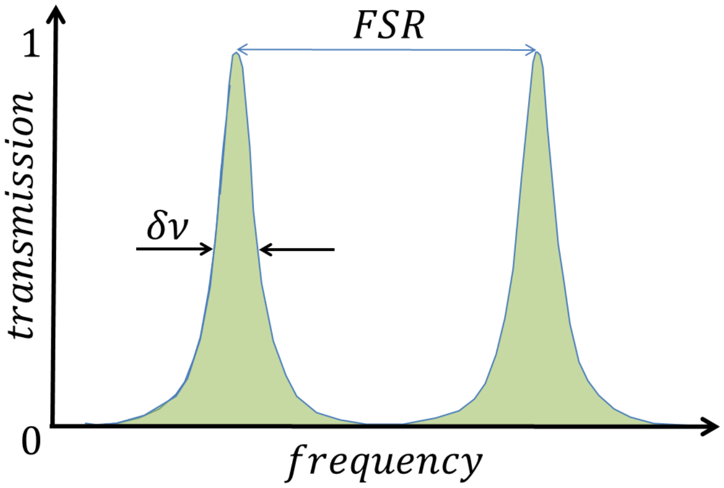

Figure 3. FP cavity transmission spectrum illustrating the $FWHM$ linewidth and the free spectral range FSR.

7.3 Construction of the Fabry-Pérot cavity

7.3.1 Source comb at 333 MHz

The signal frequency comb from the 333-MHz OPO described in Chapter 5 was locked at 1.46 µm and was used as the source comb for an external FP cavity employed to increase the mode spacing to 10 GHz. The design of this Ti:sapphire-pumped OPO was presented in [15]. Before mode filtering, the repetition rate f_{REP} and carrier-envelope-offset f_{CEO} of the frequency comb at 1535 nm were stabilized to a radio-frequency (RF) reference. Following this, the cavity length of the FP was locked to the Rb-stabilized diode laser emitting light at 780 nm wavelength, leading to a demonstration of comb filtering to 10.66 GHz. Subsequently the FP cavity was locked to the comb directly. In this case a Rb-stabilized diode laser was used for FP cavity alignment to ensure efficient comb filtering at 10.3 GHz. In all FP locking experiments the f_{CEO} was detected by heterodyning the supercontinuum light from the PCF with the non-phase-matched pump-signal sum-frequency light from the OPO. The frequency f_{REP} was acquired with a fast Si photodiode. For a 1-second gate time Allan deviations of 0.27 Hz and 1.5 mHz were measured for f_{CEO} and f_{REP} respectively. The locking of f_{CEO} in the comb filtering is important, because of the

7.3.2 Fabry-Pérot cavity specification

We considered a range of cavity designs employing different free spectral ranges (FSR). Since our goal was to demonstrate 10-GHz mode spacing frequency combs, the calculated standing wave resonator length L had to be 15 mm. The free spectral range (FSR) can be calculated as

$$\Delta\nu = \frac{c}{2L} \tag{108}$$

We decided to employ a plane-plane cavity design because mode matching requires no more than beam collimation and the cavity length can be adjusted to any value, enabling combs of flexible spacings to be realized. In the case of the FP cavity locking to the ECDL, it was composed of two low-dispersion flat mirrors, with a reflectivity of 99% over 1.0-1.1 µm and a GDD of less than 2 fs^2 over that region. At 1.050µm the GDD was -30 fs^2. The FP cavity length was tuned to around 15 mm to achieve an FSR of 10 GHz, the 30th harmonic of the repetition rate of the incident comb source. The f_{CEO} locking is important in coupling the comb to the Fabry-Pérot cavity. The comb spacing must be sub-harmonic of the FP cavity spacing and this can be ensured by locking the f_{CEO}

$$\begin{aligned} f_{REP} &= \frac{f_{FP}}{N} \\ nf_{REP} + f_{CEO} &= mf_{FP} \end{aligned} \tag{109}$$

For efficient frequency comb filtering, the actual comb mode offset (f_{CEO}) must changed so that the filtering is efficient (see Figure 4). On other hand the FP cavity length can be changed so that it matches the comb modes.

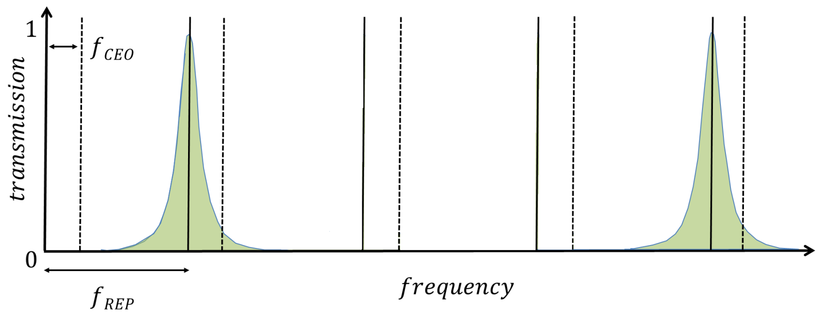

Figure 4. Fabry-Pérot filtering by matching the su-harmonic comb mode spacing with the FSR.

Our FP cavity had a FSR of 10 GHz which corresponded to a mirror separation of 15 mm. Such a cavity will pass every 30th mode of the frequency comb with all other modes being suppressed resulting in a 10-GHz mode spacing. Firstly, the OPO and ECDL beams were recollimated down to 4-mm in diameter which corresponded to a Rayleigh length of 8.18 m for Gaussian beam at 1535 nm wavelength. The beam from the OPO was overlapped with the single mode ECDL beam before they were coupled into the FP cavity (see Figure 5).

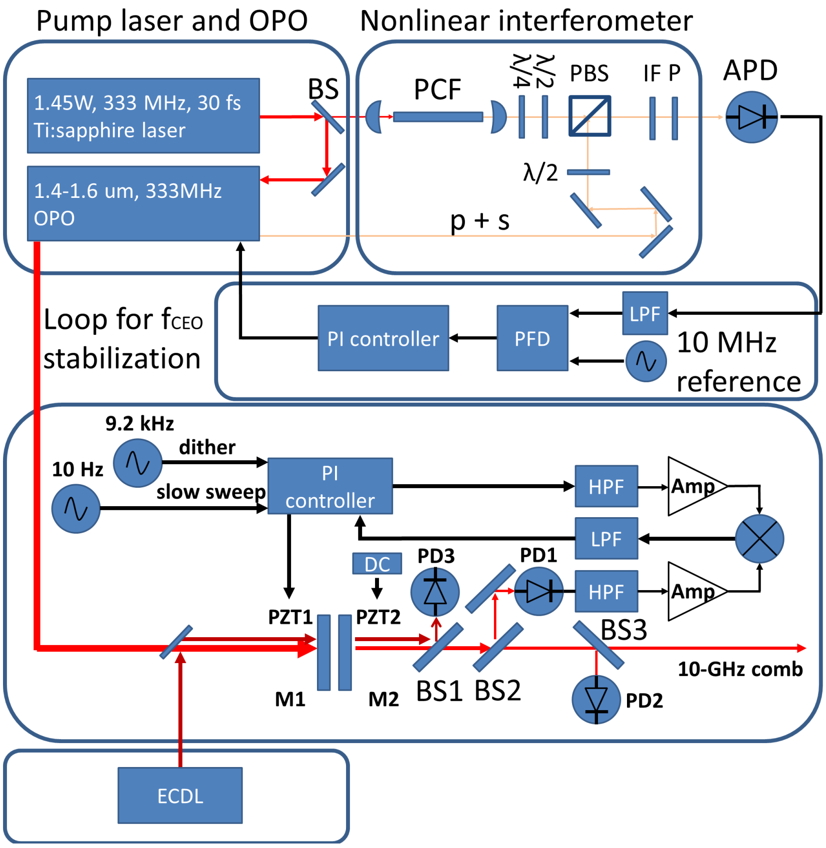

Figure 5. Comb-filtering system, showing the locking scheme of the OPO and FP cavity. A nonlinear interferometer was used for detecting the f_{CEO} frequency of the signal, a loop for stabilizing the f_{CEO} and a stabilized comb filter. PCF, photonic crystal fiber; PBS, polarization beam-splitter; IF, interference filter; P, polarizer; APD, avalanche photodiode; PZT, piezoelectric transducer; PI controller, proportional-integral controller; PFD, phase-frequency detector; LPF, low-pass filter; HPF, high-pass filter; Amp, amplifier; PD, photodiode; ECDL, external cavity diode laser.

In the case of the ECDL, the Rayleigh length was 16 m since the central wavelength of the ECDL was 780 nm. The ECDL was used not only to lock but also to align the FP cavity since the angular alignment of the mirrors using the comb was made difficult by the extreme sensitivity of the transmitted intensity to the FP length. After the FP cavity, another dichroic mirror separated the OPO frequency comb and the ECDL beams. The first FP cavity mirror was mounted on a ring type PZT1 so that the OPO and ECDL beams could pass through the centre of the mirror (see Figure 6). The maximum piezo displacement was 3 μm for 150 V applied voltage. The outer piezo diameter was 15 mm and the inner diameter 8 mm. The unloaded resonant frequency of the PZT is above 300 kHz. On this piezo a dither frequency was applied which changed the cavity length for the purpose of locking to the peak transmission of the cavity. After acquiring the dithered ECDL light, we were able to stabilize the cavity length via a feedback loop. The second FP cavity mirror M2 was mounted onto a translation stage enabling several millimetres manual cavity length tuning. A second PZT2 (9.1μm, 0-150V, EO0505D08F, Thorlabs) was placed inside the translation stage for fine cavity length adjustment and enabled adjustments of the free spectral range (FSR). The PZT2 maximum displacement was 9.1 μm for 100 V and its dimensions were 6.5-mm × 6.5-mm × 10 mm. The voltage on PZT2 was driven via a low noise piezo-driver (Newport Microdrive Controller, 0-150 V). For acoustic noise isolation, rubber mounts were placed between the 20 cm × 20 cm aluminium breadboard and the post holders. The use of rubber mounts improved the passive stability of the FP cavity. Before the use of rubber mounts, an obvious acoustic noise frequency around 1 kHz could be measured when the cavity length locking loop was activated. Subsequently, because of improved passive stability we were able to stabilise the FP cavity length directly to the comb.

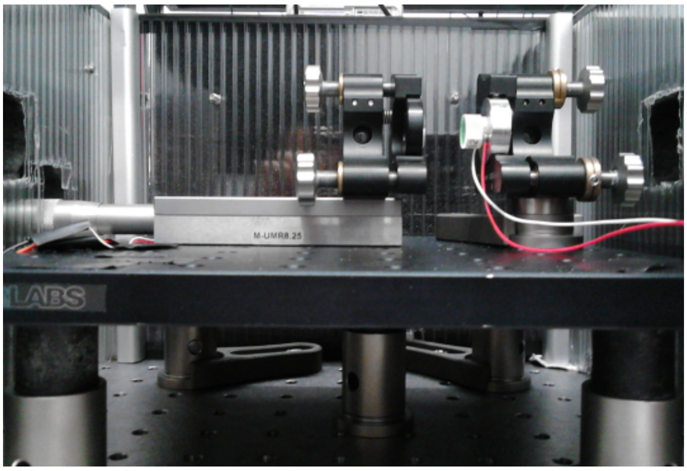

Figure 6. Fabry-Pérot cavity, showing the low-profile design and the breadboard supported on rubber isolators.

The FP cavity output was split into two channels using a dichroic mirror (BS1) which reflected 780-nm wavelength on the PD3 and transmited broadband pulses from 1-1.5 μm. The signal acquired on the PD3 was used for the FP cavity locking to the ECDL and BS2 was used to reflect the comb from 1.3-1.6 μm for direct FP cavity locking to the comb. The OPO light was detected with the PD1 detector (InGaAs, DET 10C/M, Thorlabs) where the locked and filtered frequency comb was focused onto detector PD2 (GaAs, ET-4000 from EOT). PD1 provided an error signal for the FP cavity length locking directly to the comb while PD3 provided the error signal for the FP cavity length locking directly to the ECDL, and PD2 was used to monitor the filtered frequency comb.

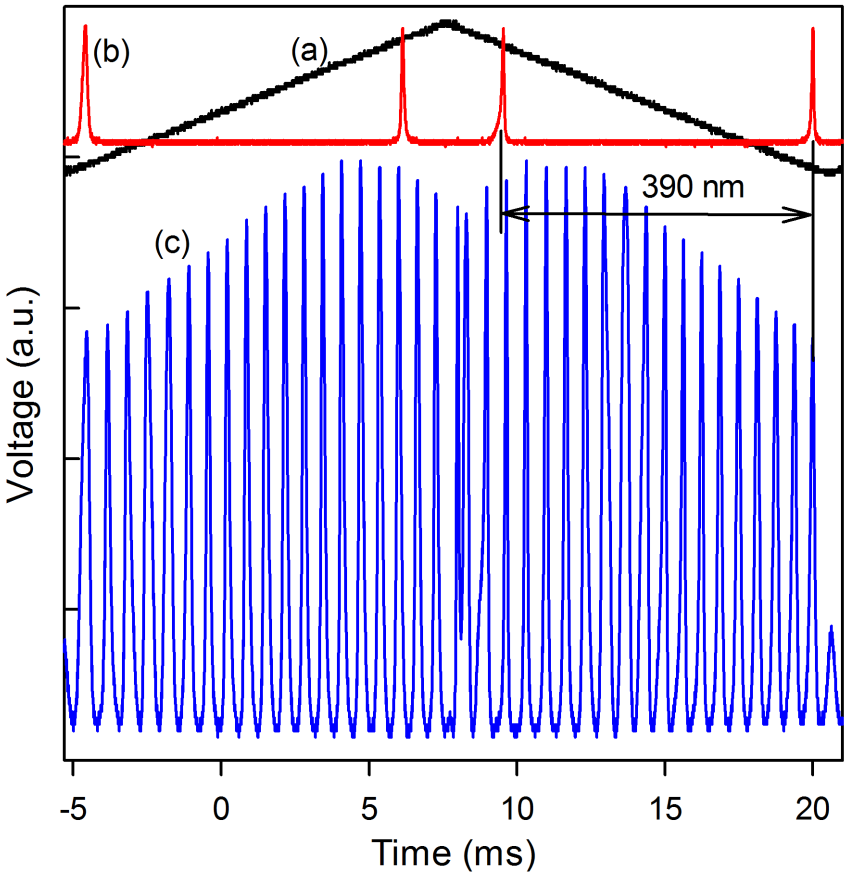

Figure 7. (a) The sweep voltage applied onto the PZT, (b) the transmitted ECDL power through the FP cavity, (c) the transmitted comb power through the FP cavity.

As the triangular drive signal was applied to PZT2, the transmitted ECDL light together with transmitted comb was monitored (see Figure 7). The frequency comb signal detected by PD1 is presented in Figure 6(c). This signal was used for the angular alignment of the ECDL and OPO light into the FP cavity. A triangular voltage of 10 V applied onto PZT2 corresponded to a displacement of 910 nm. The two transmission peaks in Figure 7(b) are separated by 390-nm displacement which equals half of the ECDL wavelength. The simultaneously measured signal of the filtered frequency comb contained 16 transmission peaks. Those multiple transmission peaks at slightly different FP cavity length arise because the frequency comb contains not single, but multiple evenly spaced frequencies. When the frequency comb is stabilized to a reference the transmitted light of the comb has a stable average power and repetition rate frequency. If the comb is not locked the output power fluctuates due to the Vernier effect because even a 25 nm FP cavity length change results in a different set of modes being passed by the filter. A slight change of the FSR selects a different set of comb modes and therefore changes the transmitted power.

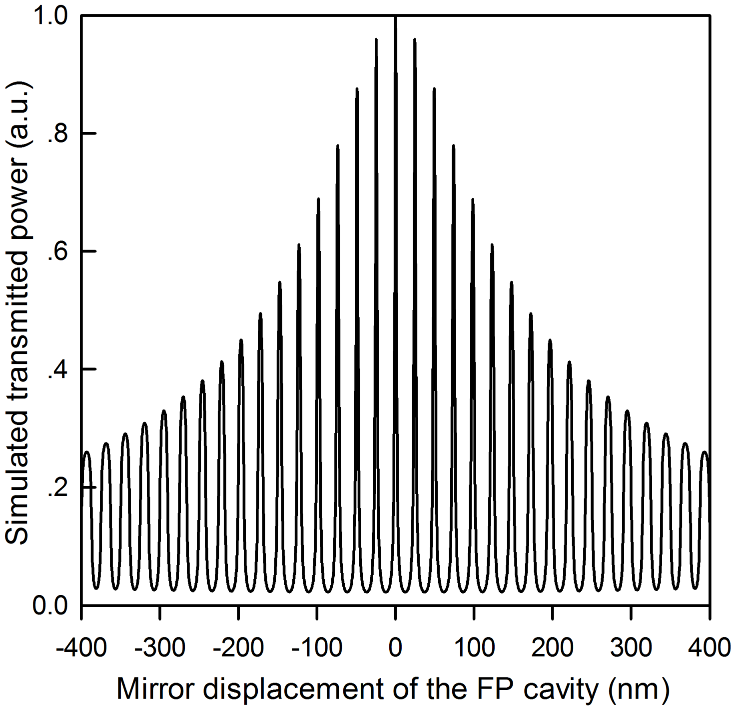

Figure 8. The simulated FP transmission as the cavity length is scanned and when the incident comb has a repetition rate of 333.3 MHz and the free spectral range of the FP cavity spacing is 10.66 GHz. The simulation done by Dr. Zhaowei Zhang.

The comb power transmitted as the filter cavity length is scanned can be compared with a simulation (see Figure 8) in which an initial 333-MHz mode spacing frequency comb at 1500 nm wavelength is filtered by a 14.07-mm FP cavity resulting in a 10.66-GHz mode spacing. The simulation shows good agreement with the experimental results presented in Figure 6(c). In both cases 16 transmission peaks are observed over a 390 nm displacement. The fringe intensity mismatch between the simulated and experimental data is thought to be caused by a slight misalignment and/or by imperfect mode matching of the OPO light into the FP cavity for the OPO.

7.4 Length stabilization of the Fabry-Pérot cavity

7.4.1 FP cavity locked to the ECDL

The filtered comb was detected by a fast photodiode and its RF spectrum is shown in Figure 9. It is clear that a comb with a mode spacing of 10 GHz was generated. This result was achieved without the FP cavity length locking. The FP cavity was composed of two low-dispersion flat mirrors, with a reflectivity of 99% over 1.0-1.1 µm and a GDD of less than 2 fs^2 over that region. The FP cavity length was tuned to around 15 mm to achieve an FSR of 10 GHz, the 30th harmonic of the repetition rate of the incident comb source. The side mode suppression was 15 dB. Optical spectra of the incident (red dashed line) and filtered output (blue solid line) combs are shown in Figure 10. The wavelength shift appeared due not exactly flat dispersion curve of the FP mirrors.

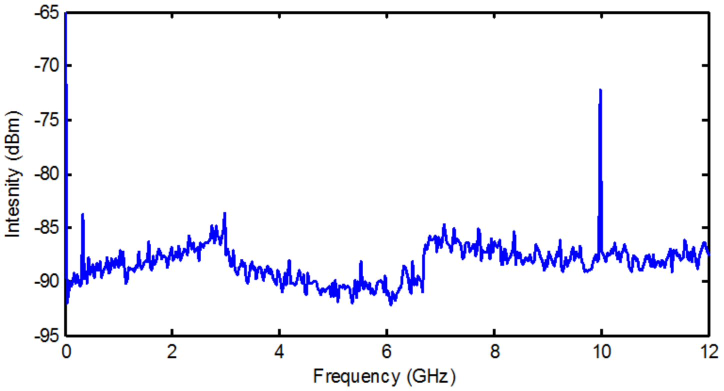

Figure 9. RF spectrum of the filtered comb.

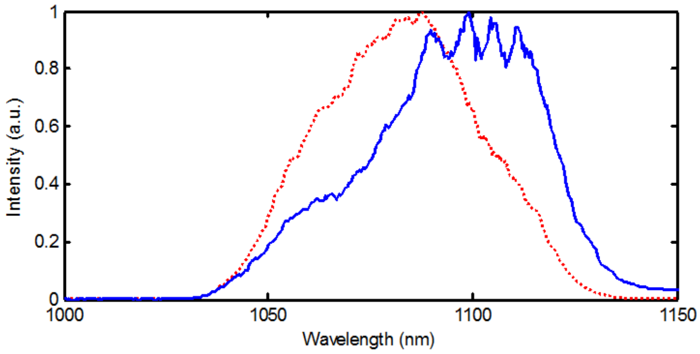

Figure 10. Optical spectra of the incident (red dashed curve) and filtered (blue solid curve) combs. The shift between the instant and filtered spectrum thought to be associated with the dispersion of FP mirrors. RBW=100 kHz.

The passive stability of the FP cavity was monitored with a slow photodetector (PD1). We monitored the average output power from the FP cavity. A typical result is shown in Figure 11. The photodetector was not saturated, and it can be seen that the transmission power was changing around the maximum value. The transmitted power was not stable, varying by a significant amount over a 1-ms time scale. Under these conditions it would be extremely challenging to use the transmitted average comb power as an error signal for FP cavity length stabilization.

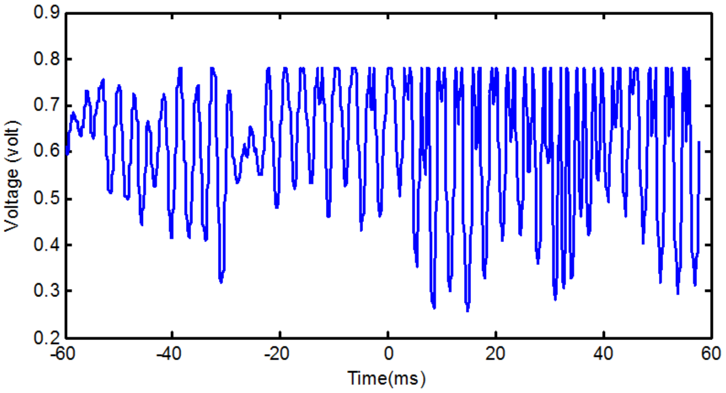

Figure 11. Photodetector signal, indicating the transmission of the comb through the passive FP cavity.

We evaluated the potential for stabilizing the FP cavity to a single-frequency Rb-stabilised external cavity diode laser (ECDL). The mirror spacing was tuned to 15 mm to achieve an FSR of 10 GHz. When the ECDL was transmitted through the FP cavity, a low-frequency (10 Hz) sweep signal was applied to the PZT through the ‘Sweep In’ port of a proportional-integral (PI) amplifier used for the locking experiment. Large transmission peaks were detected when one of the cavity modes matched the central wavelength of the ECDL. A high-frequency dither signal (7.4 kHz, V_{p-p}=200 mV) generated from a low-harmonic-distortion oscillator was applied to the PZT. After the ECDL light passed through the FP cavity, PD3 detected the dithered ECDL signal. The acquired signal was high pass filtered, amplified and mixed with the same amplified 7.4 kHz frequency. The low pass filtered (LPF) output from the mixer generated a derivative signal of the ECDL transmission peak (see Figure 12). The acquired derivative signal was used as an error signal. It was connected to the ’error in’ input of the PI amplifier. The output signal from the PI controller was applied to PZT1 for the cavity length stabilization. As a result, the FP cavity was locked to a single-frequency ECDL.

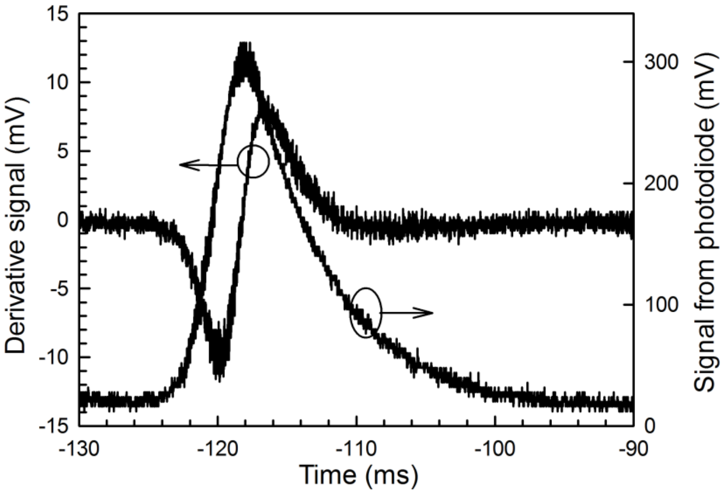

Figure 12. The transmission peak from PD1 (right scale) presented with the derivative from the mixer (left scale).The FP length was scanned via PZT1.

Since the FP cavity length was only locked to the ECDL transmission peak, it does not mean that it will necessarily match with the frequency comb transmission maximum. The repetition rate of the pulses from the OPO is 333 MHz which means there is a certain cavity length of the FP which is necessary for the 333-MHz repetition rate comb to fulfil the filtering condition for the FP cavity. To ensure efficient frequency comb transmission an additional low noise DC-voltage was applied to PZT2. The signal recorded on the photodetector (PD3) is presented in Figure 13. Over a measurement time of 10 ms, the standard deviation was 0.01 mV, corresponding to a cavity stability of better than 0.6 nm, which would be more than sufficient to stabilize the transmitted frequency comb,assuming its mode spacing was stabilized to another reliable reference.

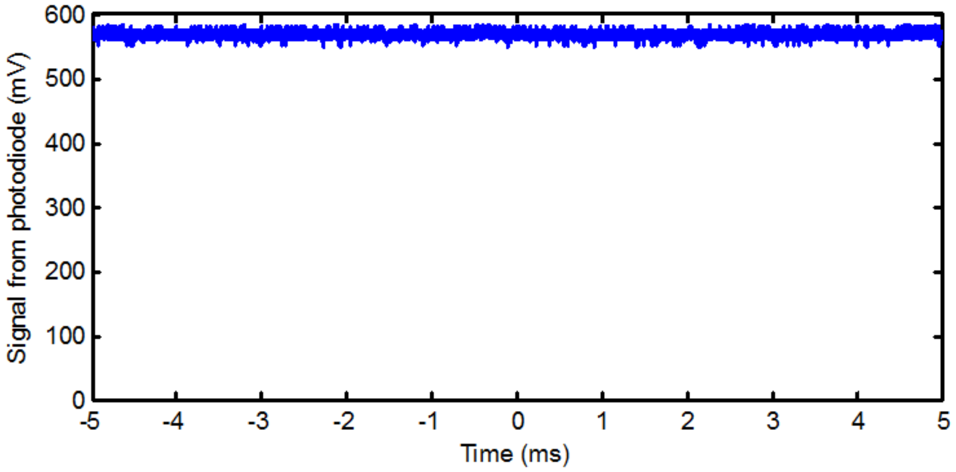

Figure 13. Measured signal on the photodiode while the cavity was locked.

7.4.2 Direct comb locking

The mirrors used to lock the FP cavity were not coated for the OPO signal wavelength. Therefore, although stabilized, the current embodiment could not be used to filter the OPO comb. Mirrors with appropriate reflectivity at both 0.78 µm and in the OPO wavelength-band would be required to implement the comb filtering. Laseroptik (LO) designed mirror coatings to satisfy the requirements. Together with improved passive stability of the FP cavity, these mirrors allowed it to be stabilized directly to a maximum in the frequency comb transmission. We used the same dither locking electronics as were used in the FP cavity locking to the ECDL to ensure stable transmission of the filtered frequency comb (see Figure 5). For locking the FP directly to the comb, the mirrors were changed (see Figure 14).

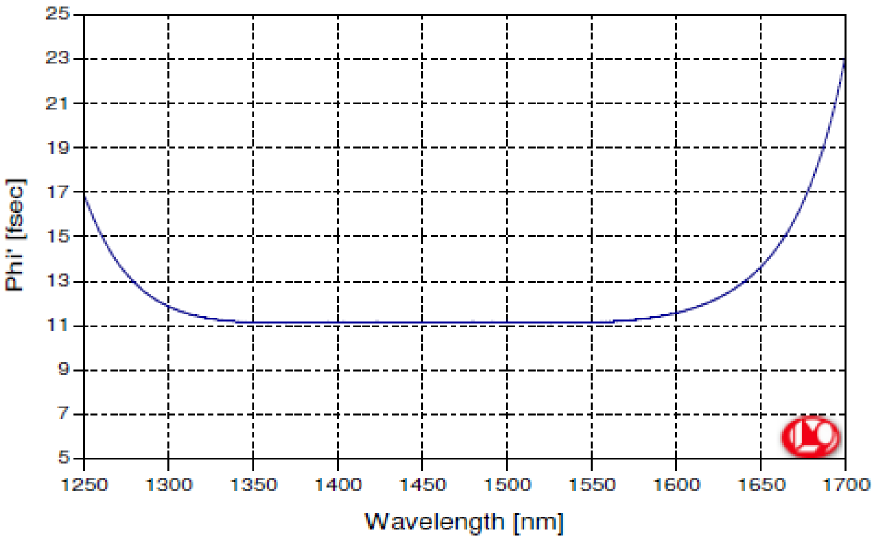

Figure 14. Time-delay curve

The FP cavity contained two low dispersion planar 99 % reflectivity mirrors covering the wavelength range from 1.35-1.6 µm. High reflectivity mirrors reduce the output power, but ensure narrower transmission peaks with good frequency sideband suppression. These mirrors were also coated for 780 nm wavelength with 99 % reflectivity, corresponding to the wavelength of the Rb-stabilized external cavity diode laser (ECDL) which was used for FP cavity alignment since the ECDL is single mode laser and it is easier to use it for alignment than the comb. Before the FP cavity, the ECDL and comb beams were overlapped. Then the efficiently filtered comb was used for locking the FP cavity. The time-delay curve of the mirrror coating is shown in Figure 14. A constant time-delay is critical for insuring an invariant free spectral range (FSR) across the full bandwidth of the OPO pulses. As we can notice from the presented data, the time-delay is quite flat for the wavelengths from 1350-1560 nm.

The FSR of the FP cavity was locked to the 31st harmonic of the OPO frequency comb. A New Focus (LB1005) proportional-integral (PI) amplifier was used for the FP cavity length locking. The output from the PI amplifier containing the dither signal was connected to PZT1 in the FP cavity. A 10.66-Hz sine wave was introduced to the 'sweep in' of the PI amplifier to produce a transmission peak at PD1 for the filtered frequency comb. The high frequency dither modulation (9.2 kHz, 40 mV peak-peak , corresponding to 0.8-nm cavity length change) was generated in a low noise lock-in amplifier (SRS810 DSP). The dither signal was applied on to PZT1 to generate a low distortion oscillation on top of the transmitted comb signal via the 'mod in' port of the PI amplifier. The acquired signal was high pass filtered, amplified and mixed with the same amplified 9.2 kHz frequency. The acquired derivative signal was used as an error signal. It was connected to the 'error in' input of the PI amplifier. The output signal from the PI controller was applied to PZT1 for the cavity length stabilization. As a result, the FP cavity was locked directly to the comb. When the frequency comb was fully stabilized together with the FP cavity length, a stable transmitted power was obtained. The filtered and fundamental signals from PD2 are presented in Figure 15.

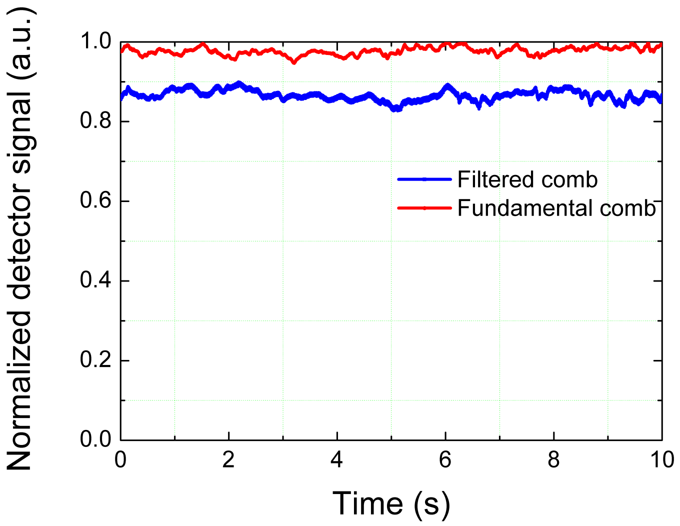

Figure 15. The power of the fundamental and filtered frequency combs over 10-seconds observation time.

Over 10 seconds the measured photodetector signal gave a peak to peak variation of 7%. This variation corresponds to a cavity length change of around 0.6 nm (from simulation). The filtered frequency comb power instability is determined by fundamental frequency comb instability. The relative intensity noise (RIN) power spectra of the fundamental and filtered frequency comb are presented in Figure 16. Over a 10-seconds time window an RMS power variation of 0.99% and 1.3% for the fundamental and filtered frequency combs was recorded. This suggests that our FP cavity length locking loop does not add significant noise. The FP cavity length could remain locked for several tens of minutes. The limitations for maintaining the locking were sensitivity to strong vibrations or the PZT1 drifting out of locking range since the FP cavity length would thermally expand or contract over time. In this case, the locked FP could track the unlocked repetition rate of the Ti:sapphire laser. Spectral filtering results for the FP locked directly to the comb are presented in the following section.

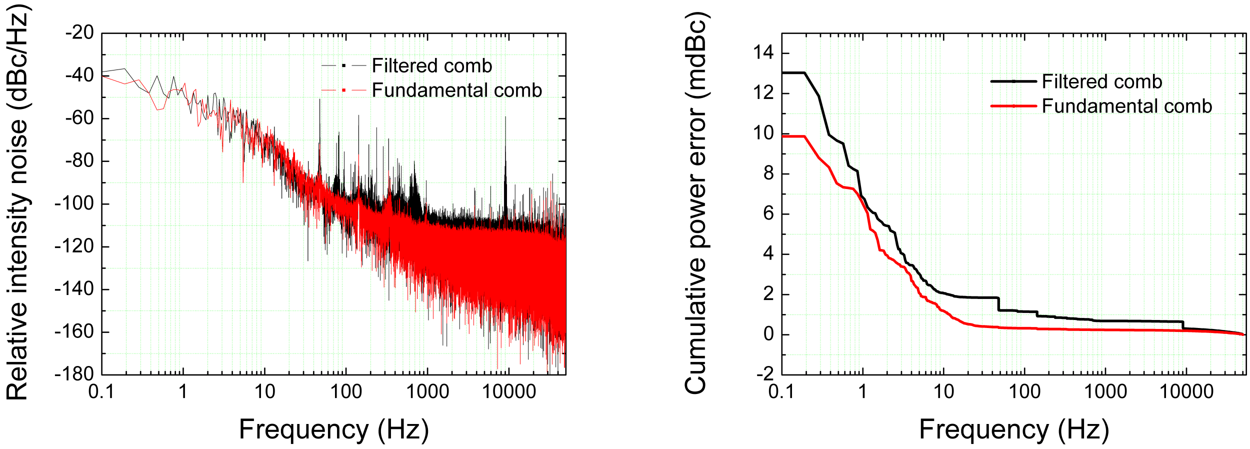

Figure 16. (a) Relative intensity noise and (b) power variation of the the fundamental and filtered combs.

7.5 10-GHz comb generated by filtering with a stabilized Fabry-Pérot cavity

The filtered frequency comb was detected and stabilized on the signal from the fast photodiode PD1 and the corresponding filtered frequency comb spectrum in the radio-frequency (RF) domain detected by PD2 is presented in Figure 17. The RF spectrum shows a frequency comb with a 10.66-GHz mode spacing with a side mode suppression of 19 dB. Cascaded FP cavities can be implemented for obtaining higher side mode suppression. The optical spectrum of the fundamental and filtered stabilized frequency combs were recorded after beam splitter BS1 and are indicated in Figure 18. The measured power of the transmitted frequency comb was 0.3 mW where in comparison the fundamental power before FP cavity was 20 mW. The transmitted power corresponds to 1.5 % of the fundamental power. A 96.8 % decrease in power is expected due to the spectral filtering from 333 MHz to 10.66 GHz, however a small additional decrease in power might be related to imperfect mode-matching of the fundamental and harmonic combs associated with the use of plane-plane mirrors in the FP cavity. The measured FWHM bandwidth of the spectrum was 25 nm which was quite similar to the bandwidth measured for the fundamental OPO comb spectrum.

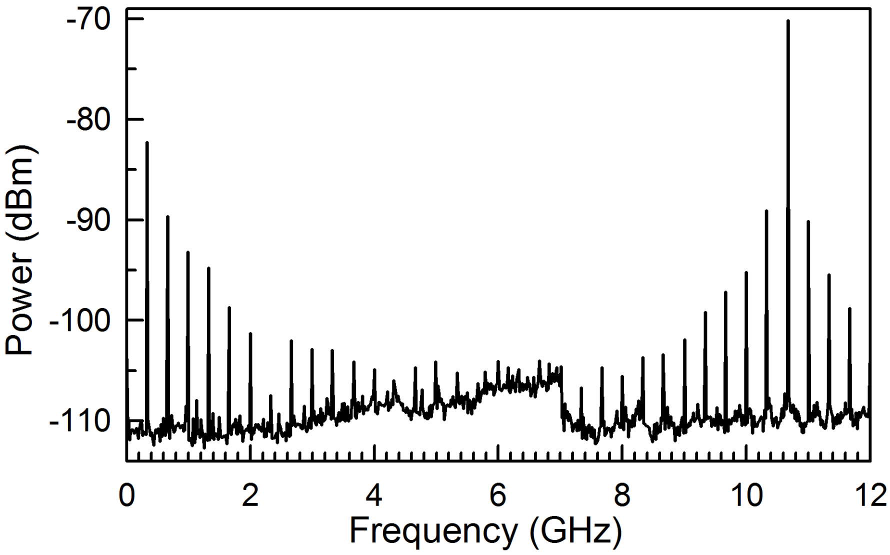

Figure 17. RF spectrum of the transmitted comb at 10.66-GHz frequency, recorded by PD1 with a resolution of 1-kHz.

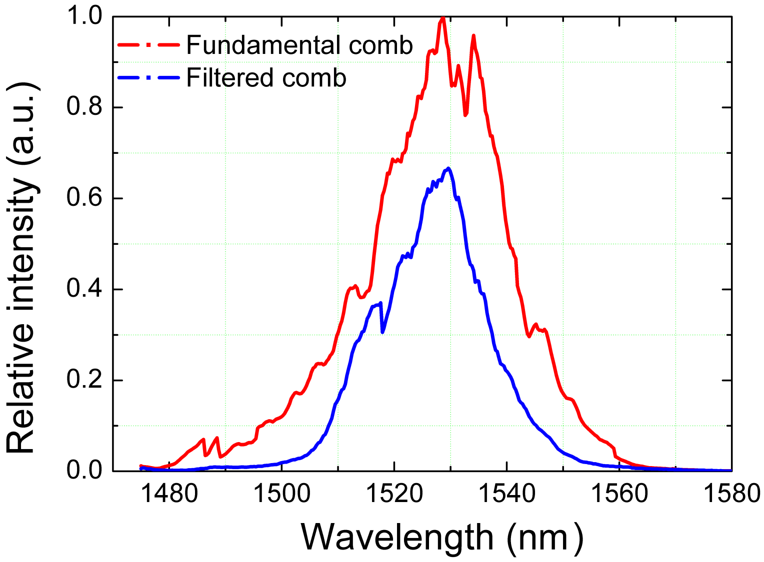

Figure 18. The incident (red curve) and filtered (blue curve) optical spectra of the frequency combs. The measurement resolution was 2 nm.

The 10.3-GHz mode spacing frequency comb achieved by directly locking the FP cavity to the comb was resolved with a high-resolution Fourier transform infrared (FTIR) spectrometer [25, 26] (see Figure 19). A long travel motorized stage (Thorlabs Part No.: DDSM100/M) containing two retroreflectors was used to change the optical path difference (OPD) of the two interferometer arms by up to 40 cm, resulting in a spectral resolution of 0.025 cm^{-1}. This spectral resolution corresponds to 0.75 GHz in the frequency domain.

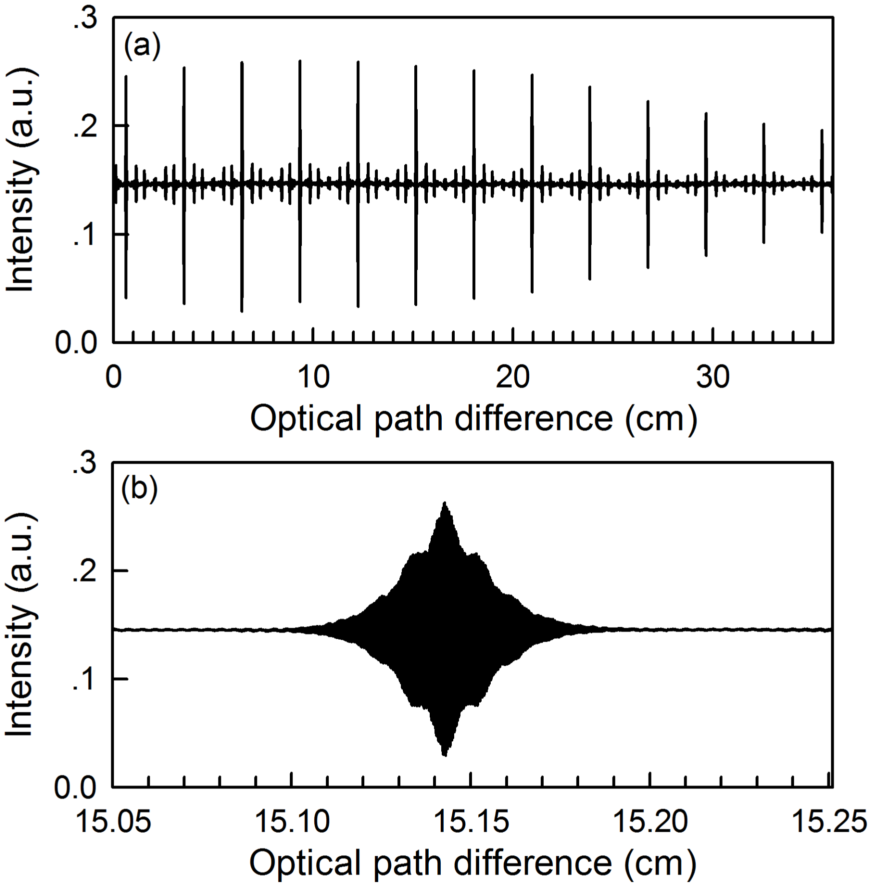

Figure 19. (a) Measured interferogram of the 10.3-GHz comb, and (b) one of the sub-interferograms (zoomed).

The FTIR interferometer was calibrated by a 632.8-nm He-Ne reference laser. The apodized optical path difference for the calculation of the spectrum was 36-cm which corresponds to a resolution of 0.028-cm^{-1} or 0.83-GHz. The interferograms were sampled with a 16-bit digital acquisition card at a sampling rate of 2-Msamples per second.

The generated interferogram of the comb is presented in Figure 19(a). The pulse spacing in the time domain was about 97 ps which means with a 36-cm OPD we can acquire 13 interferograms of the filtered combs. The time window is equal to 36 cm divided by the speed of light, resulting in a 1200-ps gate time. The satellite interferograms are due to the small reflections from the Ge and Si windows which were used as long pass filters. These satellites were removed manually before the calculation of the transmitted spectrum via Fourier transforming the interferogram. An arbitrary interferogram is shown in Figure 19(b). The retrieved spectrum contained comb lines which are too closely spaced to see therefore we zoomed in (see Fig. 20(a), (b), (c)). We can clearly distinguish individual modes separated by 10.3 GHz frequency. The spacing of 10.3 GHz corresponds to about 14-mm distance between FP cavity mirrors. Therefore, in this result, the use of high reflectivity plane-plane mirrors resulted in effective mode filtering to the 31st order harmonic of the 333-MHz fundamental frequency comb.

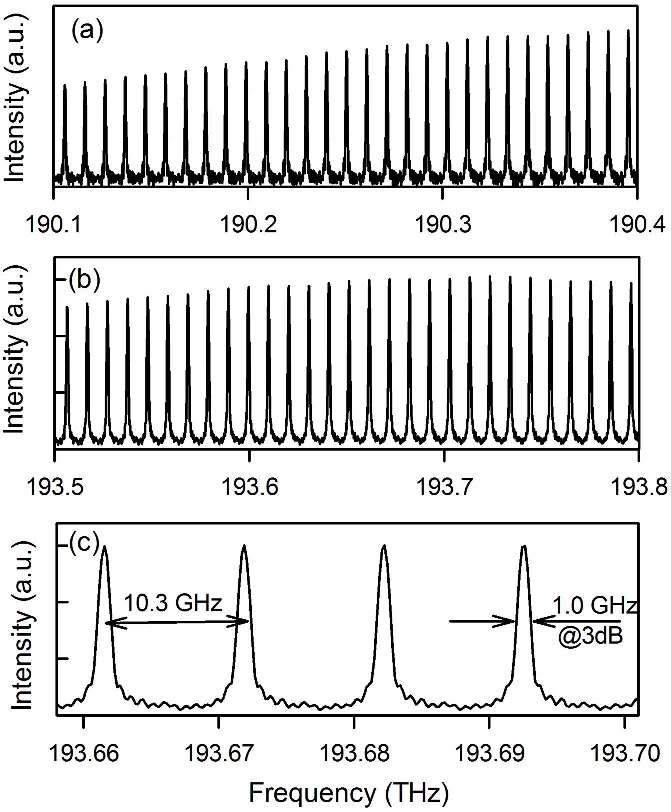

Figure 20. Spectra of the 10.3-GHz comb shown with spans of (a, b) 300 GHz and (c) 40 GHz.

The resolution of the FTIR measurement is 1.0 GHz which matches the measured linewidth of the frequency comb line (see Fig. 20(c)). This result represented the first example of a comb line resolved spectrum from an OPO based frequency comb system.

7.6 Conclusions

The longitudinal modes of a 333-MHz OPO frequency comb were filtered to >10 GHz by employing a Fabry-Pérot cavity whose length was locked to the ECDL and directly to the fundamental frequency comb. The FP cavity was locked to filter the comb up to 10 GHz. In this way we achieved reliable multi-GHz laser frequency combs by FP filtering. A 333-MHz sideband suppression of up to 19 dB was measured which could be improved by a factor of two if a double-pass system were used. The FP cavity locking stability was improved by increasing the vibration isolation of the system which was essential to achieve good locking performance of the cavity and therefore the filtering of the comb. The filtered comb modes were resolved with a 0.83-GHz resolution Fourier-transform spectrometer. Such a fully stabilized multi-GHz optical frequency comb can potentially be used in precision spectroscopy, as a wavelength calibrator of spectrometers or in other metrology applications. This work was reported in reference [19].

References

[1] S. A. Diddams, L. Hollberg, and V. Mbele, ”Molecular fingerprinting with the resolved modes of a femtosecond laser frequency comb,” Nature 445, 627–630 (2007).

[2] A. Bartels, D. Heinecke, and S. A. Diddams, ”10-GHz self-referenced optical frequency comb,” Science 326, 681 (2009).

[3] T. Steinmetz, T. Wilken, C. Araujo-Hauck, R. Holzwarth, T. W. Hänsch, L. Pasquini, A. Manescau, S. D'Odorico, M. T. Murphy, T. Kentischer, W. Schmidt, and T. Udem, ”Laser frequency combs for astronomical observations,” Science 321, 1335–1337 (2008).

[4] F. Quinlan, G. Ycas, S. Osterman, and S. A. Diddams, ”A 12.5 GHz-spaced optical frequency comb spanning >400 nm for near-infrared astronomical spectrograph calibration,” Rev. Sci. Instrum. 81, 063105 (2010).

[5] C. E. Cramer, C. H. Li, A. J. Benedick, G. A.G., K. F.X., D. F. Phillips, D. Sasselov, A. Szentgyorgyi, and R. L. Walsworth, ”Astro-comb: revolutionizing precision spectroscopy in astrophysics,” in IAU Symposium 253 (2008).

[6] T. Steinmetz, T. Wilken, C. Araujo-Hauck, R. Holzwarth, T. W. Hänsch, L. Pasquini, A. Manescau, S. D'Odorico, M. T. Murphy, T. Kentischer, W. Schmidt, and T. Udem, “Laser frequency combs for astronomical observations,” Science 321, 1335–1337 (2008).

[7] A. A. Savchenkov, A. B. Matsko, V. S. Ilchenko, I. Solomatine, D. Seidel, and L. Maleki, ”Tunable optical frequency comb with a crystalline whispering gallery mode resonator,” Phys. Rev. Lett. 101, 093902 (2008).

[8] D. Huang, E. A. Swanson, C. P. Lin, J. S. Schuman, W. G. Stinson, W. Chang, M. R. Hee, T. Flotte, K. Gregory, C. A. Puliafito, and et, ”Optical coherence tomography,” Science 254, 1178–1181 (1991).

[9] K. L. Vodopyanov, I. Makasyuk, and P. G. Schunemann, ”Grating tunable 4-14 μm GaAs optical parametric oscillator pumped at 3 μm,” Opt. Express 22, 4131–4136 (2014).

[10] F. Adler, K. C. Cossel, M. J. Thorpe, I. Hartl, M. E. Fermann, and Jun Ye, ”Phase-stabilized, 1.5W frequency comb at 2.8-4.8 μm,” Opt. Lett. 34, 1330-1332 (2009).

[11] R. A. McCracken, I. Gianani, A. S. Wyatt and D. T. Reid, ”Multi-color carrier-envelope-phase stabilization for high-repetition-rate multi-pulse coherent synthesis,” Opt. Lett. 40, 1208-1211 (2015).

[12] T. I. Ferreiro, J. Sun, and D. T. Reid, ”Composite 1-GHz Optical Parametric Oscillator Frequency Comb from 400 - 1900 nm,” Opt. Express 19, 24159-64 (2011).

[13] X. P. Zhang, J. Hebling, A. Bartels, D. Nau, J. Kuhl, W. W. Rühle, and H.Giessen, ”1-GHz-repetition-rate femtosecond optical parametric oscillator,” Appl. Phys. Lett. 80, 1873-1875 (2002).

[14] M. Vainio, M. Merimaa, L. Halonen, and K. Vodopyanov, ”Degenerate 1-GHz repetition rate femtosecond optical parametric oscillator," Opt. Lett. 37, 4561- 4563 (2012).

[15] K. Balskus, S. M. Leitch, Z. Zhang, R. A. McCracken, and D. T. Reid, ”1-GHz harmonically pumped femtosecond optical parametric oscillator frequency comb,” Opt. Express 23, 1283-1288 (2015).

[16] W. Li and J. Yao, ”Optical frequency comb generation based on repeated frequency shifting using two Mach-Zehnder modulators and an asymmetric Mach-Zehnder interferometer,” Opt. Express 17, 23712-23718 (2009).

[17] T. Sizer, ”Increase in laser repetition rate by spectral selection,” IEEE J. Quantum Electron. 25, 97–103 (1989).

[18] T. Udem, J. Reichert, R. Holzwarth, and T. W. Hänsch, ”Absolute optical frequency measurement of the Cesium D1 line with a mode-locked laser,” Phys. Rev. Lett. 82, 3568–3571 (1999).

[19] Zhaowei Zhang, Karolis Balskus, Richard A. McCracken, and Derryck T. Reid, ”Mode-resolved 10-GHz frequency comb from a femtosecond optical parametric oscillator,” Opt. Lett. 40, 2692-2695 (2015).

[20] D.A. Braje, M. S. Kirchner, S. Osterman, T. M. Fortier, and S. A. Diddams, ”Astronomical spectrograph calibration with broad-spectrum frequency combs,” Eur. J. Phys D 48, 57-66 (2008).

[21] M. S. Kirchner, D. A. Braje, T. M. Fortier, A. M. Weiner, L. Hollberg, and S. A. Diddams, ”Generation of 20 GHz, sub-40 fs pulses at 960 nm via repetition-rate multiplication,” Opt. Lett. 34, 872-874 (2009).

[22] T. I. Ferreiro, T. P. Lamour, J. Sun and D. T. Reid, ”1.4 GHz femtosecond comb generation by Fabry-Pérot filtering of optical parametric oscillator frequency comb,” Electronics Letters 49, 833 (2013).

[23] J. M. Vaughan, ”The Fabry-Pérot Interferometer. History, Theory, Practice and Applications” (IOP Publishing, 1989).

[24] Airy G. B., "On the phenomena of Newtons rings when formed between two transparent substances of different refractive powers," Philosophical Magazine 2, 20-30 (1833).

[25] K. A. Tillman, R. R. J. Maier, D. T. Reid, and E. D. McNaghten, ”Mid-infrared absorption spectroscopy across a 14.4 THz spectral range using a broadband femtosecond optical parametric oscillator,” Appl. Phys. Lett. 85, 3366–3368 (2004).

[26] Z. Zhang, T. Gardiner, and D. T. Reid, ”Mid-infrared dual-comb spectroscopy with an optical parametric oscillator,” Opt. Lett. 38, 3148-3150 (2013)

[27] P. R. Griffiths and J. A. de Haseth, ”Fourier Transform Infrared Spectroscopy,” (John Wiley and Sons, 2007).

Chapter 8. Absolute frequency measurement

All absolute frequency measurements are carried out relative to a ceasium fountain primary frequency standard, which realises the SI definition of the second. The best ceasium standards have instrict uncertainties of 10^{-16} [1, 2]. The microwave transition at 9.2 GHz frequency is transfered to optical domain by a frequency comb and used for a measurement of optical frequencies. The spectrum of frequency combs consists of thousands well-defined longitudinal modes separated by the repetition rate of the laser. Since extremely stable frequency standards have been demonstrated [3], these well-defined optical frequency standards can be used in a number of applications such as atomic spectroscopy or astronomy [4, 5, 6, 7, 8, 9]. Narrow linewidth fully stabilized ultrashort laser combs are used in atomic physics, high resolution spectroscopy and frequency metrology. CW lasers linewidths down to several Hz have been measured [10, 11]. Optical frequency standards based on ions with alkali atomic structure (Ca^+, Sr^+, Yb^+ and Hg^+) have natural linewidths from 0.2-3 Hz. An optical lattice clock based on Sr atoms has been reported with systematic uncertainty to 1.5×10^{-16}. The optical lattice clock was measured against a NIST Cs fountain clock via phase coherently locked fs laser based optical frequency comb. Fractional frequency uncertainties of 1.9×10^{-17} and 2.2×10^{-17} have been achieved for the (199)Hg^+ and (88)Sr^+ ions by beating these two optical frequencies with one optical frequency comb referenced to ceasium fountain clock [12, 13]. The best to date frequency uncertainty of 8.6×10^{-18} was measured by comparing two (27) Al^+ ion clocks [14].

In this chapter I present the results of absolute frequency of a CW laser obtained by heterodyning a frequency comb line from an OPO with the CW laser light referenced to a Rb transition. The acquired heterodyne beat in the radio frequency (RF) region can be easily compared with the well-known Rb reference. The linewidth of the comb line was determined by heterodyning a frequency comb line with an ultra-narrow linewidth CW laser. From frequency noise PSD measurement a spectral distribution of the noise was determined. This noise characteristic was used to identify external/internal noise sources [15]. Moreover, from such acquired data the linewidth of the comb lines could be calculated. The feedback loop bandwidth of the locked systems could be estimated and compared with unlocked systems from the frequency noise PSD. The difference in the acquired PSD data showed at which frequencies the noise was suppressed, allowing the real servo loop bandwidth to be estimated.

8.1 Introduction

It has been challenging to establish well-defined frequencies in the optical domain because of the complicated connection between optical and microwave frequencies until the invention of modelocked femtosecond Ti:sapphire laser in 1991. Different methods have been developed over decades but the real breakthrough was achieved after the development of ultrafast lasers which enabled frequency metrology. Using these sources a direct, phase-locked relationship between the optical and microwave domains could be made [16]. For the contributions to the development of laser based precision spectroscopy including the optical frequency comb technique John L. Hall and Theodor W. Hänsch received a Nobel Prize in 2005 [16, 17]. High accuracy frequency standards become an important method not only for new generation optical clocks [18, 19], but also for such applications as high resolution spectroscopy. Very accurate frequency domain comb lines with narrow linewidths can be used to determine the exact spectroscopy of atoms and molecules from the UV to the mid-IR region. Broadband and tunable pulses from OPOs can cover broad wavelength ranges in the near- and mid-IR region at once which enables simultaneous CO_2, acetylene, H_2O and other molecular detection. Since the frequency comb from an OPO is linked directly with the microwave source, the resulting phase locked relationship ensures high precision frequency combs [20, 21].

Frequency combs can be achieved by locking the carrier phase of the modelocked laser and repetition rate to a frequency standard based on Cesium or Hydrogen. In the measurements described later in this chapter our frequency comb was referenced to a hydrogen maser (H-maser) optical reference. The H-maser clock oscillates at 10 MHz frequency which was the reference frequency for all of our devices used in the laboratory. The use of the H-maser clock can ensure the fractional stability of the frequency comb's repetition rate or carrier-envelope-offset to 1×10^{-12} for a 1-second gate time. The H-maser clock can be referenced to a GPS disciplined rubidium oscillator which has better long term stability (>100s). The referenced frequency combs can be used in metrology directly for measuring transition frequencies [22, 23, 24, 25, 26, 27, 28, 29]. There were a number of experiments at National Institute of Standards and Technology (NIST) and other facilities proving that the performance of the optical clocks are not limited by locked frequency combs [30]. Two-comb comparison has been demonstrated by measuring the ratio of two optical frequencies. By comparing two combs an uncertainty of 3×10^{-21} was obtained [31].

The first ever self-referenced high peak power optical frequency combs were based on Ti:sapphire lasers [32, 33]. The phase-locked frequency combs opened new ground for spectroscopy [34]. The repetition rate of these lasers could be tuned up to tens of GHz [35]. After several years self-referenced fiber based frequency combs were developed [36] which are now the most common practice in commercial systems since such systems are compact, efficient and relatively cheap. However, the drawback of fiber based systems are high frequency noise and relatively broad linewidth of the comb lines. Low quality factor cavities and nonlinear effects increase the linewidth which is not the case for solid state lasers. In general much faster feedback bandwidth must be employed in order to compensate the noise, unless the system is extremely stable and isolated from environmental noise sources [37]. Many other frequency comb sources for molecular spectroscopy have been developed during the following years [39, 40, 41, 42, 43, 44].

In this metrology study we used a femtosecond OPO based on a PPKTP crystal pumped by a 30 fs Ti:sapphire laser to produce frequency combs with a 1560-nm central wavelength.

This OPO was developed to generate broadly tunable frequency combs from 1.0-4.2 μm for high resolution spectroscopy but it can be used for optical frequency metrology as well. For this reason we shipped our 333-MHz repetition rate OPO together with the pump laser to the Laboratoire Temps-Frequence based in Neuchatel (Switzerland) to do absolute frequency measurements, investigate the noise properties of an optical frequency comb and the stability of it. The development and full stabilization of the frequency comb from the OPO is presented in Chapter 3-5. Here we tuned the OPO wavelength output to 1560 nm. The stabilization of the femtosecond OPO was achieved by locking the repetition rate of the Ti:sapphire laser and the carrier-envelope-offset frequency of the signal pulses at a 1560-nm central wavelength. In the first place we did an absolute frequency measurement by heterodyning the comb line from an OPO with a Rb stabilized CW laser operating at 1560 nm wavelength. The OPO frequency comb was used to phase coherently measure the absolute optical frequency of the ^{87}Rb D_2 F=2-3 transition line. The mode number of the frequency comb was determined and therefore the absolute frequency of the CW laser calculated. In addition, the noise properties of f_{CEO}, f_{REP} and the linewidth of a comb line at 1557 nm of phase-locked system were measured. The comb line properties were determined by acquiring the heterodyne beat signal between the cavity stabilized ultra-narrow linewidth CW laser and the comb line. The properties were retrieved through the frequency discriminator technique which was applied on the frequency noise PSD of the heterodyne beat. The comb linewidth experiences a substantial increase because of repetition rate noise and an insignificant increase because of f_{CEO} locking. A linewidth of 70 kHz with fractional instability of 10^{-12} for a 1-second gate time for an optical comb line at 1557 nm was measured. The measured fractional stability of the repetition rate was limited by the stability of the RF oscillator.

8.2 Experimental setup

For determining the absolute frequency of the frequency comb line, exact knowledge of the laser repetition rate f_{REP} and carrier-envelope-offset frequency f_{CEO} are needed. Every stabilized frequency comb can be expressed as

$$f(n) = nf_{REP} \pm f_{CEO} \tag{110}$$

where the carrier-offset-frequency f_{CEO} represents the shift of the comb from 0 Hz. The sign of the f_{CEO} in the experiment is determined by the observation of the heterodyne beat as the reference frequency is changed. The determination of the sign will be explained in detail later on. Each frequency comb mode can be controlled and stabilized through the variation of f_{REP} and f_{CEO}.

For an absolute frequency measurement, a fully stabilized frequency comb of the OPO can be achieved by stabilizing both the repetition rate f_{REP} of the Ti:sapphire laser and the carrier-envelope-offset (CEO) frequency f_{CEO} of the signal pulses oscillating in the OPO cavity. In this experiment a frequency comb at 1560 nm central wavelength was achieved by synchronously pumping a 4-mirror ring type optical parametric oscillator (OPO) with a 333-MHz repetition rate Ti:sapphire pump laser centered at 800 nm wavelength (see Figure 1). The repetition rate directly scales up with the change of the cavity length which can be locked via cavity-length control. Approximately 20 mW of the depleted Ti:sapphire laser's power was used to detect the repetition rate with a high speed InGaAs photodiode (DSC40S). We used the third harmonic of f_{REP} since we did not have a bandpass filter (BPF) for higher order harmonics. Nevertheless the third harmonic enhanced the sensitivity to f_{REP} fluctuations and therefore the locking quality. After amplification, the acquired third harmonic was phase-compared with a 1 GHz reference frequency in a frequency mixer (an analog phase comparator). This 1-GHz external reference from a frequency synthesizer was phase-locked to an active 10-MHz H-maser. When the feedback loop was activated, the repetition rate of the laser was locked to the 10-MHz reference source. The acquired error signal from the frequency mixer gave an output depending on the phase error. The output was amplified in a high voltage amplifier by employing Laser Quantum's TL-1000 [45] unit whose output was connected to two PZTs placed inside the Ti:sapphire cavity for f_{REP} locking. f_{REP} was stabilized via the combination of these two fast and slow piezoelectric transducers (PZTs). The tuning coefficients were $\frac{\Delta f_{REP}}{\Delta V_{PZT1}}$=2 Hz V^{-1} for the fast PZT1 and $\frac{\Delta f_{REP}}{\Delta V_{PZT2}}$=20 Hz V^{-1} for the slow PZT.

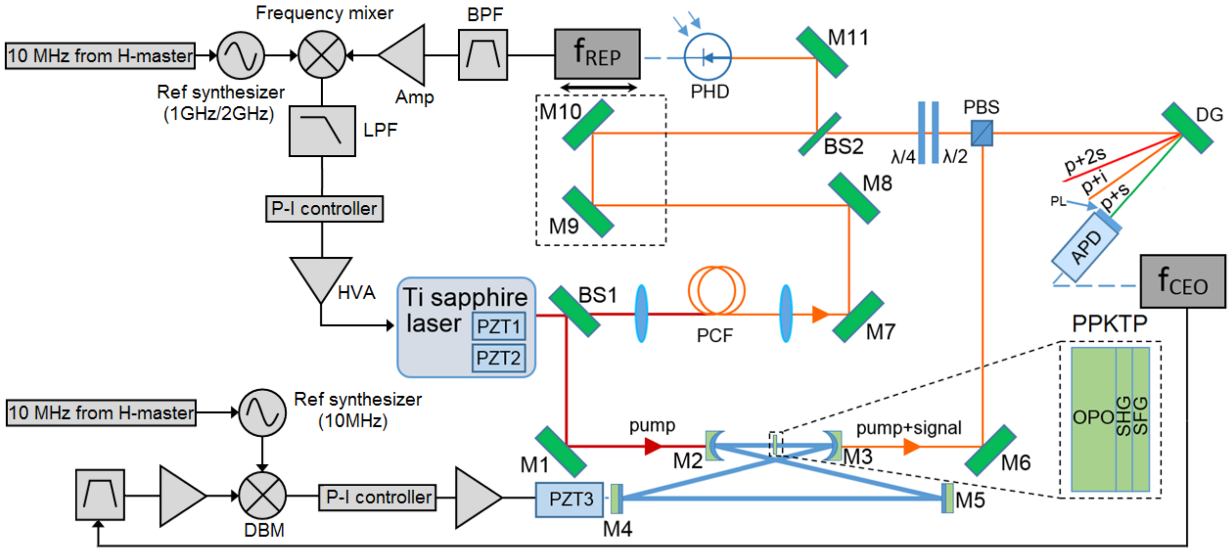

Figure 1. Layout of the PPKTP based OPO: OC, output coupler; PD, photodiode; PBS, polarizing beam splitter; DG, diffraction grating; APD, avalanche photodiode; PCF, photonic crystal fiber; BS, beam splitter. The frequencies f_{REP} and f_{CEO} were stabilized with two separate control loops.

We observed that f_{CEO} scaled up with the repetition rate. As the repetition rate changed, a change of f_{CEO} was also noticed on the order of 11 MHzV^{-1}. When the repetition rate is locked, the phase and group velocity mismatch is still in play. Every optical element placed inside the laser cavity will affect the carrier-envelope-offset via the group velocity and phase velocity mismatch. When the repetition rate of the Ti:sapphire laser is stabilized, the acquired f_{CEO} must be locked to achieve fully stabilized frequency comb. This stabilization was achieved with a feedback applied to PZT3 placed inside the OPO cavity.

The f_{CEO} of the signal pulses was acquired by heterodyning coherent pump supercontinuum light at 529 nm with non-phasematched pump-signal sum-frequency generation (SFG) light from the OPO [46]. A home-made phase-frequency-detector (PFD) was used for the phase stabilization of the f_{CEO} to a 10-MHz reference frequency (H-maser). As the phase fluctuations between the reference frequency and the f_{CEO} were obtained, the corresponding output from the PFD was acquired. Our PFD could measured phase fluctuations of up to $\pm 32\pi$. The large range of the PFD makes it easier for the feedback loop to track large phase changes which can be suppressed via a servo-controller (LB1005 servo controller) whose output is connected with PZT3 placed inside the OPO. Once the frequency comb was fully stabilized, the output coupled signal centered at 1560 nm was coupled into a single mode fiber and combined on an InGaAs biased detector (Thorlabs DET01CFC) with a common CW laser wavelength for heterodyne beat detection (see Figure 2).

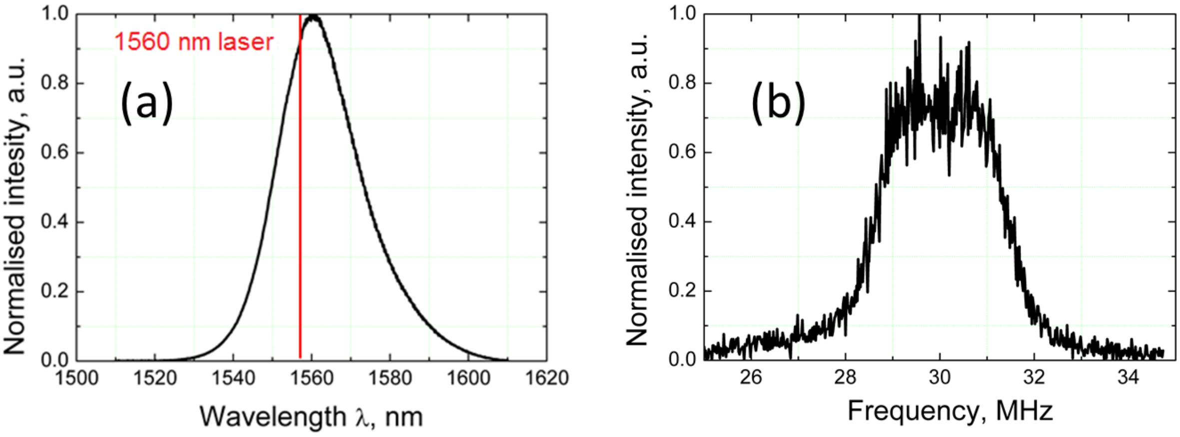

Figure 2. (a) The OC broadband pulse from OPO in comparison with a CW light, (b) The heterodyne beat between the CW laser and OPO for absolute frequency measurement.

The CW laser wavelength was frequency doubled and locked to a Rb D_2 transition line. From the mode number determination and the beat frequency an absolute frequency of the Rb D_2 transition line could therefore be calculated. The beat between the CW laser locked to a Rb transition and the frequency comb spectrum from the OPO at 1560-nm are shown in Figure 2 (b). The bandwidth of 3 MHz was measured because of the wide Rb transition line used for the CW laser's wavelength locking and the additional noise contribution because of the feedback loop.

In Figure 3 the scheme for the optical frequency measurement of a frequency doubled 1.6 μm DFB-CW-laser [47] is shown. The CW laser was stabilized to a D_2 transition line by absorption spectroscopy. The CW laser mode was heterodyned against one OPO comb line resulting in a heterodyne beat frequency. As mentioned already, if the carrier-envelope-offset, repetition rate

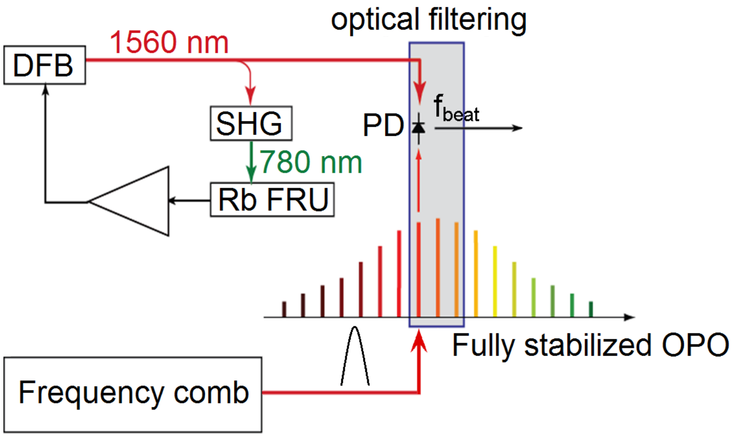

Figure 3. Measurement scheme for the absolute frequency measurement of Rb-transition stabilized CW laser. DFB is 1560-nm laser, whose second harmonic frequency locked to the Rb transition line; SHG: second-harmonic generation; FRU: frequency referenced unit; PD: photodiode.

and the beat frequency with the comb are known, an absolute frequency of the CW laser from the OPO frequency comb mode number can be extracted.

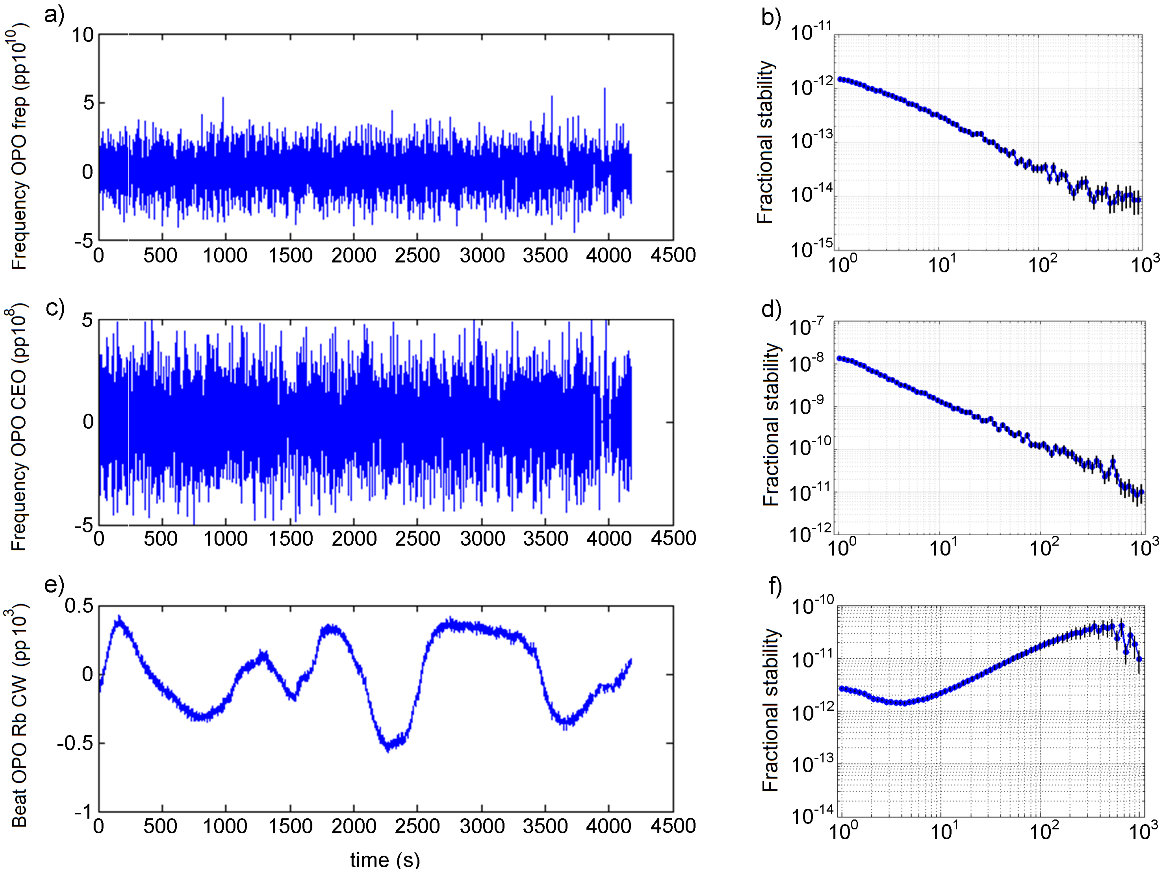

Figure 4. (a), (c), (e) represents f_{REP}, f_{CEO} and f_{BEAT} raw data and (b), (d) and (f) represent fractional instabilities accordingly calculated from Allan variance at different gate times.

To ensure that only common wavelengths were heterodyned on the detector, a bandpass filter was used. The acquired beat note was increased in strength by optimizing waveleplates, bandpass filters and polarizations. We managed to increase the strength of the beat note between one comb tooth and the Rb locked CW laser so that the four channel Menlo counter FXM50 was able to measure it. The acquired 20-dB signal to noise ratio (RBW=100 kHz) beat note was used to determine the comb number and then to calculate the absolute frequency of the Rb transition. We simultaneously counted the repetition rate f_{REP}, carrier-envelope-offset f_{CEO} and the beat note f_{BEAT} frequencies. The fractional frequency instabilities or Allan variance of the measured frequencies are presented in Figure 4. The left side of Figure 4 shows the raw data of the f_{REP}, f_{CEO} and f_{BEAT} measurements correspondingly and the right side presents the calculated Allan variance of each data set. The fractional frequency instability was calculated for 1-second gate time. From the raw data the Allan variance for other gate times up to 1000 seconds was calculated. The frequency fluctuations were measured simultaneously using a multi-channel digital frequency counter (Menlo frequency counter FXM50). The FXM50 counter is a Π-type counter which was measuring the frequency wihout averaging it. The data was recorded for 1-s gate time. From the measurement the Allan deviation was extracted for different gate times. The difference between the Π-type and Λ-type counters explained in Chapter 4.

The fractional instability of the repetition rate and carrier-envelope-offset frequency were calculated by dividing their Allan variance by the repetition rate f_{REP} harmonic (we detected the 45th harmonic) and the 10-MHz reference frequency for the f_{REP} locking accordingly. The measured frequencies of f_{REP} and f_{BEAT} can be stabilized to 10^{-12} level for a 1-s gate time. The locking of f_{REP} was limited by the RF oscillator used as a reference source for all locking loops. The f_{BEAT} fractional stability was calculated in optical domain (Allan variance divided by 384.228-THz frequency). In the case of the carrier-envelope-offset f_{CEO} the fractional instability was as low as 10^{-15}. It is more important to achieve better stability of f_{REP} than the stability of f_{CEO}. For example, the fractional instability for mode number of 1,000,000 will be much higher since the measured fractional instability of f_{REP} must be multiplied by the mode number. As a result, comb instability is mainly affected by the quality of f_{REP} than the f_{CEO} locking and by the H-Maser's stability [48].

With the frequency counter we were able to calculate fractional fluctuations of the measured frequencies from the absolute values. These absolute frequencies were used to calculate the mode number of the frequency comb line. From the beat note the optical frequency of the Rb transition can be expressed as

$$\frac{f_{Rb}}{2} = n f_{REP} \pm f_{CEO} \pm f_{BEAT} \tag{111}$$

where f_{Rb} = 192.114 THz since the CW laser frequency was locked to the ^{87}Rb D_2 F=2-3 transition line. When we heterodyne the modes, the beat can appear on both sides of the comb line tooth. For this reason a sign determination is needed. If the beat note when the repetition frequency of the Ti:sapphire laser is increasing is also increasing, the Rb locked laser's frequency is on the lower side of the comb tooth. The f_{BEAT} has negative sign. If a repetition rate increase reduces the f_{BEAT} frequency, it means that the sign is positive i.e. the CW laser's frequency is higher than the comb line frequency. The CW laser frequency is on the higher frequency side of the comb tooth. For the determination of the f_{CEO} sign, the reference frequency for the f_{CEO} locking was increased by 1 MHz and the frequency of the f_{BEAT} beat measured. The increase of the beat frequency gave negative sign while a decrease yielded positive sign for f_{CEO}. Once all signs were clarified and frequencies identified, the mode number n of the frequency comb line could be calculated using

$$n = \frac{\frac{f_{Rb}}{2} \pm f_{CEO} \pm f_{BEAT}}{f_{REP}} \tag{112}$$

n should be an integer number, which from the experimental data was found to be true to about 0.0001. There are many small uncertainties which limit the accuracy of determining the exact beat frequency, repetition rate or carrier-envelope-offset frequencies and therefore the mode number n. For example, our CW laser, which was locked by saturation absorption to a Rb line, was not stable (see Figure 5(a)). Figure 5(b) illustrates oscillations which correspond to the fluctuations of the CW laser frequency at 780 nm. The Rb locked CW laser was not stable. The low frequency drift of the f_{BEAT} was evident for every measurement. We think the variation of the CW laser's frequency was due to etalon fringes in the laser setup which can shift with temperature fluctuations. Up to a 20-kHz f_{BEAT} variation was measured. This shift couples into the measurement of the beat note and therefore to the uncertainty of the determination of mode number and the calculation of the Rb transition line. These two beats were measured in different labs with different counters. They were roughly adjusted in order to compare quantitatively the two measurements. The goal at this point was only qualitative. Once the measurement was running, the beat could stay locked for several hours until the f_{CEO} of the frequency comb degraded below the 35-dB signal-to-noise ratio (at RBW=100 kHz) necessary for our electronics. The loss of the beat strength was due to the thermal drift, and the temperature of the laboratory. The f_{CEO} frequency locking could be be quickly reacquired by some careful adjustments. Here we present f_{REP}, f_{CEO} and f_{BEAT} measurements obtained at the same time.

8.3 Absolute mode number and frequency determination

The absolute mode number can be measured using two methods. The first one involves a second well known frequency source (reference). In this case we are measuring the frequency within the uncertainty of the repetition rate of the laser and f_{CEO}. It is easier to use this method for higher repetition rate systems since the spacing in terms of frequency between comb lines is bigger. On the other hand we can use a method which does not require a reference. We can determine the absolute frequency or/and the mode number by slowly changing the repetition rate so that different comb modes will heterodyne beat with the same CW laser.

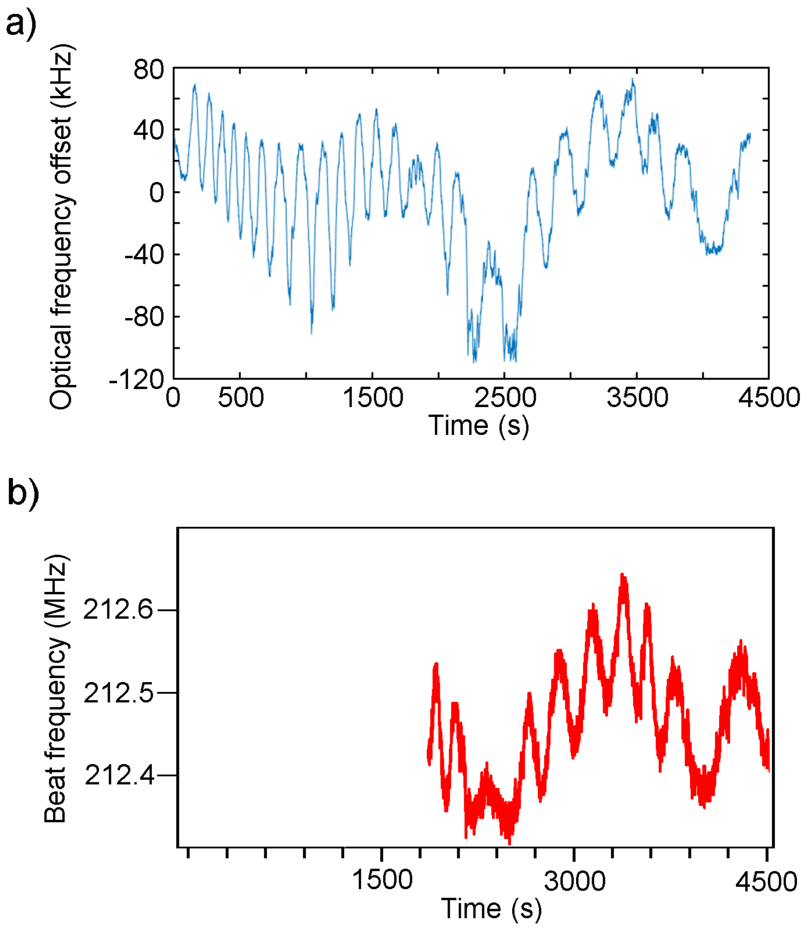

Figure 5. (a) The heterodyne beat frequency between the CW laser and the OPO, (b) The direct measurement of the CW laser frequency at 780 nm between the frequency-doubled laser locked to the Rb transition and another 780-nm reference laser (locked to another Rb transition).

Unfortunately the mode number n must be changed by a significant amount which means the modelocked laser's repetition rate must remain stable when it is changed by at least several tens of thousands Hz which is not easy to do in our case. Our modelocked laser lost repetition rate locking if the repetition rate was changed by more than 5 kHz. Ring type cavities are more sensitive to cavity length tuning than linear ones. Lets say, if our mode number is 600,000, then the different comb modes will be heterodyne beat with the Rb locked CW laser only when the f_{REP} reference frequency on the synthesizer will be changed by 555 Hz. It means that only 9 different modes will be heterodyned with the CW laser before losing the repetition rate locking. The laser cavity length cannot be changed by a significant amount. Also the uncertainty of the heterodyne beat is higher than 5 kHz which makes it much harder to determine when the CW laser mode is heterodyned with a second, third and so on frequency comb line. The gate time of the frequency counter must be increased by a significant amount in order to reduce the heterodyne beat uncertainty. Therefore we decided to use the first method for mode number and absolute frequency determination.

As the heterodyne beat was acquired, the sign of the f_{CEO} and f_{BEAT} must be determined. For this f_{REP} was increased by 40 Hz in frequency and the f_{CEO} increased by 1 MHz. As a result, the measured f_{BEAT} frequency was shifting depending on which side of the frequency comb mode the CW laser frequency was located (see Figure 6(a)). As we increased the repetition rate by 40 Hz, the heterodyne beat shifted in frequency by almost 8 MHz. This was the case since we are beating about the 500,000th mode with the single mode CW laser. Consequently the 40-Hz increase must be scaled up by 600,000 in order to see the real shift in frequency domain. Notice, we are using the third harmonic for repetition rate locking and therefore the calculated value must be divided by 3 in order to know the exact change in the frequency domain of the heterodyne beat. The heterodyne beat is shifting with the carrier-envelope-offset too. As we increased the reference frequency for f_{CEO} locking, the heterodyne beat also reduced by 1 MHz. The heterodyne shift can be imagined by looking into the RF spectrum presented in Figure 6(b). As the repetition rate of the Ti:sapphire laser was increased, the distance between the Rb locked CW laser and the comb line reduced resulting in a smaller f_{BEAT} frequency. It means that the CW laser's frequency is bigger than the comb tooth frequency. As we increased the f_{CEO} frequency by 1 MHz, the f_{BEAT} frequency was reduced by 1 MHz. The sign is therefore determined to be negative too.

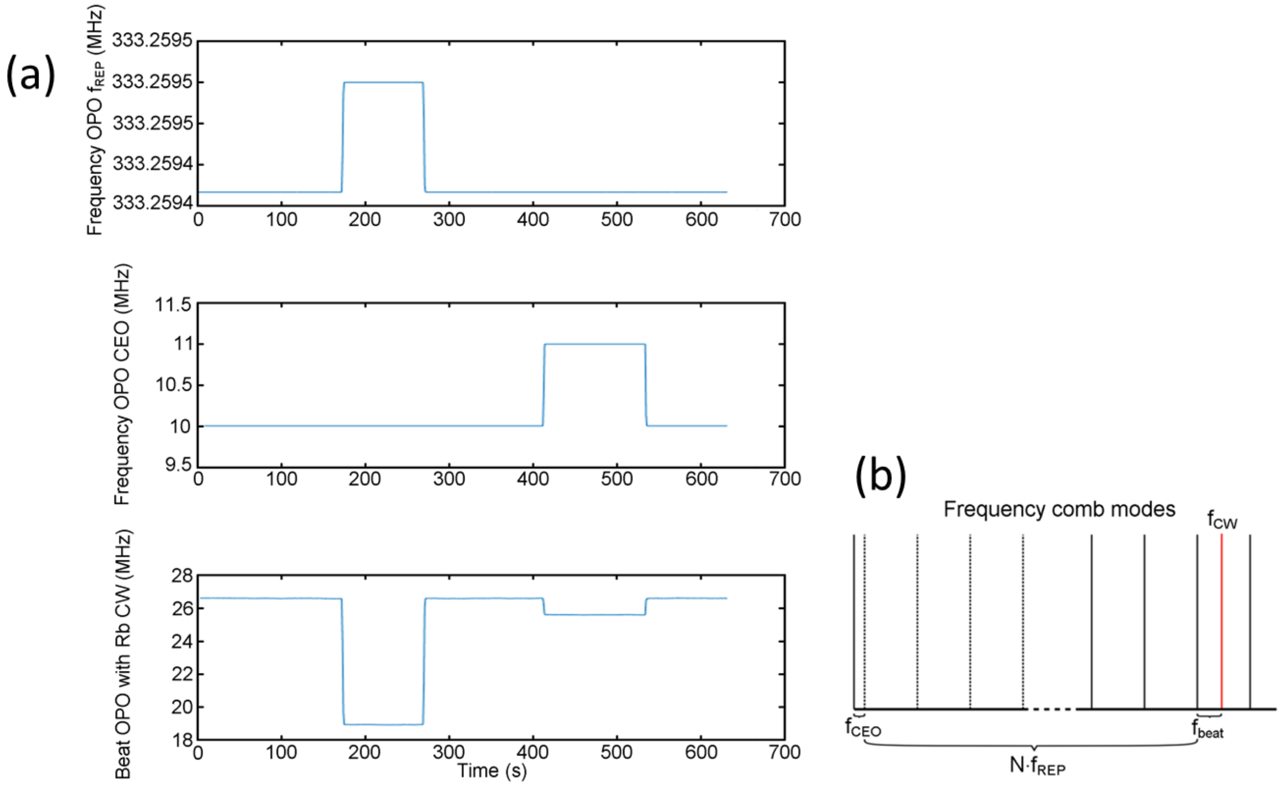

Figure 6. (a) The measured frequency of beat note when the repetition rate and carrier-envelope-offset frequencies are changed by 40 Hz and 1 MHz accordingly, (b) The frequency comb mode spacing in frequency domain in comparison with a Rb stabilized CW laser.

As the sign of the variables was defined, we were able from the measured absolute frequencies of f_{REP}, f_{CEO} and f_{BEAT} to calculate the frequency comb mode number which was heterodyned with the common CW laser frequency. The calculated mode number was 576,445 (see Table 1). This corresponded to a frequency of 192,114,057,632.8 Hz. The theoretical frequency of the well-defined Rb locked CW laser is 192,114,057,601.6 Hz. This result has a frequency offset of 31.2 kHz. The uncertainty comes from a fluctuating Rb locked CW laser since the Allan deviation of the repetition rate f_{REP} was 0.00046 Hz resulting in a 265.16-Hz uncertainty for a 576,446 mode number. The f_{CEO} instability adds 0.084-Hz instability, but the main noise comes from the CW laser since the calculated Allan variance of the beat note f_{BEAT} was 37.5 kHz. The heterodyne beat had a linewidth of about 1 MHz which results in an absolute frequency measurement uncertainty. The main reasons for the frequency shift of the laser from the reference Rb frequency are probably the Doppler background in the error signal of the laser stabilization, the effect of the residual amplitude modulation of the laser that results from the current modulation applied to generate the error signal, and of course the effect of the etalon fringes due to some fibered components.

Table 1. Absolute frequency calculation and comparison with a commercially available fiber laser based frequency comb.

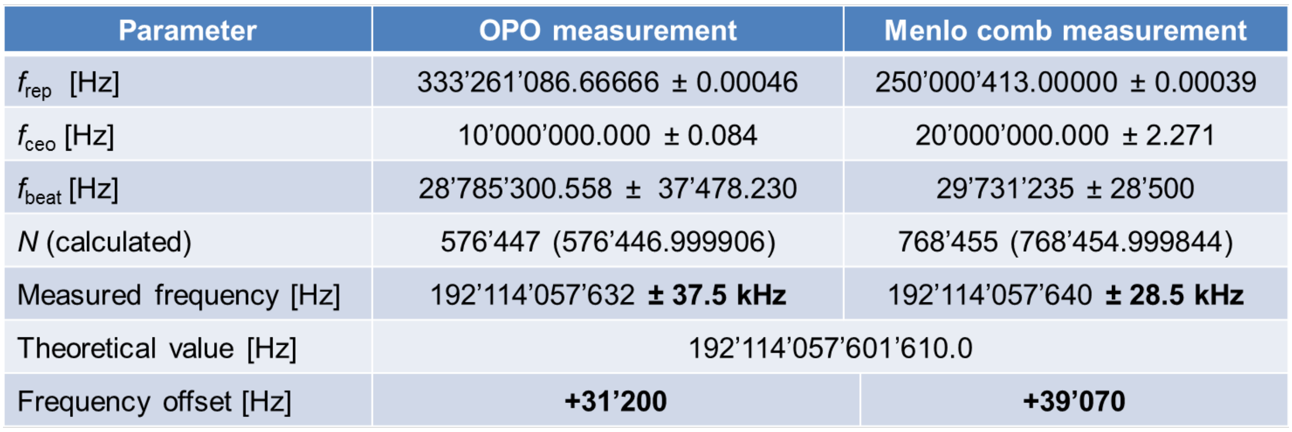

Parameter	OPO measurement	Menlo comb measurement
f_{rep} [Hz]	333'261'086.66666 ± 0.00046	250'000'413.00000 ± 0.00039
f_{ceo} [Hz]	10'000'000.000 ± 0.084	20'000'000.000 ± 2.271
f_{beat} [Hz]	28'785'300.558 ± 37'478.230	29'731'235 ± 28'500
N (calculated)	576'447 (576'446.999906)	768'455 (768'454.999844)
Measured frequency [Hz]	192'114'057'632 **± 37.5 kHz**	192'114'057'640 **± 28.5 kHz**
Theoretical value [Hz]	192'114'057'601'610.0	
Frequency offset [Hz]	**+31'200**	**+39'070**

The frequency counter measures with mHz resolution. We did not measure directly frep due to the lack of sensitivity of the counter. For frep, we used a high harmonic at 15 GHz (45th harmonic) and frequency down-converted it in the counter measurement range (<50 MHz). This enabled us to measure the frequency with mHz resolution. The value of frep was obtained by $(f_{counter} + f_{synth})/45$. That is the reason why we got a better resolution and can give f_{rep} at the 5th digit after the point. The f_{ceo} and f_{beat} are measured at the mHz level buy directly pluging the signal into the counter.

The absolute frequency measurement of the OPO was compared with an Er-fiber comb (FC1500-250 from Menlosystems, 250 MHz repetition rate). The measured frequency offset was similar for both combs. We think the main contribution of the uncertainty came from the Rb stabilized CW laser stabilization scheme. Both extracted values exhibit an offset to a few tens of kHz due to interferometric noise in the Rb-stabilized laser.

By counting f_{REP}, f_{CEO} of the frequency comb and f_{BEAT} of the heterodyne signal between an OPO comb line and a 1557-nm CW laser (frequency doubled and stabilized to a ^{87}Rb D_2 F=2-3 transition via saturated spectroscopy setup), we were able to demonstrate the first metrology application of a femtosecond OPO frequency comb. A frequency of $384,228,115.347 \pm 0.015$ MHz of the CW laser was calculated. This result overlaps with the frequency determined using a commercial Er:fiber comb.

8.4 Frequency discriminator

The analysis of the noise properties of a heterodyne beat signal can be made using a phase locked loop (PLL) [15] where the PLL is based on a frequency to voltage converter. This type of frequency discriminator is based on a voltage-controlled oscillator (VCO). The VCO (Mini-Circuits ZX95-209-S+) was phase locked to the RF heterodyne beat signal via a high bandwidth PI controller whose output was connected to the VCO. As a result the VCO follows the frequency fluctuations of the heterodyne beat since the voltage on the VCO corresponds to the fluctuations of the frequency noise of the heterodyne beat. If the feedback loop bandwidth is high enough, the VCO can track any frequency fluctuations $\delta\nu(t)$ which represent different processes going on in the system. As a result frequency fluctuations will be followed by voltage fluctuations $\delta V(t)$. The discriminator slope D_ν [V/Hz] is the main parameter of such a frequency discriminator. It possesses the sensitivity to convert frequency fluctuations $\delta\nu(t)$ to voltage fluctuations $\delta V(t)$. Different devices have different discriminator slopes. The higher the discriminator slope, the better conversion of the frequency noise which is achieved. If we know the PSD output voltage and the discriminator slope D_ν [V/Hz], the frequency noise PSD can be calculated

$$S_{\delta\nu}(f) = \frac{S_V(f)}{D_\nu^2} \tag{113}$$

where $S_{\delta\nu}(f)$ [$\mathrm{Hz}^2\ \mathrm{Hz}^{-1}$] is the frequency noise PSD of the input signal and $S_V(f)$ [$\mathrm{V}^2\ \mathrm{Hz}^{-1}$] is the voltage noise PSD. A voltage from the PI controller can be calibrated to the frequency noise within the bandwidth of the feedback loop if the $[\frac{V}{Hz}]$ relationship is known. The PLL characteristics are adjusted via the PI controller for which the gain and bandwidth can be adjusted over a large scale. An operating schematic of the PLL discriminator, used for the linewidth determination of the frequency comb tooth, is presented in Figure 7.

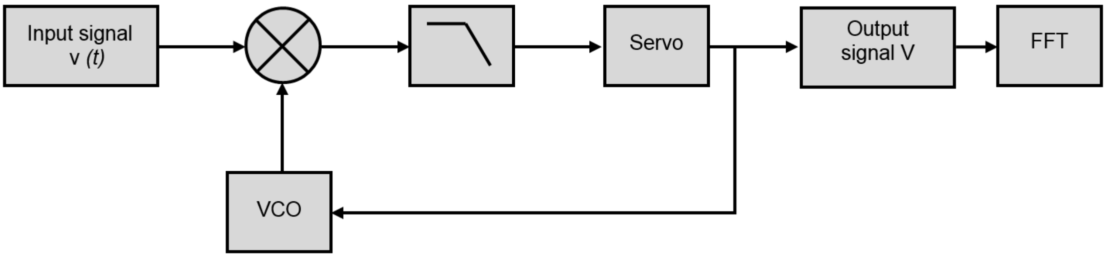

Figure 7. PLL configuration: VCO - voltage-controlled oscillator; FFT - fast Fourier transform.

The VCO operated in the 199-210 MHz region with a 1.5-MHz V^{-1} sensitivity. A ZAD 1+ mixer was used for phase detection. The difference frequency was low pass filtered (LPF) at 10-MHz frequency so that high frequencies were affected. Then the signal was used as an error input for a high bandwidth proportional-integral (PI) servo controller whose corner frequency (low pass frequency) could be adjusted from 10 Hz to 1 MHz.

8.5 Frequency comb linewidth and noise characterization

The frequency noise PSD of the heterodyne beat signal between the comb line of the OPO centered at 1557-nm and the cavity stabilized ultra narrow linewidth CW laser was analyzed. The noise properties of the comb line could be extracted from the frequency noise PSD measurement. The schematics for detecting the heterodyne beat were the same as mentioned earlier except we changed the CW laser from Rb locked one to an ultra stable one with a linewidth of less than 10 Hz. A 50/50 splitter (AFW Technologies, FOBC-2-15-50-C) was used to combine the light from the OPO and the CW laser. Before it, the broadband pulse from the OPO was spectrally filtered to about 0.3-0.4 nm (37-49 GHz) width by a diffraction grating (DG), which corresponded to about 130 comb lines passing the filter. Then the comb was combined with the single mode CW laser on the fiber coupled photodiode (Thorlabs DET01CFC). A heterodyne beat at 20-25 MHz frequency with a SNR of more than 30 dB for a 100-kHz RBW was detected (see Figure 8).

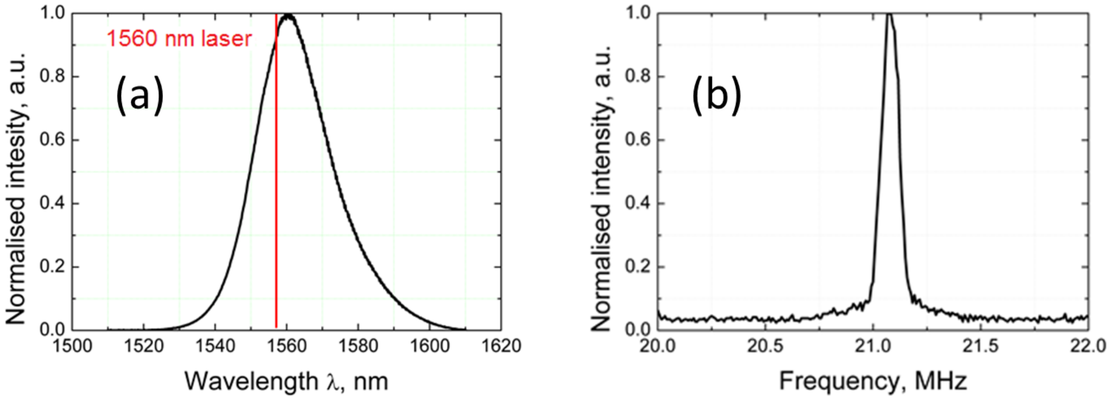

Figure 8. (a) Spectrum of the pulse from OPO in comparison with the ultra stable narrow line CW lasers linewidth, (b) Heterodyne beat between an OPO comb line and an ultra stable narrow linewidth CW laser. RBW=10 kHz.

After the heterodyne signal had been acquired, it was filtered, amplified and mixed with a reference signal to give a frequency around 207 MHz. Then this signal in the ZAD 1+ mixer (Mini-circuits) was demodulated with the PLL based frequency discriminator at 207-MHz frequency [49]. After the frequency mixer the filtered error signal was plugged into the New Focus PI controller (LB1005 servo controller) whose output was split into two channels. The first signal was used to adjust the voltage controlled oscillator so that the mixed frequency was locked at 0 Hz. The second demodulated beat signal was connected to a FFT spectrum analyzer (SR770

FFT Network Analyzer) for the frequency noise measurement. The measured optical comb line $S_V(f)$ noise could therefore be demodulated by the analog PPL frequency discriminator. The measured $S_V(f)$ noise PSD was used to determine the linewidth of the comb tooth.

The frequency noise contribution of the ultra-stable CW laser to the measured heterodyne beat frequency noise is insignificant. The frequency noise of the heterodyne beat corresponds only to the frequency noise of the comb line. The retrieved frequency noise spectral power density (PSD) of the locked f_{BEAT} is presented in Figure 9. The noise contribution of the frequencies to the linewidth are represented in the dotted black line [38]. The calculated value of the comb linewidth was about 70 kHz. The linewidth of the tooth was determined by noise in the repetition rate Nf_{REP} and f_{CEO}. In case of f_{REP}, noise was acquired in the range from 200 Hz to 3000 Hz, the frequency noise PSD which is present in the optical line noise spectrum. These noise peaks contributed the most to the optical linewidth calculated from the measured frequency noise spectrum. The repetition rate noise was scaled up to the frequency of the N-th comb line and showed that repetition rate locking is the main noise source to the optical linewidth. The residual integrated phase noise had a servo bump at around 1 kHz frequency which was related to the bandwidths of the PZTs placed inside the Ti:sapphire laser. We measured the transfer function of the f_{REP} control via the fast PZT. The measured feedback bandwidth was limited by the PZT resonance to 2 kHz frequency. The frequency noise PSD of the heterodyne beat confirms this. In our configuration, the noise of the optical line at low frequencies (below 3 kHz) is determined by the repetition rate noise while the f_{CEO} impact is small. The f_{CEO} impact to the linewidth lies around the 27-30 kHz frequency band. This noise is associated with our green pump source used to pump the Ti:sapphire laser (presented in Chapters 4 and 5). The servo bump of the f_{CEO} feedback loop should be limited to several hundreds of Hz to kHz range [37].

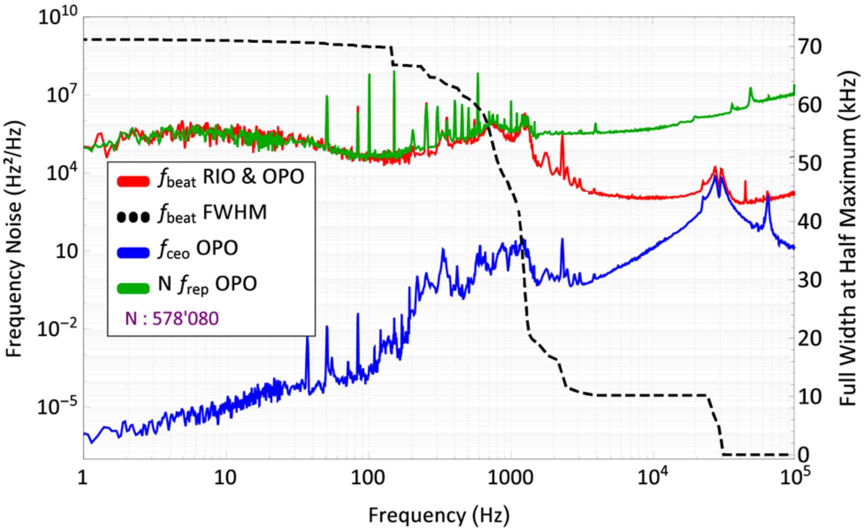

Figure 9. Frequency noise PSD of an optical line of the OPO at 1557 nm and corresponding contribution of f_{CEO} and Nf_{REP}. The optical linewidth retrieved from the frequency noise PSD using the approximation of Di Domenico et al [38] is also shown on the right vertical axis.

Repetition rate stabilization to an RF reference was achieved by applying a feedback voltage via a PI controller to two PZTs placed inside the Ti:sapphire laser cavity. In the first place, the third harmonic of f_{REP}=333 MHz was detected with a high speed InGaAs photodiode (DSC40S, up to 16 GHz). Once the repetition rate was stabilized, the frequency noise of the repetition rate was measured by the SpectraDynamics noise measurement system controller (SDI-NMSC equipment from SpectraDynamics). The signal was compared with the reference frequency. The schematic of the principle is shown in Figure 10. We took the same third harmonic and compared it against a 1-GHz frequency from a synthesizer referenced to the same H-maser with the SDI-NMSC unit. A 1-GHz frequency was taken directly from a TL-1000 commercial repetition rate locking device provided by Lasers Quantum and was amplified by +10 dB with an LNA-4050 RF amplifier to provide the +0 dBm signal strength required for frequency noise measurement.

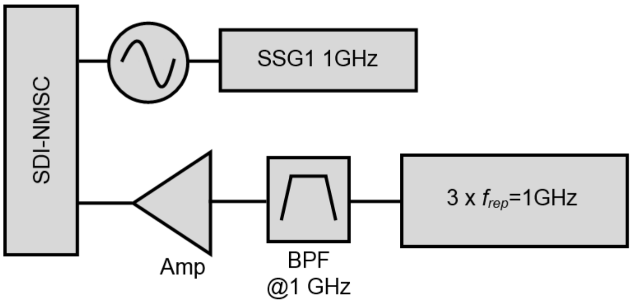

Figure 10. Schematics of the repetition rate phase noise measurement. The band-pass-filtered (BPF) 3rd order repetition rate harmonic was compared with 1-GHz reference.

The reference signal of 1-GHz frequency was taken from synthesized signal generator which was used for f_{REP} locking. Since we used the same synthesizer and detected signal for phase noise measurement as for repetition rate locking, it was an in loop phase noise measurement. The measured PSD of the locked and free-running repetition frequencies is shown in Figure 11.

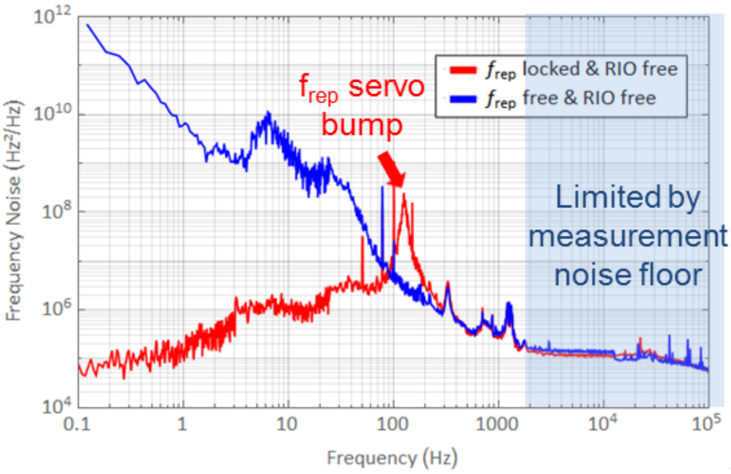

Figure 11. Frequency noise PSD of the stabilized and free-running repetition rate f_{REP}.

Our feedback loop could suppress frequencies below 100 Hz. This is the frequency where the measured locked and free-running frequency noise PSD curves separates. After the improvement of our feedback loop by employing a commercial TL-1000 unit for repetition rate locking, we were able to increase the bandwidth of our feedback loop to about 1 kHz, which is evident in Figure 12. The low frequency noise was reduced by our feedback loop in the range from 1 Hz to 1 kHz compared to the H-maser. An out of loop measurement for the locked repetition rate was done for comparison. With the high speed InGaAs photodiode we could detect repetition rate harmonics up to 16 GHz (DSC40S). The signal at 15-GHz frequency was too low to mix in the ZX05-24MHz-S+ frequency mixer and therefore we used four LNA-14G (+5V power supply) amplifiers to amplify the acquired signal so that we could efficiently extract an error signal. Into the second channel of the mixer a +12 mdB signal strength from an Agilent synthesizer (Agilent Technologies E82570, 250 kHz-40 GHz) at 14.99667510 GHz frequency was introduced. The error signal was set at 0 Hz. This error signal was used for phase noise and then for the frequency noise of the locked repetition rate measurement with the FFT network analyzer (SR770). The frequency noise PSD data for the out of loop measurement are presented in Figure 12. The servo bandwidth was around 1 kHz frequency, except in this case the low frequency noise was limited by the RF reference. For comparison the measured frequency noise of the heterodyne beat is presented. The frequency noise of the heterodyne beat at frequencies lower than 1 kHz was determined by the repetition rate locking quality and the RF reference noise floor. An improvement could be made by stabilizing the repetition rate to a better performance RF reference.

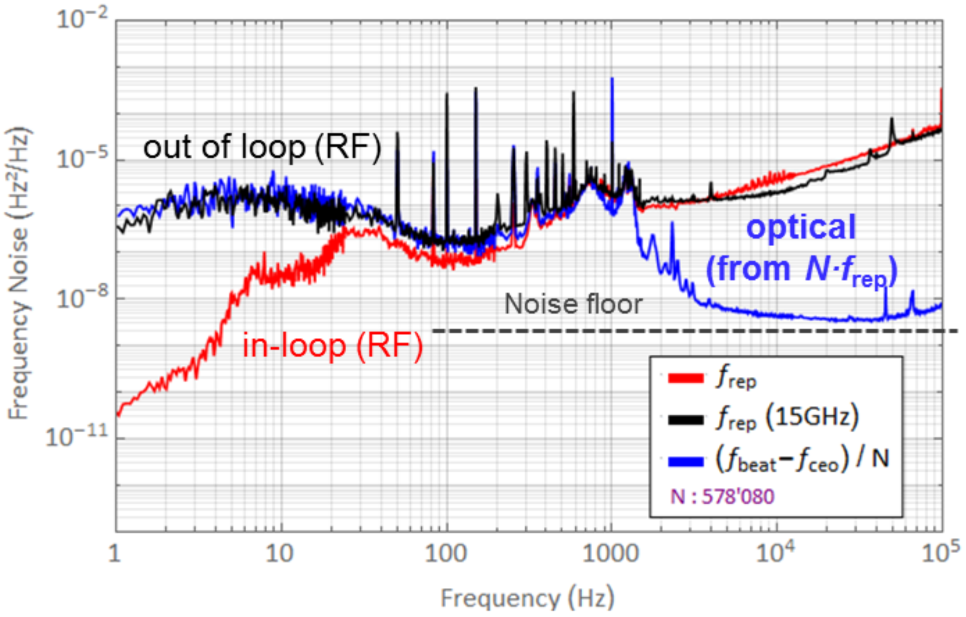

Figure 12. Out of loop (blue), in-loop (red) frequency noise measurements of the repetition rate f_{REP} compared with the heterodyne beat frequency noise.

The cumulative phase noise of the locked repetition rate in out of loop measurement is presented in Figure 13. The total measured phase noise from 1 Hz to 100 kHz was 1.1 rad.

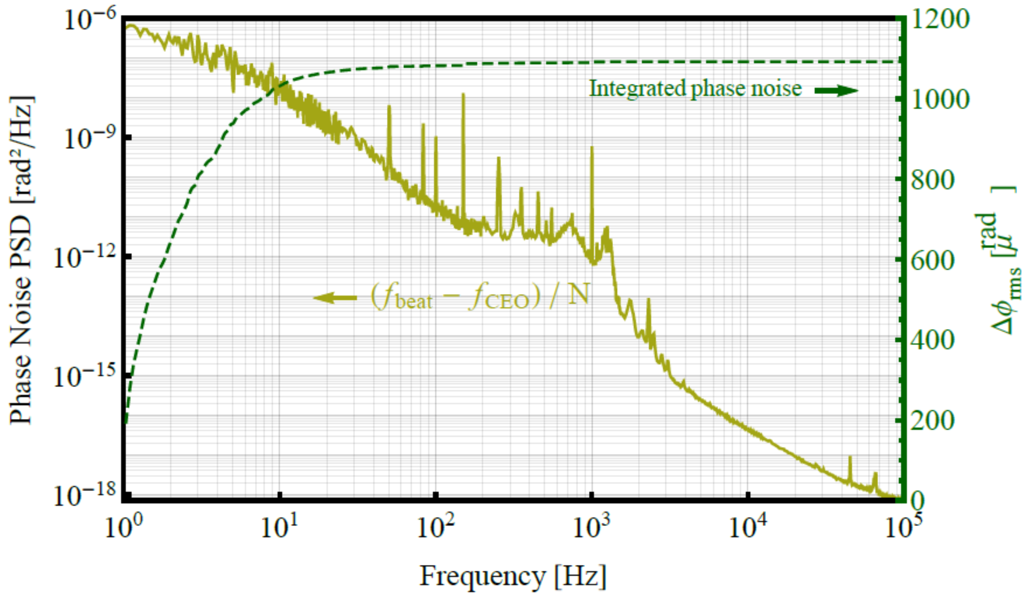

Figure 13. Cumulative phase noise of the locked repetition rate in out of loop measurement.

Along with the repetition rate phase and frequency noise PSD measurements, a noise characterization of the locked f_{CEO} was performed. The locked f_{CEO} acquired with avalanche photodetector and recorded by RF spectrum analyzer is presented in Figure 14 showing tight f_{CEO} locking limited by the resolution of the device.

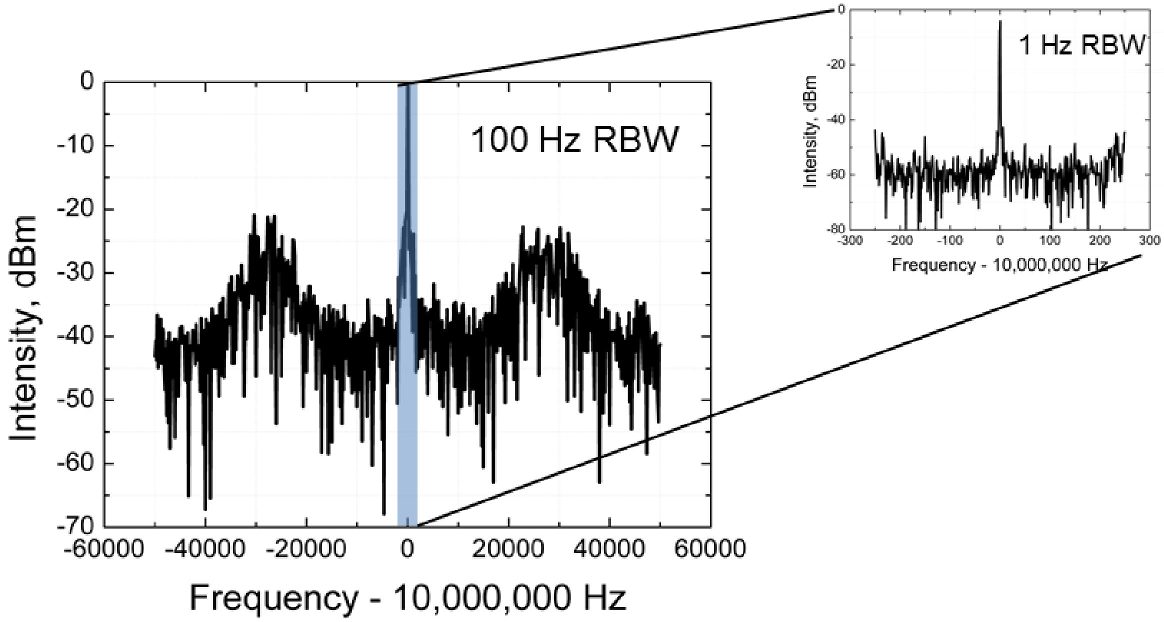

Figure 14. RF spectrum of the locked signal f_{CEO} at 1560-nm central wavelength recorded with 100-Hz resolution bandwidth. Inset: instrument limited 1-Hz resolution bandwidth showing locked f_{CEO} at 10 MHz frequency

A digital phase detector (DXD 200 MenloSystems module) was used to detect the phase fluctuations between the locked carrier-envelope-offset f_{CEO} and a 10-MHz external H-maser reference source. The DXD 200 module can be used not only for f_{CEO} stabilization but also for frequency noise detection. The phase detector can track $\pm 32 \times 2\pi$ phase difference of two introduced signals. The output signal from the phase counter was plugged into an analog to digital converter to generate a signal in voltage. The phase discriminator factor was $D_\varphi = \frac{3.3V}{32*2\pi} = 0.016[\frac{V}{rad}]$. The voltage noise PSD is related to the phase noise and frequency by

$$S_{\delta V}(f) = D_\nu^2(f) S_{\delta\nu}(f) = D_\varphi^2(f) S_{\delta\varphi}(f) \tag{114}$$

where D_ν is frequency discriminator slope, $S_{\delta\nu}$ is the frequency noise PSD, D_φ is the phase discriminator and $S_{\delta\varphi}$ is the phase noise PSD. The frequency noise PSD and phase noise PSD are related by

$$S_{\delta\nu}(f) = f^2 S_{\delta\varphi}(f) \tag{115}$$

resulting in a frequency sensitivity of the phase discriminator of

$$D_\nu(f) = \frac{D_\varphi(f)}{f} \tag{116}$$

The error signal was sent to a SR770 FFT network analyzer for phase noise measurement. By knowing the phase discriminator slope, we could calculate the frequency sensitivity for the DXD200 device and therefore the frequency noise PSD of the f_{CEO} which is presented in Figure 15.

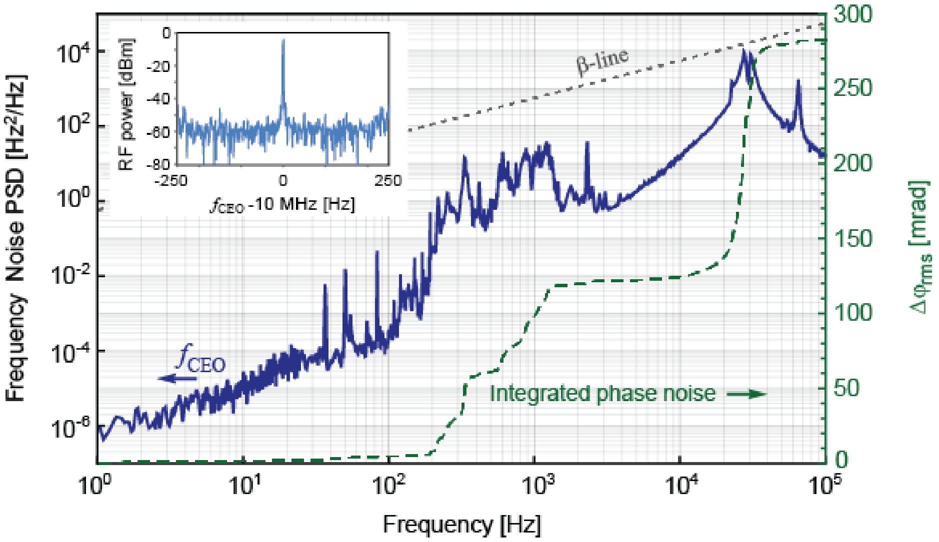

Figure 15. Frequency noise of the locked f_{CEO} of the OPO. The integrated cumulative phase noise of 300 mrad measured. The inset shows the coherent peak in the CEO RF beat (500-Hz span with 1-Hz resolution bandwidth).

The f_{CEO} frequency of the signal pulse was locked via a fast piezo (PZT3) placed inside the OPO cavity. As we presented, the carrier-envelope-offset contribution to the linewidth of the comb line was about 10 kHz. The main contribution of the noise was measured at 27-30 kHz frequencies which is related with our Pure Finess green pump laser. For a frequency comb from an OPO a reversal point in the f_{CEO} relation with the pump alignment was found similar to that presented in [50]. The reversal point was important for achieving better f_{CEO} stabilization and therefore reducing the linewidth of the comb line. There is a particular point of alignment where we are reducing the relative intensity noise (RIN), which leads to a much better stabilization of the f_{CEO}. At that point the contribution of the Ti:sapphire pump power fluctuations to the f_{CEO} noise can be minimized ensuring the smallest possible linewidth of the comb line. This effect was measured during the optimization of the heterodyne beat locking. As one of the adjusment mirrors for the green Pure Finesse CW laser light was adjusted, a better locking of the f_{CEO} was acquired. There was a certain position where better locking could be achieved and it was related with the better overlap between the green pump and modelocked pulse oscillating in the Ti:sapphire laser resulting in supression of high frequency noise fluctuations of the Ti:sapphire laser which were coupled to the OPO.

8.6 Conclusions

We have carefully measured the absolute frequency of the ^{87}Rb D_2 F=2-3 transition, by counting f_{REP}, f_{CEO} and f_{BEAT} acquired by heterodyning one comb line from an OPO with a 1557-nm CW laser, which was locked to a Rb cell using a saturated absorption method. A frequency of $192,114,057.632 \pm 0.037$-MHz of the CW laser was calculated which overlaps with the frequency determined using a commercial Er:fiber comb. The measured uncertainty of the absolute frequency was 15 kHz. The frequency stability of the beat note was 10^{-11} at a 1-s gate time in the optical domain while the repetition rate fractional instability was 10^{-12} and for the carrier-envelope-offset was 10^{-8}. The H-masers stability was 10^{-12} for a 1-s gate time. The reduction of the CW laser sensitivity to temperature fluctuations could increase the stability of the beat note and therefore reduce the uncertainty in the absolute frequency determination of the comb line.

Fully characterized noise properties of the frequency comb at 1557 nm were presented. The ultrashort pulses at 1557 nm were generated in a PPKTP based synchronously pumped OPO. These pulses were fully stabilized and referenced to a H-maser source via repetition rate and carrier-envelope-offset feedback loops. For the purpose of characterization, the heterodyne beat between the comb line from the OPO and the ultra narrow cavity stabilized laser was acquired. The tight lock of the optical comb line resulted in a 70 kHz linewidth (1 second). In comparison a 100-kHz linewidth of the Er-fiber comb (FC1500-250 from Menlosystems) was measured. The noise properties demonstrated that the linewidth is mainly limited by the repetition rate since f_{CEO} contribution is almost negligible for all frequencies. The main noise contribution is at frequencies lower than 4-5-kHz compared to 100-kHz in case of the fiber comb, which means that it should be much easier to achieve a tight phase lock characterized by the linewidth of the comb line. A feedback bandwidth of 100-kHz is challenging to achieve whereas 4-5-kHz is relatively easy. In our system the main limitation are PZTs which can not reach higher bandwidth than 1 kHz. The implementation of diode current feedback or a new type of PZT holder could increase the feedback bandwidths up to thousands of kHz resulting in much better f_{CEO} and f_{REP} locking. Better stability performance could be obtained by referencing the frequency comb to an ultra narrow linewidth CW laser.

References

[1] S. Weyers, V. Gerginov, N. Nemitz, R. Li and K. Gibble, "Distributed cavity phase frequency shifts of the caesium fountain PTB-CSF2," Metrologia 49, 82–87 (2012).

[2] J. Guena, M. Abgrall, D. Rovera, P. Laurent, B. Chupin, M. Lours, G. Santarelli, P. Rosenbusch, M. Tobar, R. Li, K. Gibble, A. Clairon, S. Bize, "Progress in atomic fountains at LNE-SYRTE," IEEE Trans. Ultrason. Ferroelectr. Freq. Control 59, 391–410 (2012).

[3] L. Hollberg, S. Diddams, A. Bartels, T. Fortier, and K. Kim, "The measurement of optical frequencies," Metrologia 42, 105-124 (2005).

[4] J. L. Flowers and B. Petley, "Progress in our knowledge of the fundamental constants of physics," Rep. Prog. Phys. 64, 1191–1246 (2001).

[5] S. N. Lea, "Limits to time variation of fundamental constants from comparison of atomic frequency standards," Rep. Prog. Phys. 70, 1473–1523 (2007).

[6] T. M. Fortier and others, "Precision atomic spectroscopy for improved limits on variation of the fine structure constant and local position invariance," Phys. Rev. Lett. 98, 070801 (2007).

[7] A. Antognini and others, "Proton structure from the measurement of 2S-2P transition frequencies of muonic hydrogen," Science 339, 417–420 (2013).

[8] T. Steinmetz, T. Wilken, C. Araujo-Hauck, R. Holzwarth, T. W. Hänsch, L. Pasquini, A. Manescau, S. D'Odorico, M. T. Murphy, T. Kentischer, W. Schmidt, and T. Udem, "Laser frequency combs for astronomical observations," Science 321, 1335–1337 (2008).

[9] D. A. Braje, M. S. Kirchner, S. Osterman, T. M. Fortier, and S. A. Diddams, "Astronomical spectrograph calibration with broad-spectrum frequency combs," Eur. J. Phys D 48, 57-66 (2008).

[10] J. Alnis, A. Matveev, N. Kolachevsky, T. Udem, and T. W. Hansch, "Subhertz linewidth diode lasers by stabilization to vibrationally and thermally compensated ultralow-expansion glass Fabry-Perot cavities," Physical Review A 77, 053809 (2008).

[11] B. C. Young, F. C. Cruz, W. M. Itano, and J. C. Bergquist, "Visible lasers with subhertz linewidths, " Physical Review Letters 82, 3799 (1999).

[12] T. Rosenband and others, "Frequency ratio of Al^+ and Hg^+ single-ion optical clocks; metrology at the 17th decimal place," Science 319, 1808–1812 (2008).

[13] A. A. Madej and others, "$^{88}Sr^+$ 445-Thz single-ion reference at the 10^{-17} level via control and cancellation of systematic uncertainties and its measurement against the si second," Phys. Rev. Lett. 109, 203002 (2012).

[14] C.W. Chou, D. B. Hume, J. C. J. Koelemeij, D. J.Wineland, and T.Rosenband, "Frequency comparison of two high-accuracy Al^+ optical clocks," Phys. Rev. Lett. 104, 070802 (2010).

[15] L. D. Turner, K. P. Weber, C. J. Hawthorn, and R. E. Scholten, "Frequency noise characterisation of narrow linewidth diode lasers," Optics Communications 201, 391-397 (2002).

[16] T. W. Hansch, "Nobel lecture: passion for precision," Rev. Mod. Phys. 78, 1297–1309 (2006).

[17] J. L. Hall, "Nobel lecture: defining and measuring optical frequencies," Rev. Mod. Phys. 78, 1279–1295 (2006).

[18] S.A. Diddams, Th. Udem, J.C. Bergquist, E.A. Curtis, R.E. Drullinger, L. Hollberg, W.M. Itano, W.D. Lee, C.W. Oates, K.R. Vogel, D.J. Wineland, "An Optical Clock Based on a Single Trapped $^{199}Hg^+$ Ion," Science 293, 825 (2001).

[19] U. Sterr, C. Degenhardt, H. Stoehr, C. Lisdat, H. Schnatz, J. Helmcke, F. Riehle, G. Wilpers, C. Oates, L. Hollberg, "The optical calcium frequency standards of PTB and NIST," C. R. Phys. 5, 845 (2004).

[20] T. Hansch, "Nobel lecture: Passion for precision," Reviews of Modern Physics 78, 1297-1309 (2006).

[21] J. Ye, H. Schnatz, and L. Hollberg, "Optical frequency combs: From frequency metrology to optical phase control," IEEE Journal of Selected Topics in Quantum Electronics 9, 1041-1058 (2003).

[22] Feng-Lei Hong, Atsushi Onae, Jie Jiang, Ruixiang Guo, Hajime Inaba, Kaoru Minoshima, Thomas R. Schibli, Hirokazu Matsumoto, and Kenichi Nakagawa, "Absolute frequency measurement of an acetylene-stabilized laser at 1542 nm," Opt. Lett. 28, 2324-2326 (2003).

[23] C. S. Edwards, G. P. Barwood, H. S. Margolis, P. Gill, W. R. C. Rowley, "High-precision frequency measurements of the $\nu(1) + \nu(3)$ combination band of (C_2H_2)-C-12 in the 1.5μm region," Journal of Molecular Spectroscopy 234, 143-148 (2005).

[24] Alan A. Madej, A. John Alcock, Andrzej Czajkowski, John E. Bernard, and Sergei Chepurov, "Accurate absolute reference frequencies from 1511 to 1545 nm of the $\nu(1) + \nu(3)$ band of (C_2H_2)-C-12 determined with laser frequency comb interval measurements," Journal of the Optical Society of America B-Optical Physics 23, 2200-2208 (2006).

[25] Alan A. Madej, John E. Bernard, A. John Alcock, Andrzej Czajkowski, and Sergei Chepurov, "Accurate absolute frequencies of the $\nu(1) + \nu(3$ band of (C_2H_2)- C-13 determined using an infrared inode-locked Cr:YAG laser frequency comb," Journal of the Optical Society of America B-Optical Physics 23, 741-749 (2006).

[26] Jie Jiang, John E. Bernard, Alan A. Madej, Andrzej Czajkowski, Sibyl Drissler, and David J. Jones, "Measurement of acetylene-*d* absorption lines with a self-referenced fiber laser frequency comb," Journal of the Optical Society of America B-Optical Physics 24, 2727-2735 (2007).

[27] Moon, H.S., W.K. Lee, and H.S. Suh, "Absolute-frequency measurement of an acetylene-stabilized laser locked to the P(16) transition of (C_2H_2)-C-13 using an optical-frequency comb," IEEE Transactions on Instrumentation and Measurement 56, 509-512 (2007).

[28] Mitsuru Musha, Yosuke Tamura, Kenichi Nakagawa, Ken-ichi Ueda, "Practical optical frequency measurement system around 1.5μm based on an acetylene-stabilized laser-locked optical frequency comb," Optics Communications 272, 211-216 (2007).

[29] Balling, P. and P. Kren, "Absolute frequency measurements of wavelength standards 532 nm, 543 nm, 633 nm and 1540 nm," European Physical Journal D 48, 3-10 (2008).

[30] L. S. Ma and others, "Frequency uncertainty for optically referenced femtosecond laser frequency combs," IEEE J. Quant. Electron. 43, 139–46 (2007).

[31] L. A. M. Johnson, P. Gill and H. S. Margolis, "Evaluating the performance of the NPL femtosecond frequency combs agreement at the 10^{-21} level," Metrologia 52, 62-71 (2015).

[32] R. Holzwarth, T. Udem, T. W. Hansch, J. C. Knight, W. J. Wadsworth, and P. S. J. Russell, "Optical frequency synthesizer for precision spectroscopy," Physical Review Letters 85, 2264 (2000).

[33] D. J. Jones, S. A. Diddams, J. K. Ranka, A. Stentz, R. S. Windeler, J. L. Hall, and S. T. Cundiff, "Carrier-envelope phase control of femtosecond mode-locked lasers and direct optical frequency synthesis," Science 288, 635-639 (2000).

[34] M.J. Thorpe, K.D. Moll, R.J. Jones, B. Safdi, J. Ye, "Broadband Cavity Ringdown Spectroscopy for Sensitive and Rapid Molecular Detection," Science 311, 1595 (2006).

[35] A. Bartels, D. Heinecke, and S. A. Diddams, "10-GHz selfreferenced optical frequency comb," Science 326, 681-681 (2009).

[36] B.R. Washburn, S.A. Diddams, N.R. Newbury, J.W. Nicholson, M.F. Yan, C.G. Jorgensen, "Phase-locked, erbium-fiber-laser-based frequency comb in the near infrared," Opt. Lett. 29, 250 (2004).

[37] F. Quinlan, T. M. Fortier, M. S. Kirchner, J. A. Taylor, M. J. Thorpe, N. Lemke, A. D. Ludlow, Y. Jiang, and S. A. Diddams, "Ultralow phase noise microwave generation with an Er:fiber based optical frequency divider," Optics Letters 36, 3260-3262 (2011).

[38] Gianni Di Domenico, Stephane Schilt, and Pierre Thomann, “Simple approach to the relation between laser frequency noise and laser line shape”, Appl. Opt. 49, 4801 (2010).

[39] Holman, R.J.Jones, A. Marian, S.T.Cundiff, J.Ye, “Detailed studies and control of intensity-related dynamics of femtosecond frequency combs from mode-locked Ti : sapphire lasers,“ Ieee Journal of Selected Topics in Quantum Electronics 9, 1018-1024 (2003).

[40] S.A. Meyer, J.A. Squier, S.A. Diddams, “Diode-pumped Yb:KYW femtosecond laser frequency comb with stabilized carrier-envelope offset frequency,“ Eur. Phys. J. D. 38, 19 (2008).

[41] J. Jiang, C. Mohr, J. Bethge, M. Fermann, I. Hartl, in CLEO Europe and EQEC 2011. Conference Digest, Paper PDB 1. OSA Technical Digest (CD) (Optical Society of America, Washington, 2011).

[42] C. Erny, K. Moutzouris, J. Biegert, D. Kuhlke, F. Adler, A. Leitenstorfer, U. Keller, “Mid-infrared difference-frequency generation of ultrashort pulses tunable between 3.2 and 4.8 μm from a compact fiber source,“ Opt. Lett. 32, 1138 (2007).

[43] N. Leindecker, A. Marandi, R.L. Byer, K.L. Vodopyanov, “Broadband degenerate OPO for mid-infrared frequency comb generation,“ Opt. Express 19, 6296 (2011).

[44] C. Wang, T. Herr, P. Del’Haye, A. Schliesser, R. Holzwarth, T.W. Haensch, N. Picque, T. Kippenberg, in CLEO:2011—Laser Applications to Photonic Applications. Paper PDPA4, OSA Technical Digest (CD) (Optical Society of America, Washington, 2011).

[45] http://www.laserquantum.com/products/detail.cfm?id=54

[46] T. I. Ferreiro, J. Sun, and D. T. Reid, “Frequency stability of a femtosecond optical parametric oscillator frequency comb,“ Opt. Express 19, 24159–24164 (2011).

[47] R. Matthey, F. Gruet, S. Schilt, and G. Mileti, accepted for publication in Optics Letters (2015).

[48] http://www.t4science.com/products/

[49] S. Schilt, N. Bucalovic, L. Tombez, C. Schori, V. Dolgovskiy, G. Di Domenico, M. Zaffalon, P. Thomann, “Frequency discriminators for the characterization of narrow-spectrum heterodyne beat signals: Application to the measurement of a sub-hertz carrier-envelope-offset beat in an optical frequency comb,“ Rev. Sci. Instrum. 82, 123116 (2011).

[50] K. Holman, R. Jones, A. Marian, S. Cundiff, and J. Ye, “Detailed studies and control of intensity-related dynamics of femtosecond frequency combs from mode-locked Ti:sapphire lasers,“ IEEE Journal of Selected Topics in Quantum Electronics 9, 1018-1024 (2003).

Chapter 9. Conclusions

This chapter reviews the experimental work presented in the thesis and contains conclusions from the results. I will discuss the performance of the frequency comb systems based on OPO, the results from Fabry-Pérot filtering, locking the f_{CEO} of the comb to an optical frequency (ECDL), absolute frequency measurement of a diode laser, and future work which should improve the system performance.

9.1 Technical summary and conclusions

In Chapter 3 the 333-MHz repetition rate Ti:sapphire laser and the OPO system were presented. A modelocked Ti:sapphire laser emitted 32 nm bandwidth pulses at 800 nm centre wavelength. The measured pulse duration was 29 fs with an average output power of 1.45 W. The laser was used to pump a ring-type 4-mirror PPKTP-based OPO. The OPO was able to produce visible sum-frequency pulses, which were necessary for f_{CEO} detection.

Chapter 4 presented a fully stabilised frequency comb in the mid-IR region tunable from 1.95-4.00 μm. Part of the pump pulse was used to generate supercontinuum in a PCF, which was combined with the OPO sum-frequency mixed light for f_{CEO} detection. The f_{CEO} of the idler pulse was stabilised to a 10-MHz external reference via a feedback loop. The implementation of a new design of PPKTP crystal enabled us to produce continuously tunable combs operating across >2000-nm in the mid-IR. The integrated cumulative phase noise from 1 Hz-64 kHz was 1.2 rad over an observation time of 1 second. The primary noise contribution appeared in the 25-35 kHz range. This noise increase was caused by intensity fluctuations in the pump source for the Ti:sapphire laser which coupled into the OPO as both intensity and phase noise. The results showed a broadly tunable and lockable frequency comb at every idler wavelength in the mid-IR region. The new crystal design made it possible to ensure a strong heterodyne beat for every idler wavelength which was not demonstrated before. This technology can be applied for every periodically poled nonlinear crystal and therefore a strong SFM light can be generated which is needed for f_{CEO} detection. The results were presented at CLEO:2015 USA and CLEO:Europe Munich and published in Optics Letters.

In Chapter 5 I demonstrated for the first time a femtosecond harmonically pumped OPO frequency comb, whose repetition frequency was increased by a factor of three (1 GHz) compared to its Ti:sapphire pump laser (333 MHz). Allan variance measurements from both the fundamentally-pumped and harmonically-pumped OPOs showed comparable results. The integrated phase noise (1 Hz–64 kHz) of the f_{CEO} frequency increased by around 1-rad under harmonic pumping, with the increase arising in the 300–1000 Hz band associated with acoustic noise contributions to the resonator stability. The results showed that harmonic operation did not substantially compromise the frequency-stability of the comb. In this way I showed that it is possible to obtain similar phase noise and jitter performance from a harmonically pumped

OPO compared with another, which is pumped fundamentally.

Chapter 6 demonstrated a new method to stabilize the f_{CEO} of a 1030 nm Yb:fiber laser comb which used an ECDL. I also decribed a linear f_{CEO} stabilization method for a 1-GHz OPO synchronously pumped by a Ti:sapphire laser. An external cavity diode laser was developed and characterized for use as an optical reference in an f_{CEO} locking scheme for the pump pulses. An Allan deviation of 235 kHz at a 50 s gate time was measured for the Yb:fiber laser. This method bypasses the nonlinear interferometer limitations related to pump-supercontinuum generation in a PCF as the repetition rate increases, which is important because operation at 1-GHz frequency begins to reach the limit of the conventional OPO comb locking scheme. Such direct comb stabilization to an optical standard is promising as the repetition rate of the pump laser increases even further. In a linear stabilization method there is no nonlinear process involved which is unlike the case for the f-2f method, where we are using a nonlinear crystal within the interferometer. Here we are not limited by the nonlinear effects which are extremely sensitive to the pump pulse peak power. This enables us to use higher repetition rate lasers, which have lower peak power.

In Chapter 7 a low-finesse Fabry-Pérot cavity was implemented to achieve a multi-GHz mode spacing. The longitudinal modes of a 333-MHz OPO frequency comb were filtered to >10 GHz by employing a Fabry-Pérot cavity whose length was locked to the ECDL and directly to the fundamental frequency comb. A 333-MHz sideband suppression of up to 19 dB was measured after a single pass of the Fabry-Pérot cavity. The use of a Fabry-Pérot cavity enables us to significantly increase the mode spacing of the comb from the multi-MHz to the multi-GHz region, which is extremely important for such applications as astronomical spectrograph calibration. At the moment there is only one company, which produces 10-GHz modelocked Ti:sapphire lasers and the use of simple Fabry-Pérot cavity bypasses the need for a high repetition rate laser which is not cost effective in comparison with a Fabry-Pérot cavity.

Finally, in Chapter 8 an absolute frequency measurement was performed. We measured the absolute optical frequency of the ^{87}Rb D_2 F=2-3 transition, by counting the f_{REP}, f_{CEO} and f_{BEAT} frequencies acquired by heterodyning one comb line from the OPO with a 1557-nm CW laser, which was locked to a Rb cell using the saturated absorption method. A frequency of $192,114,057.632 \pm 0.037$ MHz of the CW laser was inferred from this measurement, a result which overlaps with the frequency determined using a commercial Er:fiber comb. The measured uncertainty of the absolute frequency was 15 kHz. The frequency stability of the beat note was 10^{-11} at a 1-s gate time in the optical domain while the repetition rate fractional instability was 10^{-12} and for the carrier-envelope-offset was 10^{-8}. The H-maser stability was 10^{-12} for a 1-s gate time. The measurement accuracy was limited by the stability of the microwave frequency standard and by interferometric noise in the fiberized setup of the Rb-stabilized laser. The tight lock of the optical comb line resulted in a 70 kHz linewidth. The main limitation was the PZTs which could not reach a higher bandwidth than 1 kHz. The main result is that we determined the frequency of a Rb transition, which was in good agreement with the value retrieved using a commercial Er:fibre comb. The OPO comb showed great potential in these measurements and moreover, demonstrated that it could surpass the current systems available in the market by careful improvements.

9.2 Future improvements

The integrated phase noise (1 Hz-64 kHz) of the f_{CEO} frequency for the idler pulse was around 1.2-rad, while for the harmonic operation the cumulative phase noise was around 2.7 rad. The best performance of the comb stabilisation was obtained by some careful adjustments and by optimising the setting of the internal gain of the pump laser which resulted in a cumulative phase noise of 0.3 rad for the signal pulses locked at 1.56 µm. Nevertheless, the characteristic increase of the noise was the same: the noise was increasing in the 300–1000 Hz band associated with acoustic noise contributions to the resonator stability, which couples directly to f_{CEO} in a femtosecond OPO. The dominant noise for all the measurements was at 27-kHz from the pump laser. We could improve the results straight away by replacing the pump source and the noise at 1-kHz frequencies could be suppressed by increasing the locking loop bandwidth. The environmental stability in the laboratory is critical for suppressing the noise at 1-kHz frequency. In the OPO two PZTs were used for locking the f_{CEO} which as we found out could not suppress higher than 1 kHz frequency noise. The stability of f_{CEO} could be improved by using a position-sensitive-detector (PSD) [1]. The approach uses low-cost components, requires no nonlinear interferometry, offers long-term stability to the few-MHz level (or 1% of f_{REP}), has a wide capture range and is compatible with feed-forward techniques which can enable f_{CEO} stabilization at MHz loop bandwidths.

In the new method for stabilizing the offset frequency of a 1030 nm Yb:fibre laser comb, the comb was locked to a Rb transition line. In the first experiment, we measured an Allan deviation of 2 MHz at a 1 s gate time. The locking performance could be improved by implementing a hardware-based approach and by replacing a quite noisy galvanometer motor with a PZT actuator. In a second experiment, the f_{CEO} of a 1-GHz OPO was stabilised. The measured Allan deviation was several Hz at a 1 second gate time which was a huge improvement. In both experiments, an ECDL was used as an optical reference in an f_{CEO} locking scheme for the pump pulses. The Rb-stabilised ECDL could be improved by using more sensitive electronics, which could require less dither amplitude which is obvious in the phase noise results. The phase noise PSD measurements revealed a poorer locking in comparison with when a supercontinuum based lock was used due to the MHz-level linewidth of the ECDL. Nevertheless, the demonstrated stability of the comb without the need for a nonlinear interferometer reduced the complexity of the detection scheme and increased the range of pump sources, which could be used in f_{CEO} stabilisation. The stability of the comb was sufficient for spectroscopy applications.

All those generated combs could be filtered to multi-GHz mode spacing in a low-finesse Fabry-Pérot cavity. A 333-MHz sideband suppression of 19 dB could be improved in a double-pass system. The FP cavity locking stability could be improved by isolating it better from mechanical and vibrational noise. For example, rubber mounts between the breadboard and post holders could further improve the stability of the system. This is essential in order to achieve good Fabry-Pérot cavity locking and therefore effective filtering of the frequency comb. Moreover, introducing boxing and beam pipes around the optical beam path could shield the system from air turbulence and sudden temperature changes.

9.3 Outlook for OPO frequency combs

One of the main areas of emphasis in this thesis is the generation of novel frequency combs in the mid-IR region. An extension of the wavelength into the longer wavelength mid-IR region is inevitable with the main application being focused on spectroscopy. For example, materials like OP-GaAs allow fs OPOs to reach 5.6 μm [2]. Potentially a very atractive nonlinear crystal is ZGP, which can be pumped only above 2 μm but offers longer mid-IR wavelengths which can be used in the sensing, security and medical sectors. The comb extension to higher wavelengths drives the evolution of the modelocked pump lasers too. Modelocked lasers such as Cr^{2+}:ZnSe or Cr^{2+}:ZnS have been improving over the last years and their longer wavelengths (2.3 μm) enabled crystals like ZGP to be pumped. Increasing the pump repetition rate of the comb is also beneficial, because higher repetition rate combs with high average power are in demand for applications in astronomy and metrology. In the future we can expect to see the frequency comb wavelength being pushed further into the infrared with mode spacings reaching 10 GHz and above.

References

[1] Karolis Balskus, Melissa Fleming, Richard A. McCracken, Zhaowei Zhang and Derryck T. Reid, "Carrier-envelope offset frequency stabilization in a femtosecond optical parametric oscillator without nonlinear interferometry," submitted to Optics Letters.

[2] Viktor O. Smolski, Sergey Vasilyev, Peter G. Schunemann, Sergey B. Mirov, and Konstantin Vodopyanov, "Cr:ZnS Laser-pumped Subharmonic GaAs OPO with an Instantaneous Bandwidth 3.6-5.6 μm," CLEO: 2015 OSA Technical Digest (online) (Optical Society of America, 2015), paper SW4O.2 (2015).